Weld Residual Stress Profiles for Structural Integrity Assessment

Thesis

The Open University

Faculty of Mathematics, Computing & Technology

Department of Engineering and Innovation

Materials Engineering Group

WELD RESIDUAL STRESS PROFILES FOR STRUCTURAL INTEGRITY ASSESSMENT

by

JINO MATHEW

March 2015

A THESIS SUBMITTED TO THE DEPARTMENT OF ENGINEERING AND INNOVATION OF THE OPEN UNIVERSITY FOR THE DEGREE OF DOCTOR OF PHILOSOPHY

DATE OF SUBMISSION: 31 MARCH 2015

DATE OF AWARD: 29 OCTOBER 2015

ProQuest LLC.
789 East Eisenhower Parkway
P.O. Box 1346
Ann Arbor, MI 48106 – 1346

Abstract

Economic and safe management of operating nuclear power plants can be highly dependent on the structural integrity assessments for safety critical pressure vessels and piping components. In engineering fracture assessment procedures the full (3-D) residual stress field at a welded joint is usually simplified by considering a representative one-dimensional profile through the wall-thickness of the stress tensor component acting normal to the crack face. The stress intensity factor, calculated from this estimated through-thickness stress profile, is used directly in the fracture assessment. Therefore, assessments of defects in welds can be highly sensitive to the through-thickness residual stress profiles assumed in the calculations. There is a need for reliable characterisation of residual stresses in welded structures such as in stainless steel girth welded pipes as there are a lot of discrepancies in the current methodologies used. For example, bounding residual profiles found in fitness for service assessment procedures have been based on examination of residual stress measurements, finite element weld simulation and expert judgment. This approach suffers from the drawback that the upper bound curve can increase as more measurements and data scatter are obtained. The consequence of this is that structural integrity assessments of defective plant can be over-conservative by a large margin, and may lead to unnecessary and costly repair or inspection.

This thesis illustrates how a neural network model, can be developed and applied to predict through-thickness residual stress profiles in austenitic stainless steel pipe girth welds for simplified fracture assessments. The model is validated by comparing predictions with new experimental measurements made using neutron diffraction and contour method. The new measurements were undertaken by fabricating six pipe girth welds with a range of wall-thickness, weld heat input and weld groove geometries. The robustness of the

developed artificial neural network (ANN) approach is demonstrated by sensitivity studies in input variables and training data. The performance and suitability of the ANN approach is discussed by comparison with stress profiles recommended in defect assessment procedures. This is followed by an evaluation of whether the use of neural network bounding profiles can lead to non-conservative estimates of stress intensity factor in fracture assessments. The neural network approach shows sufficient potential to be developed into an alternative prediction tool for use in fracture assessment of welded components.

Acknowledgements

First of all it gives me immense pleasure to thank Prof. John Bouchard and Dr. Richard Moat for their invaluable guidance and supervision. I would like to express my deep sense of gratitude to Prof. Mike Fitzpatrick (Head of the department) for his continuous support during the project. The research was funded by Lloyds Register Foundation, EDF Energy and AMEC and their support is greatly acknowledged. Special thanks to Dr. Foroogh Hosseinzadeh and Dr. Sanjoo Paddea for their contribution especially in applying Contour method during the project.

Neutron beam time allocated at the Institut Laue-Langevin is gratefully acknowledged. I also acknowledge the support from beamline scientists Dr. Alex Evans and Dr. Thilo Pirling. I would like to sincerely thank the R6 residual stress sub-group for useful discussions and constructive feedback. I acknowledge Dr. John Francis and Mr. Paul English for fabrication of test specimens. I am indebted to Mr. Pete Ledgard, Mr. Damian Flack, Mr Ian Norman and Mr. Stan Hiller for their workshop support and assistance with many of the experiments. I would also like to thank Dr. Yeli Traore, Dr. Burak Toparli, Dr. David Githinji, Mr. Jeferson Oliviera and other colleagues for their assistance during the project. I thank all the staff members in my department for their helpful suggestions.

I leave my word of thanks to my friends for their continuous support and encouragement. Last but not the least; I thank my better half Neenu, for her patience and love throughout the project duration.

Jino Mathew

March 2014

Dedicated to the memory of

Late Dr. Raja Sundaresan

Chief scientist, Non-ferrous materials research development centre (NFTDC)

Previously Associate Director, ARCI, India

For his encouragement, mentorship and motivation to pursue a research career.

Preface

This thesis is submitted for the degree of Doctor of Philosophy of The Open University, United Kingdom. The work described in this thesis was carried out in the Department of the Engineering and Innovation, Faculty of Mathematics, Computing and Technology, between February 2011 and March 2015 under the supervision of Prof. John Bouchard, Dr. Richard Moat and Prof. Michael Edwards Fitzpatrick.

Except where clearly referenced, the work is entirely the author's own work. None of this work has been submitted for a degree or qualification at this or other university. Some of the results of this work have been published in an academic journal, conference proceedings and as oral or poster presentations as listed below:

Mathew, J., Moat, R.J., Bouchard, P.J. (2013) Prediction of Pipe Girth Weld Residual Stress Profiles Using Artificial Neural Networks. *ASME Pressure Vessels & Piping Division Conference*, Paris, France, July 14-18, PVP2013-97491.

Smith, M.C., Muransky, O., Smith, D., Do, S.C., Bouchard, P.J., **Mathew, J.** (2014) Modelling and Measuring Residual Stresses in Pipe Girth Welds: Lessons From the Style Framework 7 Project. *ASME Pressure Vessels & Piping Division Conference*, Anaheim, California, USA, July 20-24, 2014, PVP2014-29005.

Mathew, J., Moat, R.J., Bouchard, P.J. (2014) Optimised Neural Network Prediction of Residual Stress Profiles for Structural Integrity Assessment of Pipe Girth Welds. *ASME Pressure Vessels & Piping Division Conference*, Anaheim, California, USA, July 20-24, 2014, PVP2014-28845.

Mathew, J., Moat, R.J., Bouchard, P.J., Fitzpatrick, M.E. (2013) Prediction of weld residual stress profiles using neural networks, Poster Presentation, NMUM seminar, Warwick, UK

Mathew, J., Moat, R.J., Paddea, S., Fitzpatrick, M.E., Bouchard, P.J., Prediction of residual stresses in girth welded pipes using an artificial neural network approach, *International journal of pressure vessels and piping* (Under review)

Table of contents

Chapter 1

Introduction

1.1 Background

Fusion welding is the most widely used joining process in the power generation, petrochemical and construction industries. Over the past decade, characterisation of welding-induced residual stresses in pressure vessel and piping systems has received increasing attention from mechanical engineering research communities owing to its impact on the economy and safety of operating plant. The application of heat during a welding process results in complex transient temperature fields and can introduce high magnitude residual stresses in the component upon cooling. This can have an adverse effect on the lifetime and performance of welded components, as the presence of tensile residual stresses can be detrimental leading to crack initiation and growth, for example from stress corrosion cracking or creep, and an increased risk of catastrophic failure by fracture [1].

Residual stresses are generated as a result of some form of displacement misfit; for example owing to differential thermal expansion or localised plastic deformation [2]. In multi-pass welds, the weldment is subjected to transient thermal-mechanical cyclic loading conditions that may harden or soften the material. Quantifying the magnitude and distribution of residual stresses in these components with high certainty is a challenging task because of the large number of interacting factors such as welding parameters, geometry, composition, microstructure, phase transformations, and the thermal and mechanical properties of the weld and parent materials, [3] and [4]. Therefore management

of residual stresses in the design, manufacture and operation of functional plants still represent a major challenge for engineers.

Whenever defects (flaws or cracks) in power plant components are discovered during construction or routine inspection of high value or safety critical structures, an assessment of the life, integrity and safety of the structure may be required. The method of assessment used depends on the industry concerned. Fracture mechanics based assessment procedures, such as R6 [4] account for the interaction of primary and secondary loads where stresses due to mechanical loading such as pressure, self-weight or long range structural constraint are categorised as primary loads and those due to temperature variation and welding residual stress are considered as secondary loads. The outcome of this engineering critical assessment will determine whether defects are repaired, components replaced or whether a rigorous inspection regime need to be implemented to monitor further degradation.

For instance, EDF Energy recently temporarily shut down four advanced gas cooled nuclear reactors (AGR) of similar design as a precautionary measure after finding a large defect associated with a non-stress relieved stainless steel girth weld in one of the boilers at Heysham 1 power station [5]. Evidently the origin and structural significance of this defect with respect to the safety of the plant needs to assessed before the reactors can be taken back on line. Such assessments rely upon predictive models which have been extensively validated [6]. Figure 1.1 provides an overview of nuclear power stations currently operating in the UK with their net capacity and lifetime. Interestingly seven out of sixteen stations entered decommissioning after 1997, resulting in a decline of the generation of UK's electricity by nuclear power. Therefore, life extension of the UK's AGRs may potentially save billions of pounds for the economy. On the other hand, safety of operating power plants is of paramount importance as unexpected structural failure can lead to disasters and should be avoided at any cost.

Station	Reactor type	NET capacity in Megawatts (MW)	Year commissioned	Age in years
Hunterston B	2 AGRs	890	1976	37
Hinkley Point B	2 AGRs	870	1976	37
Hartlepool	2 AGRs	1,180	1983	30
Heysham 1	2 AGRs	1,160	1983	30
Dungeness B	2 AGRs	1,040	1983	30
Heysham 2	2 AGRs	1,220	1988	25
Torness	2 AGRs	1,190	1988	25
Sizewell B	1 PWR	1,191	1995	18

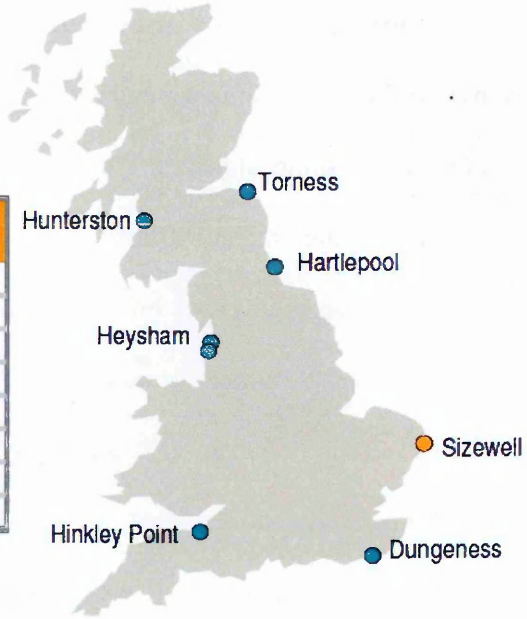

Figure 1.1. Details of the operating nuclear power stations in the United Kingdom [6]

For through-thickness measurement of residual stresses in a component, non-destructive techniques based on diffraction particularly neutron diffraction and synchrotron X-ray diffraction are usually employed. Likewise deep hole drilling, sectioning and the contour method techniques are the most frequently applied destructive methods to determine the magnitude and distribution of residual stresses through the wall thickness. In spite of the fact that a diverse range of techniques is available for measuring residual stresses, all methods have their respective advantages and disadvantages. A general classification of techniques is to group them as destructive, semi-destructive and non-destructive. Destructive and semi- destructive methods employ an inverse process to calculate the relaxed stresses during cutting or drilling operations performed on the specimen. In semi-destructive methods, only a small portion of material is destroyed while the remaining part of the component stays intact. Non-destructive techniques do not alter the component and commonly consist of diffraction based methods that apply the principle of Bragg's law.

Structural integrity assessment codes such as BS7910 [7], R6 [4] and API 579 [8] simplify the three dimensional residual stress field at a welded joint by selecting an idealized one-dimensional stress distribution along a line through the wall thickness. Bounding profiles recommended in BS7910 and the R6 procedure for defect assessments have been developed based on examination of residual stress measurements accumulated over many years, finite element weld simulation and expert judgment. This approach suffers from the drawback that the upper bound curve can increase as more measurements are obtained. The consequence of this is that structural integrity assessments of defective plant can be overly conservative by a large margin, and may lead to unnecessary and costly repair or inspection.

Finite element (FE) modelling of the welding process is increasingly being used to provide a full field residual stress characterisation by simulating the complex interaction between heat flow and material properties over a wide range of temperatures [9]. However, the final residual stress distributions can be biased by the analyst's judgements in appropriate assumptions, boundary conditions and modelling procedures. Moreover, the FE simulations are complex because of the large number of interacting factors that need to be considered and importantly model predictions need to be validated with experimental measurements for safety-critical applications.

With rapid development in measurement techniques such as neutron diffraction, the contour method and incremental deep hole drilling (IDHD), higher quality and more reliable data are becoming available characterising through-thickness residual stress profiles in weldments. Thus there is an opportunity to utilize the increasing database of high quality measurement data.

Artificial neural networks (ANNs) [10] are flexible non-linear models based on empirical regression that can be applied to multi-variate, noisy datasets to discover complex relationships, which is particularly useful when there is a large set of example data available for training and where it is difficult to provide a physically-based modelling solution. ANNs can offer very high processing speed, have the ability to learn and generalize solutions from a set of specific examples to solve problems in pattern recognition, data analysis, optimization, classification and control [11]. In this thesis, a novel method based on artificial neural networks is developed to predict through-thickness residual stress profiles for austenitic stainless steel pipe girth welds and validated using new experimental measurements.

1.2 Objectives

The objective of this thesis is to address the research question, "Can artificial neural networks trained using historical measurements be used to characterise generic though-wall residual stresses profiles in austenitic stainless steel pipe girth welds?" The work includes:

- Development of an ANN approach for predicting through thickness residual stress profiles in pipe girth welds using historical experimental measurements for training.
- Validation of the method by acquiring new high quality measurements using multiple experimental techniques such as neutron diffraction and the contour method.
- Studies that demonstrate the robustness of the developed ANN approach.
- Development of upper bound profiles using the artificial neural network that are more realistic than profiles currently in use.

1.3 Layout of the Thesis

The work commences with a review of the literature relevant to addressing the research question. Chapter 3 presents residual stress results from neutron diffraction and contour method measurements on six new as-welded pipe girth welds that are later used for validating the new modelling approach. The ANN modelling is described in Chapter 4 elucidating how the network is trained, selection of governing input parameters and how the modelling results compare with the validation residual stress measurements. Chapter 5 discusses how the ANN prediction can be used to define upper bound residual stress profiles. The conservatism of the ANN profiles is evaluated by inspecting the variation in stress intensity factor for postulated defects of increasing size and comparing the results with stress intensity factors based on measured profiles and the simplified bounding solutions given in current assessment codes. This chapter concludes with a general discussion illustrating the scope of the project and how the profiles can be used in structural integrity assessments. Finally, conclusions are presented in Chapter 6 with ideas for future work.

Chapter 2

Literature review

2.1 Residual stresses

2.1.1 Introduction to residual stresses

Residual stresses are defined as the stresses that exist within the material in the absence of any external loads or constraints and are self-equilibrating in nature i.e. resultant force and moment generated must be zero in the structure. Residual stresses are introduced as a consequence of fabrication processes such as welding, machining, forming and also as a result of heat treatment, impact and abrasion. Residual stresses are generated as a result of some form of misfit; for example owing to differential thermal expansion or localised plastic deformation [2]. The residual stresses introduced during fabrication of structures can combine with tensile structural loads and may lead to unexpected or premature failures. The presence of tensile residual stresses in components can be detrimental leading to crack initiation and growth, for example from stress corrosion cracking or creep, and an increased risk of catastrophic failure by fracture [1].

Residual stresses have been classified as type I, II and III [12] according to the length scale over which they equilibrate. Type I refers to the macro-stresses that develop in a component on a scale several times larger than the grain size of the material or the scale of the structure typically of the order of several millimetres. Type II and type III are the micro-residual stresses that vary on a length-scale of an individual grain and within a single grain respectively. Type II stresses are generally present in polycrystalline or multi-phase materials as inter-granular stresses resulting from plastic anisotropy and type III

stresses are associated often with point defects and dislocations appearing in individual grains. In structural integrity assessments of power plant welds containing macroscopic defects the focus is on Type I stresses rather than the role of Type II and III residual stresses in determining micro-structural behaviour and initiation of cracking [13]. Figure 2.1 gives an illustration of the different types of residual stresses and typical examples of misfits that can cause macro and micro stresses [14].

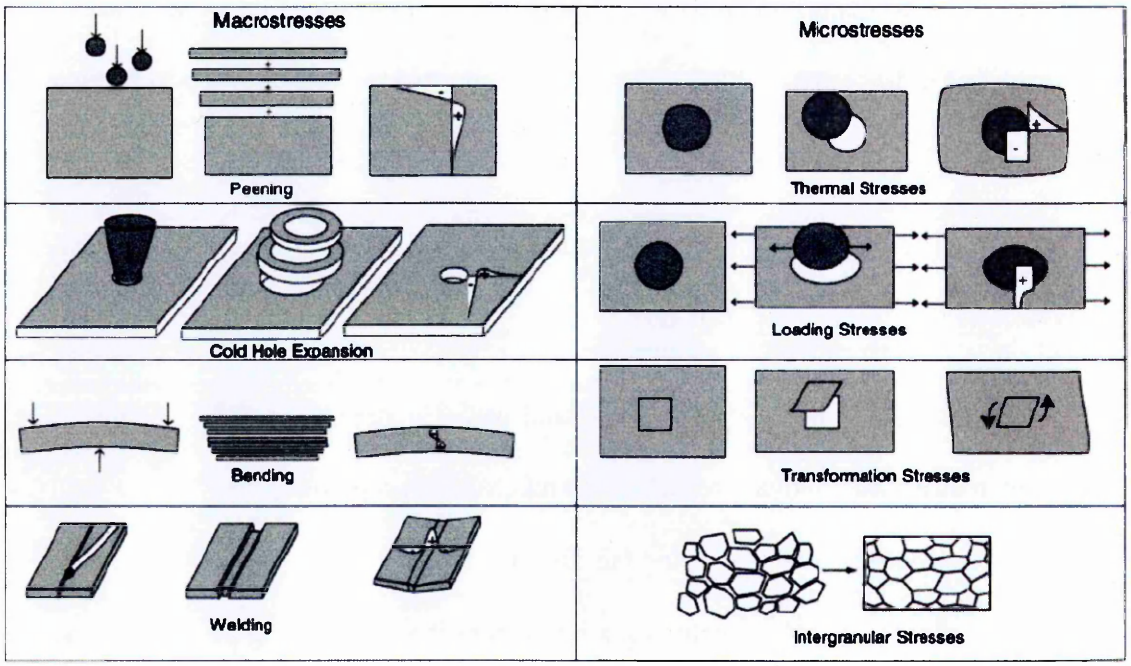

Figure 2.1. Illustration of different type of residual macro and micro stresses (process on the left, misfit in the centre and the resulting stress pattern on the right) [14].

2.1.2 Welding induced residual stresses

Fusion welding is the most widely used joining process for power generation, petrochemical and construction industries. It involves localised melting of the surfaces to be joined with or without the addition of molten filler metal. The application of heat during a welding process results in complex transient temperature fields which can introduce high magnitude tensile residual stresses in the component upon cooling. This can have an adverse effect on the lifetime and performance of welded components thereby affecting the economic and safe management of operating power plants as tensile residual stress can accelerate brittle fracture, buckling, stress corrosion cracking and creep, and reduce the fatigue life [15], [16] and [17].

The major factors that determine what residual stresses are present in welded components are as follows [3],

- The material properties of the weld and parent materials, including composition, microstructure, thermal properties and mechanical properties.
- The geometry of the parts being fabricated.
- The welding procedure including joint preparation, the welding parameters and the pass sequence in multi pass welds (final weld capping passes are critical as it can have a significant influence on the end through-thickness stress profile).
- The restraints applied to parts being welded with the aid of external fixtures.
- Initial stress state prior to welding.
- Local geometrical features such as weld start and stop positions.
- Micro-structural changes and associated phase transformation.

Moreover, in multi-pass welds, earlier passes and the heat affected zone in the near vicinity undergo thermal cyclic loading from subsequent passes causing complex material hardening/softening behaviour in the weldment [18]. The welding physics (e.g. arc and weld pool phenomena) also contribute to the final residual stress distribution. The complex interaction of these physical processes [13] is schematically represented in Figure 2.2. Residual stresses arising from fusion welding are considered to involve a combination of thermal, mechanical and metallurgical processes. Quantifying accurately the magnitude and distribution of residual stresses in a welded joint is a challenging task due to the complex interaction of many variables and non-linear nature. Presently, it is computationally challenging to account for all these factors and therefore simplifying assumptions are often required for arriving at acceptable results.

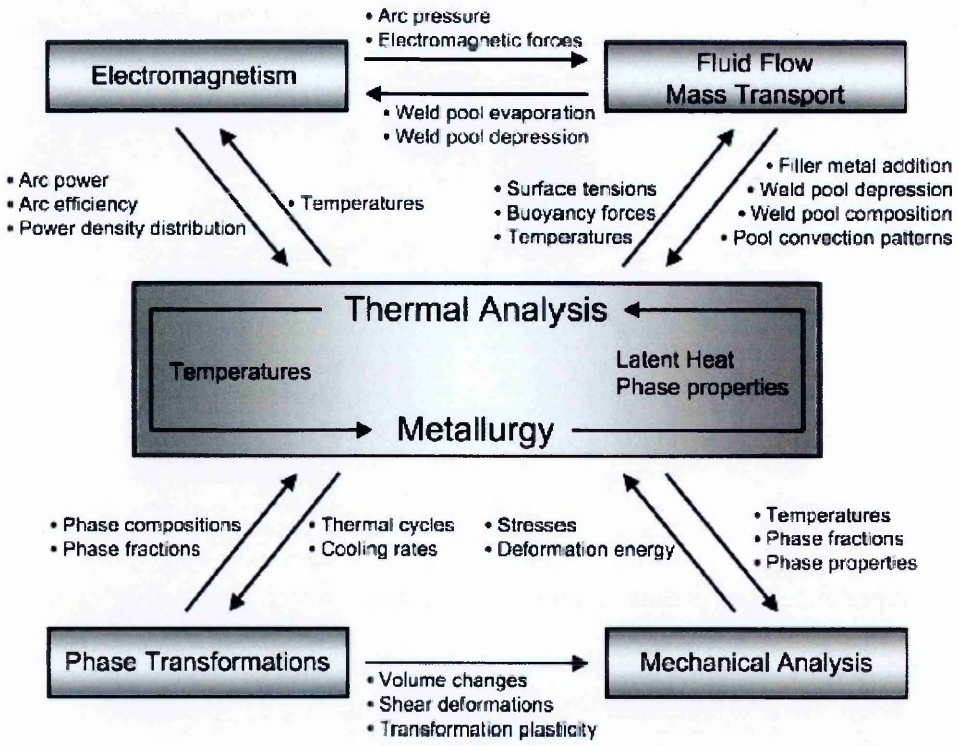

Figure 2.2. Schematic representation of interactions of physical processes in arc welding [13].

2.2 Residual stresses of stainless steel components in Nuclear Power Plants (NPPs)

Welding is still the major joining and repair technology for Nuclear Power Plant (NPP) components. The nuclear power industry places much emphasis on developing materials with better weldability and optimisation of process parameters and consumables [19]. Welding processes such as GTAW (Gas Tungsten Arc Welding), MMAW (Manual Metal Arc Welding), SAW (Submerged Arc Welding) and Narrow gap TIG (Tungsten Inert Gas) continue to dominate. Residual stresses are introduced inherently, to varying degrees, by these processes. The magnitude and distribution of residual stresses are strongly influenced by the geometry of the structure [20]. Residual stress distributions can be classified according to the geometry type and are generally grouped into the following categories [4],

1. Pipe butt welded joints
2. Pipe seam welds
3. Plate butt welded joints
4. T-butt welded joints
5. Repair welds
6. Closure welds

Circumferential butt welds are extensively used in pressure vessels, boilers, steam headers, Superheater and Reheater tubing applications which require high creep strength and thermal fatigue resistance [21].

Stainless steels can be broadly divided into five categories: ferritic, martensitic, austenitic, duplex (ferritic and austenitic) and precipitation hardened stainless steels. Austenitic steels represent the largest in terms of production within the group and can be used in service at temperatures of upto about 650 °C. The austenite structure is retained at room temperature by adding nickel as the major alloying element (>8 wt %). Type AISI

316 stainless steel is a modification of the basic stainless steel (18% Cr 8% Ni-Grade 304), with molybdenum (2-3%) which substantially improves the general corrosion resistance of the alloy, in particular resistance to pitting corrosion [22].

Other elements commonly found within these alloys include manganese, nitrogen and carbon. Type 316L is a low carbon alloy containing a maximum of 0.03% C whereas Type 316H has higher carbon content (0.04-0.1%C). Esshete 1250 is an austenitic stainless steel with high manganese content (6.5%), with added vanadium and niobium to enhance creep strength is mostly used in boiler components.

Carbon strongly favours the formation of austenite and also forms carbides: such as M_3C, M_7C_3 and $M_{23}C_6$, where M is any strong carbide forming metal (in this case chromium). $M_{23}C_6$ is the most critical carbide in austenitic stainless steels since it can have a large effect on both corrosion and creep properties of the alloy [23]. $M_{23}C_6$ can be re-dissolved on heating the steel to the solutionizing temperature (1050-1150°C) followed by quenching to produce a 'precipitate free' steel. However $M_{23}C_6$ is re-precipitated preferentially in the grain boundaries at 550-750°C. This can lead to chromium depletion adjacent to the grain boundaries rendering the alloy sensitive to intergranular corrosion, also known as 'weld decay'. Therefore it explains why post weld heat treatment of austenitic steels is not a practical solution to relieve residual stresses from welding and hence welds not subjected to heat treatment in plant applications. On the other hand, phase transformations have a critical influence on the magnitude and distribution of residual stresses especially in ferritic and martensitic steels making post weld heat treatment an indispensable part of the fabrication process. For example, Paddea et al. [24] studied the variation of residual stress distributions in ferritic-martensitic steel before and after post weld heat treatment. The peak tensile residual stresses in the vicinity of the heat affected zone were reported to reduce from 600 MPa to 120 MPa after post weld heat treatment.

However, this thesis focuses on characterising residual stresses in circumferentially welded pipes made of austenitic stainless steel.

2.2.1 Magnitude and distribution of residual stresses in weldments

The magnitude and distribution of residual stresses in weldments are strongly dependent on the geometry, external or self-restraint during welding, the material properties, the heat input and welding process. Restraint in a welded joint is predominantly influenced by the use of fabrication aids such as tack-welds, jigs and the pass sequence in the case of multi-pass welds. A reasonable assumption as per BS-7910 [7] is to consider a maximum tensile stress equivalent to the yield strength of the weld or parent material. The tensile stresses will be of magnitude approximately equal to the yield if the following conditions are met [3].

- There is restraint against the free thermal contraction of the heated material
- The thermal contraction strain from the softening temperature to ambient or pre-heat temperature is greater than the yield strain of the material. This is defined in the equation below,

$$\alpha(T_s - T_o) \geq \sigma_Y / E, \qquad (1)$$

where α is the coefficient of thermal expansion; T_s the softening temperature; T_o the ambient or pre-heat temperature; E the Young's modulus; σ_Y the yield strength at ambient or preheat temperature.

Figure 2.3 shows the through-thickness distribution of residual stresses measured at the weld-centre line of a steel butt welded plate 60 mm thick along the three different orthogonal directions with no external restraint [25]. It can be seen that residual stress distributions in the three orthogonal directions are entirely different. This can be attributed to differences in restraint. The effect of bending and membrane restraint on the transverse

residual stresses in austenitic stainless steel welded plate is demonstrated in Figure 2.4 [26].

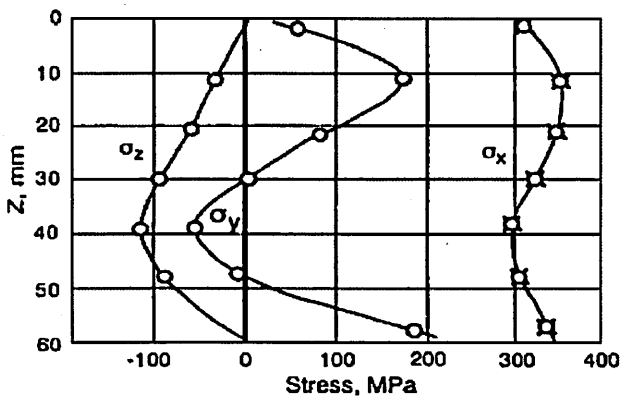

Figure 2.3. Through-thickness distribution of residual stresses measured at the weld-centre line of a steel butt welded plate, where σ_x, σ_y and σ_z are the stresses along longitudinal, transverse and through-thickness directions respectively [25].

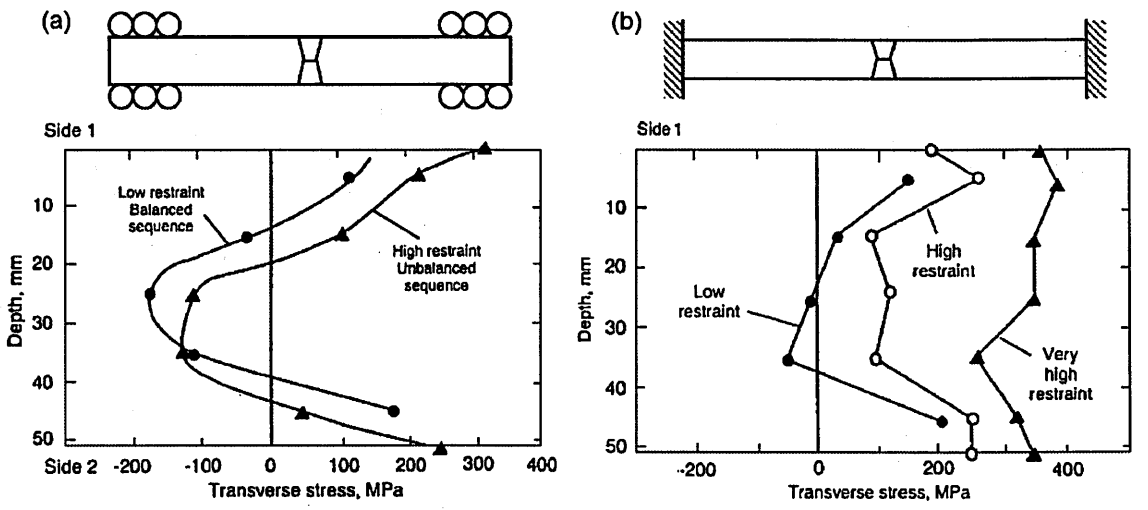

Figure 2.4. Effect of (a) bending restraint (b) membrane restraint on the transverse residual stresses in an austenitic stainless steel welded plate [26].

Circumferentially butt welded pipes are subjected to bending restraint across the weld due to the curvature of the parts being joined and also the interaction between circumferential membrane stresses and axial bending stresses which are both functions of the radial displacements of the pipe wall [27].

2.2.2 Residual stresses in austenitic steel girth welded pipes

A comprehensive range of residual stress measurements [18] were acquired in austenitic stainless steel pipe girth welds 10 – 20 years ago by the UK nuclear industry for the purpose of validating finite element residual stress simulations. Extensive residual stress measurements were performed in ten girth welded pipes 16-110 mm thick, made from various grades of AISI Type 316 austenitic stainless steel. The welded pipes cover a wide range of electrical heat input (E = 1- 2.4 kJ/mm) defined as P/v where P is the weld arc power and v is the advance rate, R/t ratio (mean radius over thickness) in the range 1.8-25, fabricated using different welding processes such as MMAW (Manual Metal Arc Welding), TIG (Tungsten Inert Gas) and SAW (Submerged Arc Welding) (see Table 2.1 for the details of girth welded pipes and stress measurements). A range of residual stress profiles were recommended for structural integrity assessment of non-stress relieved austenitic stainless steel welded pipes and the effect of different profile assumptions on the outcome of fracture assessments was illustrated. A more detailed critique about the paper is presented in section 2.4.3.

Ogawa et al. [28] measured the residual stress distributions on a 40 mm thick girth welded pipe made of austenitic stainless steel. The component consisted of two 316 stainless steel pipe sections joined together with a nickel based alloy using a single-V groove weld preparation. Maximum hoop residual stresses of magnitude 350 MPa were observed at a distance of 10 mm from the outer surface and the minimum stresses were observed close to the inside diameter. The axial residual stresses were found to be similar

in profile to the hoop but about 100 MPa lower in magnitude. Haigh et al. [29] investigated the evolution in residual stress profile by fabricating two austenitic stainless steel pipes with one having weld metal deposited up to half the pipe wall thickness and the latter with up to full wall thickness. The study was meant for the understanding of intermediate residual stresses generated partway through the welding process and evolution in residual stress profile on filling the weld.

Table 2.1 Details of austenitic stainless steel girth welded pipes and stress measurements reported in [18]. Notations: t – thickness, R/t – Radius to thickness ratio, E- electrical heat input, $\tilde{E}$ - electrical heat input per unit thickness, $\tilde{Q}$ - net heat input, $\sigma_{0.2\%\ PS}$ yield strength (0.2% proof stress), $\sigma_{1\%\ PS}$, (1% proof stress), $\sigma_{10\%\ PS}$ (10% proof stress).

	Weld C	OU20	SP19	SP37	S5VOR A & B	S5Old	S5New	S5NG	RR
t (mm)	15.9	20	19.6	37	65	65	65	62	110
R/t	25	3.8	10.5	5.3	2.8	2.8	2.8	3.0	1.8
Groove type	Double V	Outer J	Outer J	Outer J	Outer J	Outer J	Outer J	Narrow gap	Outer J
Weld type	SAW[a]	MMA	MMA	MMA	MMA	MMA	MMA	TIG	SAW
Efficiency, k	1.0	0.8	0.8	0.8	0.8	0.8	0.8	0.6	1.0
No. passes, N	4[a]	13	16	26	44	[b]	[b]	[b]	84
E (kJ/mm)	2.2	1.7	1.4	2.1	2.4	1.4	1.0	2.2	1.8
$\tilde{E}$ (J/mm^2)	136	85	69	55	37	21	15	35	17
$\tilde{Q}$ (J/mm^2)	136	68	55	42	30	17	12	21	17
Weld material	316L	316L	316L	316L	316L	316L	316L	316L	316
$\sigma_{0.2\%\ PS}$ (MPa)	476	446	446	446	446	446	446	446	483
Parent material	316L	316L	316H	316H	316H	316H	316H	316H	316
$\sigma_{0.2\%\ PS}$ (MPa)	296	264	212	287	287	287	287	287	230
$\sigma_{1\%\ PS}$ (MPa)	338	308	272	328	328	328	328	328	274
$\sigma_{10\%\ PS}$ (MPa)	480	-	-	461	461	461	461	461	-
Residual stress measurements	ND, SH, BRSL	ND	ND, SH, DH	DH	DH, SH	DH	DH	DH	DH, SH

ND, neutron diffraction; DH, deep hole; SH, surface hole; BRSL, block removal, splitting and layering.
[a]Outer V passes of double V-groove weld.
[b]Number of passes unknown.

2.3 Residual stress – Measurement and Modelling

2.3.1 Measurement of residual stresses

There is a diverse range of techniques available for measuring residual strains in welded components. The most commonly used measurement techniques are based on the strain relaxation principle (semi-destructive or destructive) or diffraction methods usually non-destructive. Other methods rely on the optical, acoustic and magnetic properties of the materials. A classification of the residual stress measurement techniques is presented in Table 2.2.

Table 2.2. Classification of residual stress measurement techniques, [30] and [31].

Measurement Technique	Stress profile 1D, 2D or 3D	Penetration	Surface/ Through-thickness
Non-destructive			
(1) Neutron diffraction	3D	< 60 mm	Through-thickness
(2) Synchrotron diffraction	3D	< 20 mm	Through-thickness
(3) X-ray diffraction	2D	< 5 μm	Surface
(4) Magnetic	1D	< 3 mm	Near Surface
(5) Ultrasonic	1D	> 10 mm	Through-thickness
(6) Raman	1D	< 1 μm	Surface
Semi-Destructive			
(1) Incremental Hole drilling	2D	1 mm	Near Surface
(2) Deep-hole drilling	2D	750 mm	Through-thickness
(3) Ring coring	2D	< 25 mm	Near Surface
(4) Incremental deep hole drilling	2D		Through-thickness
Destructive			
(1) Sectioning	2D	100 mm	Through-thickness
(2) Slitting	2D	>100 mm	Through-thickness
(3) Sach's boring	2D		Through-thickness
(4) BRSL	2D	50 mm	Through-thickness
(5) Contour method	2D	< 1000 mm	Through-thickness

Methods based on strain relaxation

The techniques relevant to pipe girth welds and the methods used to characterise residual stresses in this study are described in this section.

Incremental centre hole drilling (ICHD)

These techniques measure the strain relaxation due to material removal by using strain gauges on the surface of the specimen. Incremental hole drilling [32] is widely used for surface and near-surface residual stress measurement. The measurement procedure is relatively simple and the standardised version is available in ASTM Standard Test Method E837 [33]. A strain gauge rosette is first bonded to the surface of the component. A small hole at the centre of the strain gauge rosette is then introduced in a series of small steps and the relaxed strains are measured in all three directions. The magnitude and directions of the in-plane principal stresses are calculated from these strains as a function of drilled depth. The method can be performed in-situ and applied to a wide range of materials. However the use hole drilling method is limited by the measurement depth that can be achieved and is affected by plasticity when measuring stresses close to the yield strength of the material [34].

Block removal splitting and layering (BRSL) method

The BRSL method [35] can be used to measure residual stresses through the thickness in thick sections but destroys the sample in the process. The steps for undertaking BRSL measurements are described as [36]

- Block removal: removal of a block of material at the location where the residual stresses are to be measured
- Splitting: the block is split into two halves in such a way that the mid-plane is parallel to the inside and outside surfaces

- Layering: the process consists of removal of the layers parallel to the splitting plane from each of the halves followed by measuring the changes in dimensions for each layer.

The BRSL technique has produced measurements with an overall accuracy of ±50 MPa [37] in circumferential butt welded pipes but in recent years has become obsolete. The technique is not used in this dissertation but published BRSL measurements [18] are included in the training data for the ANN.

Deep hole drilling (DHD) method

The deep hole drilling technique developed at the University of Bristol is mainly applied to thick-section components. It is a semi-destructive method [38-40] as only a small core (sizes ranging from 5 - 20 mm in diameter) is removed from the component during measurement. The DHD method determines the residual stresses by measuring the change in distortions of a reference hole in a component after a column of material containing the reference hole at the axis is removed. Figure 2.5 shows various stages of the method [41], in the first step front and back bushes are attached on the specimen and in the second step, a small reference hole is drilled through the component at the location of interest. The diameter of the reference hole is accurately measured in step 3 using an air probe at different angular positions and at equal intervals around the hole axis. In step 4, a column of material coaxial to the reference hole at the axis is trepanned free of the component by using an electro-discharge machining technique. Finally step 5 consists of re-measuring the reference hole diameter using an air probe. Trepanning the column containing the reference hole releases residual stresses and the relaxation of the reference hole diameter is used to determine the in-plane strains and residual stress distribution.

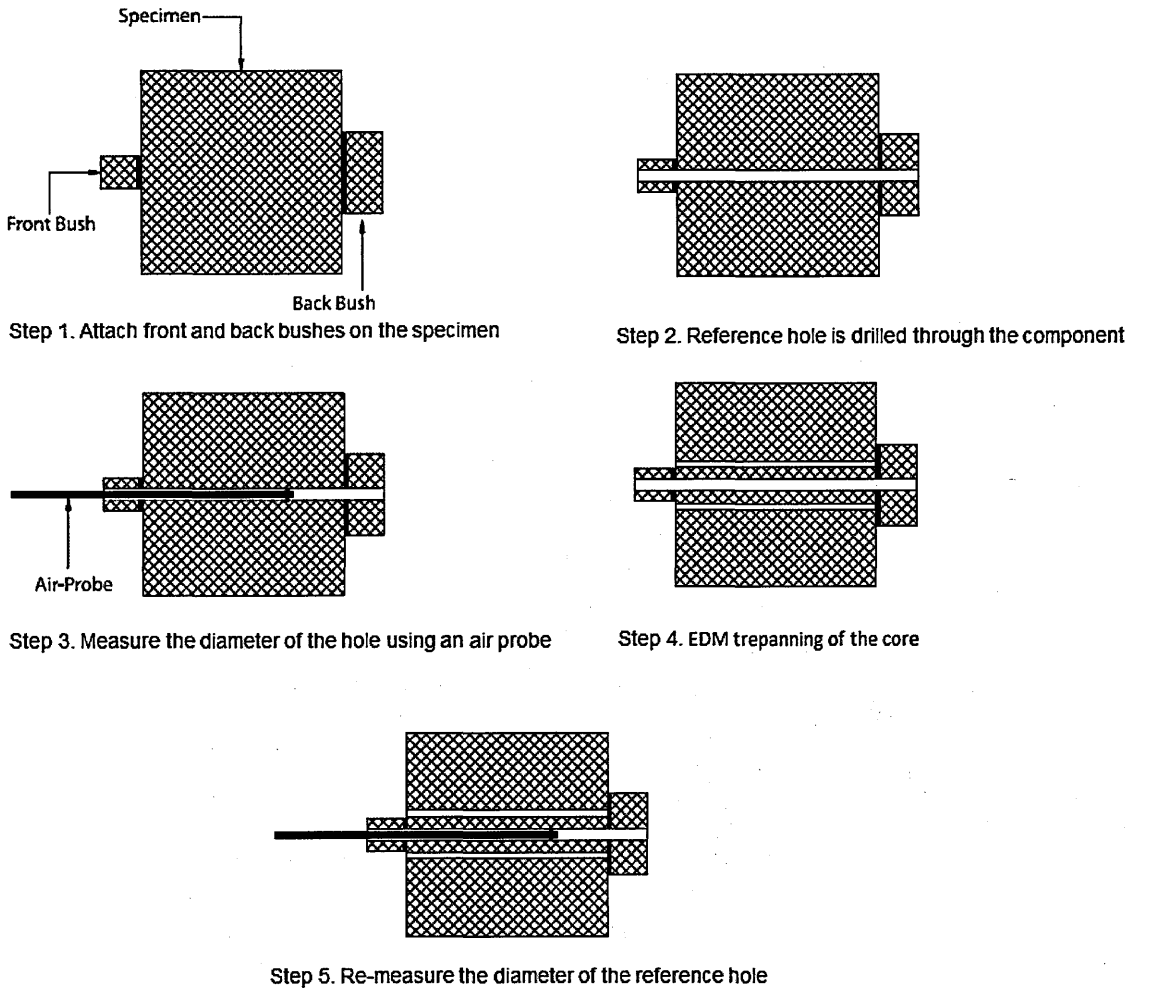

Figure 2.5. Various stages of the deep hole drilling technique [41].

Deep hole-drilling can be used for residual stress measurements over a wide range of materials and is not sensitive to the material microstructure. It has been successfully applied to measure residual stresses in complex geometries including pipe welded components, [28] and [42]. The DHD technique is capable of measuring two in-plane components of the stress tensor as a function of distance through the thickness and can be performed in-situ. Although the DHD technique has been successful in many cases there is evidence that suggests the method could fail in some cases, especially where the stresses are high and above 50% of the yield strength of the material [43, 44]. Hossain [43] reported the significance of plasticity in the residual stress distribution using the DHD technique. The incremental deep hole drilling (IDHD) technique [44, 45] was proposed to rectify this problem by trepanning the hole incrementally and using the intermediate

relaxation data after data each increment rather than measuring the hole diameter before and after trepanning in one cut. The IDHD approach has the advantage of measuring the deformation of the core without the need to account for the thermal effects during cutting. However the stresses are only determined at a limited number of intervals unlike the conventional DHD technique.

Contour method

The contour method, first proposed by Prime in 2000 [46, 47] is a destructive technique capable of measuring residual stresses in thick sections. It is based on Bueckner's principle [48], according to "If a cracked body subject to external loading or prescribed displacements at the boundary has forces applied to the crack surfaces to close the crack together, these forces must be equivalent to the stress distribution in an un-cracked body of the same geometry subject to the same external loading". The contour method measures a 2-D cross-sectional map of residual stress acting normal to the cross section of interest in a body and has been successfully applied in welds [49-50]. The component of interest is cut using wire electric discharge machining (EDM) and the deformation contours of the resulting relaxed cut surfaces are measured and used to back-calculate the residual stresses acting normal to the cut plane.

Figure 2.6 shows the superposition principle applied to determine residual stresses in a sectioned component. Illustration A (figure 2.6 from [52]) shows the original stress state in the undisturbed part. The newly formed surface deforms as residual stresses are released by the cut along the plane of interest, which is evident in illustration B. The surface distortion is measured and in step C the stresses required to force back the deformed surface to the uncut state are calculated analytically using finite element simulation. Assuming elastic conditions, superimposing the partially relaxed stress state in

B with the change in stress from C gives the original stress distribution at the plane normal to the cut.

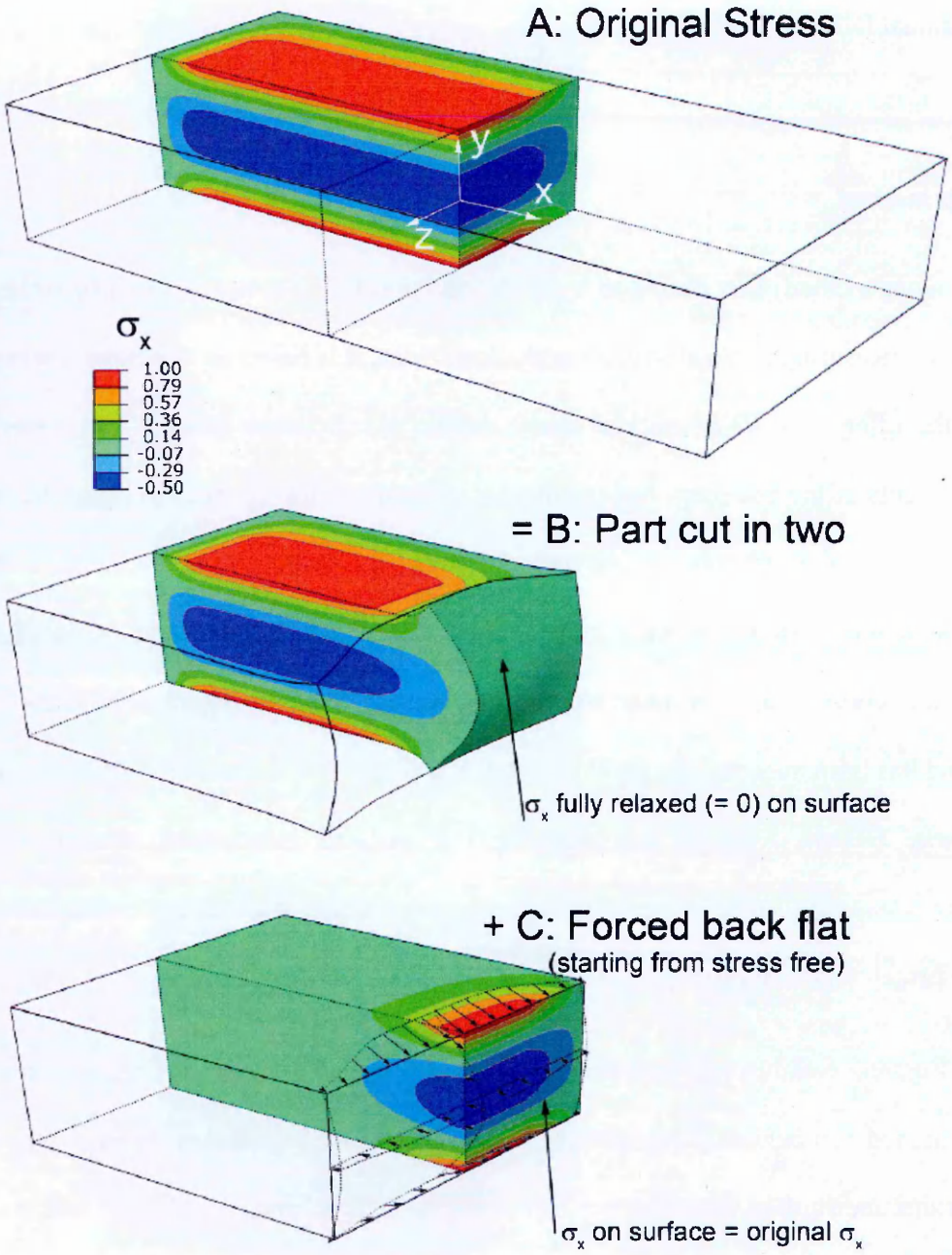

Figure 2.6. Bueckner's superposition principle applied to determine residual stresses in a sectioned part [52].

The contour method provides a full cross-sectional map of residual stress and is implemented by undertaking four steps: specimen cutting, measuring the surface deformation, data processing and finite element modelling (extensively discussed in [53]). The contour method has been validated to some extent through comparison with results from other residual stress measurement techniques such as neutron diffraction, synchrotron X-ray diffraction and slitting in welded components [54-57]. The contour method uses standard workshop equipment and is increasingly being used for stress measurements in thick section welds as it is not influenced by large grain size and crystallographic texture which can compromise diffraction techniques. Specimen cutting is one of the crucial steps in the implementation of this method because cutting artefacts can result in significant measurements errors. Any deformation during the cut is assumed to have occurred as a result of the elastic relaxation of residual stresses acting normal to the surface prior to the cut. Hence the component must be cut using a machining technique that follows a defined surface profile and has minimum kerf (width of the channel of material removed during cutting), does not introduce further residual stresses and plastic deformation.

When the internal stresses are sufficiently high the cutting step inherently holds the risk of introducing errors in measured stresses owing to plasticity and bulging effects [58]. Traore et al. [59] studied ways of mitigating and estimating plasticity induced errors in contour method measurements. The "skim" cutting mode is preferred for performing contour cuts as it is a relatively low energy regime, which provides a low roughness, minimises the thickness of the EDM affected layer and cutting induced stresses [60]. The contour method has been recently used for measurement of multiple stress components by performing more than one cut [61] or by combining with other methods, for example X-ray diffraction [62].

The application of the contour method in complex geometries such as cylinders is more challenging. In the two step approach introduced by Pagliaro et al. [52] for measuring

hoop stresses, the first axial-radial cut is meant to sever the cylinder which relaxes the hoop through wall bending moment. The amount the pipe springs open or closed during the cut is measured with the help of strain gauges and used to determine average bending moment stresses along the cylinder. In the second step, the conventional contour cut is employed to measure the remaining hoop stresses. This stress field is superimposed upon the bending stress to determine the total hoop stress in the cylinder. Recently, a one-step method [62] was applied by cutting the diametrically opposite walls of a cylinder lengthways simultaneously into two half cylinders. The deformation of both the cut surfaces was measured simultaneously relative to a single reference plane and analysed using a common coordinate system thus accounting for the release of the bending moment both along the length and through the thickness of the cylinder. The one step approach has been implemented to measure the hoop residual stresses in butt welded pipes in the present work.

Following the cut, the deformation of the cut surfaces is measured using a coordinate measuring machine (CMM). The raw data then need to be aligned, averaged and smoothed after the removal of outliers. As the surface deformation of the two cut half's are measured in different coordinate system, data alignment is necessary before it is interpolated into a common grid system or known as 'averaging'. This step essentially cancels out the shear stress affects and other sources of errors such as local cutting irregularities. The averaged data then needs to be 'smoothed' to minimise the noise and accomplished using a bivariate spline fitting [63]. A bivariate spline consists of piecewise polynomials joined at specific locations called 'knots' and the fitting process minimises the error between the data points. The smoothing process is determined by the density of the knots where the optimum fit is achieved by carrying out a least squares analysis. Low knot spacing tends to over-fit the data and too large a knot spacing may result in over-smoothing the averaged data causing a loss of spatial resolution in areas where high stress

gradients are present. In this study, a knot spacing of 7 mm × 7 mm was consistently used as it was reported to give more plausible results in a circumferentially welded P91 pipe [64]. Limitations of the contour method include the inability to measure stresses very near to the surface and that it can't be performed in-situ and results in the destruction of the component.

Methods based on diffraction X-ray, synchrotron X-ray and neutron diffraction

Diffraction based techniques [65-70] measure the shift in diffraction peak positions which can be related to changes in inter-planar spacing by Bragg's law through knowledge of the incident wavelength and scattering angle. The crystallographic planes are defined by miller indices denoted as (h k l). When X-rays are scattered from a crystalline material they can constructively interfere, generating a diffracted beam.

For a given set of crystallographic planes defined by (h k l) Bragg's equation [71] is given by,

$$2d_{hkl} \sin \theta_{hkl} = n\lambda \qquad (2)$$

with θ_{hkl} being the diffraction angle for a family of lattice planes. d_{hkl} is the inter-planar spacing and λ is the wavelength. A schematic illustration of Bragg's law for diffraction techniques is shown in Figure 2.7.

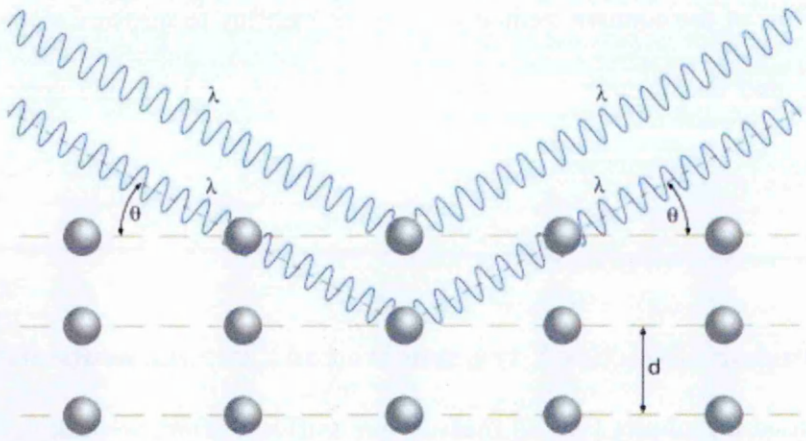

Figure 2.7. Schematic illustration of Bragg's law for diffraction techniques [72]

Laboratory X-ray diffraction [65] is generally used to perform surface or near-surface stress measurements due to its low beam penetration. Sub surface diffraction based residual stress measurements can be achieved using either neutrons or high energy X-rays at dedicated large scale facilities. Synchrotron X-ray diffraction [66] uses a high energy X-ray beam from a synchrotron source capable of achieving high depth of penetration. For example, the photon energies of the synchrotron beam used in the European Synchrotron Radiation Facility (ESRF), Grenoble possess energy levels of more than 150 keV and can penetrate several centimetres of steel.

Neutron diffraction [73] can characterise residual stresses in welded structures with a spatial resolution of less than a millimetre and large depth of penetration. Measurements can be made in two types of facility. Reactor sources produce a monochromatic beam of neutrons of given wavelength diffracted through a diffraction angle (2θ) and is used to calculate the change in lattice spacing. On the other hand at pulsed sources, a fixed diffraction angle is used and time of flight used to determine the change in lattice spacing. All the neutron diffraction work presented in this dissertation has been performed using the

monochromatic diffractometer, SALSA at the ILL Grenoble, France and techniques relevant to this instrument are discussed below in more detail.

The presence of residual stresses results in deviation of lattice spacing from its stress free value (d_{0hkl}). The strained lattice spacing (d_{hkl}) can be identified from the shift in diffraction peak position from its stress free value d_{0hkl}. Determining reliable values of d_{0hkl} is very important in neutron diffraction measurements as a small change in the value can result in significant errors in measurements. Changes in material composition, texture, grain size and inter-granular strains are examples of different factors which can affect the stress-free lattice parameter [74]. Thus it is essential to have an accurate measure of stress free reference. In general, 'stress-free' measurements are performed on 'stress-free' cubes or combs extracted from the component of interest, stress-free powder or filings that are representative of the material or far field measurements (at a position known to contain a negligible level of stresses) or by applying a force moment balance approach [75, 76].

The crystallographic strain is determined using the expression,

$$\varepsilon = \frac{d_{hkl} - d_{0hkl}}{d_{0hkl}} \tag{3}$$

Modifying equation (3), the strain ε in axial, hoop and radial directions can be calculated from the measured diffraction peaks and averaged stress free reference using the equation,

$$\varepsilon = -\frac{\left(\theta - \theta_{0(x,y,z)}\right) \times \frac{\pi}{360}}{Tan\left(\theta \times \frac{\pi}{360}\right)} \times 1000000 \tag{4}$$

The strains in the three different directions (ε_{xx}, ε_{yy}, ε_{zz}) can be converted into three dimensional stresses (σ_{xx}, σ_{yy}, σ_{zz}) assuming isotropic elasticity using the equations of generalized Hooke's law,

$$\sigma_{xx} = \frac{E_{311}}{(1+\nu_{311})(1-2\nu_{311})}\left[(1-\nu_{311})\varepsilon_{xx} + \nu_{311}(\varepsilon_{yy}+\varepsilon_{zz})\right] \quad (5)$$

$$\sigma_{yy} = \frac{E_{311}}{(1+\nu_{311})(1-2\nu_{311})}\left[(1-\nu_{311})\varepsilon_{yy} + \nu_{311}(\varepsilon_{xx}+\varepsilon_{zz})\right] \quad (6)$$

$$\sigma_{zz} = \frac{E_{311}}{(1+\nu_{311})(1-2\nu_{311})}\left[(1-\nu_{311})\varepsilon_{zz} + \nu_{311}(\varepsilon_{xx}+\varepsilon_{yy})\right] \quad (7)$$

where E_{311} and ν_{311} is the diffraction elastic Young's modulus and Poisson's ratio.

The uncertainties in the stresses can be calculated using the given set of equations

$$\Delta\sigma_{xx} = \frac{E_{311}}{(1+\nu_{311})}\left[\left(\frac{\nu_{311}}{1-2\nu_{311}}\right)(\Delta\sigma_{xx})^2 + (\Delta\sigma_{xx}+\Delta\sigma_{yy}+\Delta\sigma_{zz})^2\right]^{\frac{1}{2}} \quad (8)$$

$$\Delta\sigma_{yy} = \frac{E_{311}}{(1+\nu_{311})}\left[\left(\frac{\nu_{311}}{1-2\nu_{311}}\right)(\Delta\sigma_{yy})^2 + (\Delta\sigma_{xx}+\Delta\sigma_{yy}+\Delta\sigma_{zz})^2\right]^{\frac{1}{2}} \quad (9)$$

$$\Delta\sigma_{zz} = \frac{E_{311}}{(1+\nu_{311})}\left[\left(\frac{\nu_{311}}{1-2\nu_{311}}\right)(\Delta\sigma_{zz})^2 + (\Delta\sigma_{xx}+\Delta\sigma_{yy}+\Delta\sigma_{zz})^2\right]^{\frac{1}{2}} \quad (10)$$

Neutron diffraction is capable of measuring elastic strains in a wide range of materials with complex shapes and in relatively thick samples non-destructively. In the present work, neutron diffraction is the sole non-destructive technique used to characterise residual stresses in girth welded pipes.

Challenges in experimental measurements

Experimental methods are used to quantify residual stress levels in components of interest and/or to validate numerical models simulating the fabrication process or changes. However, there is no single method which is deemed to be the 'best' for measuring

residual stresses. In order to select an appropriate method the following issues need to be addressed [77]:

- Measurement characteristics such as information on the spatial resolution and distribution, penetration, stress type and uncertainty of each technique.
- Practical issues such as the cost, availability of equipment, measurement time and existence of a standard procedure and the level of expertise required.
- Material issues such as the composition, geometry, properties including thermal conductivity and crystalline nature, and specimen preparation required for using a particular technique.
- Reliability of near surface measurements as many of the techniques have limitations when approaching close to the edge of components.
- Agreement between results using different measurement techniques as there may be variation due to sample geometry, plasticity effects, texture, reliable stress free reference and limitations within the experimental techniques.

It is a good practice to undertake multiple experimental measurements at the same position to characterise residual stresses in weldments in order to validate numerical models and for increasing confidence in the acquired experimental data using diverse techniques as given in R6 section III.5 [4]. For example, in a recent study conducted by Woo et al. [78], neutron diffraction, contour method and deep hole drilling measurements were performed to characterise through-thickness residual stresses in ferritic steel welds with low and high heat inputs. Reasonable agreement was observed between neutron diffraction and contour method measurement but in a few cases the difference in the measured stresses was more than 200 MPa. To conclude, a perfect agreement of measured stresses using different techniques is not realistically possible in welds due to the reasons mentioned and undertaking multiple measurements is desirable to increase the confidence in the results.

2.3.2 Modelling of residual stresses

Over the past decade, numerical modelling has been applied with increasing frequency to predict residual stresses in welded components. Whilst numerical modelling is an attractive tool, the results essentially need to be validated with experimental measurements for safety-critical applications as prescribed in R6 section III.5 [4]. Residual stresses in welds are often difficult to simulate using computational techniques because of the complex interacting factors and variables involved, for example Asadi and Goldak [79] identified about 300 parameters that can affect weld deformation and residual stress behaviour using a computational weld mechanics framework.

Finite element (FE) modelling [80-82] provides a full field residual stress characterisation by simulating the complex interaction between heat flow and material properties over a wide range of temperatures. However, the final residual stress distributions are strongly dependent on the modelling assumptions and procedures used by the analyst. Moreover, the full 3-dimensional moving heat source FE simulations required to give most accurate results are complex and expensive, and for multi-pass welds at the limit of current computing capabilities.

International round robin activities have been carried out in order to benchmark weld residual stress modelling techniques. For example, the NeT (European Network on Neutron Techniques Standardisation for Structural Integrity) was founded in 2002 to develop experimental and numerical techniques for the reliable characterisation of residual stress in welds. NeT has dedicated Task Groups (TG) undertaking modelling studies in AISI 316L austenitic stainless steel, such as the TG1: a single finite length weld bead laid on the surface of a plate specimen and TG4: three superimposed weld beads in a finite length slot specimen.

An Accurate thermal analysis modelling (heat flow and heat source model), a representative material hardening constitutive model, means of simulating material phase transformation effects and application of appropriate mechanical boundary conditions are the main requirements for predicting welding induced residual stress. A mixed isotropic-kinematic hardening model is more pragmatic and available in commercial finite element packages such as ABAQUS [83]. This has been demonstrated by Smith et al. [84] where most accurate predictions of through-thickness residual stresses in a three pass groove welded in austenitic stainless steel specimen were those based on Lemaitre-Chaboche mixed hardening model [79] as shown in Figure 2.8. It is interesting to note that there is a considerable difference (about 100 MPa or more) between the predictions based on different hardening models illustrating the importance of assumptions and models used.

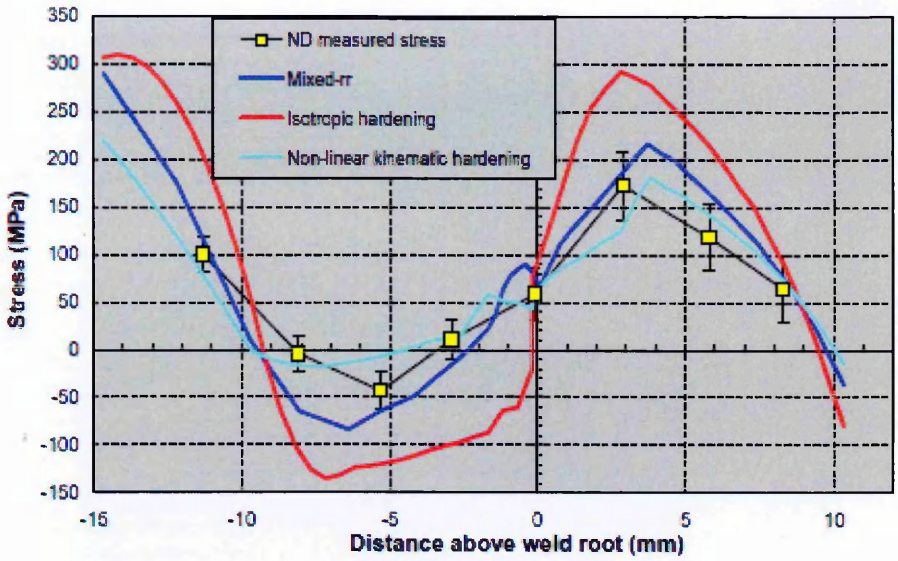

Figure 2.8. Comparison of predicted and measured stresses in a three pass austenitic stainless steel groove weld plate of dimensions (200 × 180 × 25) mm with a 10 mm deep groove [84].

There is an abundance of FE simulation results published in the literature linked to NeT research activities [86-90]. Figure 2.9 shows the comparison of measured and predicted stresses using diverse techniques at the weld centre line along the thickness of the NeT-TG1 single bead on plate specimen [90].

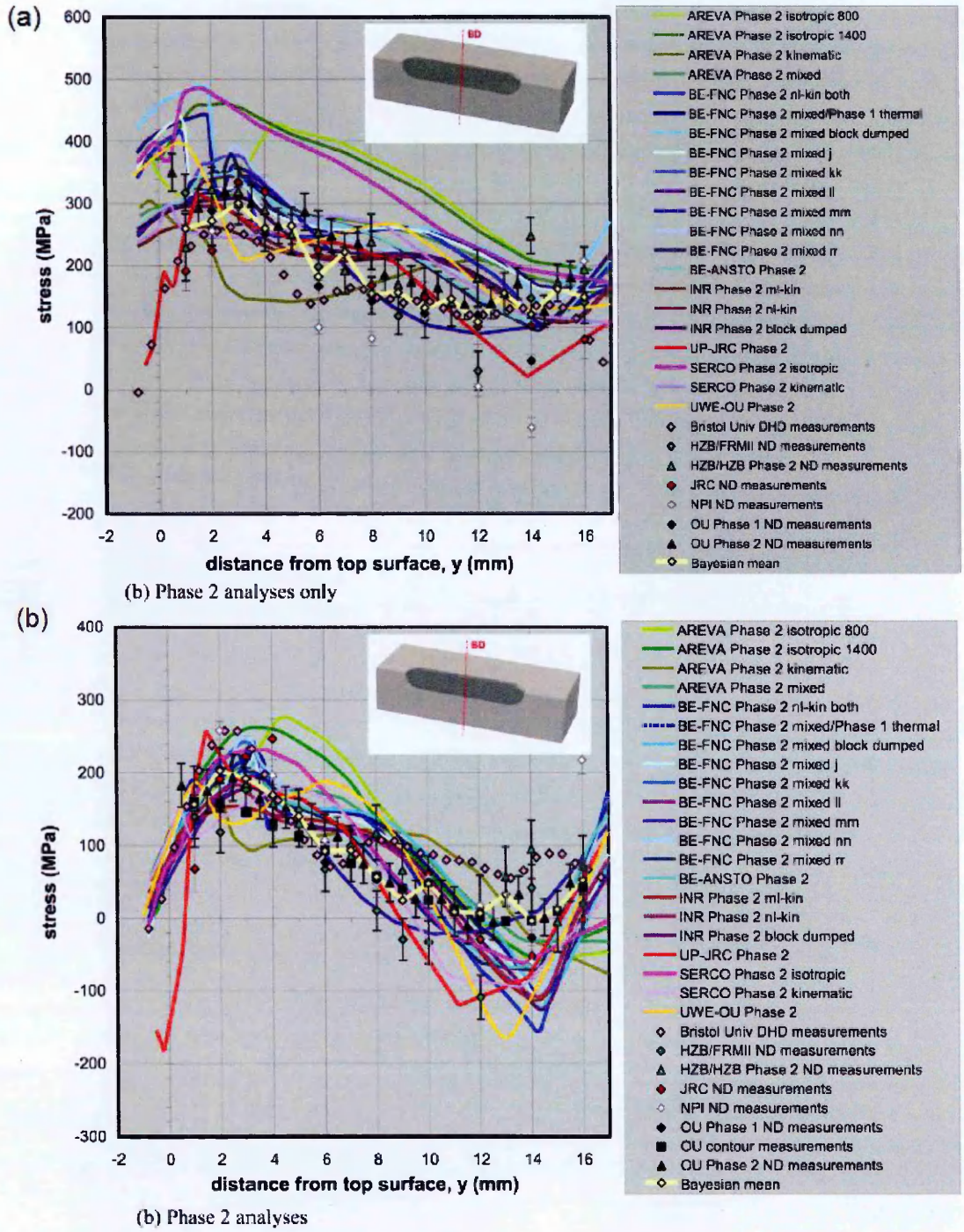

(b) Phase 2 analyses only

(b) Phase 2 analyses

Figure 2.9. Comparison of measured and predicted (a) longitudinal stresses (b) transverse stresses along line BD through the plate thickness, and mid-width and mid-length in the weld bead of NeT- TG1 specimen; plate dimensions 120 mm × 80 mm × 17 mm with a weld length of 60 mm [91].

The single weld bead on plate specimen should have been relatively simple to model using finite element methods. However, the weld bead is laid onto a relatively thin plate and the weld bead was much shorter than the length of the plate. The predicted stresses are highly sensitive to the finite element modelling assumptions and boundary conditions for this case, thus making this a challenging benchmark problem. It is evident from Figure 2.10 that there is considerable scatter observed in the modelled results. Hence, the confidence in FE predictions is questionable in complex multi-pass welds such as girth welded pipes. An example of the mismatch between the prediction and measurement which can arise is illustrated in Figure 2.10 [92] for a pipe weld where residual stress predictions are compared with contour and neutron measurements. The axial restraint imposed on the model was an important analysis parameter since significant distortion was found during welding. However, the agreement was relatively poor even when the axial restraint was employed and resulted in under-prediction of stress close to the outer surface.

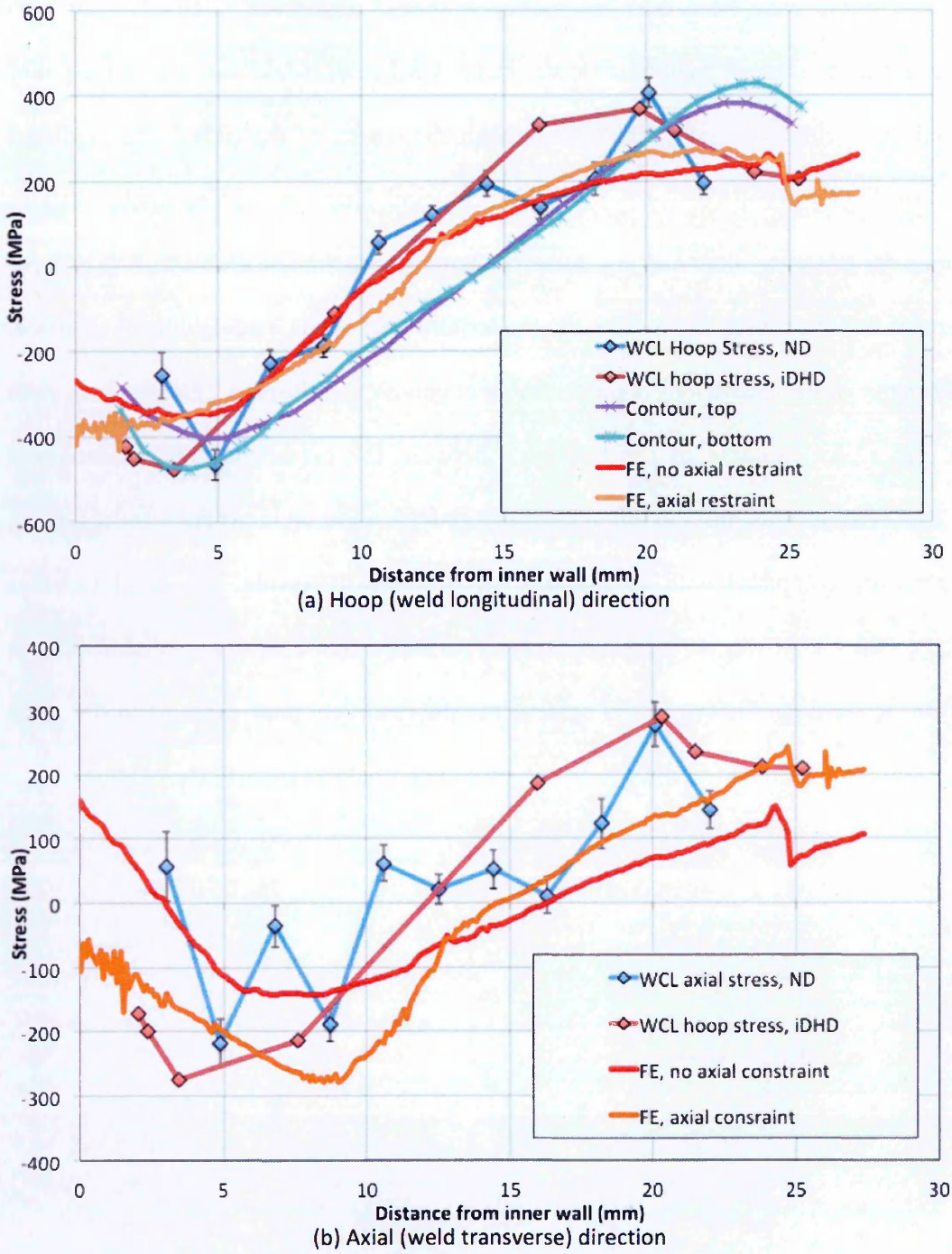

Figure 2.10. Comparison of measured and predicted (a) hoop stresses (b) axial stresses along the weld centre line of the STYLE pipe girth weld MU4-1 (t= 25 mm, R/t = 4.5, E= 1.0 kJ/mm; ND – neutron diffraction, IDHD – incremental deep hole drilling) [92].

In order to improve the consistency and reliability of predicted results in weld modelling a set of guidelines [93] has been introduced recently into the R6 procedure [4]. Although challenging and expensive, finite element modelling has been used for many years to simulate residual stress profiles in pipe girth welds, for example see [94, 95-98] and for repair welds [99, 100]. Comprehensive information is required for carrying out finite element simulations. For example, surface and weld bead profiles, physical and thermo-physical properties from room temperature up to the melting point, measured tensile stress-strain data for weld and parent material, welding parameters for all beads deposited (electrical power, arc time, torch advance rate, traverse length and start dwell time) and fabrication details permitting analysts to choose appropriate boundary conditions. Moreover, the analyst should be highly skilled and possess competent experience in modelling of residual stresses in welds. Thus, at present, application of the FE method to predict residual stresses in welded components is driven by need rather than being a mainstream design tool. Computational requirements and time required for carrying out the analysis are significantly high. In this scenario the opportunity to use historical measured residual stress data to characterise residual stresses using an ANN modelling is attractive.

2.4 Structural Integrity Assessment

Residual stresses can have a large impact in damage tolerance assessments. A thorough understanding is needed of how they may affect component life estimates [101]. By quantifying residual stresses to known levels, strategies can be implemented, to reduce design and operation costs of power plant components or to conduct inspection regimes for structures thereby improving their life. When assessing the integrity of a defective structure such as a girth welded pipe, all sources of loading which may increase the risk of failure should be taken into account [4, 7]. Loads can be categorized as primary or secondary where primary loads are those that contribute to plastic collapse, as opposed to the secondary loads which do not. Stresses due to the mechanical loading such as pressure, applied force, self-weight, or long–range structural constraint are categorized as primary loads [4, 101]. Stresses due to temperature variation or welding residual stress are often classified as secondary.

Bouchard and Withers [102] have proposed a residual stress decomposition technique for characterizing residual stress distribution by decomposing into membrane, bending, and self-equilibrated components of stress. The decomposition procedure can be particularly useful in identifying contributions of process parameters and joint restraint deepening the understanding of its role in fracture assessments. A weld residual stress profile is defined to be a detailed through-wall description of component of the residual stress tensor along a line in a body, for example σ_z shown in Figure 2.11. It can be mathematically decomposed into three simple components of macro-stress; a membrane component σ_m, a through-wall bending component σ_b and a self-equilibrated component σ_{se} expressed as follows [103] (see Figure 2.12);

$$\sigma_m = \frac{f_z}{t\Delta y},\ \sigma_b = \frac{6m_y}{t^2\Delta y} \text{ and } \sigma_{se} = \sigma_z\left(\frac{x}{t}\right) - \sigma_m + 2\left(\frac{x}{t}\right)\sigma_b \qquad (11)$$

where f_z denote the net axial force acting across the thickness t, Δy = width of strip, m_y = bending moment, t is the wall thickness and $\sigma\left(\frac{x}{t}\right)$ is the axial stress distribution across the thickness.

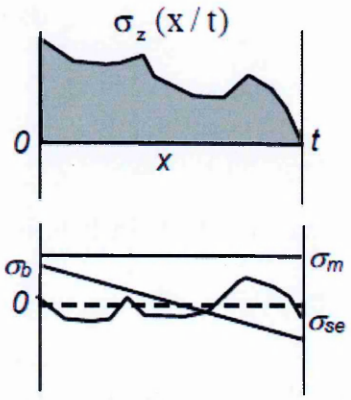

Figure 2.11. Axial stress field along a wall section decomposed into the membrane, bending and self-equilibrated components [103].

Stress decomposition can help to identify the contributions of welding process parameters and the restraint conditions thus allowing different components of stress to be treated in the most effective way in fracture assessments [103]. For R6 [4] fracture assessment purposes, the decomposed components of through-wall residual stresses are further classified as either long range, medium range or short range depending upon the elastic follow up. Accurate assessments of defects (cracks or flaws) in structures require reliable characterisation of the residual stress field present. For most practical situations determining weld residual stress profiles using measurements on mock-up components is the last resort option because of time, cost, innate scatter and reliability issues [104]. Instead a simple bounding characterisation approach is applied where a conservative description of the residual stress distribution in a specific class of weld is selected from published compendia.

2.4.1 Codes and Standards

Assessments of defects in components are performed by many industries to help develop and optimise new defect tolerant designs or to support the management of existing structures. Assessment codes and standards provide various upper bound through-thickness residual stress profiles for as-welded joints. The stress profiles are categorised with respect to the welding direction, i.e. longitudinal component parallel to the welding direction and transverse component normal to the plane of welding. For a pipe girth weld, longitudinal and transverse component of stresses correspond to the hoop and axial directions respectively. Widely used codes and standards include R6 [4], BS7910 [7] and API-579 ASME FFS-1 [8] are given as follows.

R6: Fracture mechanics based defect assessment procedure developed by the nuclear power generation industry in the UK which is maintained by EDF Energy in collaboration with AMEC, Rolls Royce, and TWI. The procedure is continuously updated based on recent research findings.

R6 Section I.5 draws attention to the classification of stresses for use in assessments and requires that all stresses should be classified into primary or secondary stresses. As stated in R6; primary stresses are those which contribute to collapse, such as applied loads or pressures and secondary stresses are those that are self-equilibrating across the section, that is, the net force or bending moment across a section due to the secondary stresses is zero. R6 accounts for the treatment of secondary stresses including short or medium range welding residual stresses. The residual stress profile of as-welded components along the wall thickness is defined in Section II.7.5 at various levels of sophistication. Level 1, the simplest characterisation approach, assumes a uniformly distributed tensile residual stress equal in magnitude to the mean material yield strength. Level 2 approach defines an upper bound profile of the residual stress through the wall-thickness based on published compendia of analytical results for different classes of welds.

A library of residual stress distributions for as-welded components commonly analysed in defect assessments is given in R6 Section IV.4. Both R6 level 1 and level 2 approaches are considered to be very conservative. The R6 level 3 approach gives a more realistic description of the residual stress field. It involves non-linear analytical modelling of the welding process sufficiently corroborated by experimental measurements as described in Section III.15 of the R6 Procedure.

API-579 ASME FFS-1: The API (American Petroleum Institute) and ASME (American Society of Mechanical Engineers) jointly introduced the standard for structural integrity assessments. Annex E of the procedure provides guidance on determining the magnitude and distribution of residual stresses in as-welded components. The profiles recommended in API provide an upper bound solution resulting from extensive finite element analysis and study of results available in literature. The stress profiles recommended in API are estimated based on welding heat input per unit volume where as other codes commonly use the welding heat input per unit area as one of the critical parameters.

BS7910: BS7910 (Guide to Methods for Assessing the Acceptability of flaws in Metallic Structures) is a British standard in which residual stress data and guidance is closely linked to the R6. Level 1, the simplest characterisation within BS7910, assumes the tensile residual stress at a welded joint equal to the yield strength of the material at room temperature. If the defect is located partly in weld metal and partly in parent metal, the residual stress should be assumed to be equal to the greater of the room temperature yield strengths of the weld or parent metal. For a defect located in a plane parallel to the welding direction, the residual stress should be assumed to be equal to the lesser of the yield strengths of the weld or parent metal. Annex Q of BS7910 provides guidance on treatment of residual stress distributions in girth welds for Level 2 analyses.

2.4.2 Fracture Assessment

Linear elastic fracture mechanics assessment for actual or postulated defects in structures of interest requires evaluation of the stress intensity factor arising from both primary and secondary loads, including residual stress. In Engineering Fracture Assessment (EFA) procedures the full (3-D) residual stress field at a welded joint is usually simplified by considering a representative one-dimensional profile through the wall-thickness of the stress tensor component acting normal to the crack face. The stress intensity factor (SIF) [105,106], calculated from this estimated through-thickness stress profile is used directly in the fracture assessment [4]. The evaluation of the stress intensity factor resulting from welding induced residual stress has become an indispensable part of structural integrity assessment procedures as the accuracy of the calculated stress intensity factor has a deciding influence on the outcome of fracture assessments [107-109].

The concept of a two-criterion Failure Assessment Diagram (FAD) to describe the interaction between fracture and plastic collapse is discussed below. Plastic collapse is controlled by overall plasticity in the defective section and fast fracture by the local crack-tip stress-strain fields. Figure 2.12 illustrates the assessment curve of the R6 FAD, the X-axis represents the parameter L_r, which denotes nearness to plastic collapse and Y-axis represents the parameter K_r, which measures the nearness to brittle fracture. The 'Failure Assessment Curve' (FAC) divides the assessed area into a safe and an unsafe region. Failure is avoided if the assessment point (L_r, K_r) lies within the curve and if the failure avoidance criterion is violated, remedial action needs to be taken which may include carrying out a more realistic fracture analysis with less conservative assumptions. K_r and L_r parameters are defined by equations (12) and (13),

$$L_r = \frac{applied\ load}{yield\ stress\ based\ limit\ load} \tag{12}$$

$$K_r = \frac{stress\ intensity\ factor}{fracture\ toughness} = \frac{K_{effective}}{K_{mat}} \tag{13}$$

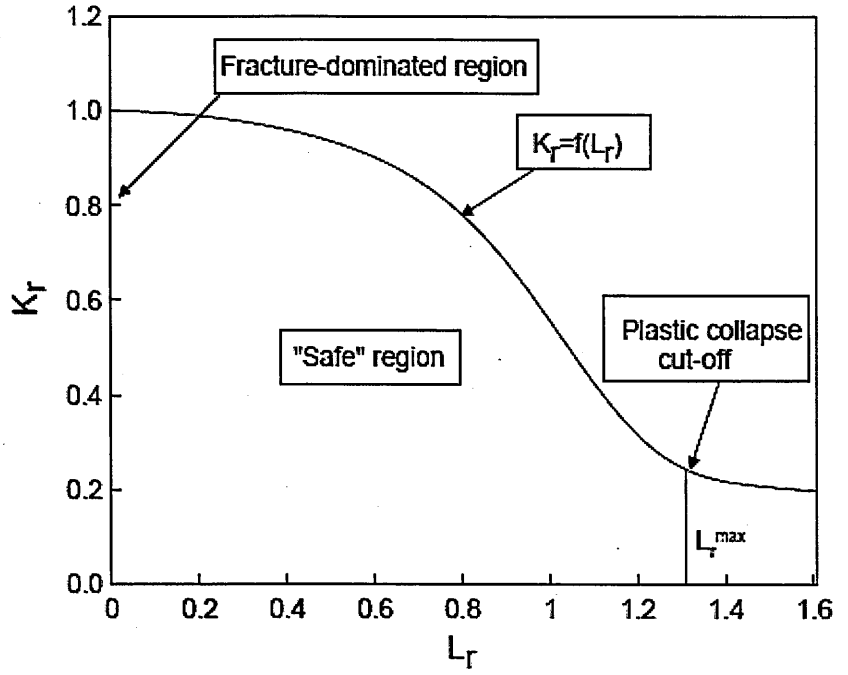

Figure. 2.12. Assessment curve of the R6 FAD [4]

$K_{effective}$ is the mode I effective stress intensity factor and K_{mat} the material toughness. The shape of the general FAD curve for the elastic regime ($L_r < 0.7$) is almost flat (K_r is about 1), meaning that the elastic crack driving force is the dominating factor. However, for $L_r > 0.7$, K_r decreases with a steep curve around $L_r = 1$ which shows that the elastic part of the crack driving force is not so dominant. The FAD was originally designed for a load-controlled situation. However, in a displacement controlled situation, plastic collapse (L_r) plays a very important role. The definition of plastic collapse can affect the determination of the L_r parameter and should be carefully chosen [4]. A review of the treatment of residual stresses in structural integrity assessment of welded structures has been discussed by many authors [107-110].

The effect of residual stress and primary loads on structural integrity cannot be considered independently due to their interaction. Moreover, interaction of residual stress and primary loads in a structure cannot be estimated by a simple addition of these factors because of the effect of plasticity [4]. Almost all procedures including R6 [4], BS7910 [7] and API [8] provide some guidelines on how to treat the interaction of residual stress with primary load. These interactions can be of complex nature and it is usually simplified by calculating an effective stress intensity factor that incorporates secondary stresses as described in BS7910 [7] and in the R6 procedure [4]. The general approach involves including an additive term, ρ factor in the K_r parameter. The ρ factor is used to calculate the effective stress intensity factor and under combined primary and secondary load conditions, K_r is calculated from:

$$K_r = \frac{K_{effective}}{K_{mat}} = \frac{K_I^p}{K_{mat}} + \frac{K_I^s}{K_{mat}} + \rho \qquad (14)$$

where K_I^s is the elastic stress intensity factor due to the secondary loads, and ρ is a factor covering interactions of residual stress with primary loads.

The V factor is a newly introduced parameter in the R6 [4] to provide an alternative to the ρ factor, for treating plasticity effects under combined primary and secondary loads given by (15),

$$K_r = \frac{K_I^p}{K_{mat}} + \frac{VK_I^s}{K_{mat}} \qquad (15)$$

2.4.3 Parametric studies

Dong [111] provided parametric equations based on a comprehensive set of finite element simulations for estimating through thickness distribution of residual stress in pipe welds based on extensive programme of analytical work sponsored by the US Materials Properties council (MPC) and industrial partners. Other outputs from this programme can be found in [112-115] and were later incorporated into API579-1/ASME FFS-1. Dong [111] classified the through-thickness transverse residual stress distributions in pipe girth welds as global bending, local bending and self-equilibrating (see Figure 2.13). Pipe thickness and radius to thickness ratio were considered as the two most important parameters that govern the transition from one type to another. However weld heat input was not explicitly modelled in this work. Recently, Dong [115] suggested areas of improvement in residual stress profiles insisting heat input should be treated as a continuous function rather than discrete categories in terms of low, medium and high heat input ranges.

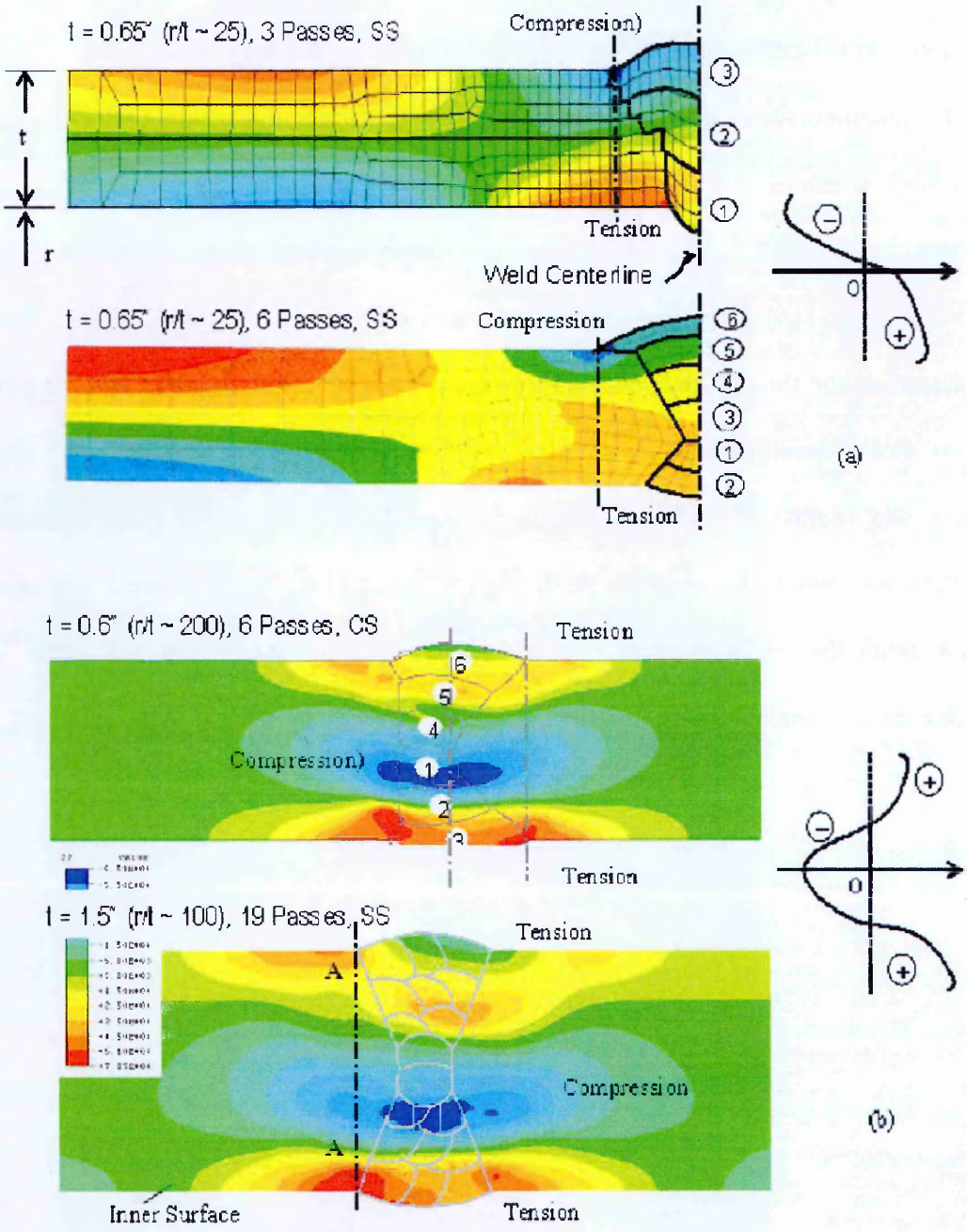

Figure 2.13. Two types of axial residual stress distributions in girth welds (a) "bending type" (b) "self-equilibrating" type [111].

Brickstad and Josefson [116] developed a numerical weld simulation procedure for determining the residual stress field in multi-pass pipe butt welds by carrying out a non-linear FE analysis. Recommendations are provided for through thickness variation of axial and hoop residual stresses while assessing the growth of surface flaws in austenitic stainless steel pipe girth welds. Bradford [117] developed prescriptions defining more realistic axial and hoop residual stress profiles based on a set of axi-symmetric finite element simulations identifying geometry and weld heat input as the governing parameters. The electrical weld heat input per unit thickness was considered for the prescription. The drawback of this approach is that the magnitude of the tensile residual stresses is under-predicted near the inside surface and the profile doesn't provide a good fit to the measured stresses close to the outer surface. Bouchard and Bradford [118] later addressed some of the short comings of the Bradford [117] finite element based prescription by proposing profiles that are more accurate compared with the measurements and simple to evaluate. The only drawback of the revised profiles was that they did not conservatively bound the stresses at the outer surface. Figure 2.14 reproduces the comparison of recommended through-wall residual stress profiles available for a typical stainless steel pipe girth weld (denoted as SP19) presented in [18]. Details of mock-up SP19 can be found in Table 2.1.

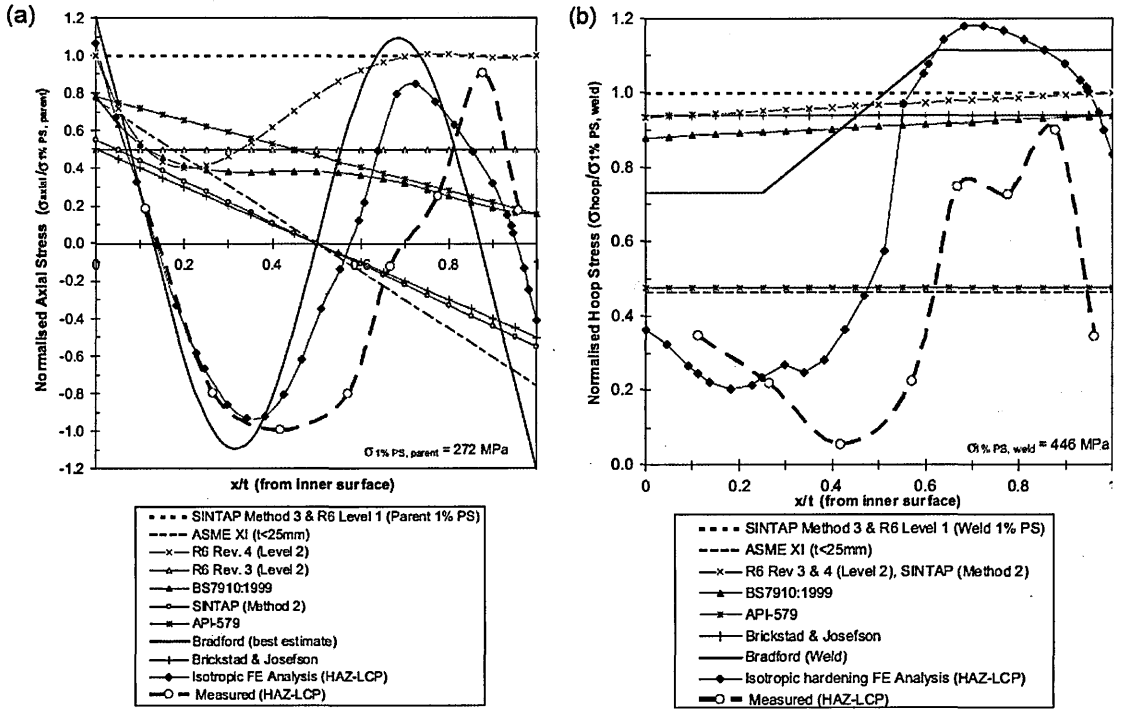

Figure 2.14. (a) Axial and (b) hoop residual stress profiles for the pipe girth weld SP19 (t = 19.6 mm, R/t = 10.5 mm, E = 1.4 kJ/mm) [18].

Bouchard [18] refined the prescription introduced by Bradford and Bouchard using a parametric function that represents the through-wall residual stress profiles of austenitic stainless steel pipe girth welds taking into account the pipe geometry (wall thickness), material properties (parent metal yield strength) and welding process (net heat input). The new formulations have been validated for a range of weld groove geometries and weld processes for a thickness range of 16-110 mm and electrical heat inputs in the range of 1.0-2.4 KJ/mm for austenitic steel girth welds.

The parametric function presented in [18] for axial stress profiles can be expressed as a combination of three stress components: membrane, bending and self-equilibrating:

$$\sigma_{axial}\left(\frac{x}{t}\right)=\sigma_y\left\{\beta\left(1-2\frac{x}{t}\right)+\alpha\sin\left[\frac{\pi}{4}\left(1-8\frac{x}{t}\right)\right]-\frac{t}{R}\left[\frac{\sqrt{2}}{4\pi}\alpha-\frac{\beta}{6}\right]\right\} \quad (16)$$

where $\frac{x}{t}$ = fractional distance through thickness from bore of pipe, R is the mean pipe radius, σ_y is the 1% proof stress of the parent material, and α, β are free parameters to be determined by fitting to measured data and optimised "by eye".

$$\alpha=\tilde{Q}(-1.25\text{x}10^{-8}\tilde{Q}^3+5.42\text{x}10^{-6}\tilde{Q}^2-8.67\times10^{-4}\tilde{Q}+5.11\times10^{-2}) \quad (17)$$

$$\beta=8.4\times10^{-3}\tilde{Q}-0.34 \quad (18)$$

valid for 10 J/mm^2 < $\tilde{Q}$ < 160 J/mm^2, where $\tilde{Q}$, the net heat input per unit thickness of pipe, is defined by $\tilde{Q}=k\tilde{E}$, k is the weld process efficiency and $\tilde{E}$ is the electrical heat input per unit thickness per unit run length. Figure 2.15 shows the axial stress profile using the Bouchard formulation (denoted as New Formulation) in comparison with experimental measurements and the Bradford Prescription [18].

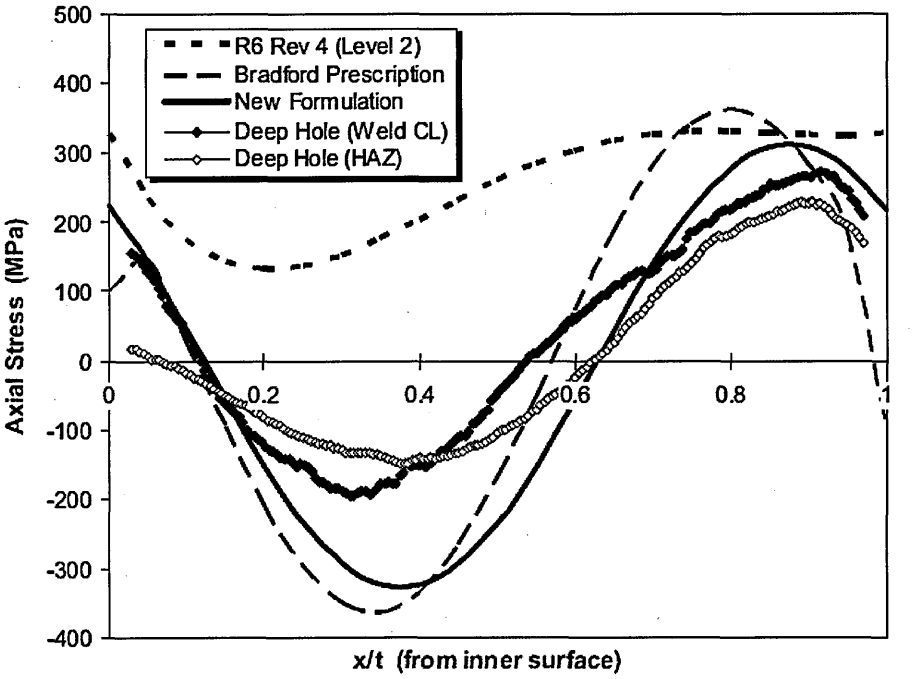

Figure 2.15. Comparison of experimental measurements and axial residual stress profiles [18].

The formulation is used in the R6 level 3 approach for fracture assessments of "structurally significant" defects in non-stress relieved austenitic stainless steel girth welds, where the weld material overmatched the parent in terms of tensile properties. Figure 2.16 presents the axial stress profiles based on equation (16) for varying heat inputs of a pipe having R/t=10.

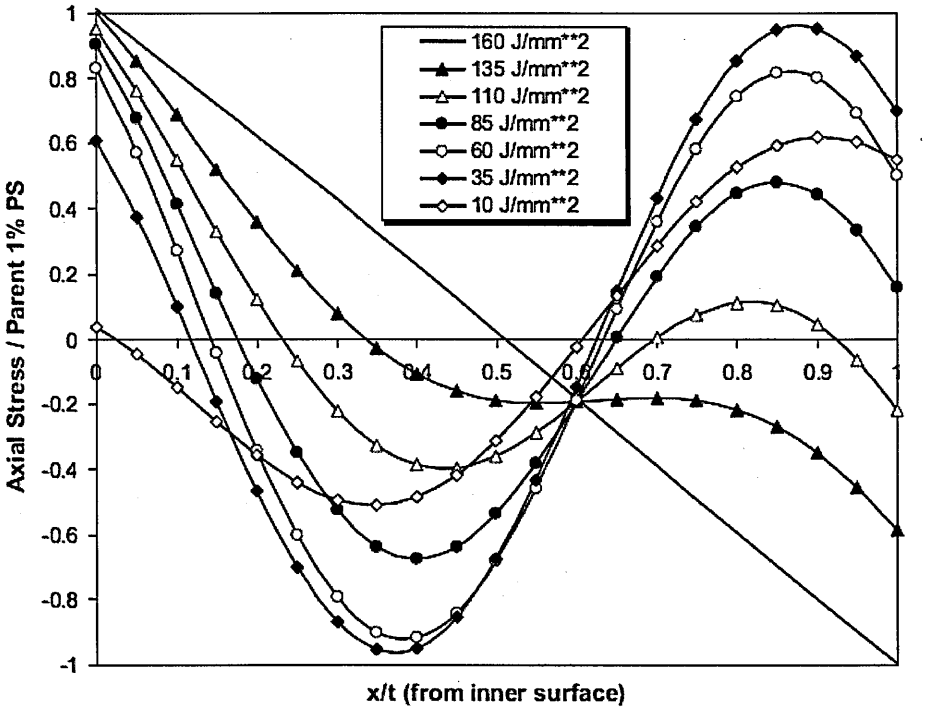

Figure 2.16. Axial residual stress profiles using Bouchard's formulation (R/t = 10) [18].

The curve fitting parameters were optimised judgementally to ensure that the profiles represent the large zone of tensile residual stress usually observed towards the outer surface of thick section welds and tensile stresses near the inside diameter. Since the prescription ensures axial force equilibrium is satisfied along a radial line, the resulting parametric profiles have a large zone of compression in the central region of the wall thickness. The consequence of this is that the stress intensity factor may be under-estimated for deep surface breaking cracks leading to potential non-conservatism in fracture assessments. The R6 procedure recommends that adequate sensitivity studies covering all sources of uncertainty such as material properties and heat input must be performed when using this formulation.

The Bouchard formulation [18] for hoop residual stress profiles can be expressed as a combination of the membrane stress and sine function.

$$\sigma_{\text{hoop}}\left(\frac{x}{t}\right)=\sigma_y\left\{(0.65-\eta)\sin\left[\frac{3\pi}{2}\left(\frac{7}{6}-\frac{x}{t}\right)\right]+(0.35+\eta)\right\}, \tag{19}$$

σ_y is the 1% proof stress of the weld material, and η is the free parameter optimised by 'eye'.

$$\eta=4.79\times10^{-3}\tilde{Q} \tag{20}$$

valid for 10 J/mm^2 < $\tilde{Q}$ < 136 J/mm^2

Figure 2.17 shows the hoop stress profile using Bouchard formulation (denoted as New Formulation) in comparison with experimental measurements and Bradford Prescription and Figure 2.18 presents the hoop stress profiles for varying heat inputs of a pipe having R/t=10.

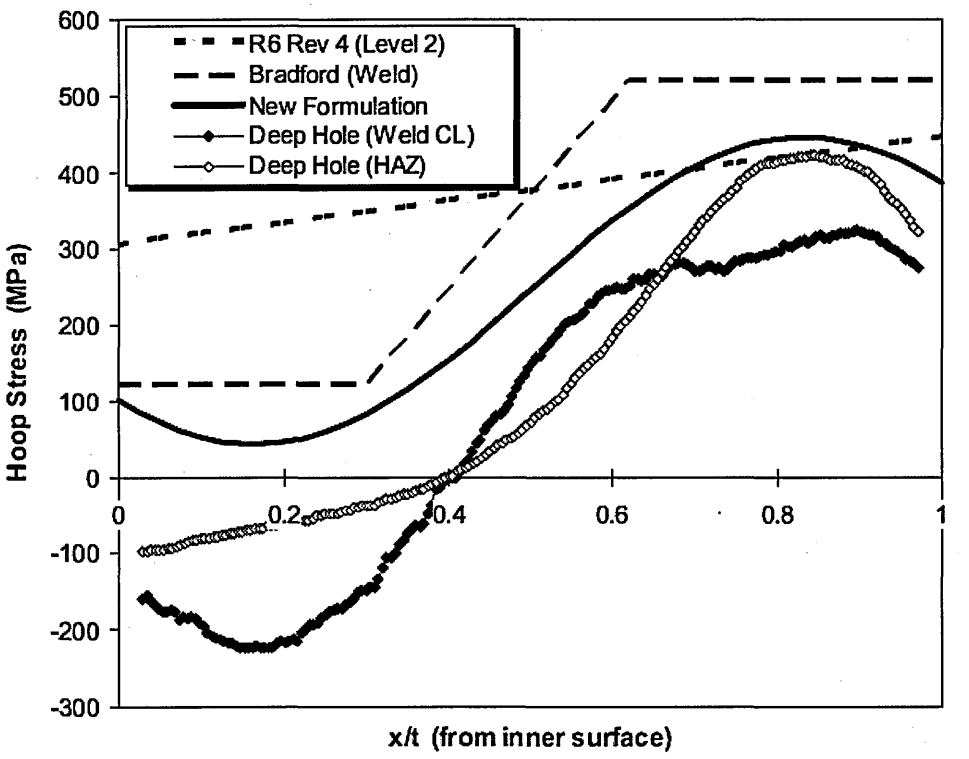

Figure 2.17. Comparison of experimental measurements and hoop residual stress profiles [18].

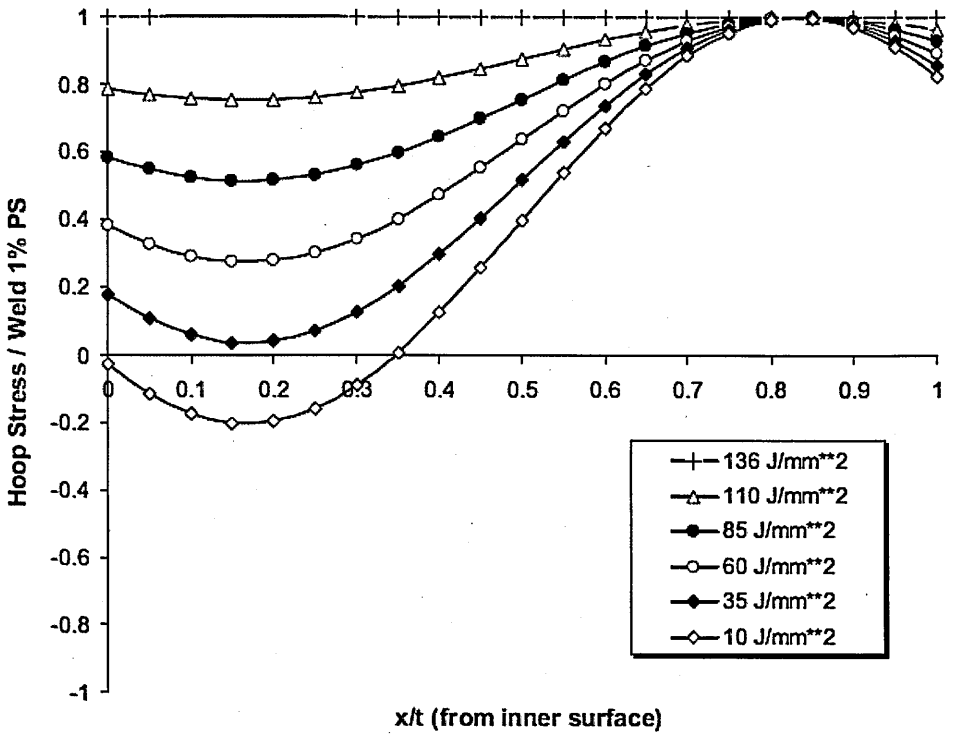

Figure 2.18. Hoop residual stress profiles using Bouchard's formulation (R/t = 10) [18].

The profiles in the hoop direction are considered to provide a more realistic description of the residual stresses and which are less conservative than the R6 level 2 upper bound profiles and Bradford prescription. However the formulation slightly over-predicts the residual stresses along the hoop direction particularly near to the inside surface as evident in the Figure 2.17.

2.4.4 Statistically based stress profiles

Weld residual stress profiles using statistical techniques have been developed recently using a Bayesian approach [119] and heuristic method [120-122] based on the combination of weighted least squares and the application of expert judgement. Both of these methods have achieved limited success in determining upper bound stress profiles to known confidence levels. Development of statistically based more accurate and reliable weld residual stress profiles requires detailed knowledge about the measured specimen and location of measurements. Best estimated residual stress profiles of multiple independent stress measurements using Bayesian statistics [123] can be achieved in two different levels. Level 0 calculates the Bayesian mean of stress measurements that are made at the same location. Level 1 fits an analytical model that reasonably represents the measurements taking into account all experimental data irrespective of whether measurements are made at the same locations. Level 0 and Level 1 approaches use Bayesian statistics and hold the advantage that it is less affected by outliers, can incorporate sources of prior information about measurements and allows analysts to include their personal judgements.

Nadri et al. [124] developed a statistical framework (see Figure 2.19) to analyse residual stress data at various levels of complexities depending on its spatial distribution. The modelling and statistical treatment of residual stress distributions in an edge welded stainless steel beam is also reported by Nadri et al. [125, 126]. Nadri et al. [127] applied this technique to analyse pipe girth residual stress data and found that it is not sufficiently rigorous and suggested ways of improving the analysis methodology. It consists of refining the statistical approach developed by Nadri [124-127] taking into account the instrumental resolution function, measurement uncertainties, enhanced treatment of stress components and by giving equal weight to each through-wall profile of the measured stresses [128].

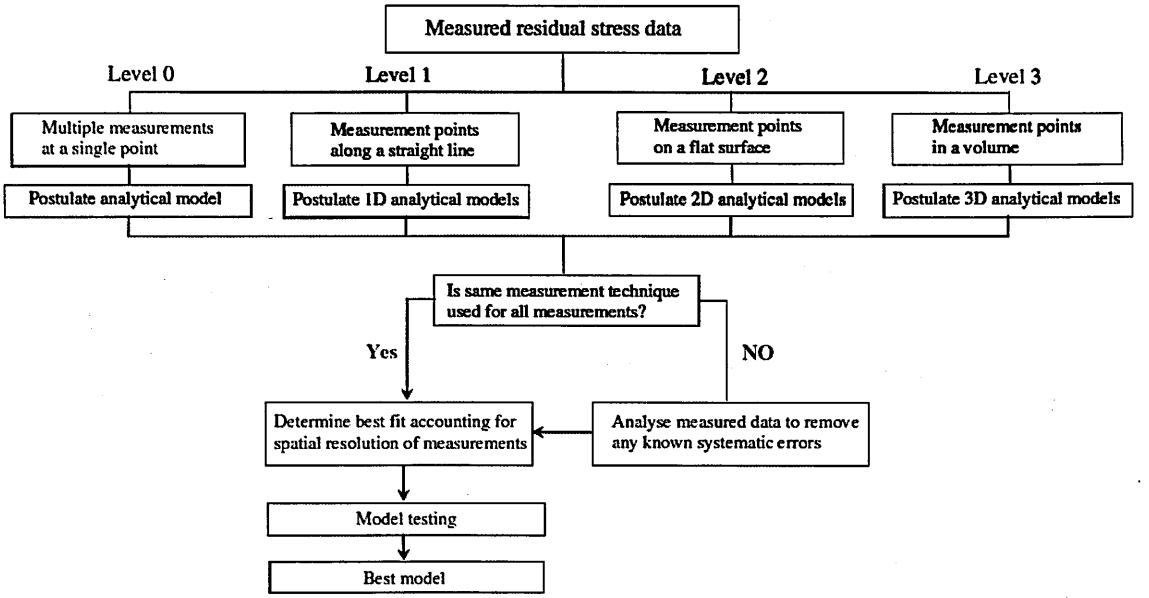

Figure 2.19. Statistical framework for analysing residual stress data developed by Nadri [124].

The Bayesian duff-data approach based on Baye's theorem applies a probability distribution of the measured datasets to determine the mean. It is capable of dealing with 'duff data' where there are relatively few data points. The approach assumes that if there are n independent stress measurements σ_k, k =1,2,3.....n and their uncertainties $\bar{\sigma}_{0k}$ from various laboratories larger than the stated error bars can be represented as a Gaussian distribution. Using the Bayesian duff-data approach the following posterior probability can be defined as given in equation (21).

$$\ln\left[\Pr ob(X/\{\sigma_k, \bar{\sigma}_k \geq \bar{\sigma}_{0k}\})\right] = const + \sum_{k=1}^{n} \ln\left[\frac{1}{|X-\sigma_k|} erf\frac{|X-\sigma_k|}{\bar{\sigma}_{0k}\sqrt{2}}\right] \qquad (21)$$

Where *erf* is the error function given by

$$erf(x) = \frac{2}{\sqrt{\pi}}\int_0^x \exp(-t^2)dt \qquad (22)$$

Within the statistical framework of Nadri [124], the Bayesian analytical method (Level 1) is an extension of the Level 0 approach used to analyse multiple stress measurements along a straight line. The method fits an analytical model function to experimental data using a least squares technique by minimising the sum of squared difference between measured and predicted data defined by,

$$\chi^2 = \sum_{k=1}^{n}\left(\frac{D_k - F_k(a_j)}{\sigma_k}\right)^2 = \sum_{k=1}^{n} R_k^{\,2} \qquad (23)$$

where F_k is the analytical model function to be fitted to experimental data

$F_k = F(D_k; a_j),\ k=1,2\ldots\ldots n$

R_k is the residual

n is the number of experimental data points

D_k are the corresponding experimental data points

σ_k are the uncertainties of the experimental data

a_j are the M unknown parameters in the analytical model

Similar to the Bayesian duff data approach, the analytical method leads to the following posterior probability,

$$\ln\left[\Pr ob(X/\sigma_k)\right] = const + \sum_{k=1}^{n} \ln\left[\frac{1-e^{-\frac{R_k}{2}}}{R_k^2}\right] \qquad (24)$$

The effect of spatial resolution is taken into account by incorporating the instrument resolution function in the level 1 approach as it may underestimate stresses at locations where there is a considerable variation. The analytical model is smeared with the instrument resolution function $H(y)$ resulting in the formation of a new analytical model F_k defined as,

$$F_k = \Phi \int f(y) H(y_k - y) dy + \psi \quad (25)$$

Where $f(y)$ is the analytical model

Φ is an experimental scaling constant that may be proportional to the time for which experiment was conducted.

ψ is the background signal and y_k is the position of measurement.

Wimpory et al. [129] observed that although the above Bayesian approach is less affected by outliers, care must be taken as in the case of where there are few data points in the average, a strong bias can occur towards data points with a relatively small quoted uncertainty. Moreover, this approach gives a large band of uncertainty which is not practically feasible to use in developing upper bound stress profiles. The stress profiles using Bayesian analysis approach provide more realistic bounding estimates of stress intensity factor than those currently used, but the results to date are insufficiently rigorous and conservative for inclusion into fracture assessment codes [128].

2.5 Summary

This chapter reviews the work reported in literature describing residual stresses and its role in structural integrity assessment. Various measurement techniques used to characterise residual stresses is described. The critical evaluation of various analytical models and finite element method is also discussed. The next chapter provide a detailed description of the residual stress measurements undertaken in newly fabricated girth welded pipes using neutron diffraction and contour method.

Chapter 3

Experimental characterisation of new pipe girth welds

3.1 Introduction

This chapter describes the fabrication process, characterisation studies and experimental measurements performed in butt welded stainless steel pipes. Measurements of residual stress were made by neutron diffraction performed using the SALSA instrument [130], ILL, Grenoble, France and the Contour method [47] using the in-house facility at The Open University, UK. The range of measurements provided extensive new data for supporting and validating the ANN approach developed in this dissertation for predicting through-wall residual stress profiles in welded pipes described in Chapter 4.

There are limited published measurements available describing through-wall distributions of residual stresses in stainless steel pipe butt welds, mostly collated in [18]. Other published sources rarely provide sufficient data related to the welding procedure such as the heat input. The data reported in [18] comprised measurements made in ten different components fabricated from austenitic stainless steel using various welding processes with net heat input (Q = 0.8 - 2.2 kJ/mm), wall thickness (t = 16 - 110 mm) and pipe mean radius to thickness ratio (R/t = 1.8 - 25). The experimental data were acquired 10 – 20 years ago by the UK nuclear industry for the purpose of validating finite element residual stress simulations.

All residual stress measurement techniques have limitations and associated uncertainties. For example, BRSL (see section 2.3.1) has low spatial resolution, neutron diffraction is very dependent on obtaining reliable stress-free lattice parameter data (which can be challenging for weld metal where the composition, texture and grain size vary) and DHD (described in section 2.3.1) has limited spatial resolution and the specific technique used at that time was susceptible to plasticity induced errors. The uncertainties associated with the historical data are estimated to be in the order of ± 50 MPa [41, 131] and could be more where the magnitude of stress is significantly high. Most of the mock-ups were made using Manual Metal Arc Welding (MMAW) with a J-prep and hence there is a lack of data representing TIG weldments with a V groove weld preparation. Moreover, there were very few experimental measurements in the dataset using neutron diffraction and none with the contour method. Figure 3.1 depicts the range of net heat inputs and thickness of welded pipes for which measurements are reported in [18]. It is evident from the figure that there are data gaps in the reported measurements especially in the region of pipes having relatively low wall-thickness which are highly sensitive to welding heat input.

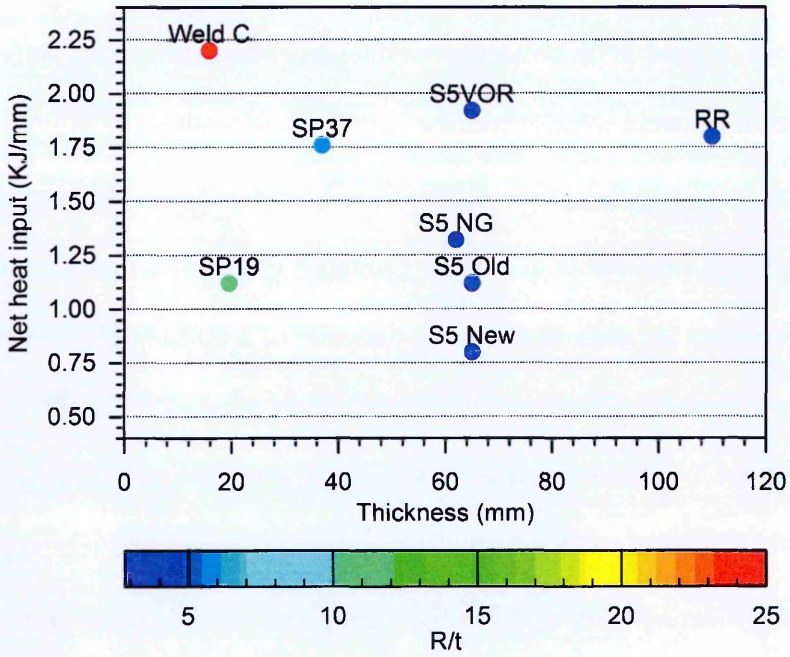

Figure 3.1. Range of austenitic stainless steel pipe girth weld mock-ups expressed as a function of net heat input and thickness [18] for which residual stress measurements have been published.

The purpose of this chapter is to present new residual stress measurements in austenitic stainless steel pipe welds to help fill the gaps in heat input, wall-thickness and R/t parameter space. Three half-inch thick pipe girth welds of outer diameter 265 mm were fabricated and residual stress measured using neutron diffraction and the contour method to extend the database of measurements in thin pipes. Three heat inputs were chosen to assess the effect of heat input. The data from these pipes were intended to add to the training data set and also for validation of the ANN approach. Welded pipes (MU4-1 and MU4-3) were measured by participating in the EU funded project STYLE [132] (thickness 25 mm and outer diameter 250 mm) and a welded pipe made from Esshete 1250 pipe (35 mm thick and 180 mm OD) was made available by EDF Energy. Figure 3.2 shows how the new set of welded pipes add to the published dataset presented in terms of heat input, component thickness and R/t ratio.

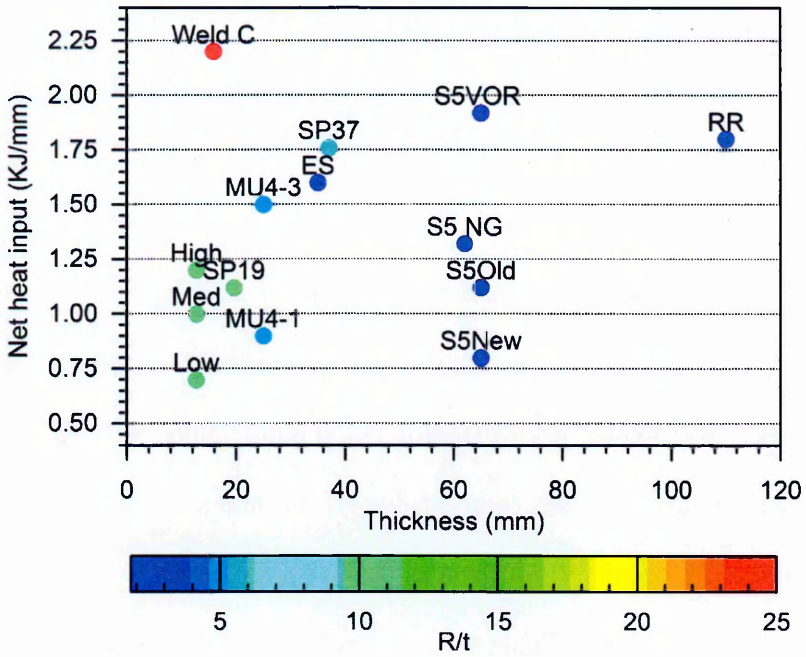

Figure 3.2. Combined range of stainless steel welded pipe components for which published residual stress data [18] were available with the new welded components (High, Med, Low, MU4-1, MU4-3 and ES) presented in terms of heat input, pipe thickness and R/t ratio.

This chapter first describes the set of half inch thick welded pipes and characterisation studies undertaken on each of the specimens. Neutron diffraction and contour method measurements performed on these pipes are discussed and compared with each other. The fabrication of STYLE project pipes (MU4-1 and MU4-3) is then discussed followed by the characterisation studies and critical comparison of stress profiles using diverse measurement techniques. Finally, studies performed on the Esshete pipe weld are discussed with particular emphasis on the measurement of axial residual stresses using the contour method. The chapter ends with a general discussion of findings based on comparisons of stress profiles using different measurement techniques at weld centre line (WCL) and heat affected zone (HAZ) locations.

3.2 Set of half-inch thick pipe girth welds

3.2.1 Manufacturing history and characterisation studies

A set of 3 butt-welded pipe components with dimensions 300 mm long, 265 mm outer diameter (OD) and 12.7 mm thick were fabricated from AISI Type 316L austenitic stainless steel under carefully controlled conditions at University of Manchester. The specimens were solution heat treated prior to welding at a temperature of 1060° C for one hour and air cooled to remove stresses induced due to the manufacturing process. The average parent metal yield strength (YS defined as the 1% proof stress) was 320 MPa and the chemical composition is given in Table 3.1. The welds had a single V-type side-wall preparation with a groove angle of 75° (schematic shown in Figure 3.3) and were made using a manual Tungsten inert gas (TIG) process with 316L filler wire. Three pipe welds were made using different electrical heat inputs of 0.7 kJ/mm (low), 1.0 kJ/mm (medium) and 1.2 kJ/mm (high) whilst the interpass temperature was maintained below 150° C.

Table 3.1. Chemical composition of the parent material

Composition %	C	Si	Mn	P	S	Cr	Ni	Mo	N
	0.02	0.51	0.94	0.034	0.00	16.7	11.1	2.07	0.061

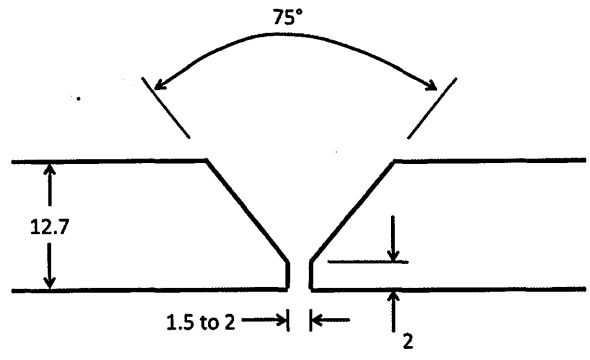

Figure 3.3. Weld groove preparation of half inch thick mock-ups.

A slot (i.e. a window) was machined in each of the pipes to facilitate neutron diffraction residual stress measurements, by reducing neutron beam attenuation and measurement time. The extracted 'plug' of material was used for metallurgical analysis and hardness measurements, as well as for preparing 'stress-free' reference specimens (denoted d_0 specimens) for the diffraction measurements. The macrographs and hardness maps were used to compare the measured residual stress distributions with the corresponding metallurgical zones i.e. the WCL and HAZ across the welded joints.

The surfaces to be examined were prepared following standard metallographic sample procedures which included grinding down to 4000 grit using silicon carbide paper and polishing in two steps using soft nap cloth coated with 3μ and 1μ diamond suspension. To reveal the weld macrographs and microstructures, the polished surfaces were etched electrolytically using 5% oxalic acid at 6V for 30 s. Macroscopic photos were taken using a Nikon Digital SLR camera and the microstructures at various locations using a Leica DMI5000 microscope. Hardness measurements were performed using a Vickers (HV) indenter, applying a load of 5 kg, using an automated Struers Duramin-A-300 hardness tester. The measurements were undertaken on several straight lines at intervals of 0.5 mm or 1 mm depending on the sample dimension with the spacing of 1 mm. The same procedure was repeated for the STYLE and Esshete pipe welds (discussed later in the chapter).

The weld macrographs and hardness maps of the half inch pipes are illustrated in Figure 3.4. In all three mock-ups, a similar pattern was observed with maximum hardness in the region close to the weld root. The magnitude of peak hardness was between 240 - 260 HV5 observed in the region near to the weld root and minimum of about 150 HV5 in the parent material. In the weld metal region, some of the weld passes would have been partially hardenened by subsequent passes. These regions are evident especially at the root of the weld where there is significant increase in hardness. In all three mock-ups, a decrease in the hardness values was observed moving from the weld to the HAZ. Moreover, there is a marked decrease in hardness moving towards the parent material, with typical values being ~200 HV5 in the HAZ, and ~160 HV5 in the parent metal. The microstructural examination (see Figure 3.5) shows the presence of a dendritic structure in the weld.

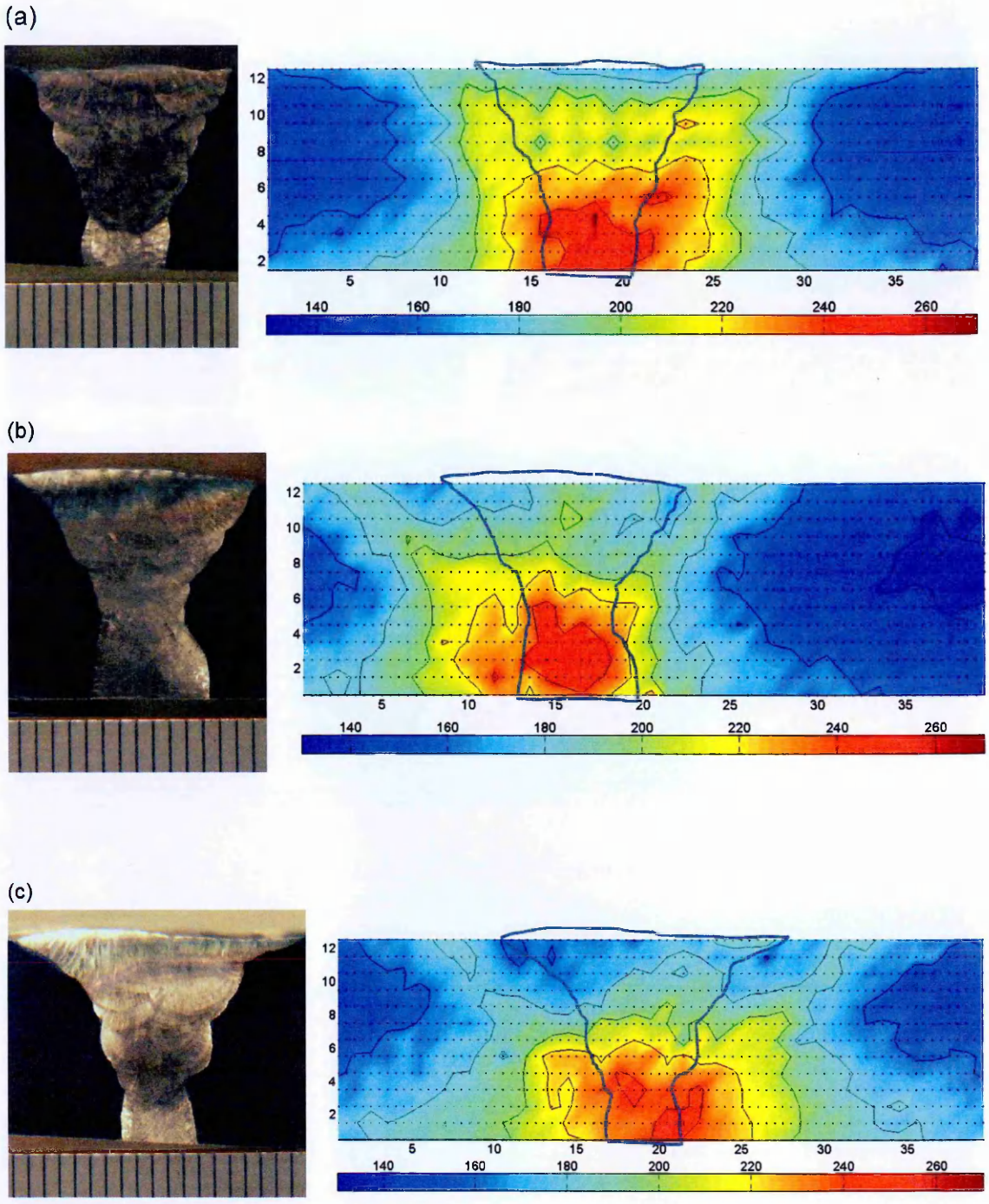

Figure 3.4. Weld macrographs and hardness maps of (a) Low (b) Medium and (c) High heat input butt welded half inch thick pipes.

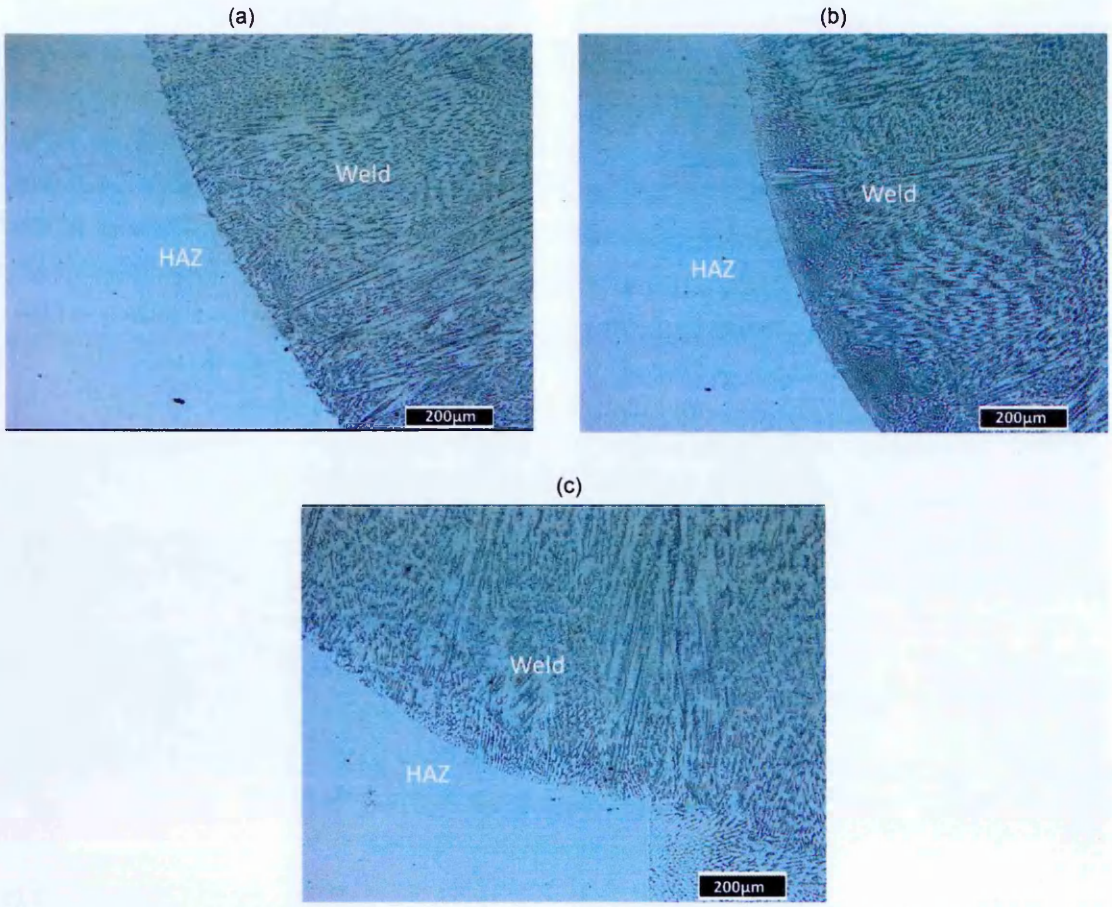

Figure 3.5. Microstructural analysis at the fusion boundary of (a) Low, (b) Medium and (c) High heat input pipes.

3.2.2 Measurement of residual stress by neutron diffraction in the half inch thick welded pipes

Experimental Procedure

Neutron diffraction is a frequently used non-destructive method for measuring residual stresses because of the appreciable depth of penetration that can be achieved which is of the order of several centimetres in stainless steel structures and because it can provide full residual stress field tensor data. For these reasons, neutron diffraction was used to measure the residual elastic strain through the thickness of the girth welded pipes at various locations of interest. The neutron experiments were conducted in two sessions, wherein the through-wall distributions of as-welded residual stresses of the two welded pipes MU4-1 and MU4-3 were measured in the first cycle, and the three half inch pipes in the second. In both experiments, neutrons with a wavelength 1.648 Å were collimated to a nominal gauge volume of (2.3 x 2.3 x 2.3) mm^3 and for analysis of the {311} reflection a diffraction angle of approximately 99° was obtained. The {311} reflection was chosen as it is less dependent on plastic strain for metals with face centred cubic crystal structure [133].

The pipe was aligned such that the beam came through the window and measured the hoop component of strain at the specified measurement points. The pipe was set-up differently on the instrument hexapod stage to do measurements of axial and radial strain components, and hoop strain component at the same positions. The same experimental procedure was followed for both cycles of experiments. A schematic illustration of the different orientations of the pipe while performing the neutron measurements is given in Figure 3.6.

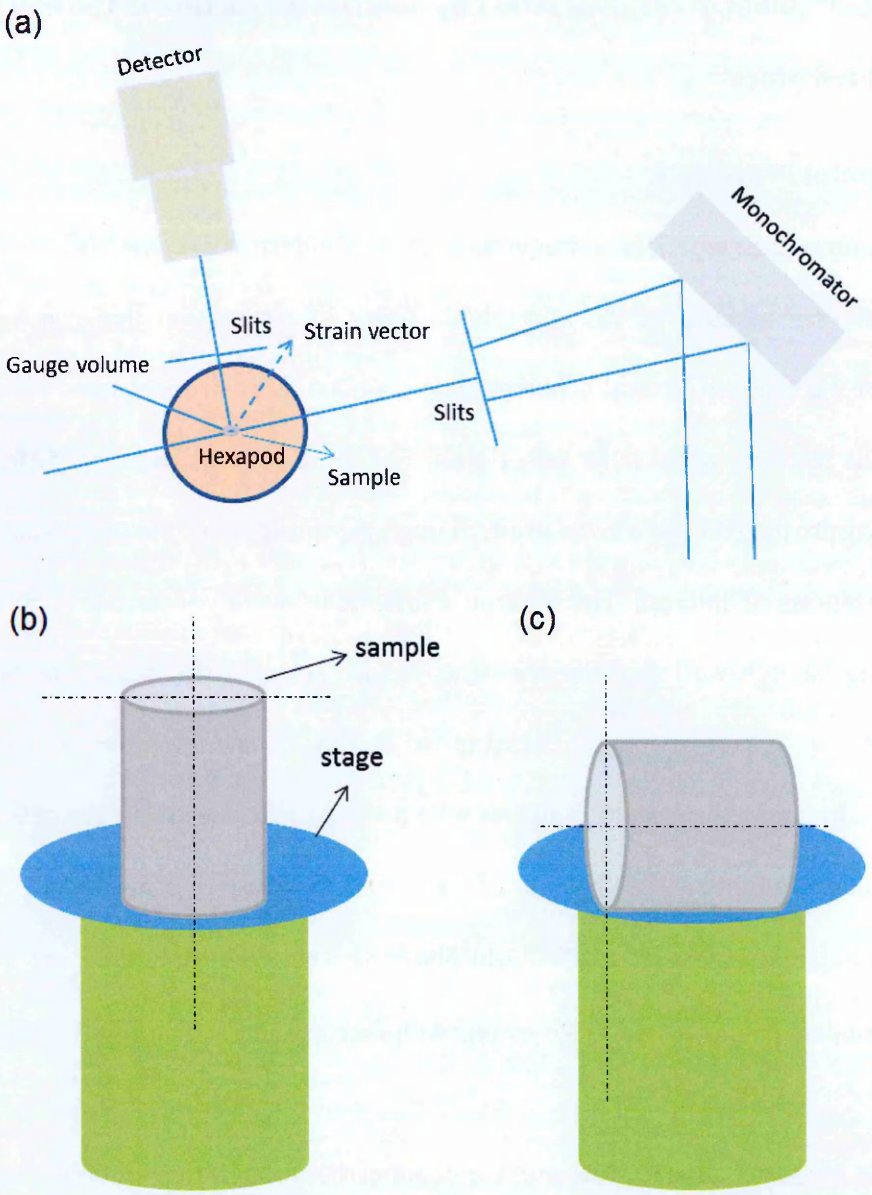

Figure 3.6. Schematic illustration of (a) setup of SALSA diffractometer, different orientations of the pipe while performing the strain measurements in the (b) hoop, (c) axial and radial directions.

An access window of dimensions 35 mm x 50 mm was machined in each of the half inch thick pipes using a die sink EDM process in preparation for neutron diffraction residual stress measurements. The residual strains were measured using neutrons at approximately 90° offset to the weld start-stop location.

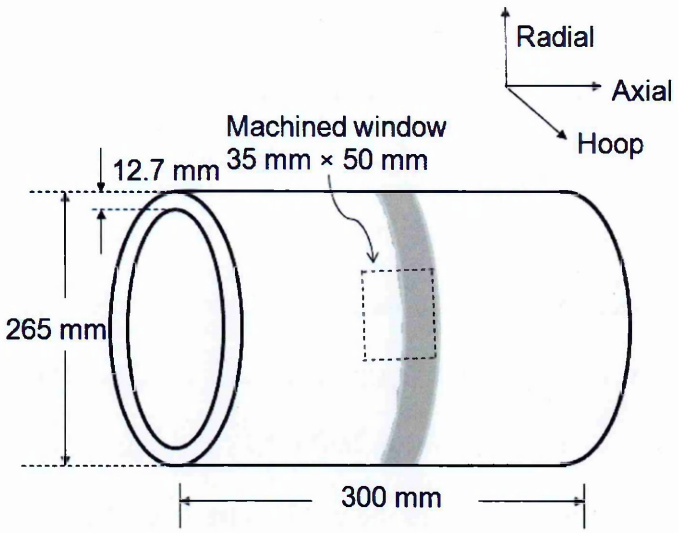

Figure 3.7. Schematic illustrating the location of the machined window in the half inch thick girth weld.

The LAMP (Large Array Manipulation Program) [134] was used for the treatment of data obtained from neutron scattering experiments. An example of the diffraction peak obtained with an exposure time of 15 min in the low heat input pipe along the axial direction is given in Figure 3.8.

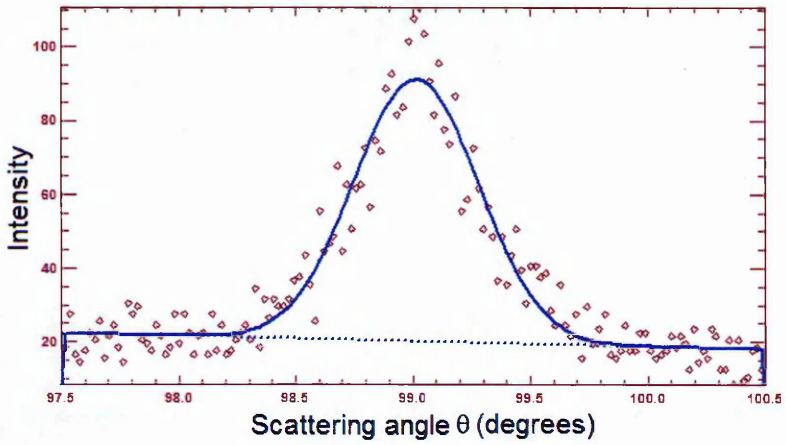

Figure 3.8. Example of diffraction peak in the low heat input pipe along the axial direction.

For stress free reference measurements, pins of weld and HAZ metal were extracted from the plug of material removed to create the window, with dimensions 5 mm x 5 mm x 12.7 mm (see Figure 3.9 (b)). Position dependent values for the stress free lattice parameter were determined by interpolating between fifteen measurements on each pin using a polynomial function. Position dependent values were also used to calculate the through wall stresses at locations between the WCL and HAZ (2 mm and 4.5 mm away from the weld centre-line) and HAZ stress free values for points further away from the HAZ (i.e. 10 mm and 14 mm away from the weld centre-line). The shift in the scattering angle observed in the stress free reference measurements at the WCL and HAZ locations is shown in Figure 3.10. It should be noted that the scatter registered in the stress free references at the WCL is significantly higher than in HAZ location.

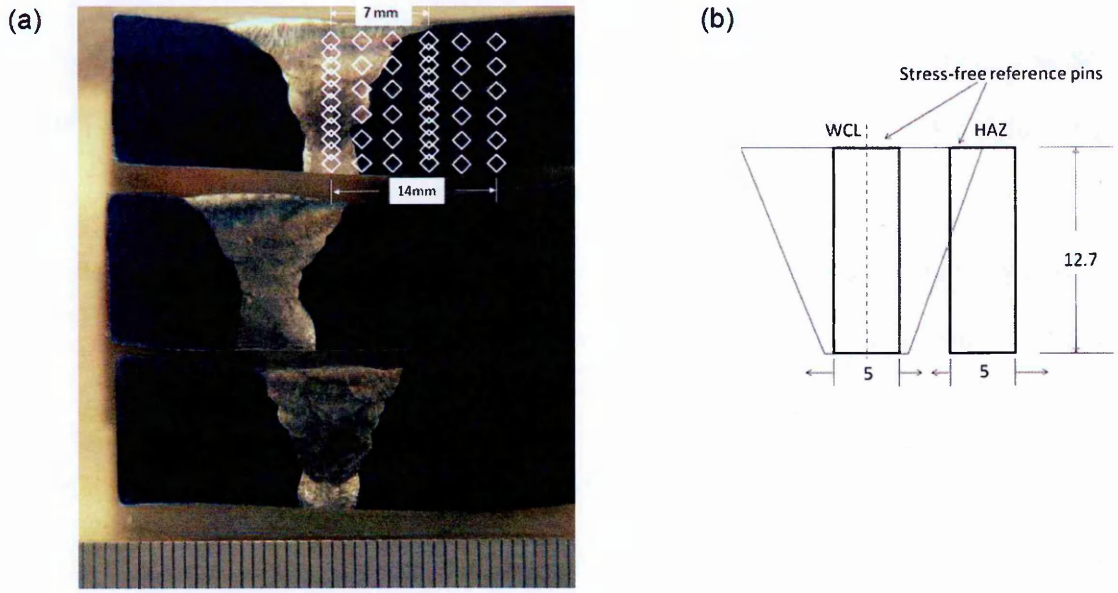

Figure 3.9. Schematic of (a) measurement array of neutron points in each of the half inch thick pipes and (b) stress free reference material extracted in the form of cylindrical pins.

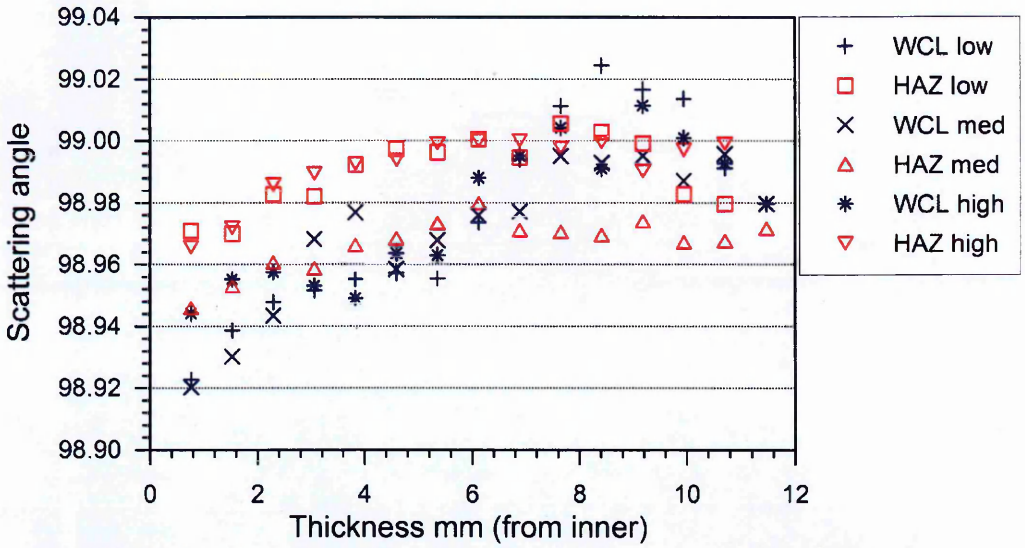

Figure 3.10. Variation of scattering angle in the stress free reference measurements of the low, medium and high heat input pipes at the WCL and HAZ locations.

Maps of stresses measured by neutron diffraction

The maps of measured stress acting in the axial direction in the low, medium and high heat input girth welds are presented in Figures 3.11-3.13. High tensile stresses were

concentrated at a distance of 2 mm away from the weld centre line in the low heat input pipe, and gradually decreased with increasing distance from the WCL. In the case of the high heat input pipe, the maximum stresses were observed to be offset from the WCL which was in a state of compression through the entire though-thickness. The results reported were unexpected as high axial stresses concentrated around the WCL are reported in [18]. Furthermore, the magnitude of tensile stresses is expected to decrease moving further away from the WCL towards the HAZ and into the parent material. However, peak stresses were observed away from the WCL in all low, medium and high heat input pipes with the WCL predominantly being in a state of compression. Overall, the highest tensile stresses were found in the low heat input pipe having a magnitude of 300 MPa, followed by the high heat input mock-up with less than 200 MPa and the medium pipe with about 150 MPa.

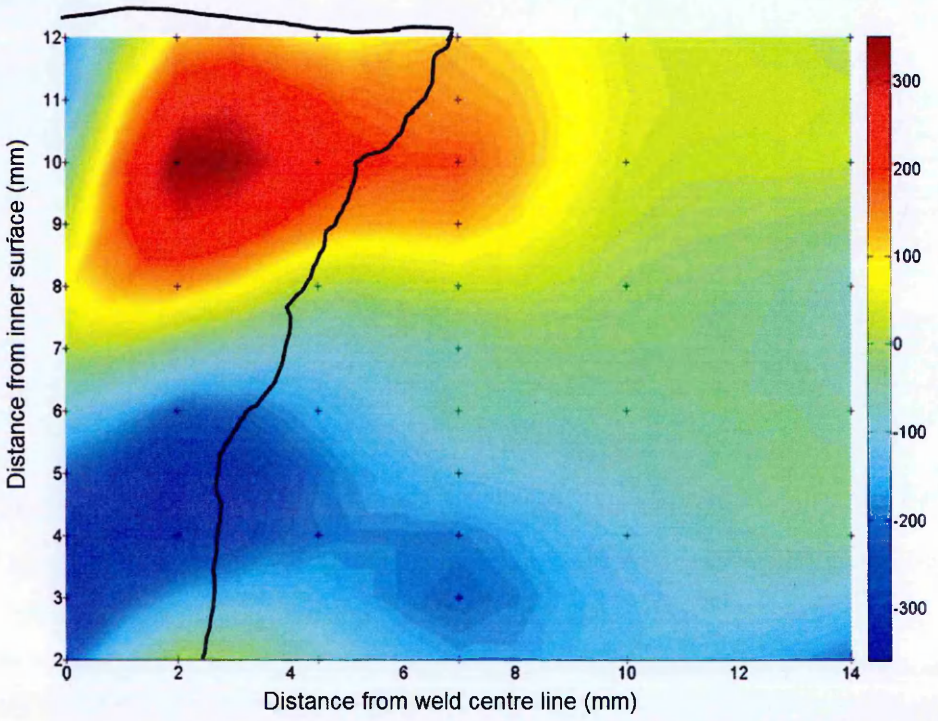

Figure 3.11. Map of axial residual stress measured by neutron diffraction in the low heat input pipe using neutron diffraction. Crosses denote actual measurement points.

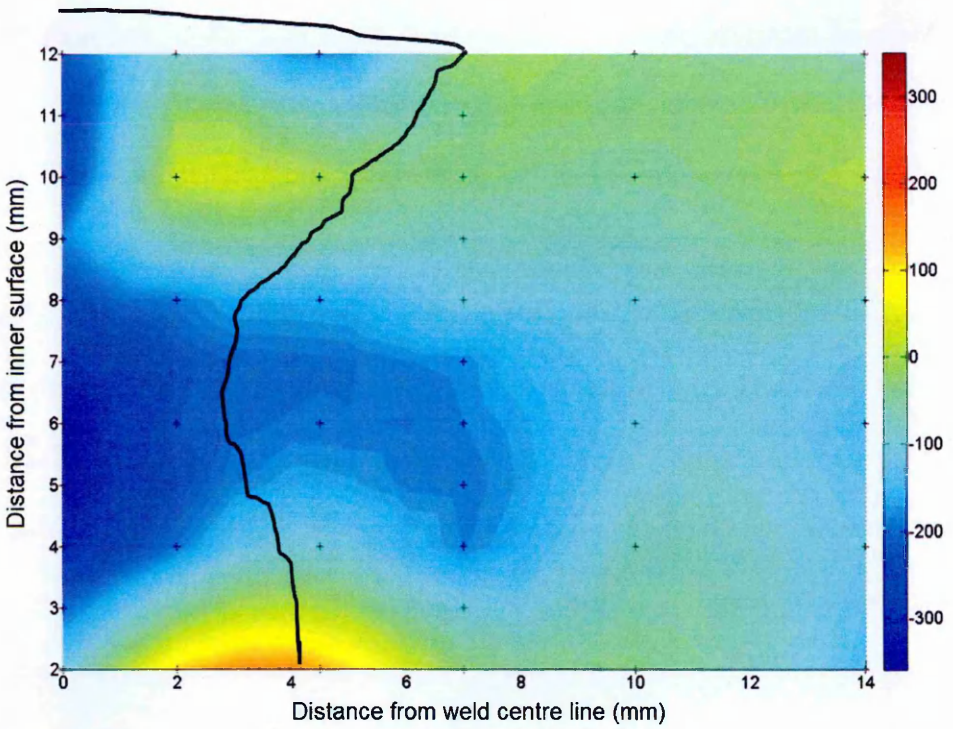

Figure 3.12. Axial stress map for the medium heat input welded pipe measured using neutron diffraction.

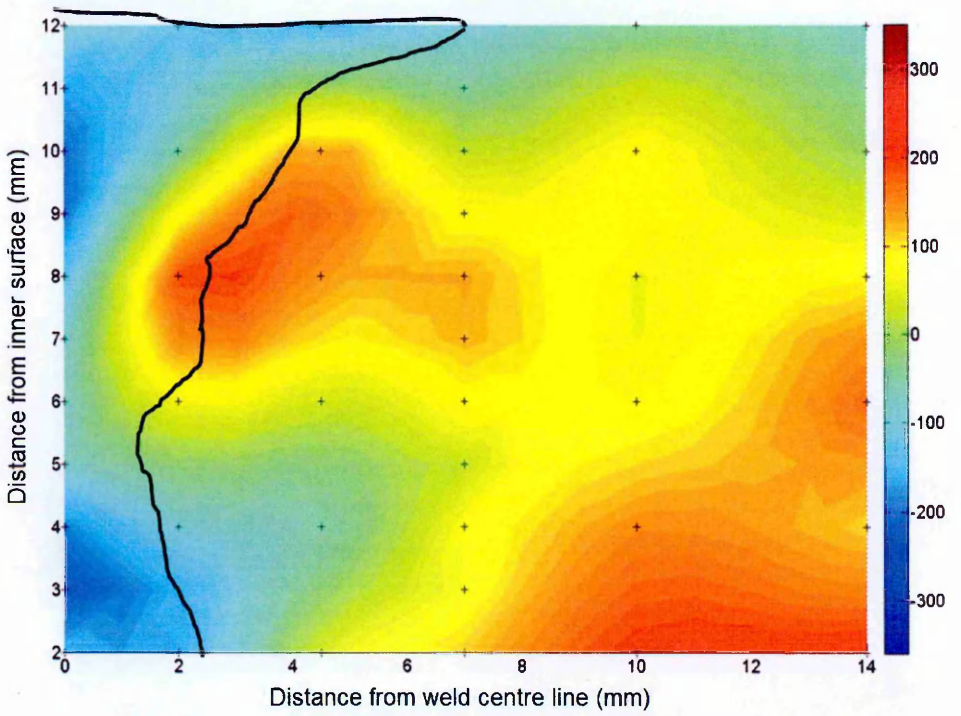

Figure 3.13. Axial stress map of high heat input welded pipe using neutron diffraction.

Maps of measured hoop residual stress in the low, medium and high mock-ups (Figures 3.14 - 3.16) exhibit the same trends, as the axial stress maps, having high magnitude compressive stresses along the weld centre line at all through-wall positions. High magnitude compressive stresses are commonly observed near the weld root in the hoop direction as reported in [18], but it is unusual to find the final weld capping passes in compression. The maximum stresses observed were at a distance of 3 mm away from the WCL in the low, medium and high heat input pipe whereas comparatively lower magnitude stresses were found to exist in the medium heat input pipe. Overall, the highest tensile stresses were found in the low heat input pipe of about 600 MPa, closely followed by the high heat input pipe with less than 500 MPa and the medium heat input pipe of about 300 MPa. Interestingly, higher stresses were observed in the HAZ when compared with the WCL which was consistently in a state of compression in all cases. This has never been reported before in austenitic stainless steel welds which questions about the present results.

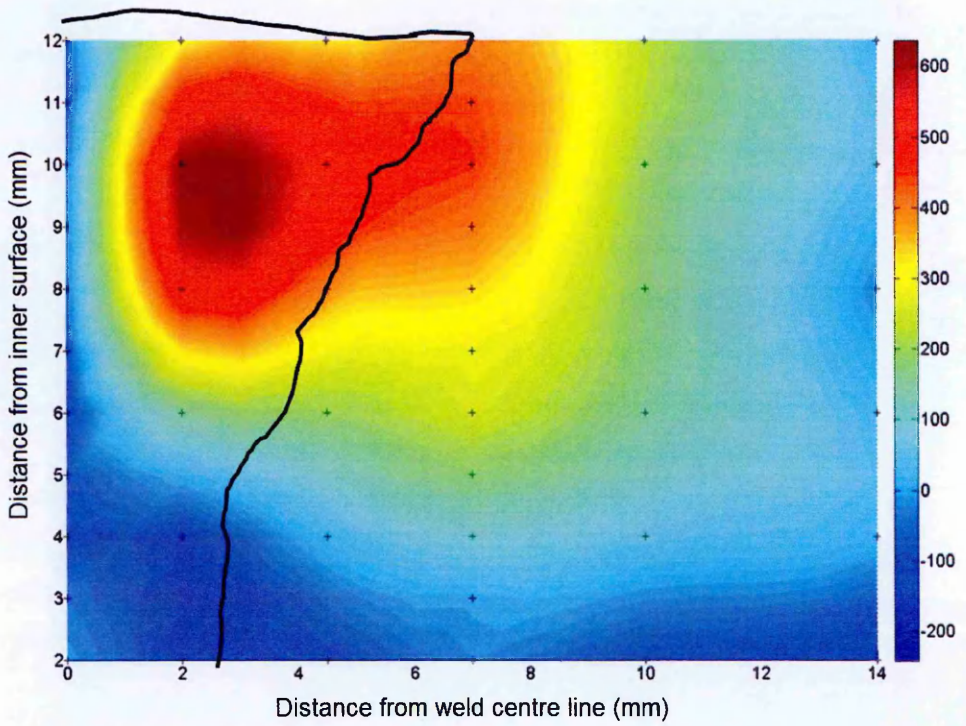

Figure 3.14. Map of hoop residual stress measured by neutron diffraction in the low heat input pipe using neutron diffraction. Crosses denote actual measurement points.

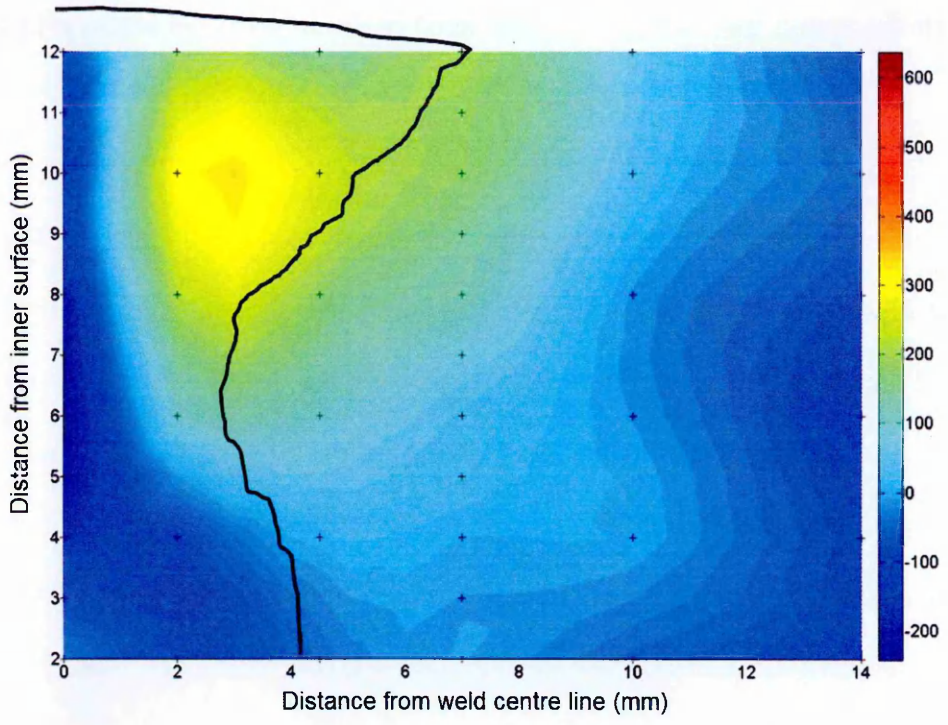

Figure 3.15. Hoop stress map for the medium heat input welded pipe measured using neutron diffraction.

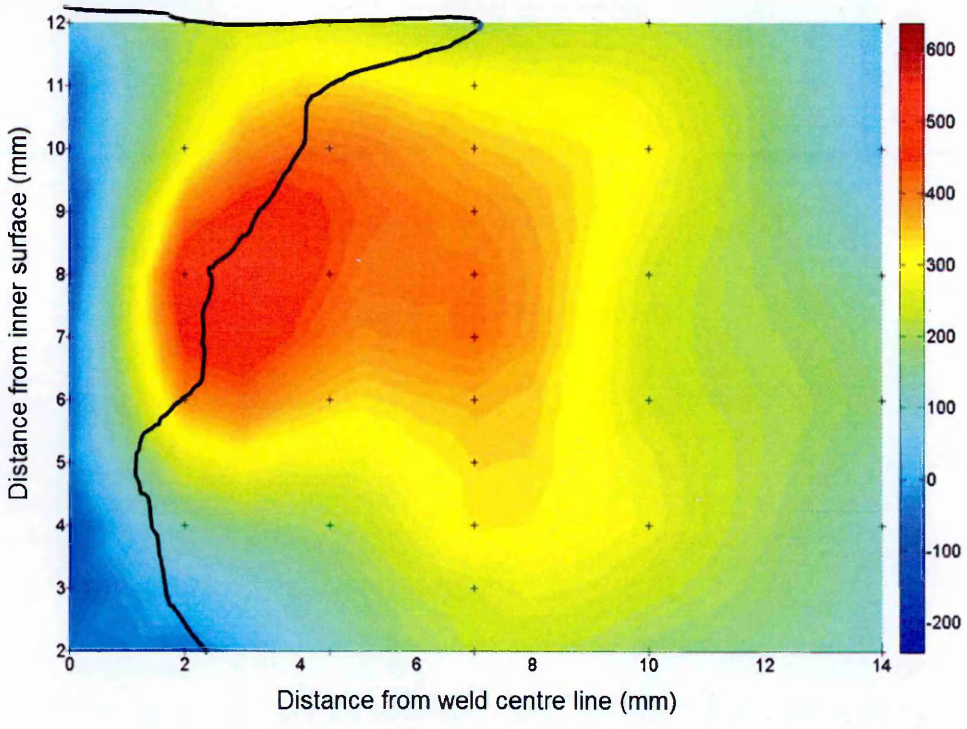

Figure 3.16. Hoop stress map for high heat input welded pipe using measured neutron diffraction.

Through-thickness line profiles of measured residual stresses at the WCL and HAZ

The axial, hoop and radial stress profiles at the WCL and HAZ of the three pipes are shown in Figures 3.17-3.19. There is no obvious pattern found in the nature of the axial stress profiles at the WCL and HAZ with respect to the different heat inputs used for welding. Likewise no effect is evident in the hoop stress profiles. Furthermore, substantial radial stresses were measured at the WCL (see Figure 3.19) in all three pipes. This is unrealistic considering that the wall-thickness of the pipes is less than 13 mm. For further investigation, the radial stresses were forced to zero assuming a state of plane stress as the pipes are relatively thin, and the resulting axial and hoop residual stress profiles examined.

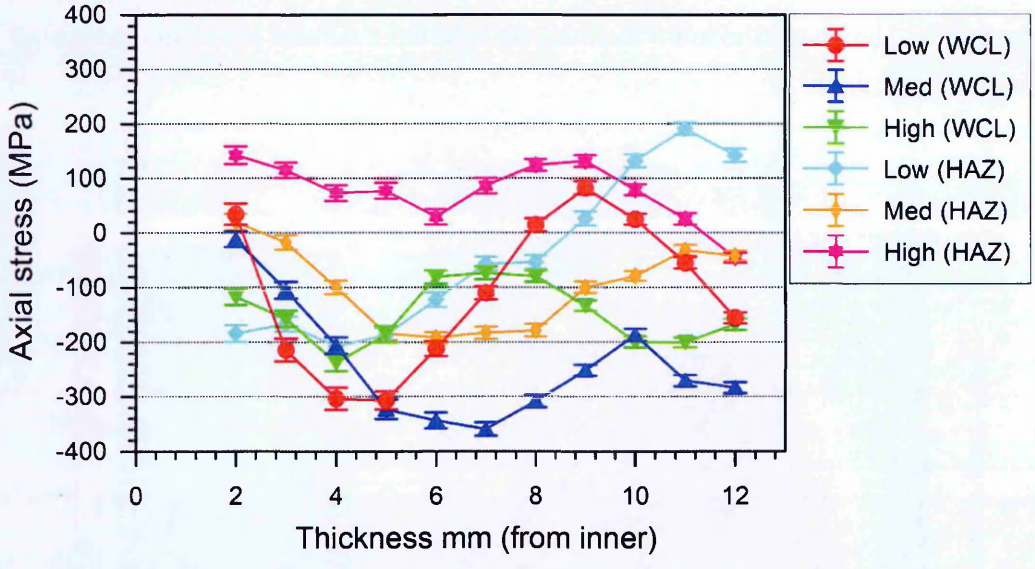

Figure 3.17. Through wall axial stress distributions in the low, medium and high heat input pipes measured at the WCL and HAZ.

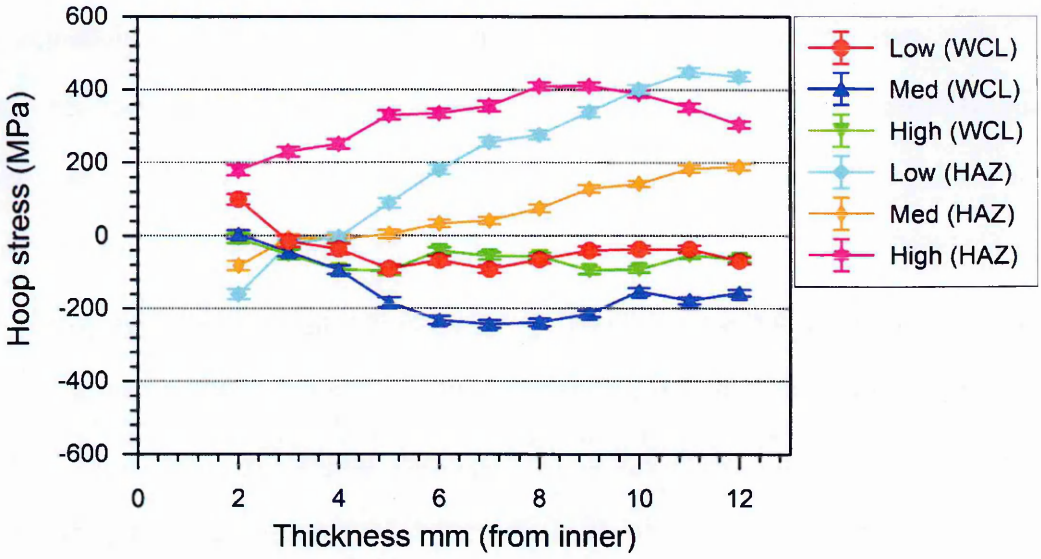

Figure 3.18. Through wall hoop stress distributions in the low, medium and heat input pipes measured at the WCL and HAZ.

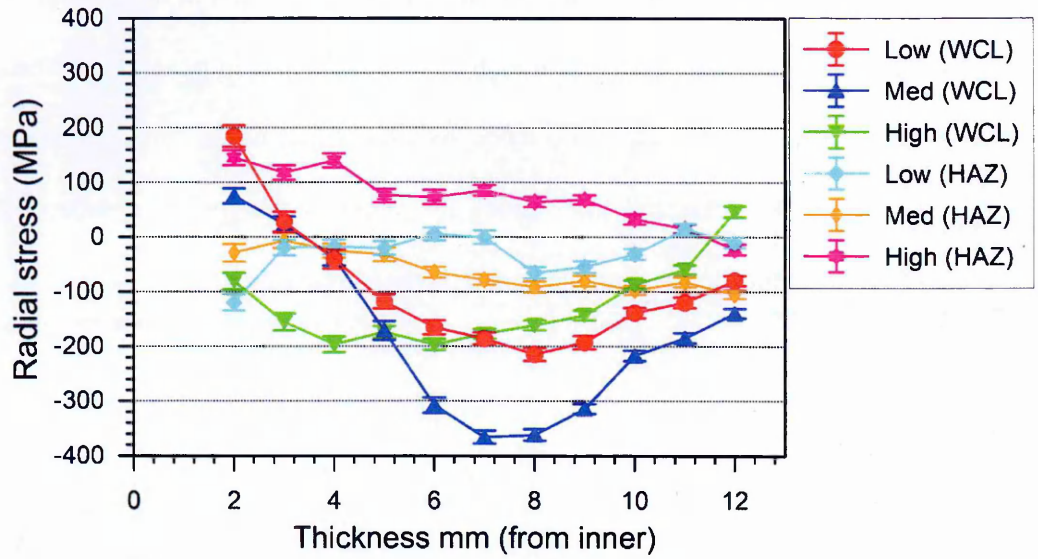

Figure 3.19. Through wall radial stress distributions in the low, medium and high heat input pipes measured at the WCL and HAZ.

The stress profiles assuming zero radial stresses in the three mock-ups are illustrated in Figures 3.20 and 3.21. In the axial direction, a specific pattern was obvious in all the stress profiles in accordance with the variation in heat inputs. The low heat input pipe had significantly lower stresses at the inner diameter along the WCL that peaked near 8 mm from the inside surface and therefore displayed the highest magnitude tensile and compressive stresses out of the three pipes. The high heat input pipe was least compressive at the ID and had a minimal change in the magnitude progressing towards the OD. As expected, the medium heat input pipe had an intermediate profile when compared to the low and high heat input pipes. There was less variation in axial stresses at the HAZ between three mock-ups. In the hoop direction, the peak stresses at the WCL of all the mock-ups were about 100 MPa. In the HAZ, the low heat input pipe had the highest tensile stresses close to the outer surface and a similar pattern was also found in the medium heat input pipe with the magnitude of stresses lower by about 100 MPa. In general, the stresses observed in all three pipes seemed to be more realistic when based on a plane stress assumption. However, it is essential to compare the stress profiles with an independent technique to gain confidence in the corrected neutron measurements.

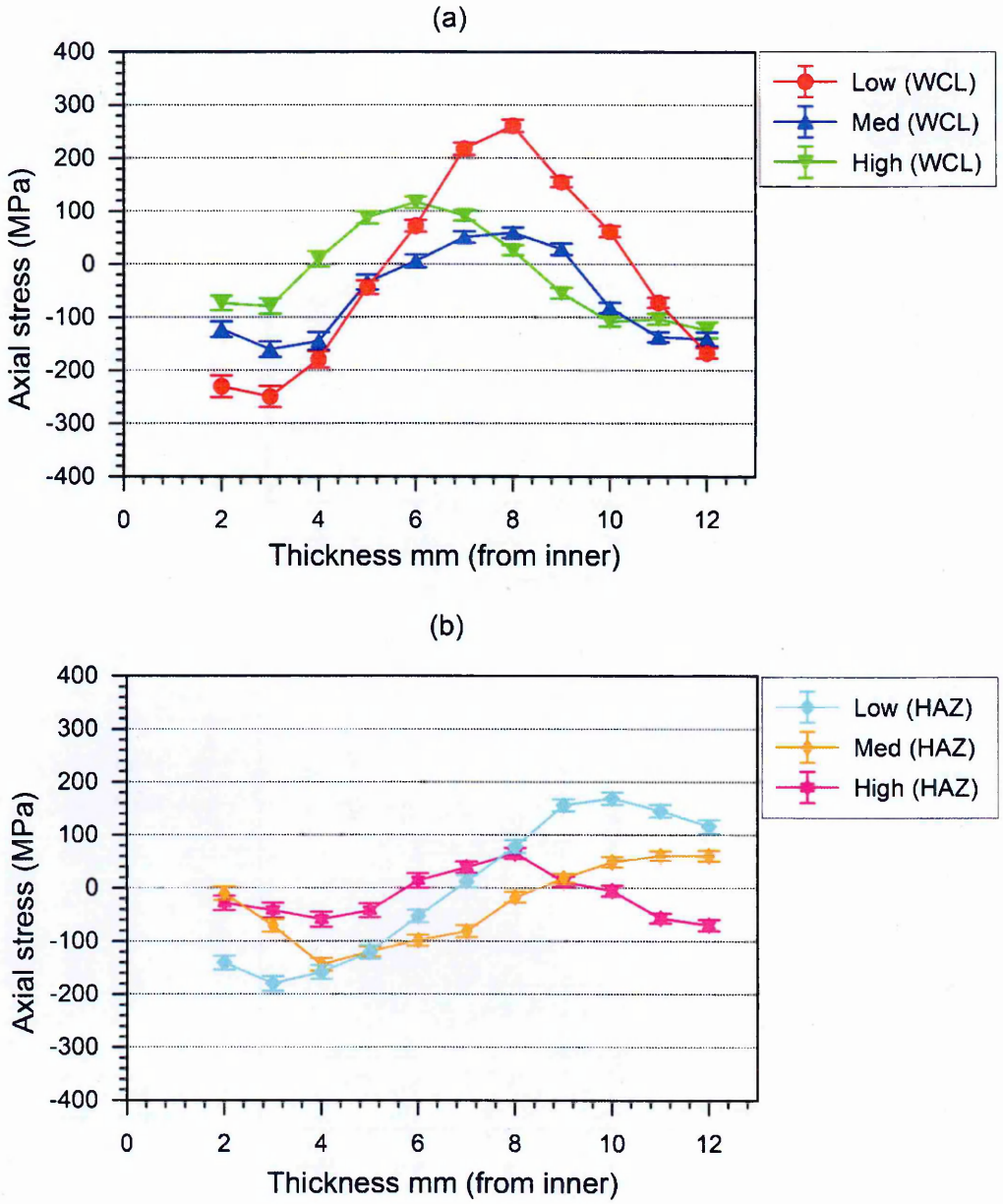

Figure 3.20. Axial stress distributions based on assumed plane stress conditions in the low, medium and high heat input pipes measured at (a) the WCL and (b) the HAZ.

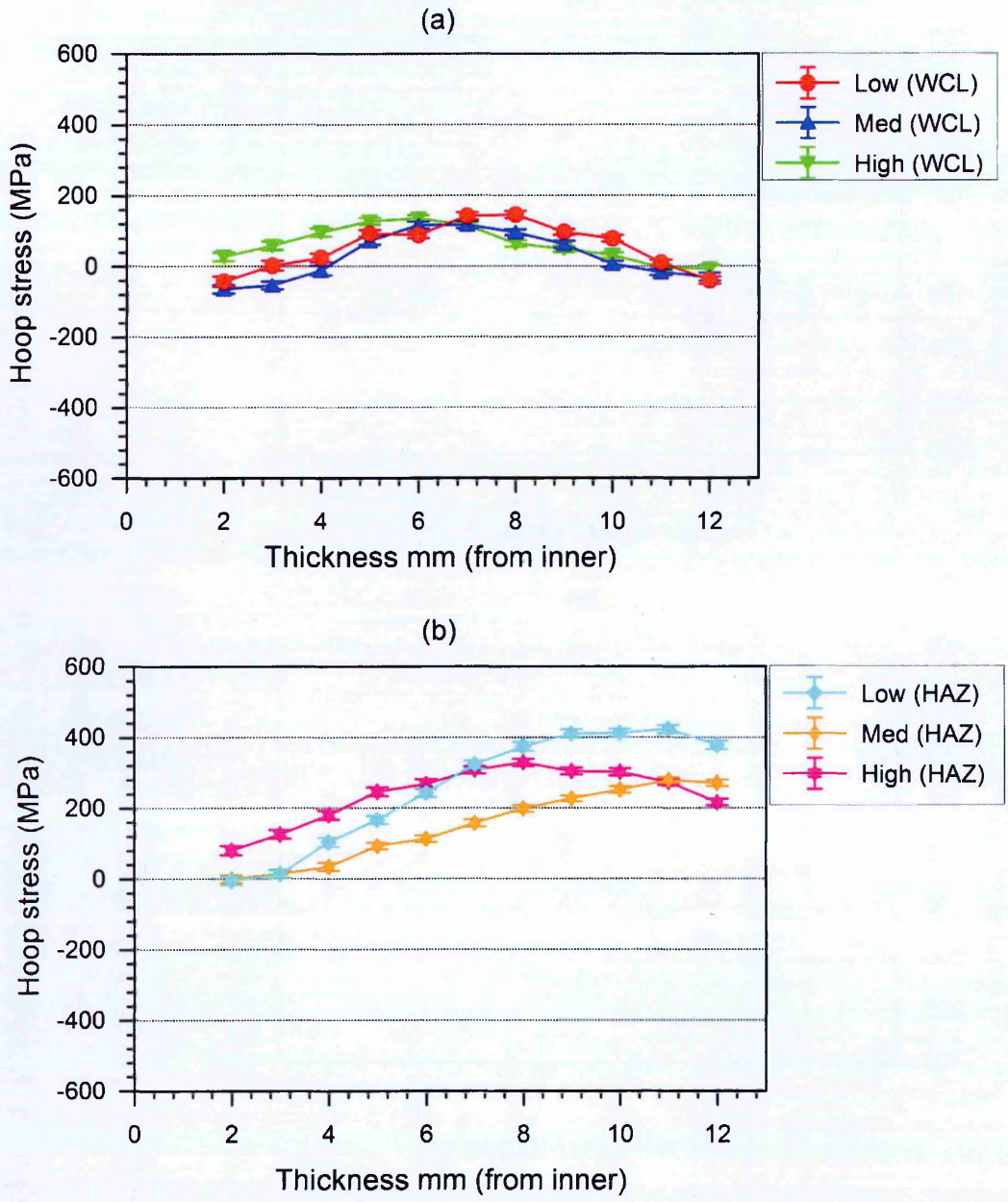

Figure 3.21. Hoop stress distributions based on assumed plane stress conditions in the low, medium and high heat input pipes measured at (a) the WCL and (b) the HAZ.

3.2.3 Contour method residual stress measurements of the half inch thick pipes

The contour method can be applied to measure a full 2-D cross sectional map of the hoop residual stresses present in thick cylindrical components [52, 62]. The 'skim' mode of WEDM (Wire Electro Discharge Machining) was implemented for the contour cuts because this promotes a good surface finish and the relatively low electrical energy, minimises changes in material and the residual stresses near to the cut surfaces. The distribution of hoop stress of the component of interest can be determined by performing a cut along a radial-axial plane using the approach reported [62] by cutting the pipe lengthways into two halves severing both the opposite thicknesses simultaneously (see Figure 3.22). A specially designed jig was used to securely clamp the pipe to prevent any opening or closure of the component during the cut. Extensive cutting trials were conducted on 300 series stainless steel material replicating the pipe geometry to optimise the cutting parameters prior to the contour cut.

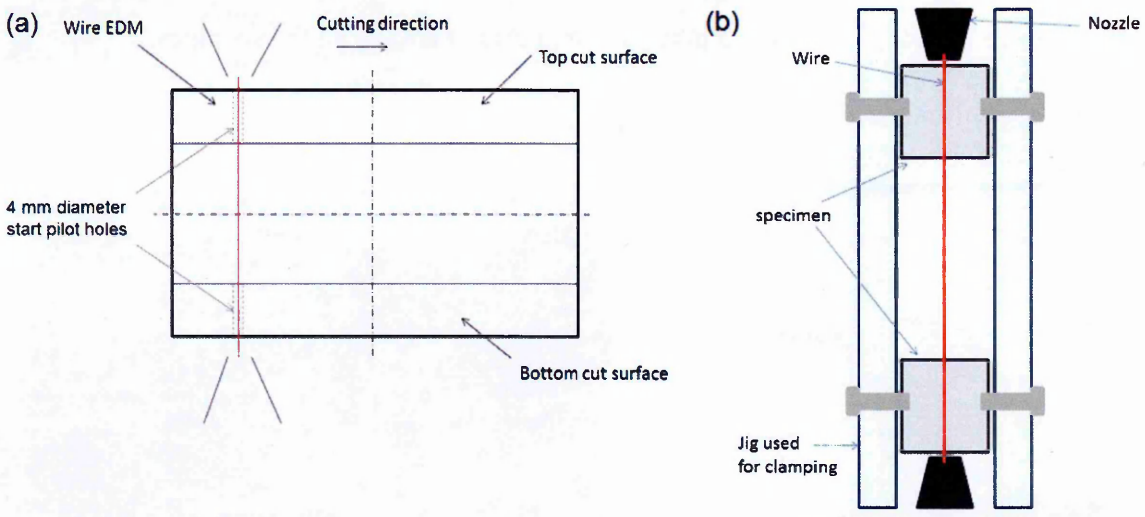

Figure 3.22. (a) Schematic of wire EDM and the resulting cut surfaces (b) Trial cuts performed in pipes (a) and (b) represent the approach reported in [62] to undertake contour cuts in pipes.

The measurement cut was made using a 'skim cut' setting of the Agie Charmille F440S wire EDM with a 0.25 mm diameter brass wire. Start pilot holes (4 mm diameter)

were drilled 15 mm from one end of the pipe to reduce opening of the cut flanks and thereby reduce the risk of introducing significant plasticity at the cut tip. The same cutting mode was used to undertake contour cuts in all the six pipes with minor modifications made to the WEDM parameters to account for the variation in wall thickness and geometry.

Coordinate measuring machines (CMM) with contact and non-contact probing mechanisms are commonly used for contour surface measurements in large engineering components. The surface deformation contours of the mating cut surfaces were measured using a common coordinate system [62] that holds the advantage of having the hoop bending moment across the pipe automatically included in the residual stress distribution along with the variation through the length of the pipe. The surface contours were measured in a temperature controlled environment using a Mitutoyo Crysta plus coordinate measuring machine (CMM) (see Figure 3.23). A touch probe system with 3 mm diameter ruby tip was used to provide a 0.5 mm × 0.5 mm grid of data in all the six pipes.

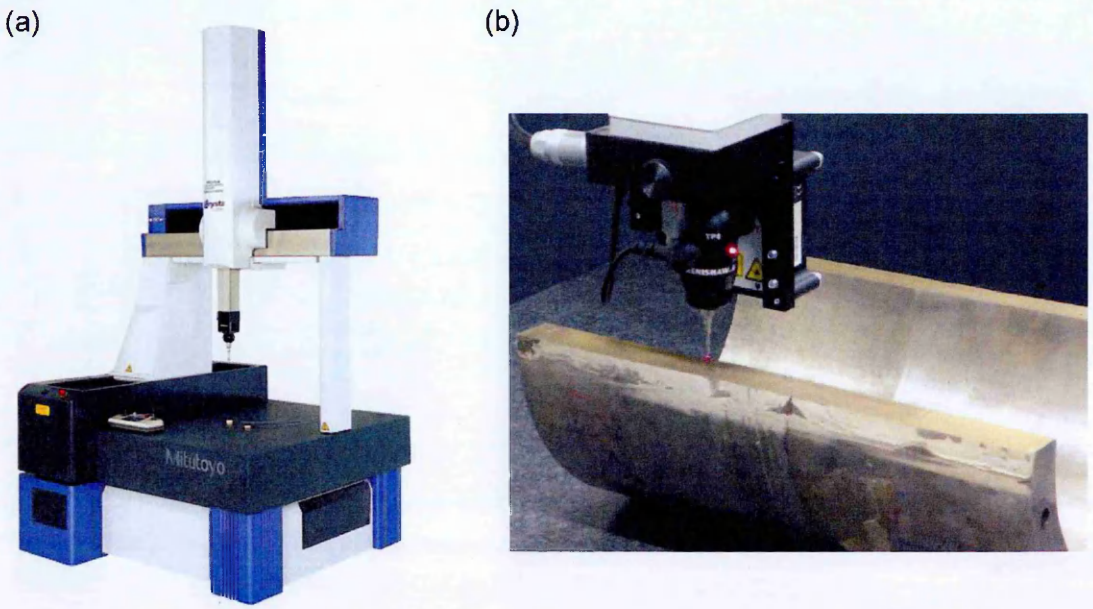

Figure 3.23. (a) Mitutoyo Crysta Plus 574 coordinate measurement machine (b) Cut pipe measured using the CMM.

The datasets corresponding to the cut surfaces were aligned by translation and rotation of one dataset, since they were measured in different local coordinate systems, mapped onto a common grid system before averaging, to eliminate shear effects. The averaged data were then cleaned to remove outliers and smoothed by curve fitting using a 3D cubic spline based algorithm [135]. A knot spacing of 7 mm was consistently used in all mock-ups as it was found to provide an optimum spline fit to the measured data of a P91 pipe [136].

For each measured pipe, an undeformed 3D model of one half of pipe was created using ABAQUS FE software [83] based on the measured perimeters of the cut faces. An example of one of the 3-D FE models of the pipe is illustrated in Figure 3.24. Linear hexahedral reduced integration elements (C3D8R) were used with a fine mesh of 1mm size at the cut surfaces and progressively coarsened around the pipe circumference as shown in Figure 3.24. The opposite of the averaged normal displacements were applied as boundary conditions to the cut faces of the model and rigid body motion restrained by using three additional displacement constraints. To back calculate the released residual stresses acting normal to the cut surface, a linear elastic FE analysis was carried out using isotropic material properties (Young's modulus and Poisson's ratio).

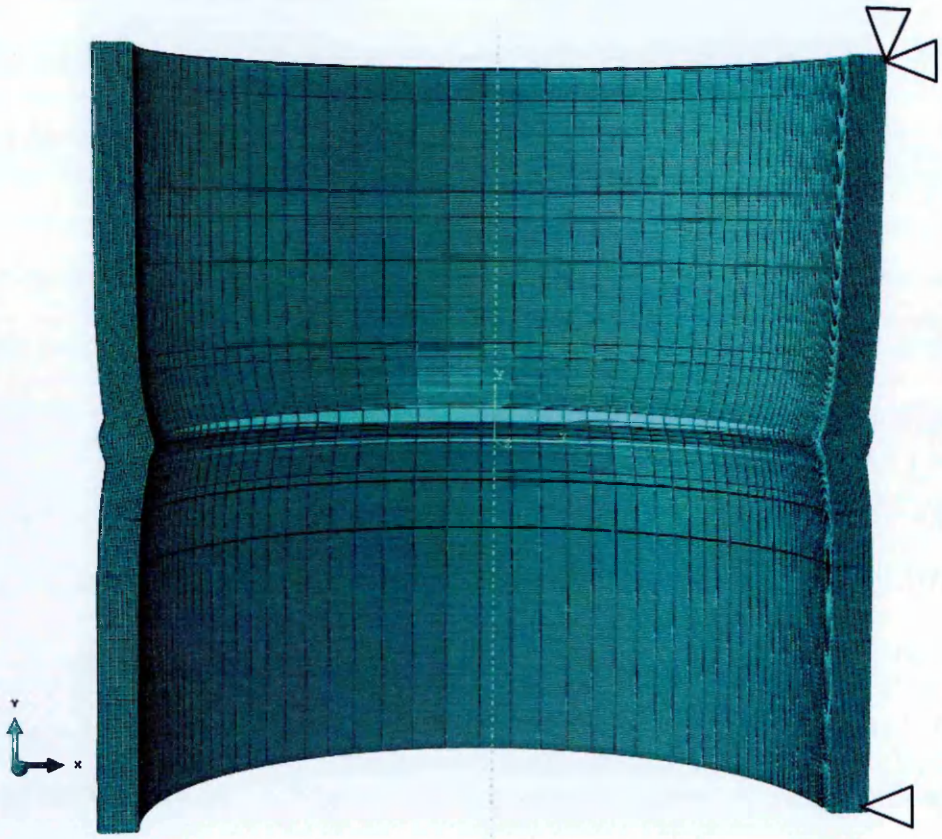

Figure 3.24. 3-D FE model of one half of a cut pipe used for back-calculating released residual stress using the contour method.

Determination of 2D Hoop stress maps using contour method

The 'Low', 'Med' and 'High' half inch pipes were severed using a single diametral-axial wire EDM cut. All of the cuts were of high quality (good surface finish and minimal artefacts). An identical procedure was implemented for undertaking contour method measurements in the STYLE (MU4-1 and MU4-3) and Esshete mock-up (see later).

The hoop stress distributions over the top and bottom surfaces of the half inch pipes are illustrated in Figure 3.25-3.27 with the respective WCL and HAZ locations marked up which were used to obtain through thickness line profiles. The stress distributions on both sides were found to agree with each other in all the three mock-ups. High tensile stresses can be observed near the outer surface whereas stresses are compressive towards the inner surface in the region of the weld. However, the low heat input mock up displayed a wide tensile region at the weld and zones of tensile stress away from the weld are also evident. The stress distributions in top and bottom surface of the medium heat input mock-ups agree with the regions of high tensile and compressive stress gradients clearly seen away from the weld. In the high heat input pipes, peak tensile stresses observed at the WCL of top surface was higher than what was observed in bottom cut surface and is associated with the localised effect of capping passes. In general, the results of the three pipes are very realistic and can be used to identify the effect of varying heat inputs on the residual stress field in thin walled cylinders.

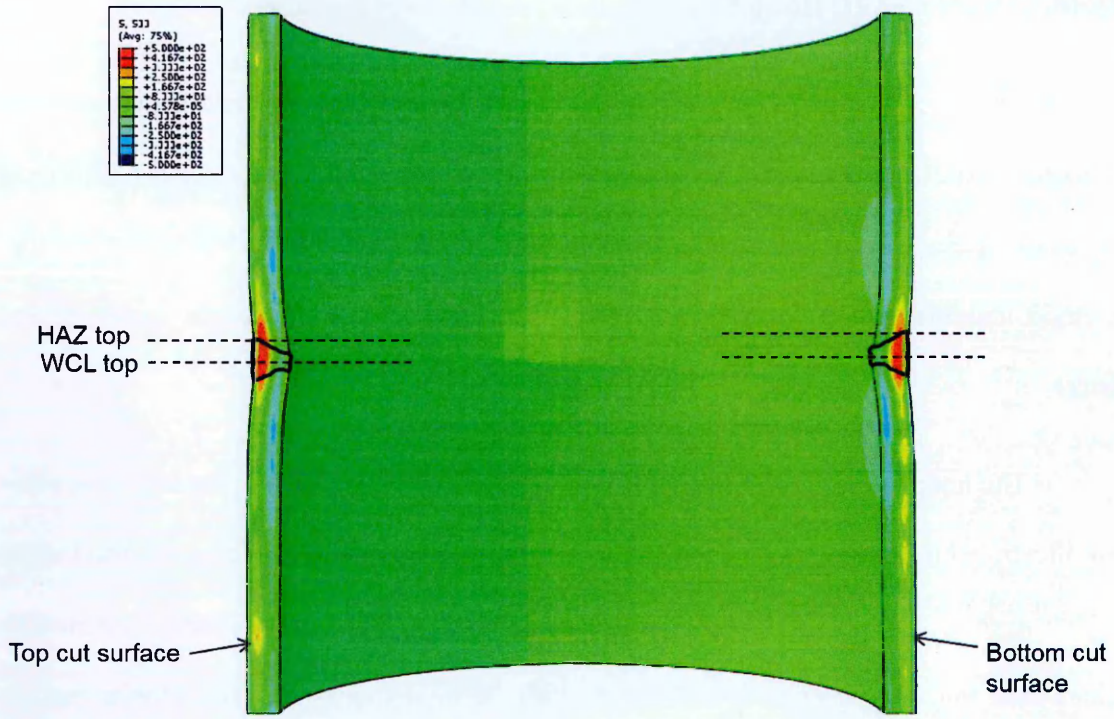

Figure 3.25. Cross-sectional view on a diametral-axial plane of a 3D finite element model of the low heat input pipe girth weld (R/t = 10, t = 12.7 mm, heat input = 0.7 kJ/mm) showing a contour map of inferred hoop residual stresses on the pipe wall cut surfaces that have been relieved during a contour residual stress measurement.

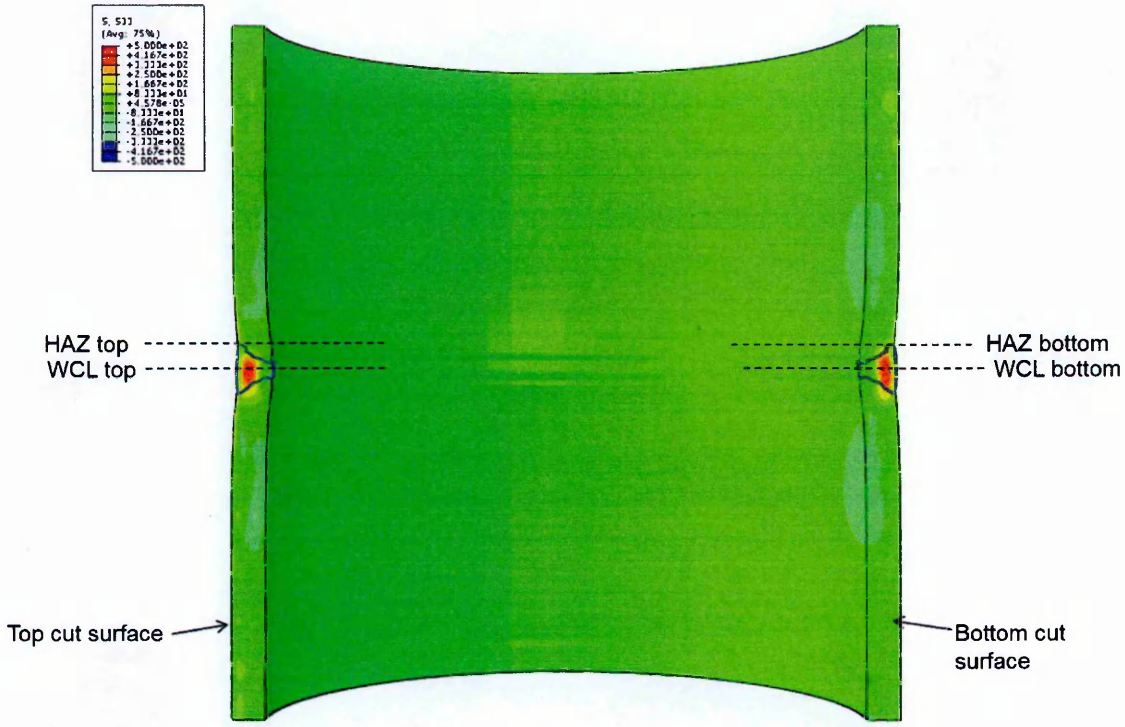

Figure 3.26. Cross-sectional view on a diametral-axial plane of a 3D finite element model of the medium heat input pipe girth weld (R/t = 10, t = 12.7 mm, heat input = 1.0 kJ/mm) showing a contour map of inferred hoop residual stresses on the pipe wall cut surfaces that have been relieved during a contour residual stress measurement.

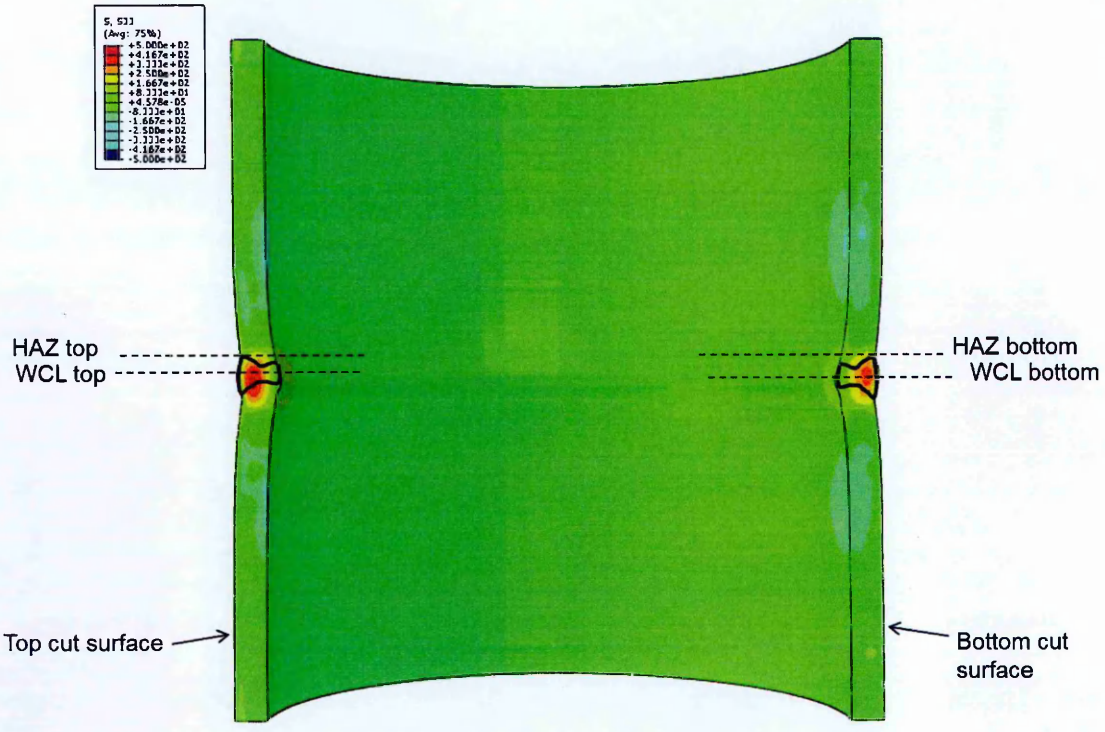

Figure 3.27. Cross-sectional view on a diametral-axial plane of a 3D finite element model of the high heat input pipe girth weld (R/t = 10, t = 12.7 mm, heat input = 1.2 kJ/mm) showing a contour map of inferred hoop residual stresses on the pipe wall cut surfaces that have been relieved during a contour residual stress measurement.

Hoop residual stress line profiles at the WCL and HAZ

The through-thickness hoop residual stress profiles obtained using the contour method at the WCL and HAZ are compared in the low, medium and high heat input mock-ups in Figures 3.28-3.30. The stress profiles measured at the top WCL and bottom WCL are found to be in excellent agreement in the low heat input pipe (see Figure 3.28). A similar pattern is observed in the case of the top and bottom HAZ profiles with nearly the same magnitude as at the WCL. The similar magnitude of stresses found at the WCL and HAZ is associated with the uniformly wide tensile region at the WCL and HAZ locations as shown in the 2D contour method map of hoop stresses (see Figure 3.25). A peak stress close to 400 MPa was found near the through wall position (x/t) = 0.8 in all the stress profiles apart from the HAZ bottom profile having a maximum tensile stress of 300 MPa.

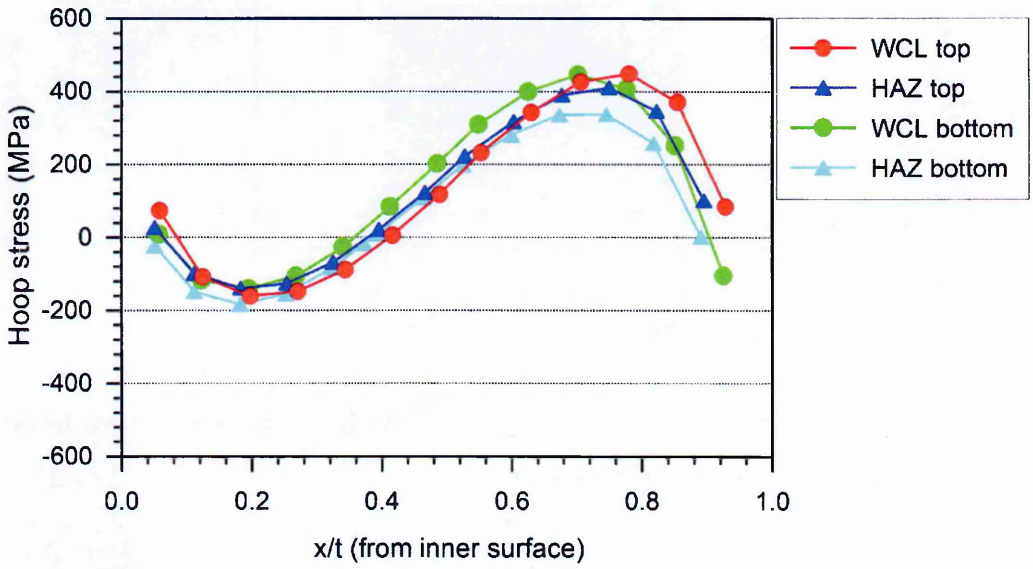

Figure 3.28. Hoop residual stress distributions at the WCL and HAZ measured using the contour method in the Low heat input pipe.

The hoop stress profiles in the medium heat input pipe (see Figure 3.29) resemble the trend observed in the 'Low' heat input pipe. Peak stresses of 400 MPa are observed at the WCL at through thickness position (x/t) = 0.7 and more than 200 MPa at the same position in the HAZ locations. The variation between the WCL and HAZ stress profiles is more evident in the high heat input mock-up (see Figure 3.30) and also there is a difference of 100 MPa in the peak stresses between the top and bottom cut surfaces at the WCL locations. However the HAZ profiles are in good agreement and closely match with each other in most of the through-thickness positions.

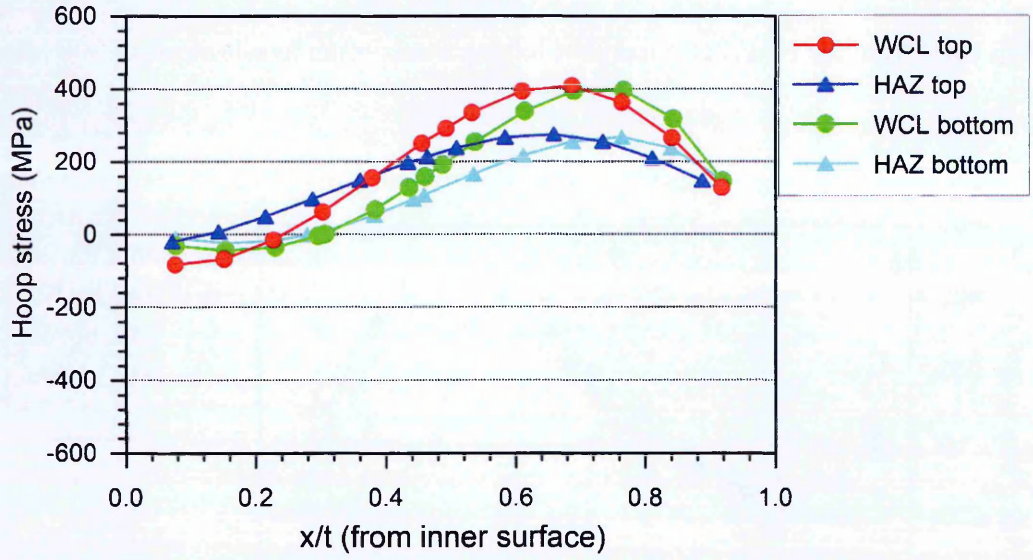

Figure 3.29. Hoop residual stress distributions at the WCL and HAZ measured using the contour method in the Medium heat input pipe.

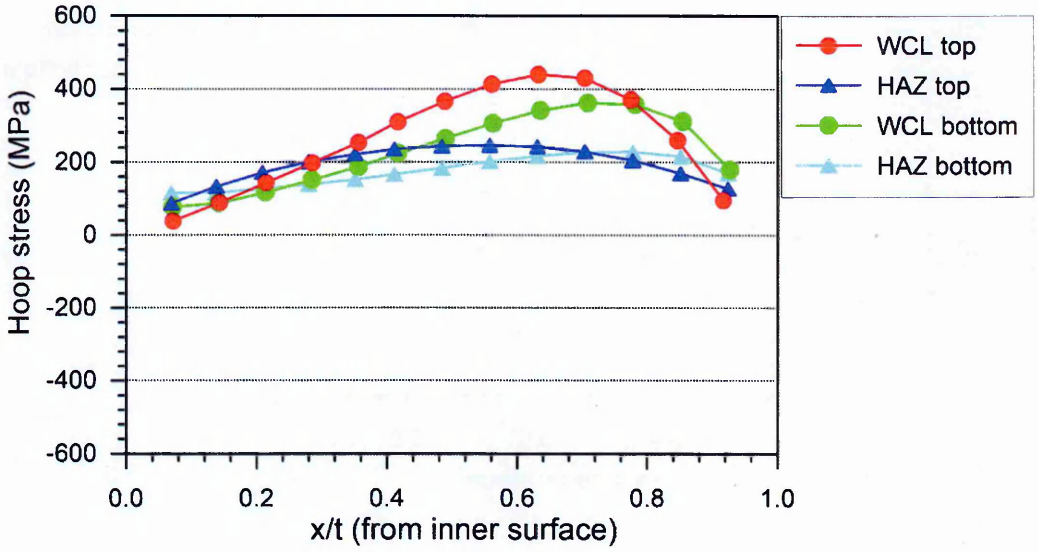

Figure 3.30. Hoop residual stress distributions at the WCL and HAZ measured using the contour method in the High heat input pipe.

Comparison of hoop residual stress profiles measured using different techniques

The hoop residual stress profiles determined using neutron diffraction based on plane stress assumption and the contour method are compared at the WCL and HAZ locations in the three half inch thick mock-ups (illustrated in Figures 3.31-3.33). A difference of up to100 MPa between measurements is not unusual as it is challenging to obtain reliable residual stress measurements in complex welded structures. In the low heat input pipe, the agreement between the measurements is poor at the WCL (see Figure 3.31) and the locations where there is some sort of resemblance is only at the measurement points close to the ID and to the outer surface. However, in the HAZ location (see Figure 3.32), fair agreement is found apart from a mismatch at points near the outside diameter where the neutron measurements suggest the presence of tensile stresses 400 MPa greater than the contour results.

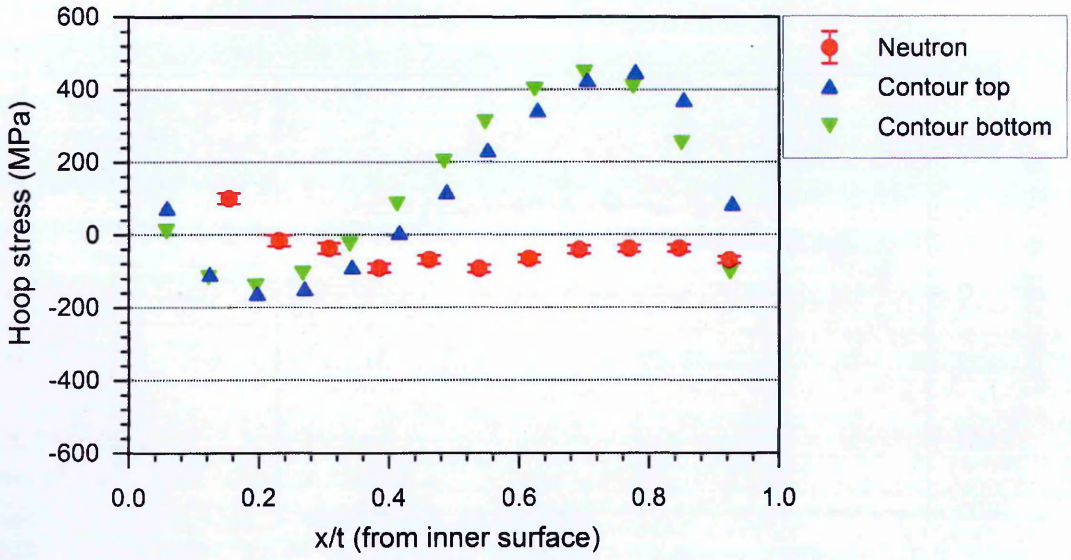

Figure 3.31. Comparison of hoop residual stress distributions at the WCL measured using neutron diffraction and the contour method in the low heat input pipe (Low).

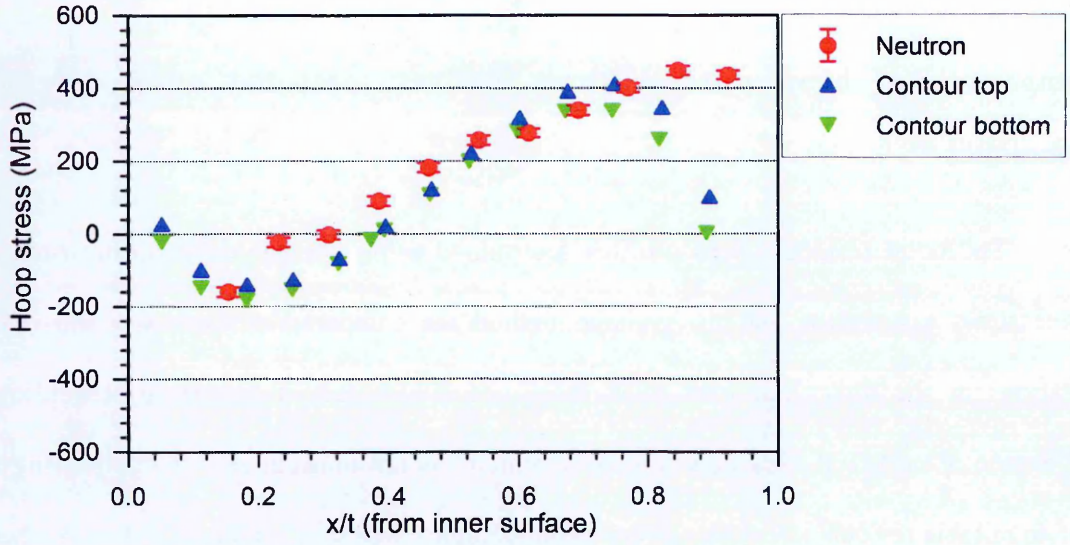

Figure 3.32. Comparison of hoop residual stress distributions at the HAZ measured using neutron diffraction and the contour method in the low heat input pipe (Low).

In the medium heat input pipe, discrepancies between the neutron and contour measurements are again evident at the WCL (see Figure 3.33) where there is a maximum difference of about 600 MPa at through wall position x/t = 0.6. Interestingly in the HAZ (see Figure 3.34), the results are conformable though the contour measurements are giving higher tensile stresses than neutron diffraction in the mid thickness region of the order of 100 MPa. Noticeably, the Medium heat input pipe had lower magnitude stresses present at the HAZ compared to the Low heat input pipe.

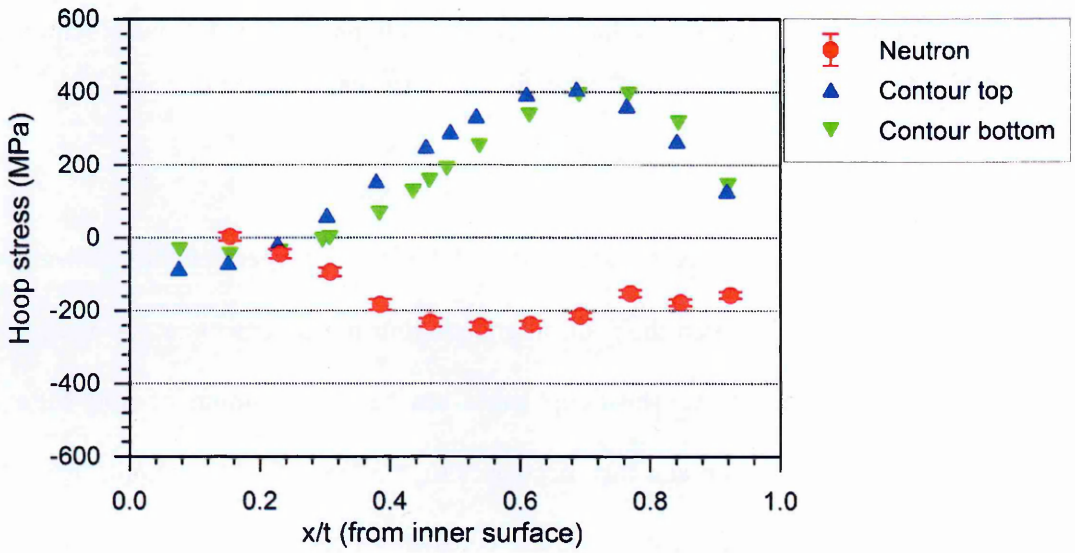

Figure 3.33. Comparison of hoop residual stress distributions at the WCL measured using neutron diffraction and the contour method in the medium heat input pipe (Med).

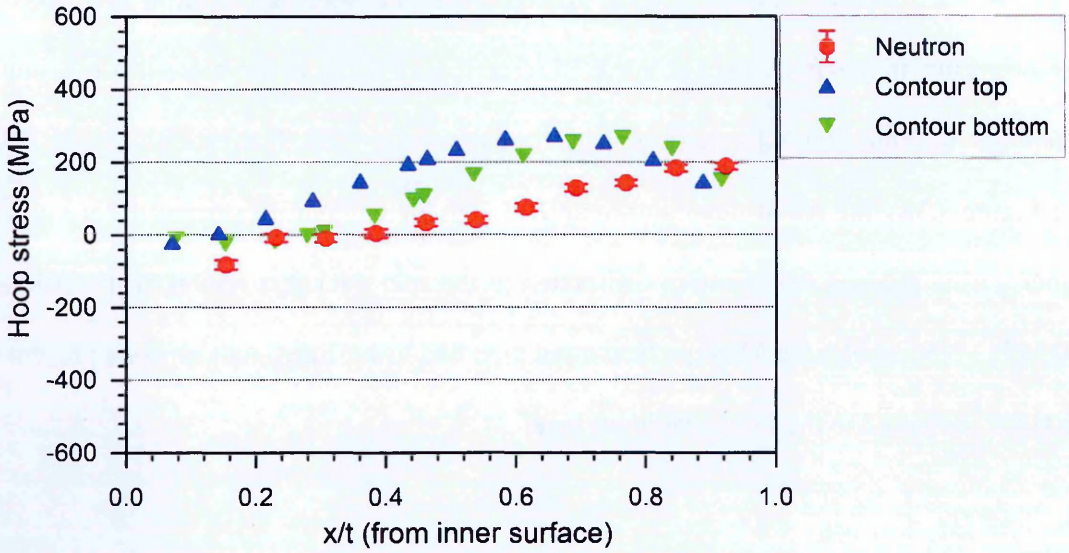

Figure 3.34. Comparison of hoop residual stress distributions at the HAZ measured using neutron diffraction and the contour method in the medium heat input pipe (Med).

In high heat input pipe (see Figures 3.35 and 3.36), a consistent pattern is observed as no agreement is found between the neutron and contour measurements at the WCL and some compatibility at the HAZ. The hoop stress reaches a maximum of 400 MPa at through wall position (x/t) = 0.6 and then decreases to less than 100 MPa approaching the outer surface. Neutron measurement values are constantly near the zero mark throughout the entire wall thickness at the WCL. This suggests that the neutron diffraction measurements at the WCL are not reliable because this pattern has never been observed in any previously published data [18].

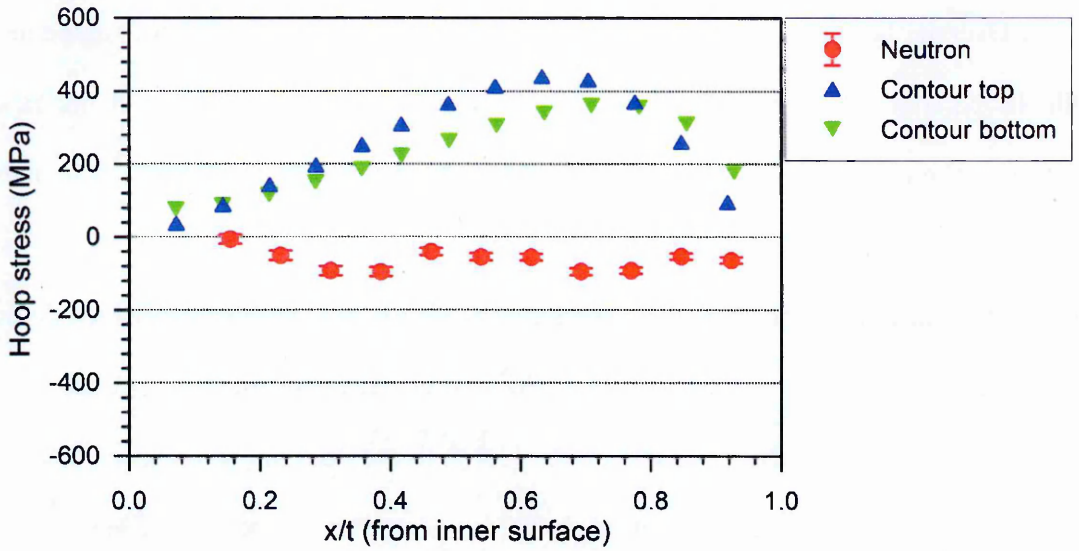

Figure 3.35. Comparison of hoop residual stress distributions at the WCL measured using neutron diffraction and the contour method in the high heat input pipe (High).

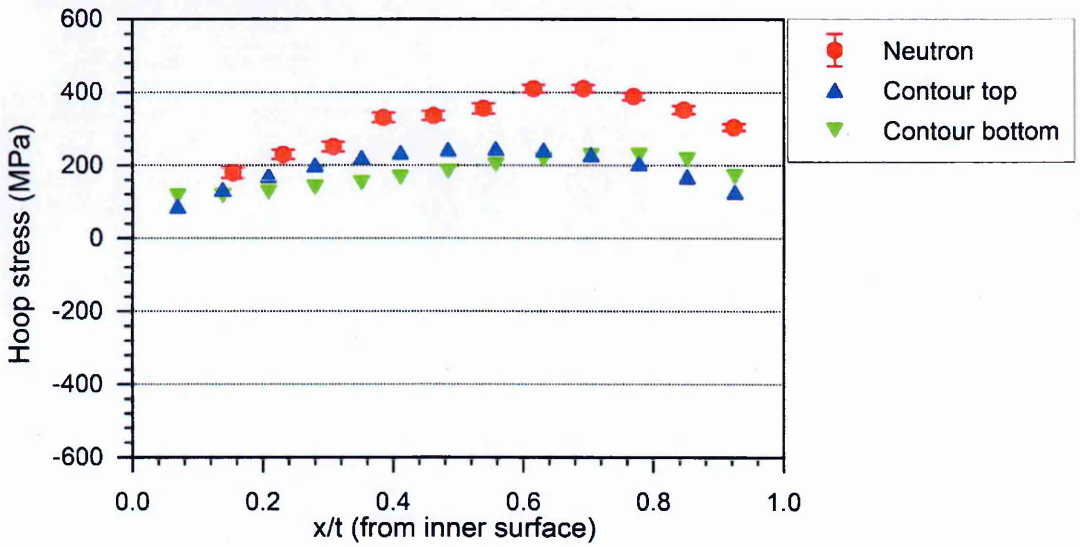

Figure 3.36. Comparison of hoop residual stress distributions at the HAZ measured using neutron diffraction and the contour method in the high heat input pipe (High).

Overall, the neutron diffraction residual stress measurements are in poor agreement with the contour measurements at the WCL and in reasonable agreement at the HAZ locations. There is more than one reason to believe that the neutron results might be incorrect at the WCL. First, the neutron measurements do not satisfy equilibrium conditions with significant radial stresses seen in all the three mock-ups and which do not tend to zero at the surfaces. Secondly, the HAZ residual stress profiles determined using neutron diffraction are consistently in agreement with the contour method measurements at both the top and bottom cut surfaces of the pipes. Moreover the pattern of WCL stress profiles found using neutron diffraction is very different from the historical measurements of austenitic stainless steel pipes reported [18]. Last but not the least, neutron measurements are highly susceptible to errors associated with stress free reference measurements in austenitic steel welds due to large grain size, plasticity, texture and the presence of inter-granular stresses [12, 73, 137].

3.3 Style welded pipe components MU4-1 and MU4-3

3.3.1 Manufacturing history and characterisation studies

STYLE (Structural integrity for lifetime management of non-RPV components) was a EURATOM Framework 7 funded project [132] which aimed to improve and optimise methods of structural integrity assessment in the ageing and lifetime management of reactor coolant pressure boundary components. Two girth welded austenitic stainless steel pipe components MU4-1 and MU4-3 were made in the STYLE project by the Institut de Soudure. The pipes were heat treated at 1040 °C followed by rapid cooling prior to welding. Two butt-welded pipe specimens with dimensions (320 mm long, 250 mm OD and 25 mm thick) were fabricated from AISI Type 316L austenitic stainless steel under carefully controlled conditions. The welds had a V-type bevel side-wall preparation an unusual wide groove (see Figure 3.37) and were made with a backing plate (removed after welding) using an automated GTAW process. The pipes were made using electrical heat inputs of 1.0 kJ/mm (108 passes) and 2.5 kJ/mm (58 passes) with an inter-pass temperature of 150° C. The weld pass sequence in the mock-ups is schematically illustrated in Figure 3.38. The chemical composition of the weld filler metal is given in Table 3.2.

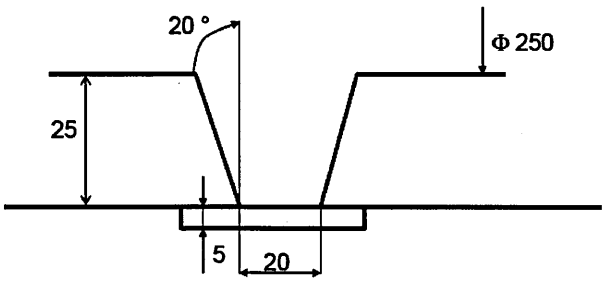

Figure 3.37. Weld groove preparation of STYLE pipes MU4-1 and MU4-3.

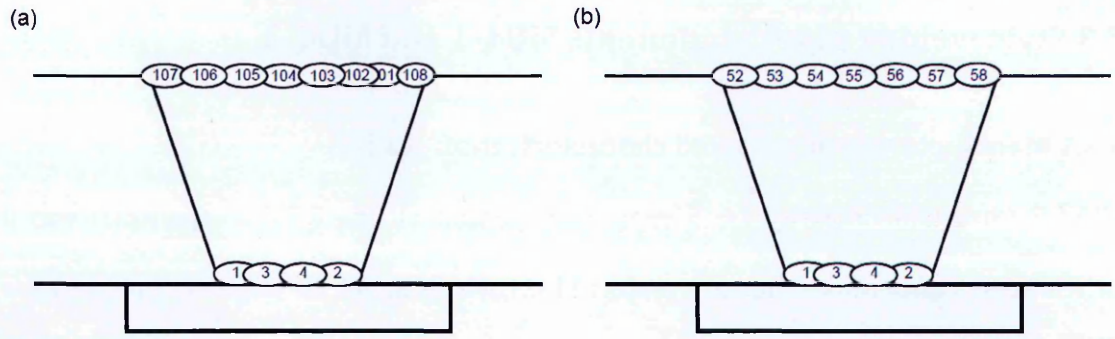

Figure 3.38.Weld pass sequence of STYLE pipe components (a) MU4-1 and (b) MU4-3.

The average parent metal yield strength (1% proof stress) was 290 MPa and weld filler wire made of type 316L having yield strength of about 450 MPa giving overmatched yield properties. The general layout and photographs of MU4-1 during welding is shown in Figure 3.39.

Table 3.2. Chemical composition of the filler metal used for GTAW process.

Composition %	C	Si	Mn	P	S	Cr	Ni	Mo	Cu
	0.01	0.86	1.6	0.02	0.00	18.2	11.1	2.6	0.1

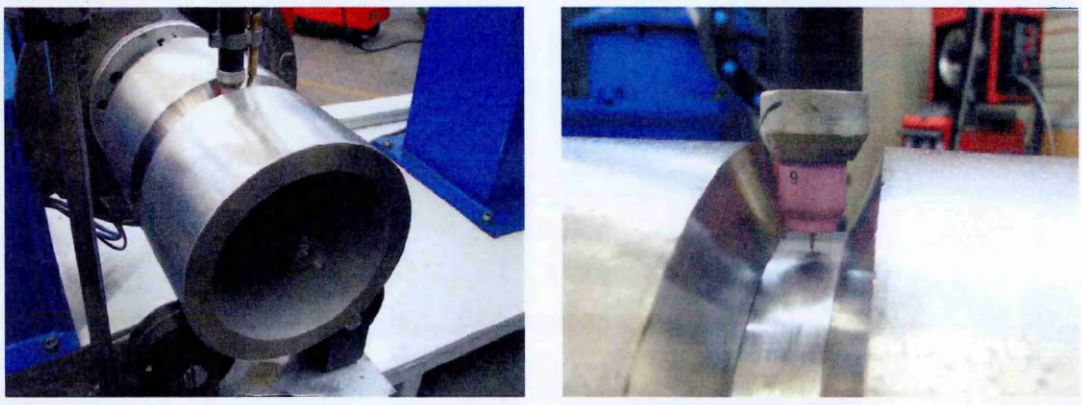

Figure 3.39. General layout and photographs of STYLE pipe MU4-1 during welding.

Macrographs and hardness maps of welded pipes MU4-1, and MU4-3 are illustrated in Figures 3.40 and 3.41. In MU4-1, a decrease in hardness values was observed moving from the weld centre line to the heat affected zone. The macros show the width of the fusion zone became smaller (~12 mm) than the initial gap of 20 mm which is considered to be very wide. The weld hardness increases at the root and this hardened zone extends into the parent material. The hot spots in the hardness maps are associated with each individual weld bead and the last capping pass is evident in both welds as it is comparatively softer and similar to the parent material. There is a notable decrease in hardness towards the parent metal, with typical values being ~220 HV5 in the HAZ, and ~160 HV5 in the parent metal. The magnitude of hardness values of the weld metal in MU4-3 was substantially lower than MU4-1. This could result from fewer weld passes deposited in MU4-3 resulting in less cyclic strain hardening. The microstructure is consistently observed as dendritic in the weld metal, see Figure 3.42.

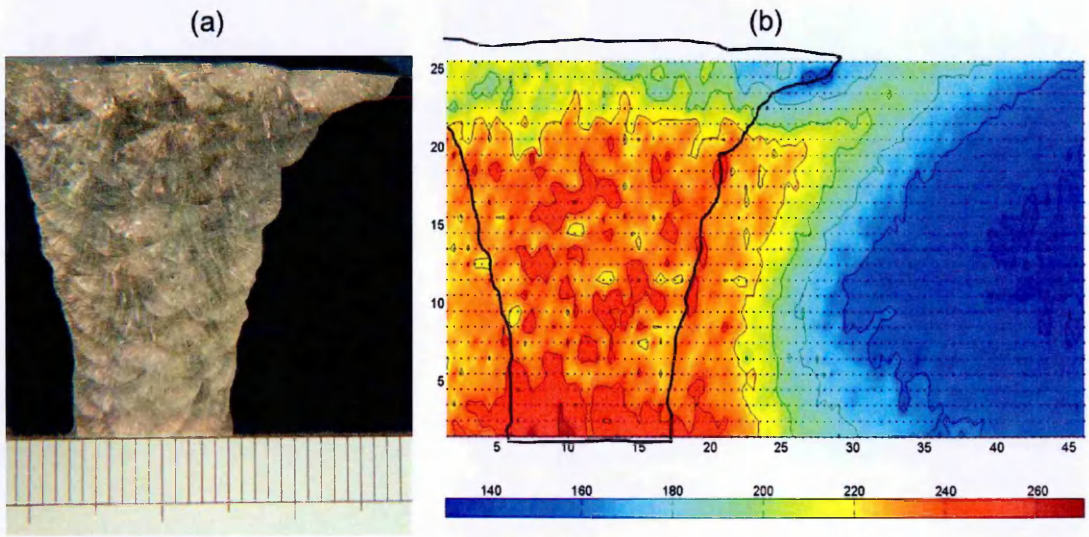

Figure 3.40. (a) Weld macrograph and (b) hardness map of MU4-1 mock up.

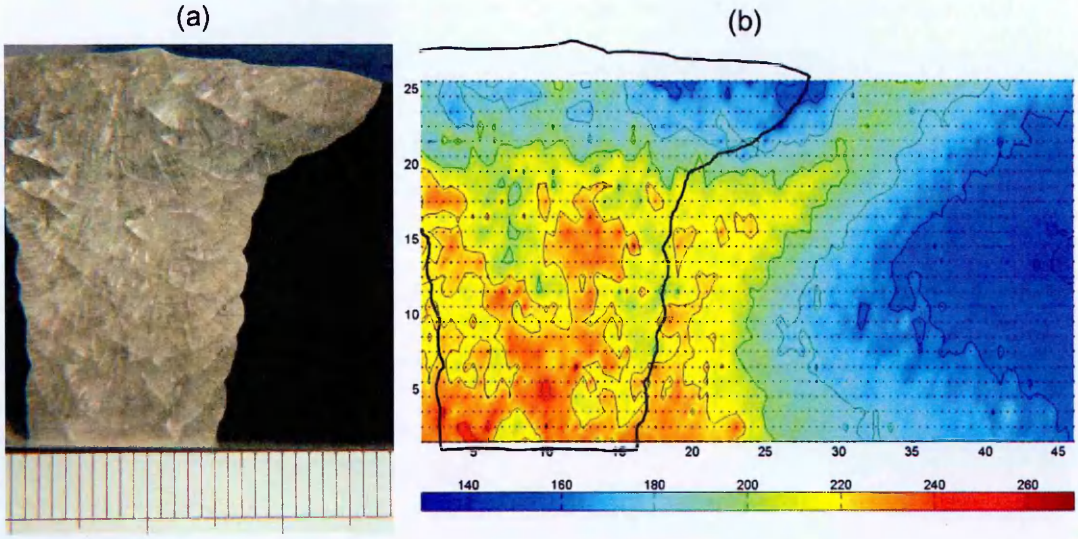

Figure 3.41. (a) Weld macrograph and (b) Hardness map of MU4-3 mock pipes.

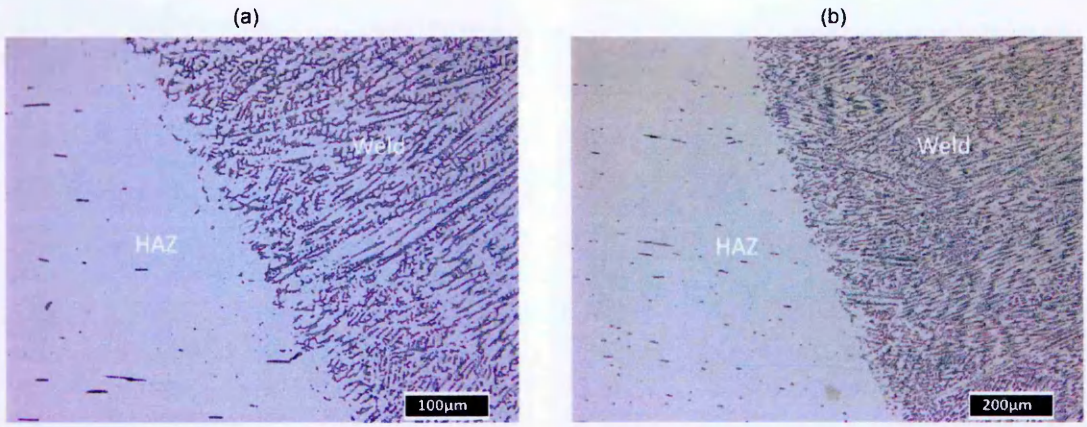

Figure 3.42. Microstructural analysis at the fusion boundary of (a) low heat input MU4-1 b) high heat input MU4-3 pipe components.

3.3.2 Neutron diffraction residual stress measurements in the STYLE welded pipes MU4-1 and MU4-3

An equivalent experimental procedure to that decribed in section 3.2.2 was followed for the neutron diffraction stress measurements in the STYLE pipes MU4-1 and MU4-3. An access window of dimensions 35 mm x 50 mm was machined in each pipe using a wire EDM process in preparation for neutron diffraction residual stress measurements. The circumferential position of the access slot (window) was determined away from deep hole drilling residual stress (DH) measurement locations and the weld start stop position (SS) as shown in Figure 3.43.

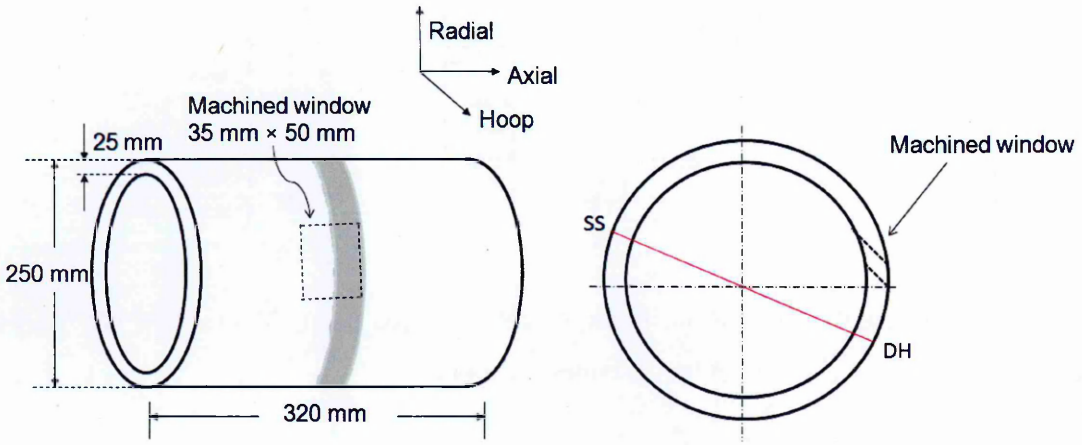

Figure 3.43. Schematic illustration of the location of the machined window in the pipe MU4-1.

Small cubes of HAZ and weld metal (four of each) with dimensions 5 mm x 5 mm x 5 mm were extracted from the removed window of material to measure the reference stress-free lattice parameter (d_0). A schematic diagram of the measurement array of 22 points in each pipe weldment and the location of the stress-free reference cubes at the WCL and HAZ are shown in Figure 3.44.

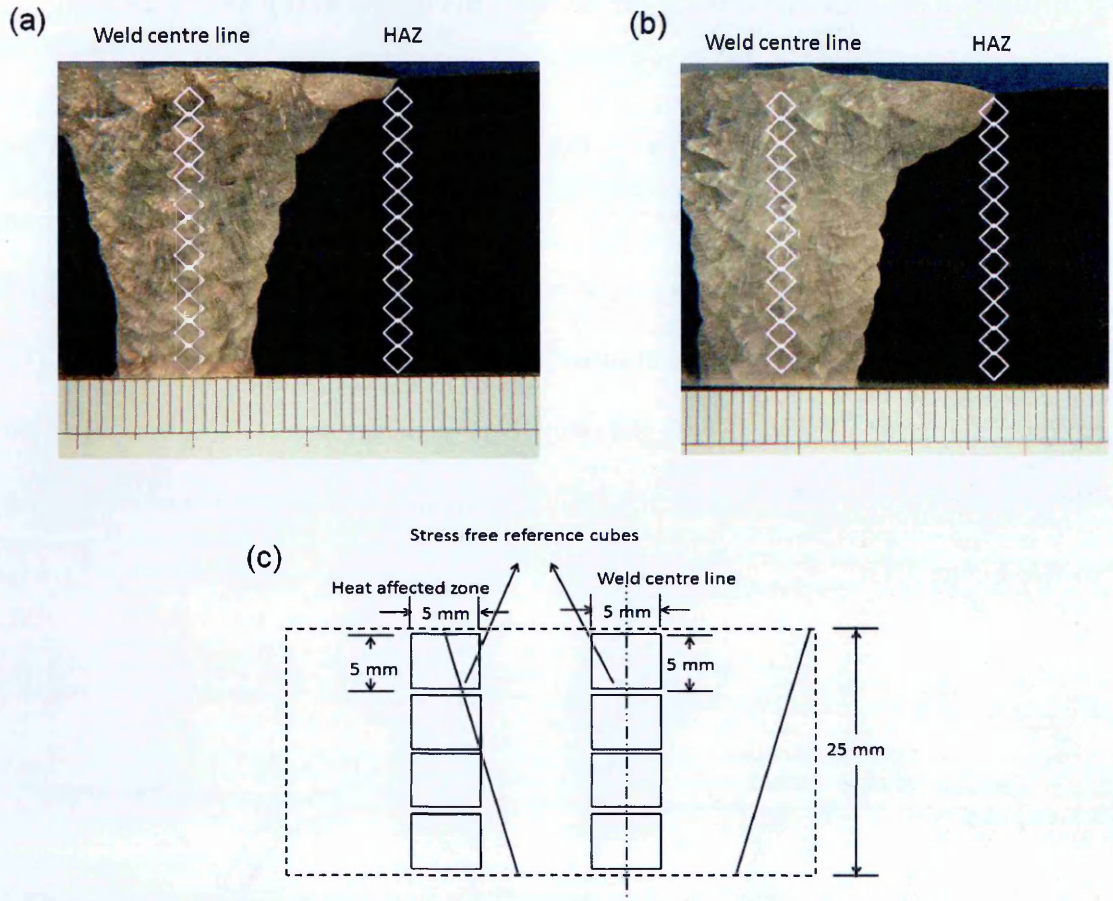

Figure 3.44. Schematic of neutron measurement positions in (a) MU4-1 and (b) MU4-3 girth weld, and (c) stress free reference cubes locations.

Owing to long neutron path lengths the diffraction measurements in the first few millimeters near the inner and outer diameter of the mock-ups MU4-1 and MU4-3, the quality of the diffraction peaks observed were relatively poor. Figure 3.45 shows an example of a poor quality diffraction peak measured along the axial direction.

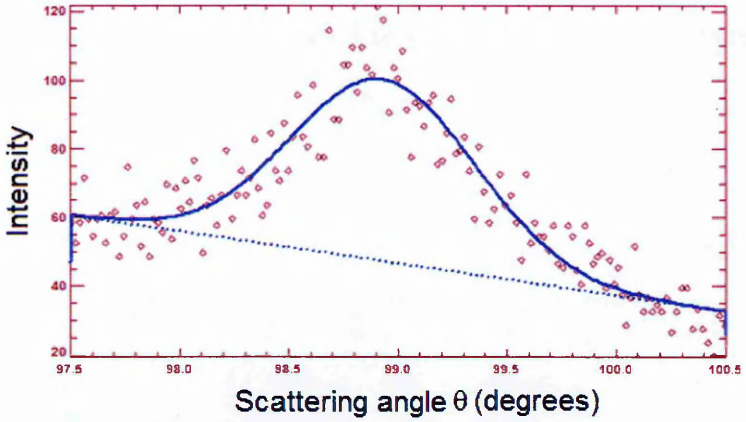

Figure 3.45. Diffraction peak near the inside diameter of MU4-1 along axial direction.

The through-wall stress profiles in the axial direction at the WCL and HAZ in MU4-1 (low heat input girth weld) and MU4-3 (high heat input girth weld) are illustrated in Figures 3.46-3.48. In MU4-1, the stress profiles at the WCL exhibit more scatter compared to the HAZ. The axial stress distributions in MU4-3 (high heat input girth weld) at the WCL and HAZ follow similar patterns with the exception that the profile at the WCL falls into compression adjacent to the outer surface. The stress profiles of the two pipes are compared, whilst some scatter is observed in the axial stress profiles for both pipes at the WCL location, the stress profiles have a similar shape. At the HAZ location, the axial profiles show the same trend but the high heat input weld has a higher tensile magnitude, inferring the presence of a membrane stress.

A similar pattern is observed in the hoop stress profiles in Figure 3.47. The maximum stresses are located at through wall position x/t = 0.8, from the inner surface, in both axial and hoop stress profiles. High magnitude compressive stresses are observed approaching the inner surface at WCL in the hoop direction of MU4-3 whereas the stresses in the HAZ remain tensile. The hoop stress profiles at the WCL have a similar shape with the high heat input distribution being slightly more tensile. Whereas at the HAZ location the high heat input profile is about 200 MPa more tensile. The radial stress profiles follow a different pattern with higher tensile stresses at the inner diameter in both WCL and HAZ

locations. A divergent pattern in the WCL and HAZ stress patterns is also observed in the radial direction towards the outer surface.

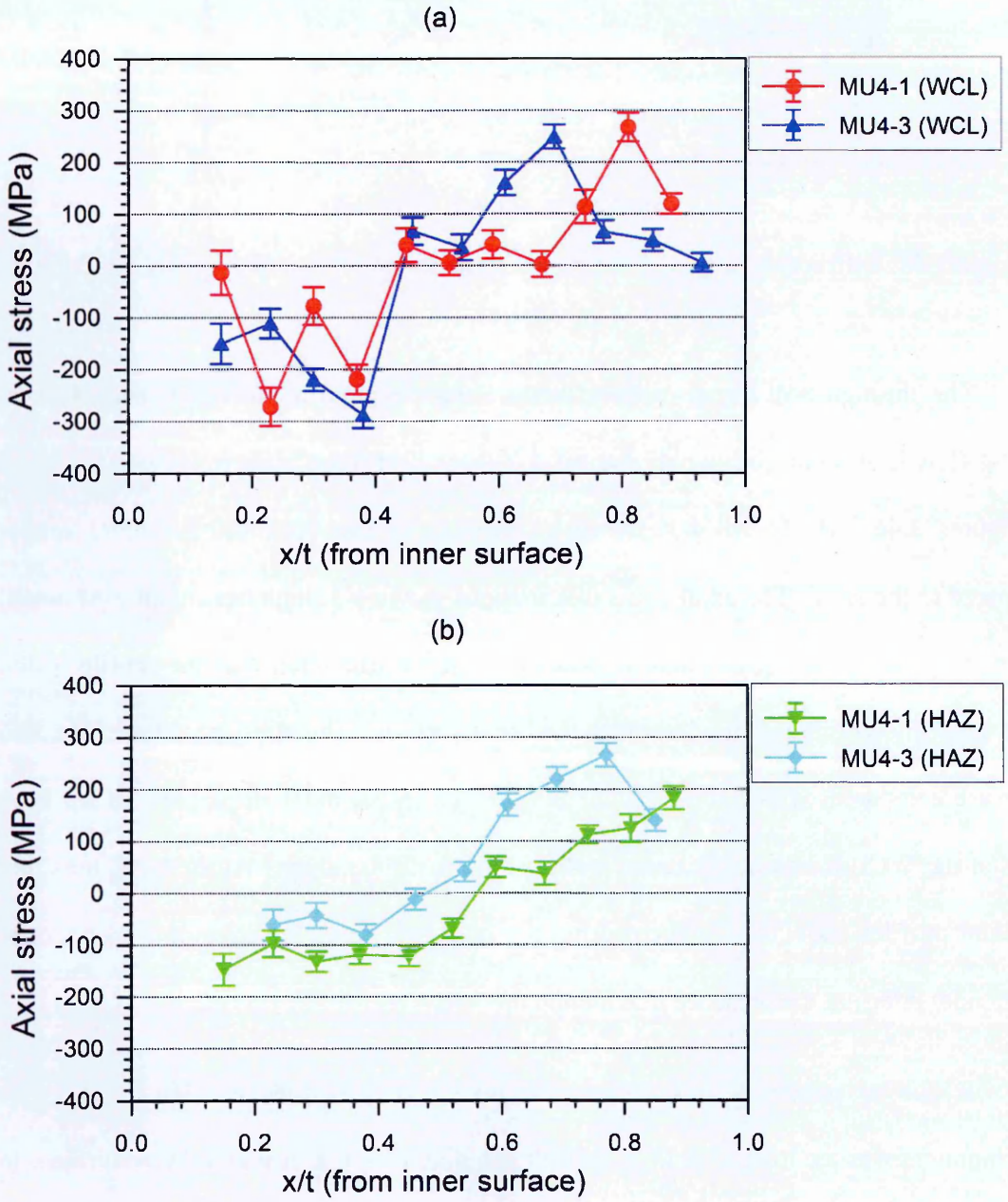

Figure 3.46. Axial stress distributions in the low heat input (MU4-1) and high heat input (MU4-3) pipes measured at the (a) the WCL and (b) the HAZ.

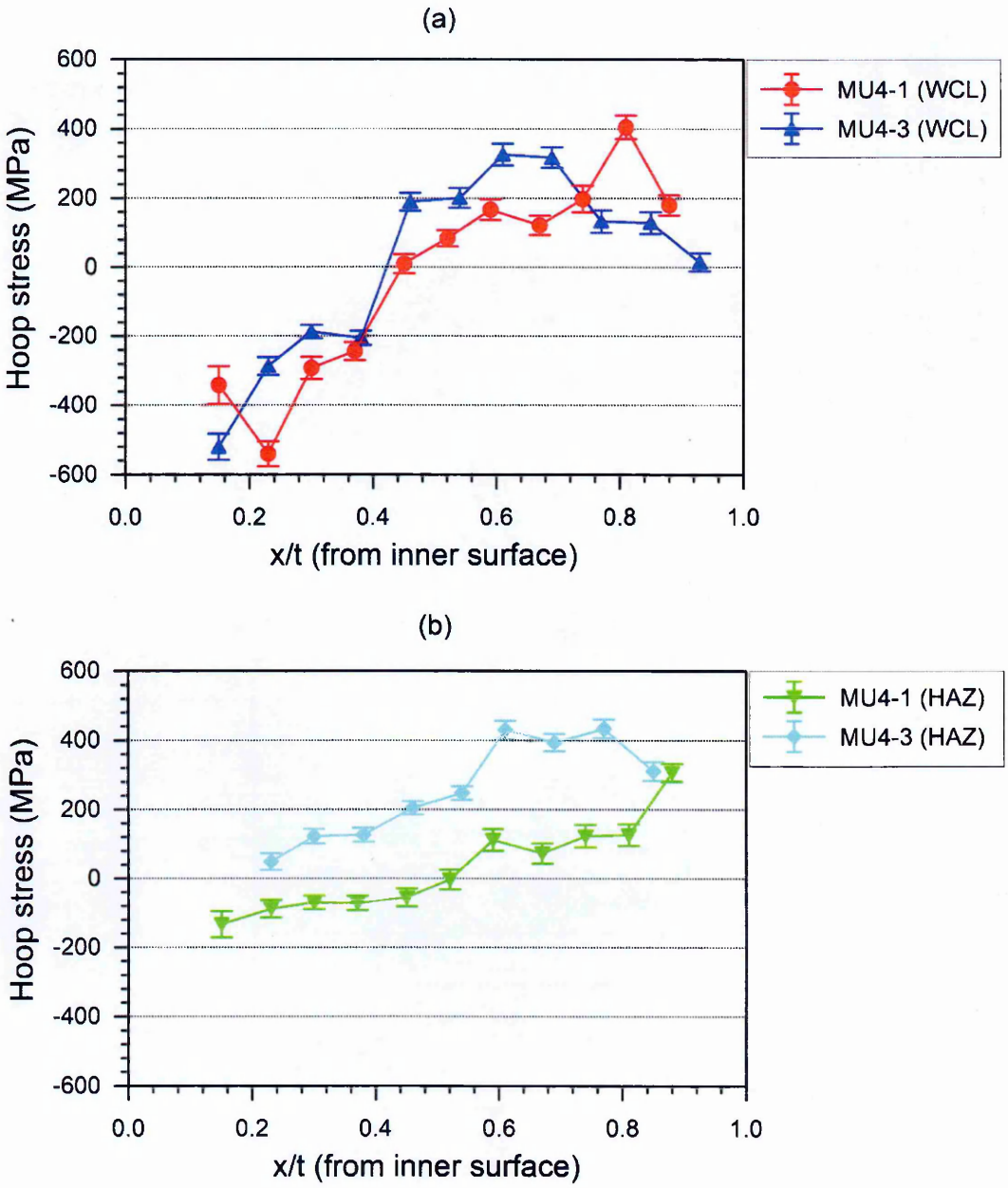

Figure 3.47. Hoop stress distributions in the low heat input (MU4-1) and high heat input (MU4-3) pipes measured at the (a) the WCL and (b) the HAZ.

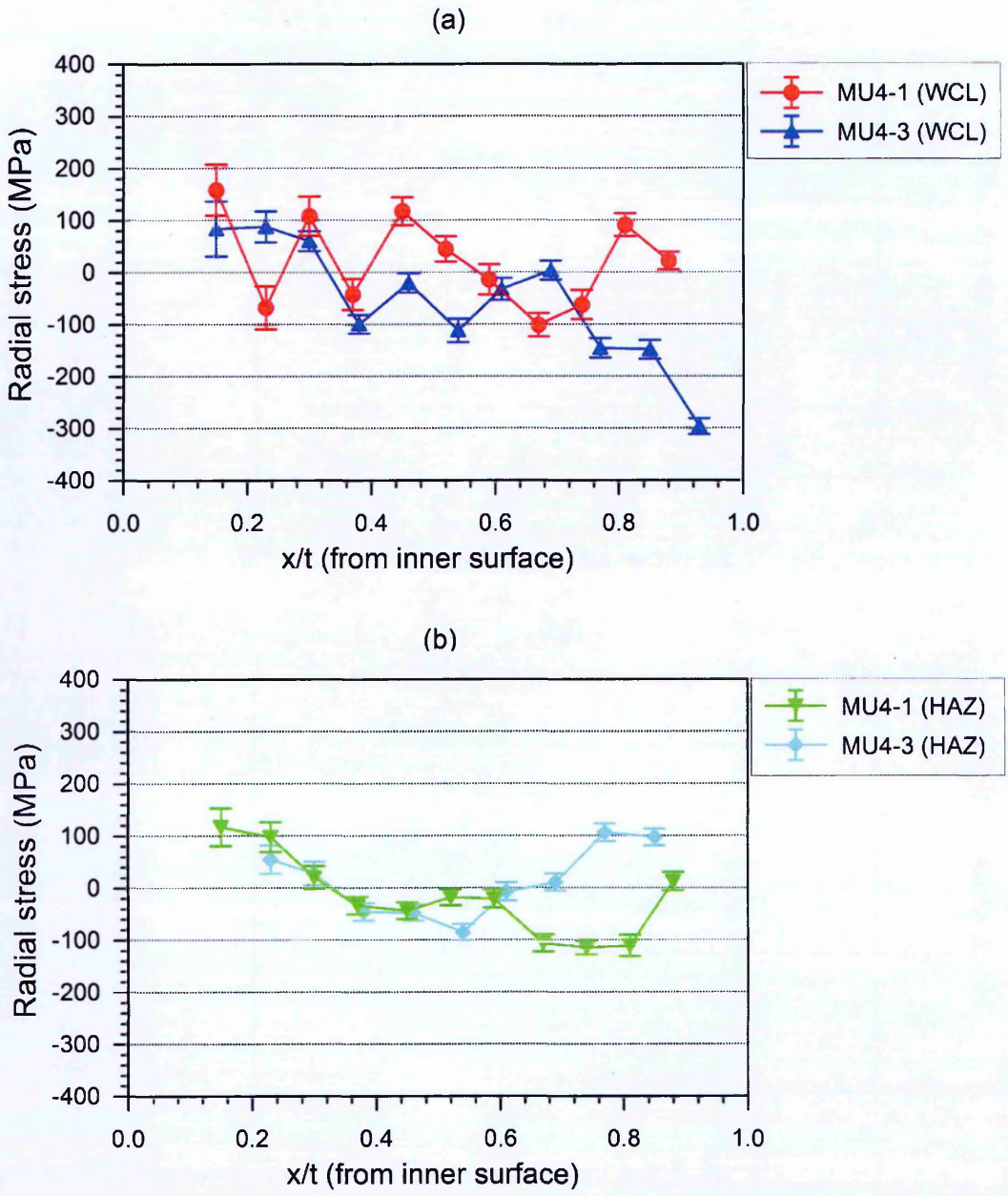

Figure 3.48. Radial stress distributions in the low heat input (MU4-1) and high heat input (MU4-3) pipes measured at the (a) the WCL and (b) the HAZ.

3.3.3 Contour method residual stress measurements of STYLE pipe weldments MU4-1 and MU4-3

The experimental procedure described in section 3.2.3 was used to undertake contour measurements in weldments MU4-1 and MU4-3. The results including 2D stress maps in the hoop direction and line profiles at the WCL and HAZ are discussed in the following sections.

Determination of 2D hoop residual stress maps using the contour method

Maps of measured residual hoop stress in pipes MU4-1 and MU4-3 are presented in Figures 3.49 and 3.50. The distributions of measured stress on the top and bottom cut faces were in excellent agreement with each other exhibiting a wide region of tensile stress prevailing at the outside surface and compressive stress near the inside surface. This could be linked with the wide weld preparation employed in the STYLE weldments. However, the wide region of tensile and compressive stresses in the weld is not evident in the MU4-3 which was made using a higher heat input and less number of passes. Zones of high stress gradients were observed away from the weld and could be associated with the wire EDM cutting issues.

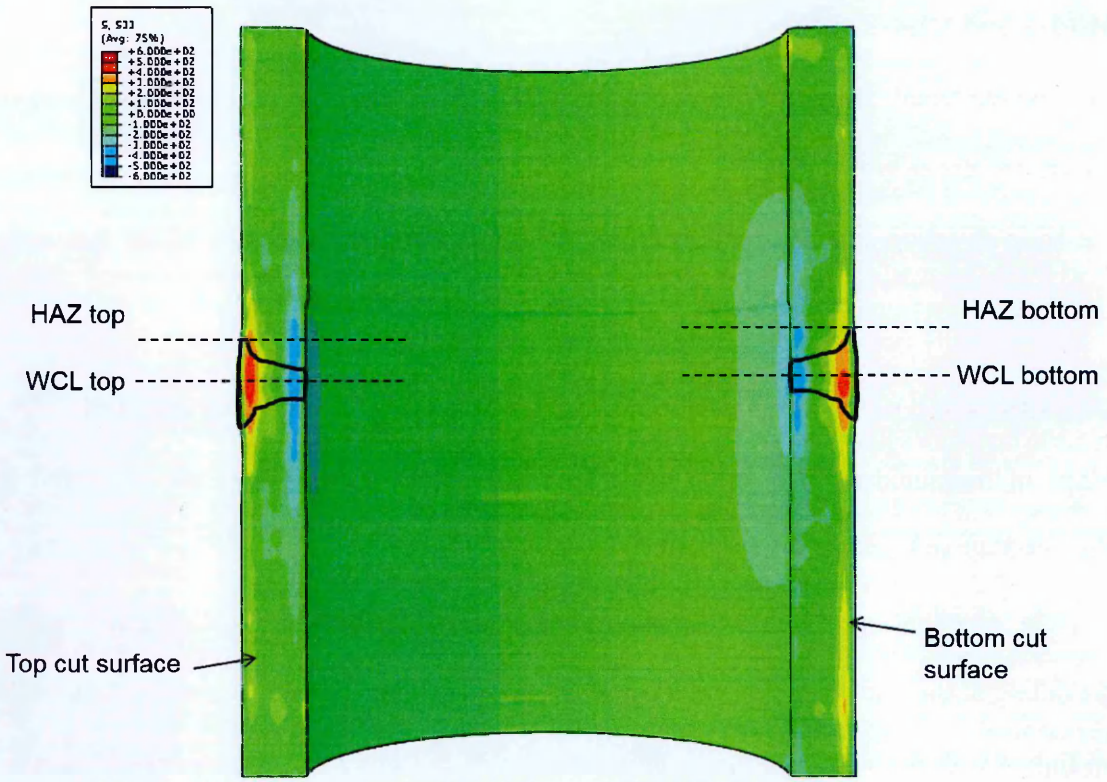

Figure 3.49. Cross-sectional view on a diametral-axial plane of a 3D finite element model of the MU4-1 pipe girth weld (R/t = 4.5, t = 25 mm, heat input = 1.0 kJ/mm) showing a contour map of inferred hoop residual stresses on the pipe wall cut surfaces that have been relieved during a contour residual stress measurement.

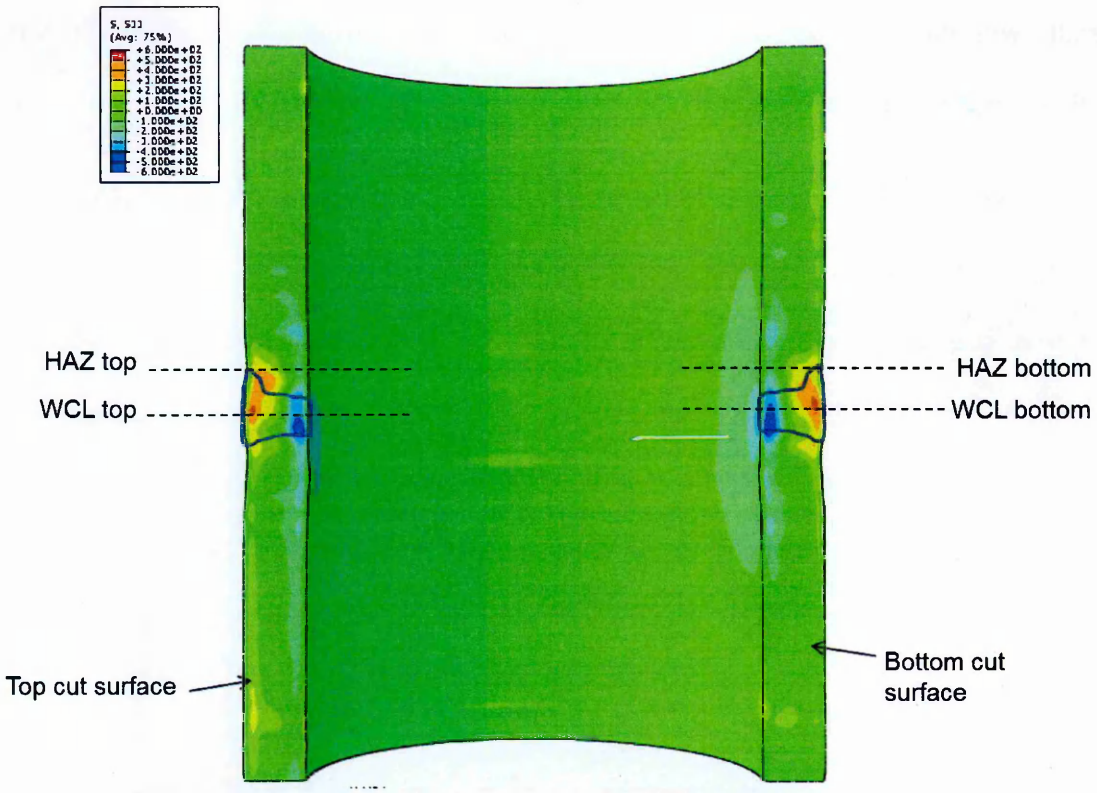

Figure 3.50. Cross-sectional view on a diametral-axial plane of a 3D finite element model of the MU4-3 pipe girth weld (R = 4.5, t = 25 mm, heat input = 2.5 kJ/mm) showing a contour map of inferred hoop residual stresses on the pipe wall cut surfaces that have been relieved during a contour residual stress measurement.

Hoop residual stress line profiles at WCL and HAZ

The residual through-wall line profiles of hoop stresses measured using the contour method in pipes MU4-1 and MU4-3 are given in Figures 3.51 and 3.52. Very good agreement is found between the top and bottom hoop stress profiles determined both at the WCL and HAZ in mock-up MU4-1 (see Figure 3.51). The peak stresses observed at the inside and outside surface are significantly higher at the WCL compared to the HAZ indicating the presence of high bending stresses along the WCL. Compressive stresses of over 500 MPa were found at through wall position (x/t) = 0.2 at the WCL and stresses were found to increase steadily moving towards the outer surface. The pattern found at the HAZ was

similar with the magnitude of peak stresses being lower in magnitude by about 200 MPa both in tension and compression.

Excellent agreement was found between the top and bottom WCL and HAZ hoop stress profiles in the high heat input mock-up MU4-3 (see Figure 3.52). In this mock-up, the peak stresses in compression were of substantially lower magnitude than found in MU4-1 both at the WCL and HAZ suggesting the presence of low bending stresses. The peak stresses for both pipe welds were found to exist at the outer surface having magnitude of about 400 MPa and 200 MPa at the WCL and HAZ respectively. Overall, the results look very convincing and are next compared with the neutron diffraction measurements performed on both pipes.

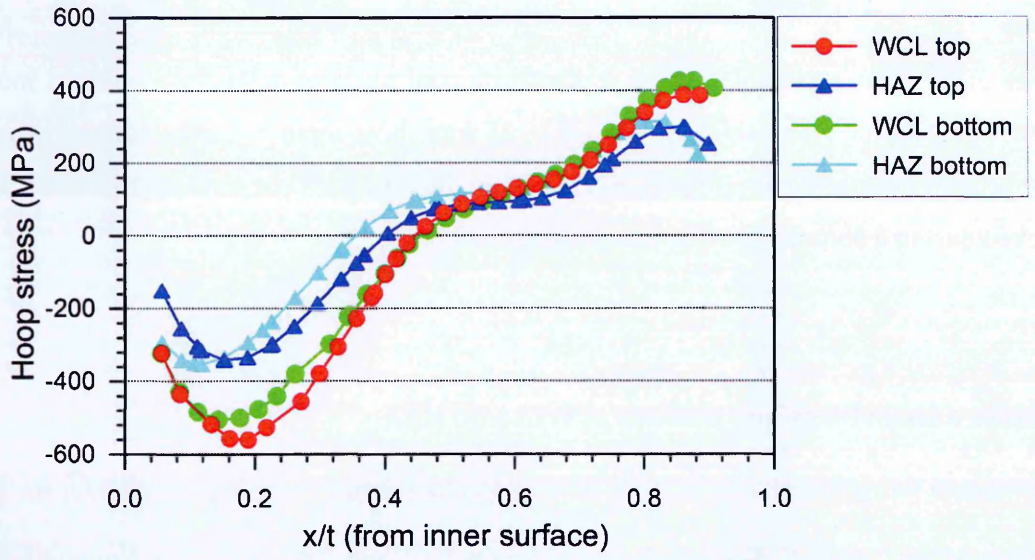

Figure 3.51. Hoop residual stress distributions at the WCL and HAZ measured using the contour method in the low heat input pipe (MU4-1).

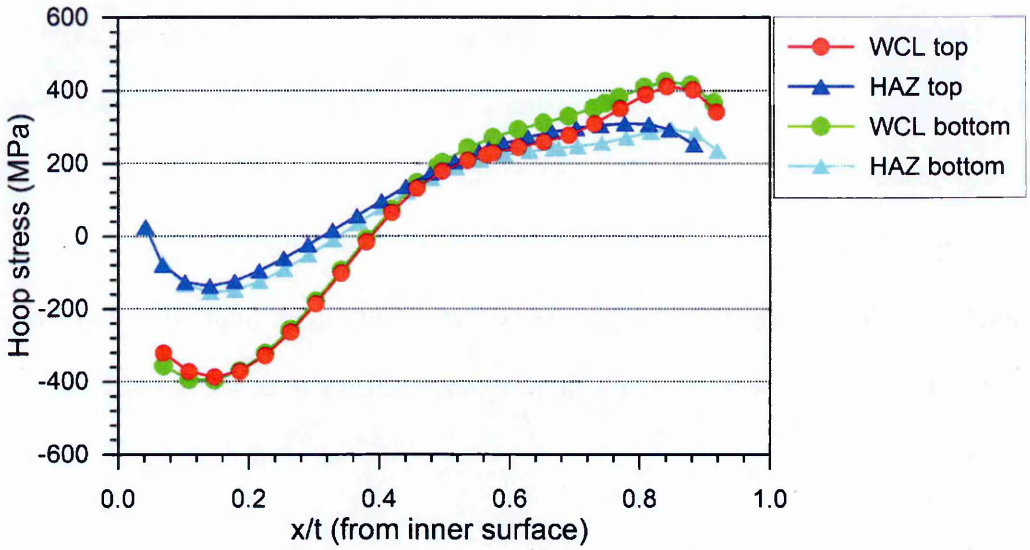

Figure 3.52. Hoop stress distributions at the WCL and HAZ measured contour method in the high heat input pipe (MU4-3).

Comparison of residual stress profiles measured using different techniques

Comparisons of measured through-wall line profiles of residual stress acting in the hoop direction measured using neutron diffraction and the contour method at the WCL and HAZ locations in mock-up MU4-1 are illustrated in Figures 3.53 and 3.54. Excellent agreement is found between the neutron and contour method results for the top and bottom cut surfaces at the WCL (see Figure 3.53). Interestingly, compressive hoop stresses of the level measured in MU4-1 are not evident in published data. The presence of these high compressive stresses near the inside surface is judged likely to be the result of the specific weld procedure employed for both MU4-1 and MU4-3; that is an unusually wide weld preparation was used with a backing plate removed by grinding after the fabrication process.

The agreement between the measurements from through wall position (x/t) = 0.2 to 0.8, is very good considering the innate scatter associated with welding residual stresses in rather complicated structures such as girth welded pipes. The difference at the inside surface may be due to the result of insufficient neutron flux required to penetrate the 25 mm thick mock-up where the diffraction peaks was found to be poor. However, most of the points are in good agreement and with each other indicate peak stresses both in tension and compression.

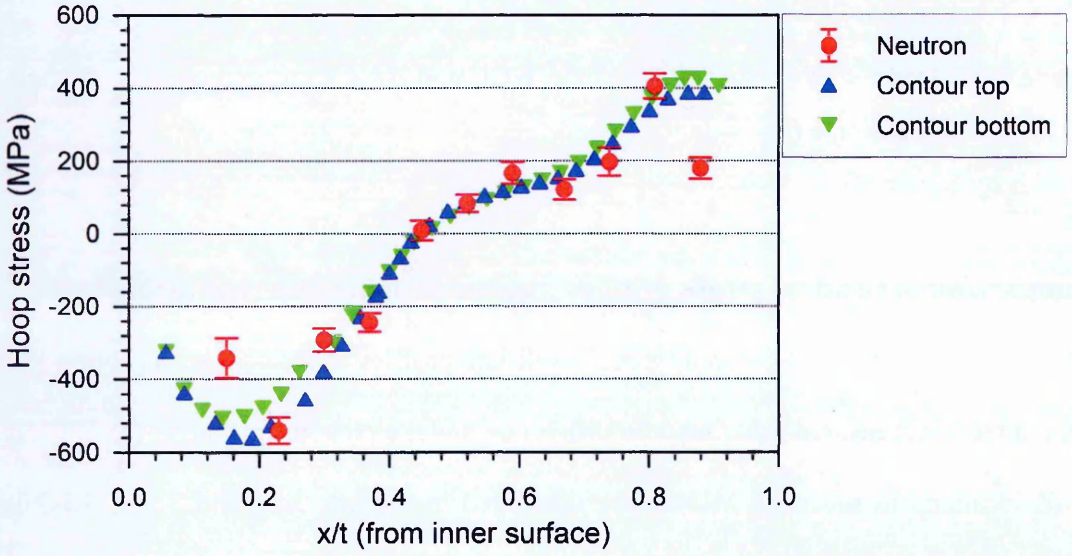

Figure 3.53. Comparison of hoop residual stress distributions at the WCL measured using neutron diffraction and the contour method in the low heat input pipe (MU4-1).

Figure 3.54 shows the comparison of hoop residual stress profiles using different techniques at the HAZ location for MU4-1. The agreement is excellent except for the mismatch approaching the inside surface at (x/t) = 0.2, where the neutron measurements are inferring more tensile stresses of the order of 100 MPa. However, the measurement points are in good agreement from through-wall position x/t = 0.3 to the outer surface. Overall, the nature of the though-thickness stress profile measured using the two techniques is similar and the agreement can be deemed as 'good'.

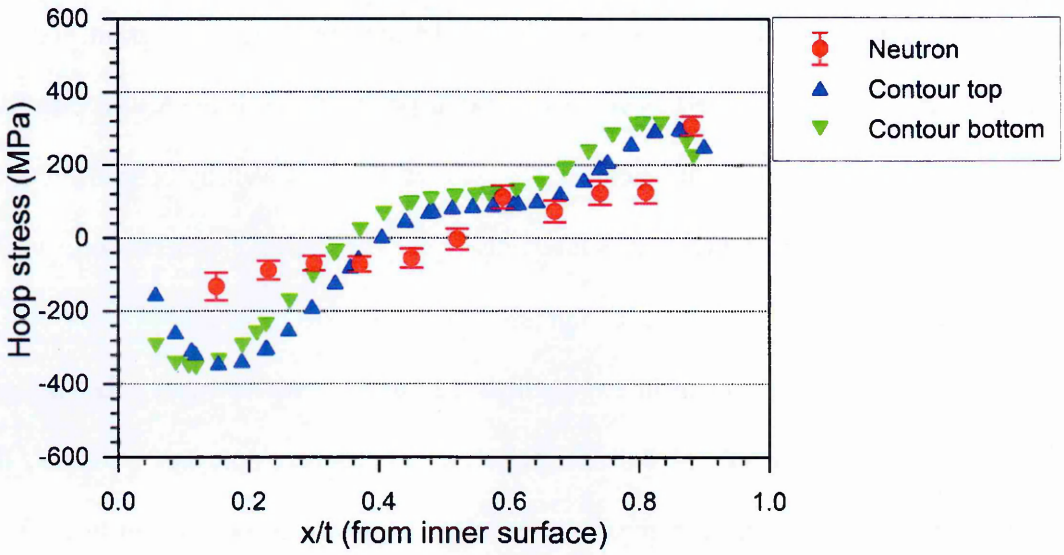

Figure 3.54. Comparison of hoop residual stress distributions at the HAZ measured using neutron diffraction and the contour method in the low heat input pipe (MU4-1).

In MU4-3 (high heat input pipe) the agreement between measurements was poor at some points especially near the outer surface ($x/t > 0.7$) where the neutron diffraction measurements are noticeably lower than the contour measurement (see Figure 3.55). The radial stresses determined using neutron diffraction (see Figure 3.48 (a)) at the three points near the outside surface are high, of the order of 300 MPa, at the outermost point. This suggests the neutron measurements that may be unreliable here because radial stresses at the surface are expected to be close to zero and the high radial stress results may be associated with uncertainties in stress-free lattice parameter measurements for the austenitic weld metal owing to compositional variations, texture, large grain sizes or plasticity [12, 73, 137]. Despite this the ageement at points along through wall positions (x/t) = 0.2 – 0.7 is fairly good and the peak stresses are captured well by both techniques. Noticeably, the neutron measurement is inferring higher compressive stresses near to the inside surface. As mentioned before, compressive hoop stresses measured in MU4-3 near the inside surface are not evident in any published historical measurement data [18] and this is likely to be the result of the specific weld procedure employed. Overall, the agreement in results from the two measurement techniques can be considered to be good excluding the points near to the outer surface.

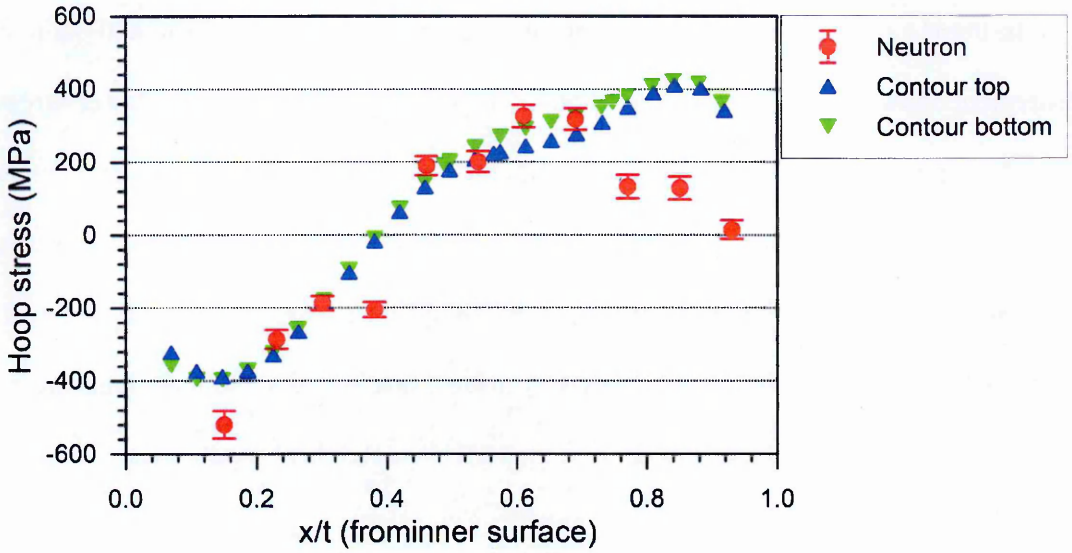

Figure 3.55. Comparison of hoop residual stress distributions at the Weld Centre Line (WCL) measured using neutron and the contour method in the high heat input pipe (MU4-3).

In the HAZ location (see Figure 3.56) the agreement between neutron and contour measurement is favourable though the latter is suggesting the presence of lower stress magnitude at most of the measurement locations. The mismatch is about 100 MPa in some points and as mentioned before, this is a common observation when comparing stress measurements using different techniques in multi-pass weldments. In general, measurements in MU4-1 (low heat input pipe) made using two diverse techniques agree better with each other than those measured in than MU4-3 (high heat input pipe).

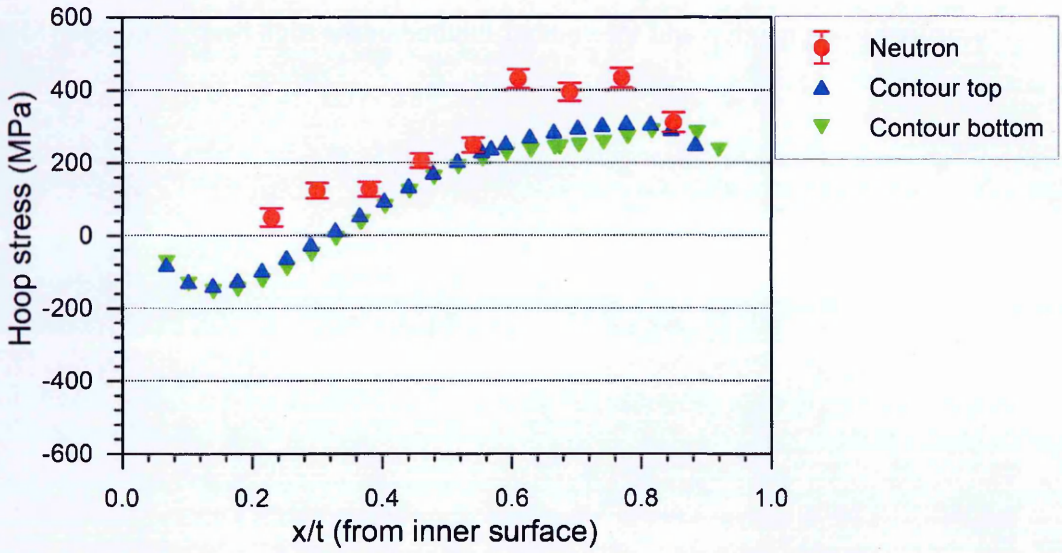

Figure 3.56. Comparison of hoop residual stress distributions at the HAZ measured using neutron and the contour method in the high heat input pipe (MU4-3).

3.4 Esshete 1250 pipe

3.4.1 Manufacturing history and characterisation studies

A series of butt-welded pipe test components were fabricated by TWI (The Welding Institute) [138] from Esshete 1250, which is an austenitic stainless steel with added vanadium and niobium to increase its high temperature strength. The chemical composition of the Esshete material is described in Table 3.3. The pipe sections were solution heat treated and quenched before welding; and thus introduced quench residual stresses in the sections. The manufacturing history of the welded Esshete pipe is schematically illustrated in Figure 3.57. The dimensions of the mock-up were 200 mm long with an outer diameter of 180 mm and 35 mm thick. The root and subsequent weld passes were deposited using manual TIG and MMA processes respectively and the root pass protrusion was removed by grinding after the completion of welding. As several welds were made in series, the pipe assembly was cut into a number of similar components with a girth weld at the mid-length of each. The weld groove preparation and pass sequence of Esshete mock up is illustrated in Figure 3.58. The chemical composition of the filler material is shown in Table 3.4. The Esshete mock-up supplied to the Open University for contour method measurement was made with an average welding heat input of 1.8 KJ/mm. The yield strength (1% proof stress) at room temperature of the Esshete 1250 parent metal and weld metal were 370 MPa and 564 MPa, respectively. Additionally conventional deep hole drilling (DHD), and incremental deep hole drilling (iDHD) were performed at the University of Bristol. Neutron measurements were not possible in this mock-up owing to high wall thickness.

Table 3.3. Chemical composition of the Esshete material.

Composition %	C	Si	Mn	P	S	Cr	Ni	Mo	N
	0.097	0.45	6.23	0.025	0.0037	14.71	9.38	0.95	0.061
	W	Co	V	Cu	Sa	Nb	B	Al	
	0.01	0.045	0.28	0.13	0.005	0.092	0.004	0.004	

Table 3.4. Chemical composition of the Esshete filler metal.

Composition %	C	Si	Mn	P	S	Cr	Ni	Mo	Nb	V
	0.1	0.4	5.5	0.03	0.01	16.5	9.0	1	0.8	0.3

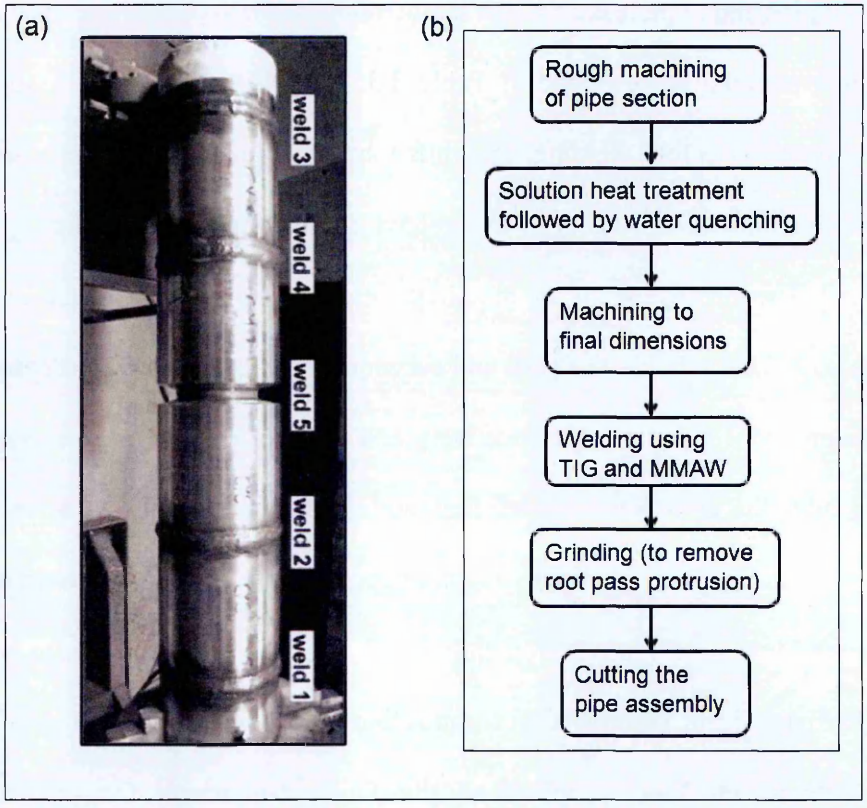

Figure 3.57. (a) Photograph of the Esshete 1250 pipe assembly containing series of girth welds (b) Manufacturing history of the welded Esshete pipe weldments [17, 18].

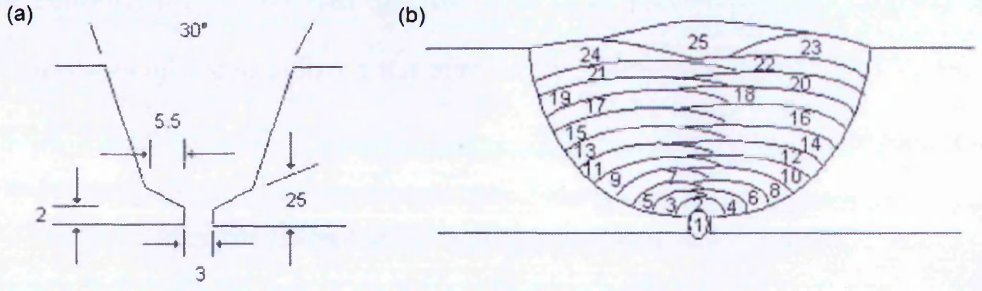

Figure. 3.58. (a) Weld groove preparation (b) Schematic showing weld pass sequence in the Esshete 1250 pipe.

Maximum hardness values in the Esshete mock-up were observed near the weld root region and the variation of hardness with respect to individual weld beads was evident in the map shown in Figure 3.59. Hardness values as high as 300 HV5 were observed near the weld root and found to decrease when moving away both along the length and through-thickness directions. The hardness values reduced to 160 HV5 approaching the parent material. The Esshete material has enhanced material properties such as higher yield strength than Type 316L stainless steel and hence there is a difference in the hardness values found compared to the other pipes discussed earlier. A dendritic microstructure was observed in the weld metal and elongated grains in the HAZ as illustrated in Figure 3.60.

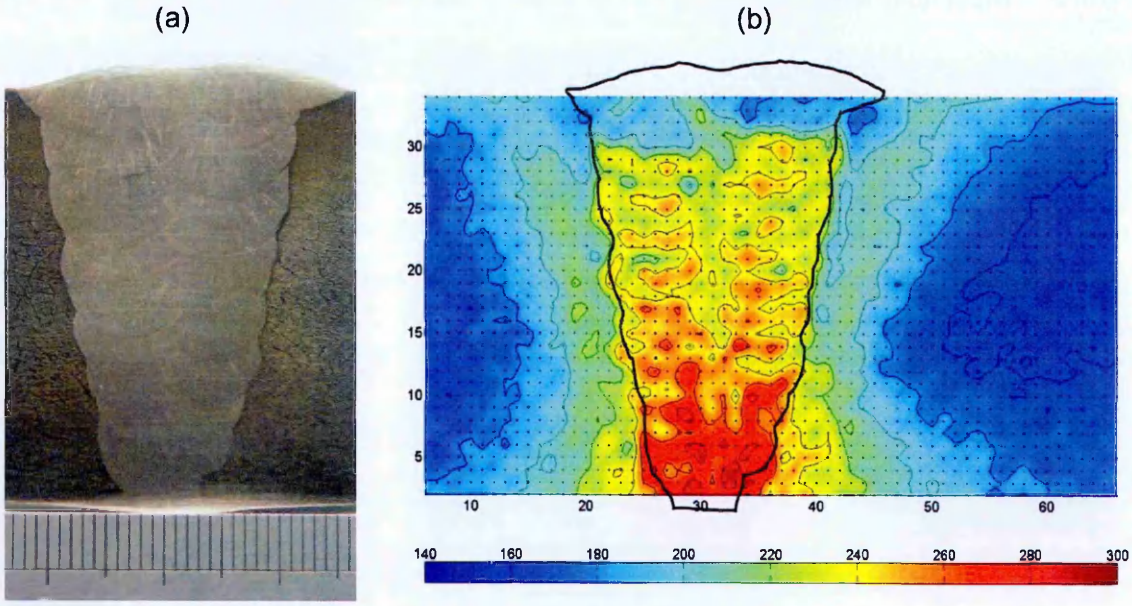

Figure 3.59. Weld macrographs and Hardness maps of Esshete weldment.

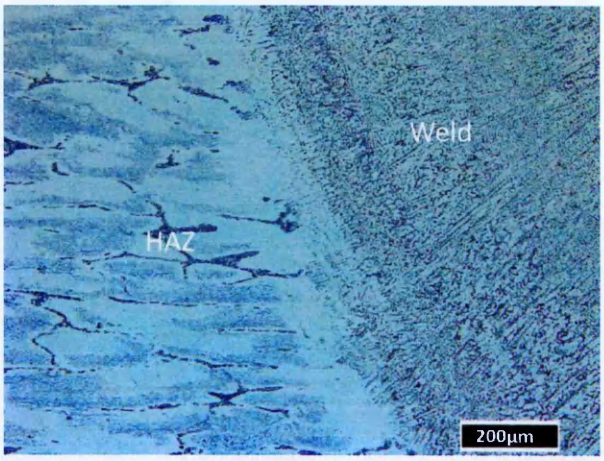

Figure 3.60. Microstructural analysis at the fusion boundary of of Esshete material.

3.4.2 Contour method residual stress measurements of Esshete 1250 pipe weldment

Determination of hoop stresses using contour method

The hoop stresses in the Esshete weldment were determined following the same procedure described in section 3.2.3. A map of measured hoop stress on a cross-section of the mock-up is presented in Figure 3.61. High tensile residual stresses can be observed near the outer surface whereas stresses are compressive towards the inner surface in the region of the weld. Regions of tensile hoop stress at mid-wall were also observed remote from the weld and are probably the consequence of the solution heat treatment of the pipe (involving a water quench) prior to welding.

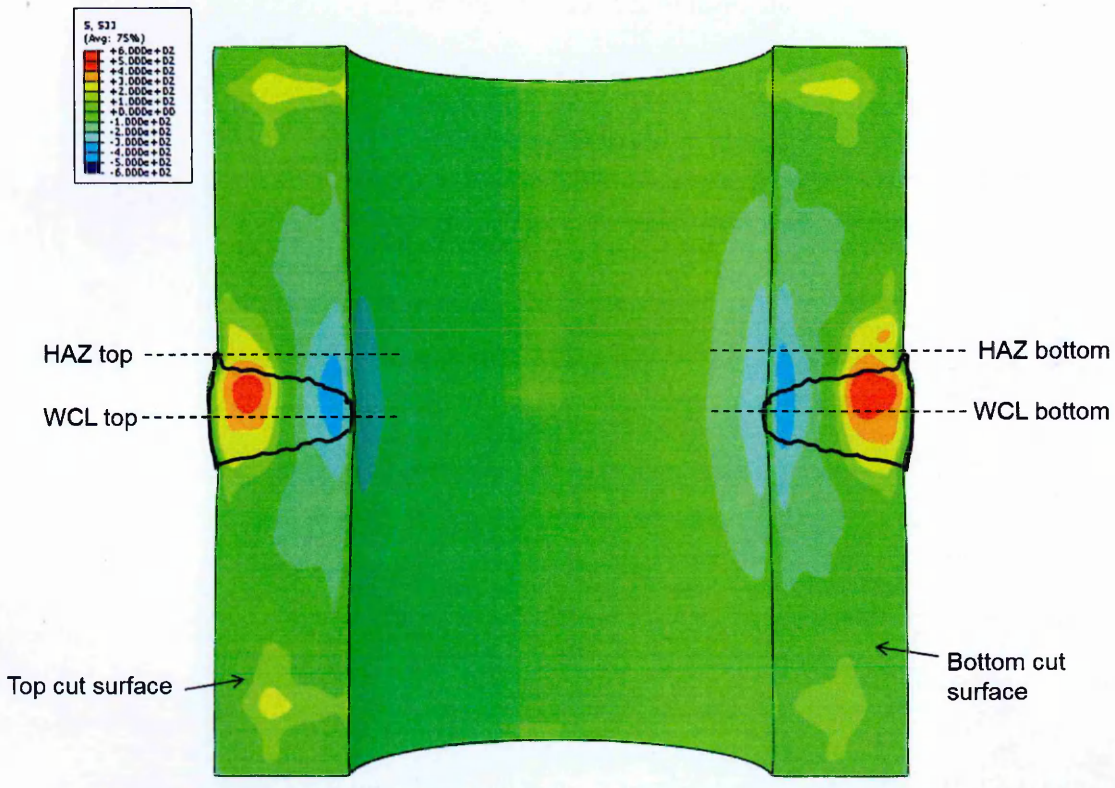

Figure 3.61. Cross-sectional view on a diametral-axial plane of a 3D finite element model of the Esshete pipe girth weld (R/t = 2.1, t = 35 mm, heat input = 1.8 kJ/mm) showing a contour map of inferred hoop residual stresses on the pipe wall cut surfaces that have been relieved during a contour residual stress measurement.

Hoop residual stress line profiles at the WCL and in the HAZ

Hoop residual stress profiles at the WCL and HAZ determined in the top and bottom cut surfaces are shown in Figure 3.62. The distribution and magnitude of residual stresses observed across the top cut surface of the pipe was similar to the bottom surface with high tensile stresses near the outer circumference falling to compression at the inner surface in the vicinity of the weld. Comparing the profiles at the WCL for the top face with the bottom suggests a difference (up to 100 MPa) in distribution approaching the outer surface; this could be associated with variations in the exact capping weld bead lay-up from top to bottom of the pipe (for eg. proximity of the start and stop positions). The HAZ profiles are also in good agreement with each other and indicate the presence of lower magnitude stresses at both the inside and outside surface than the WCL.

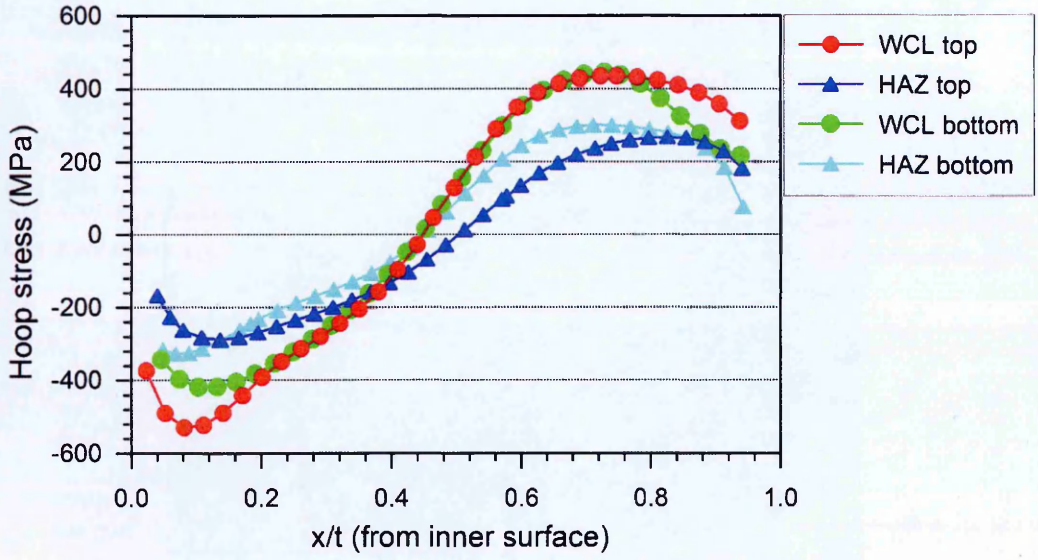

Figure 3.62. Hoop residual stress distributions at the WCL and HAZ measured using the contour method in the Esshete pipe.

The contour method results for the WCL are compared with incremental deep hole drilling reported in [139] in Figure 3.63. The pattern of the stress profile measured by the IDHD method (for through-wall position $x/t > 0.3$) is similar to the measured profile from the contour method. But the results for $x/t < 0.3$ sharply deviate from each other. The IDHD results have been deemed unreliable in this region when was realised that the measurement passed through a weld defect.

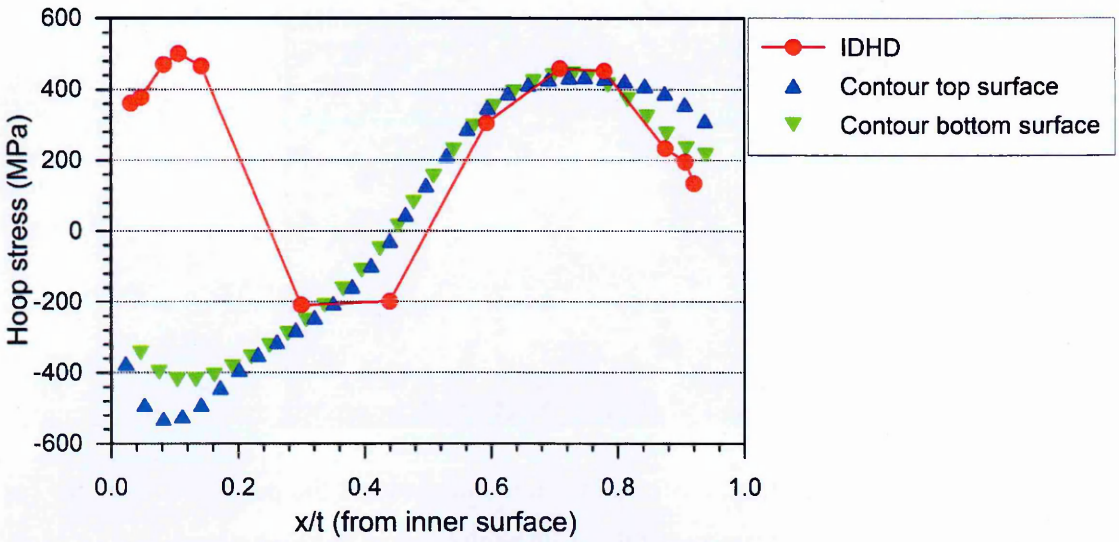

Figure 3.63. Comparison of hoop residual stress distributions at the WCL measured using IDHD and the contour method in the Esshete pipe weldment.

Determination of axial stresses using contour method

In the contour method, multiple cuts can be employed to measure more than one stress component [61]. In this work, an attempt to measure the axial stress component of the Esshete pipe was made by using a wire EDM cut across diametral-hoop plane XY as shown in Figure 3.64. The cut was performed at the WCL on one of the remaining half pipes following the contour method EDM cut for the hoop stress measurement. Sacrificial material was machined to mate with both the top and bottom of the half pipe as shown in Figure 3.65 to ensure a good quality cut surface with minimum artefacts. The surface deformation contours were measured using a Zeiss Eclipse laser non-contact coordinate

measuring machine with a point density spacing of 0.25 mm × 0.25 mm. The data analysis procedure employed was similar to that for the hoop stress measurement with additional steps implemented to account for the stress relaxation effects from the previous cut (along XZ plane). This was accomplished by applying the displacement boundary conditions applied to FE model created for determining the hoop stresses.

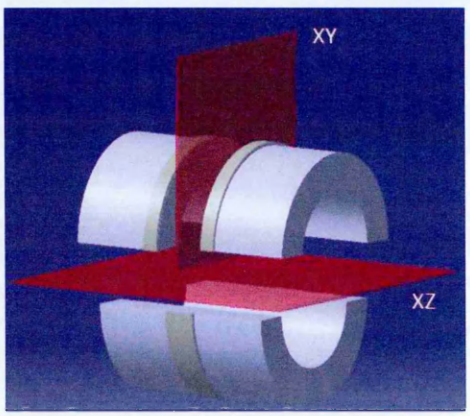

Figure 3.64 Schematic illustration of the location and plane of the performed contour cut for the measurement of axial stresses at the weld centre line in the Esshete weld.

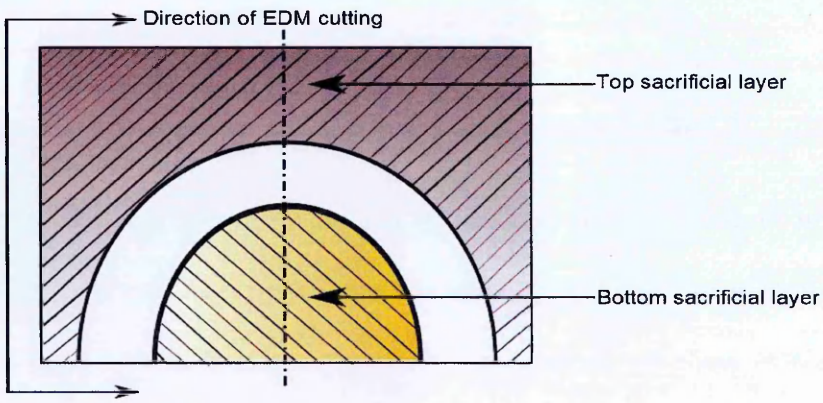

Figure 3.65. Schematic representation of the sacrificial layers attached on the Esshete mock-up for determination of 2D stresses along axial direction at the WCL.

A map showing the measured axial stress distribution at the WCL is illustrated in Figure 3.66. The axial stress residual profiles were averaged around a sector extending 45° on either side of the normal YY as shown in Figure 3.67; this is representative of the 'Average' profile. The axial stress profiles determined along different through-thickness positions at 12°, 24°, 36°....168° with respect to the flat edge (XX) in the clockwise direction are compared with each other and the averaged stress profile at the WCL of the Esshete pipe in Figure 3.68. Significant 'scatter' was observed in the measured data using the contour method ranging from 100 MPa to more than 200 MPa at many locations. This is the first time that the variation of through-thickness stresses around the circumference has been studied at the weld centre line of a girth welded pipe. The patterns of stress profiles matched closely with each other with a peak compressive stress of 250 MPa found at x/t = 0.3 with a peak tensile stresses close to 300 MPa at x/t = 0.65 - 0.85. The magnitude of stresses found to decrease approaching the outer surface with a magnitude of less than 100 MPa for all the stress profiles.

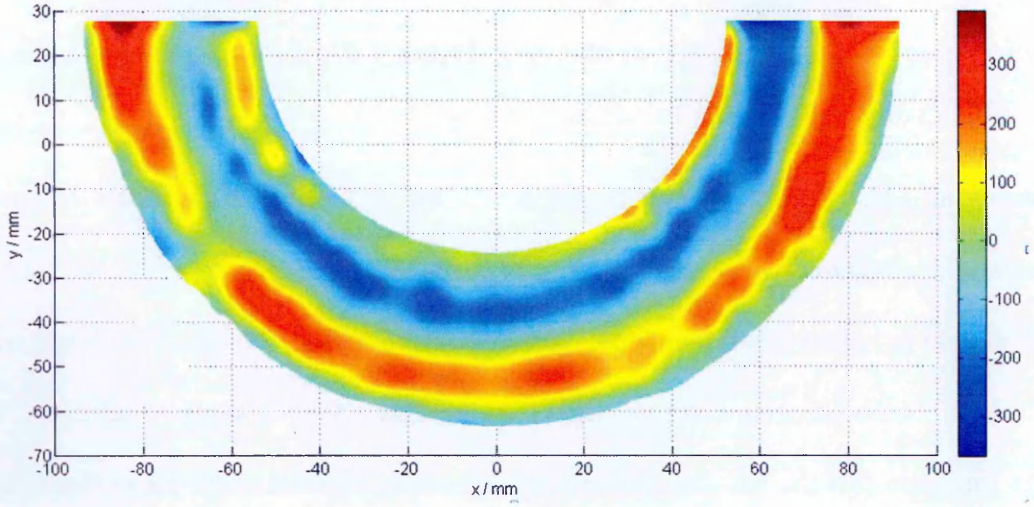

Figure 3.66. Cross-sectional view on a diametral-hoop plane of a 3D finite element model of the Esshete pipe girth weld (R/t = 2.1, t = 35 mm, heat input = 1.8 KJ/mm) showing a contour map of inferred axial residual stresses at the weld centre-line on the pipe wall cut surfaces that have been relieved during a contour residual stress measurement.

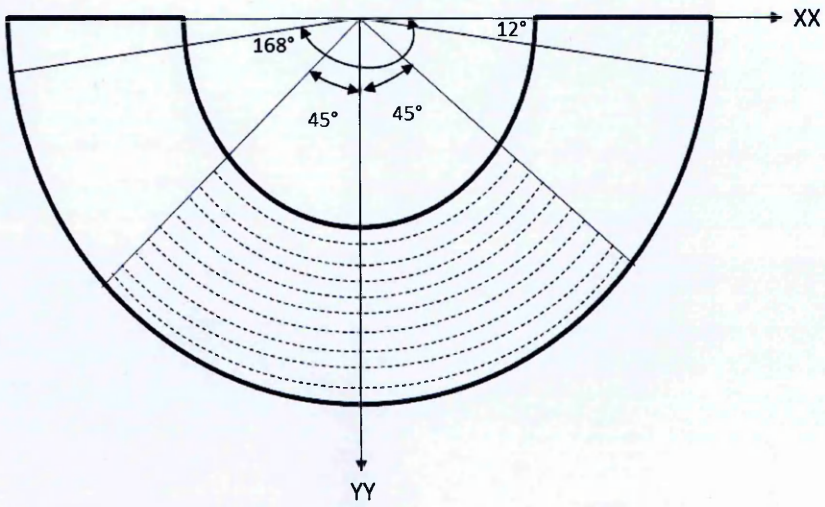

Figure 3.67. Schematic illustration of the location of through-thickness stress profiles in the Esshete weld.

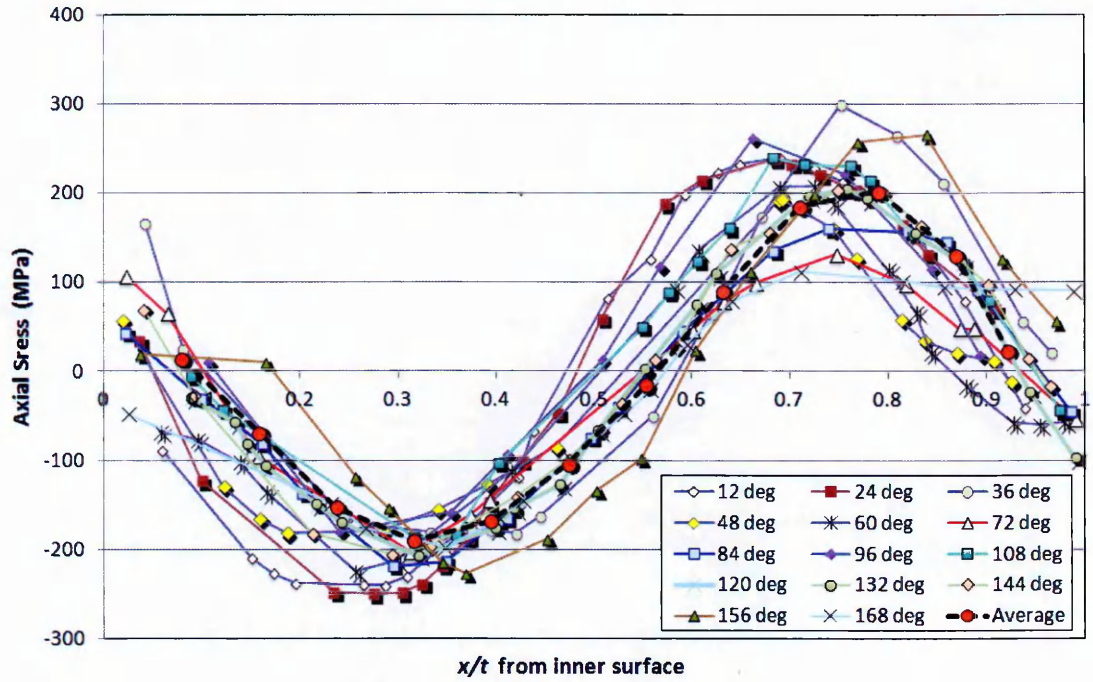

Figure 3.68. Comparison of axial stress profiles at various locations (12 deg., 24 deg., 36 deg……. 168 deg. and averaged stress profile across 45 deg across both sides of YY) at the WCL of the Esshete pipe.

The residual stress results from the IDHD measurement reported in [139] are compared with the contour measurement in Figure 3.66. The trend observed in results from the IDHD method (for through-wall position $x/t > 0.3$) is similar to the measured axial stress profile from the contour method for through-wall position $x/t > 0.3$. However, the results for $x/t < 0.3$ does not match up with the contour method measurements as the IDHD results were unreliable in this region as mentioned earlier.

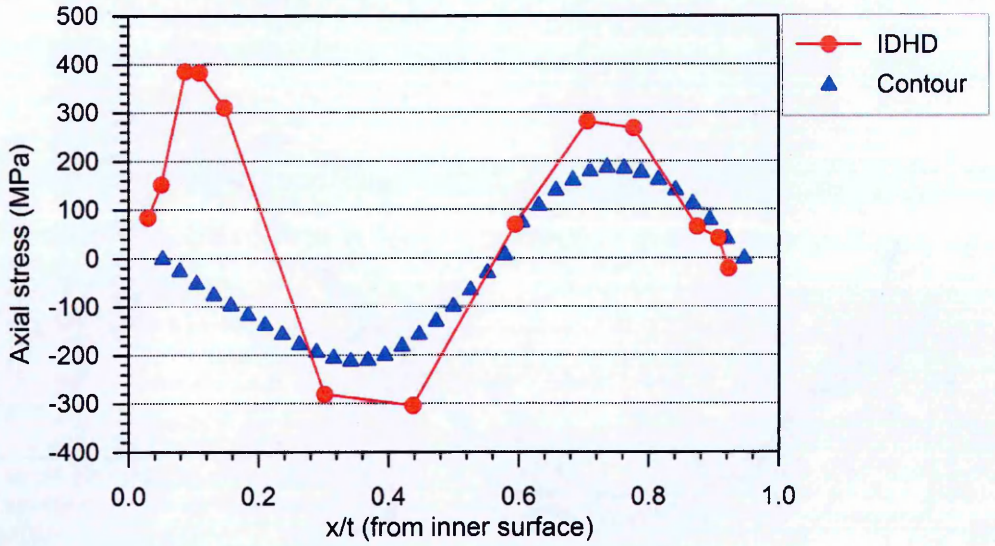

Figure 3.69. Comparison of axial stress distributions at the Weld Centre Line (WCL) measured using IDHD and contour method in the Esshete pipe.

3.5 General Discussion

The experimental measurements acquired at the WCL and HAZ locations in the hoop direction using different techniques in all the six mock-ups are compared in Figures 3.70-3.73. For convenience sake, measurements along the hoop direction at the WCL in the half inch thick pipes are compared first followed by measurements in the same pipes at the HAZ locations. In Figure 3.70, fair agreement is found between the measurements up to the through-wall position x/t = 0.5 and all the neutron measurements advance to a state of zero stress approaching the outer surface. The contour measurements however carry on reaching a peak tensile stress of 400 MPa at through wall position x/t = 0.7 and then decrease moving towards the outside diameter. The lack of agreement between the measurements is prevalent in the through thickness range (x/t) = 0.5 – 0.9. On the other hand, good agreement is found between the measurements reported in the HAZ location (see Figure 3.71) for the same pipes with a difference of 200 MPa in the peak stresses which can be attributed to the variation in heat inputs.

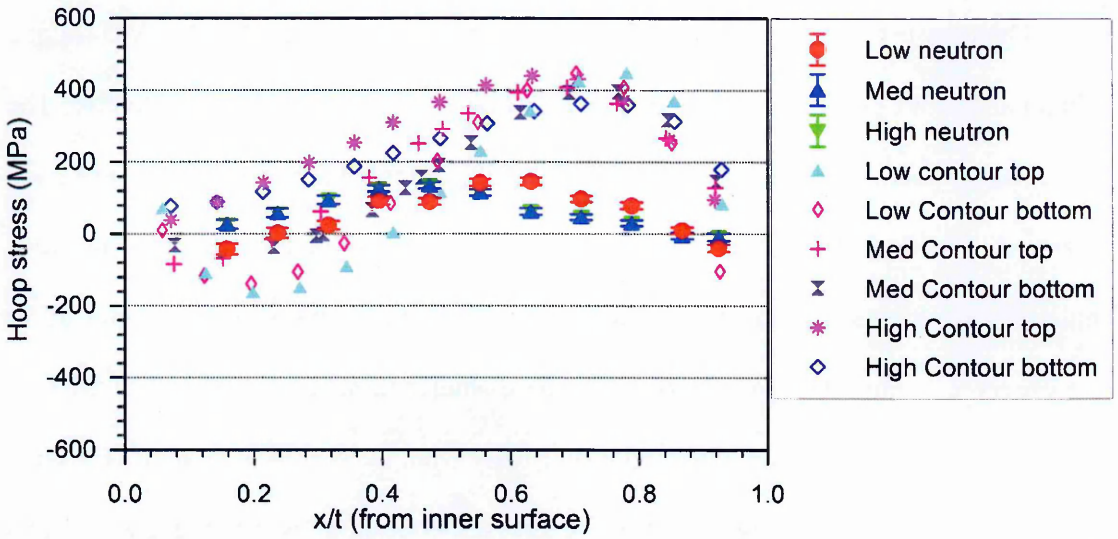

Figure 3.70. Comparison of hoop residual stress distributions at the WCL measured using neutron diffraction and the contour method in the thin pipes (Low, Med and high).

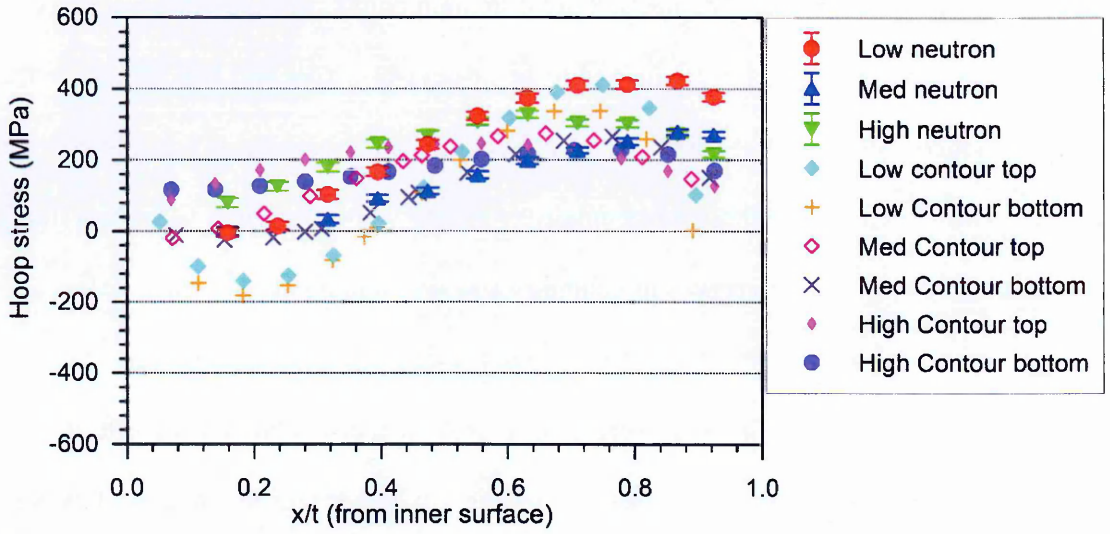

Figure 3.71. Comparison of hoop residual stress distributions at the HAZ measured using neutron diffraction and the contour method in the thin pipes (Low, Med and high).

The measurements in the hoop direction for the thicker pipes (MU4-1 MU4-3 and Esshete) at the WCL and HAZ are compared in Figures 3.72 and 3.73 respectively. The measurements obtained in the WCL (see Figure 3.72) of the three pipes exhibit very good agreement in spite of the wide scatter observed particularly in the neutron measurements. Emphasis should be given to the fact that very high compressive stresses (~ 500 MPa) were observed in the region close to the inside diameter in all three pipes. The STYLE pipes MU4-1 and MU4-3 were made with unusually wide weld prep with a backing plate removed after welding. The high compressive stresses reported in each of these weldments are believed to be the effect of the specific weld procedure used during fabrication. The yield strength of the Esshete weld material (564 MPa 1% PS) is higher than the STYLE pipes weld filler and therefore it is plausible to have compressive stresses of the magnitude reported for the Esshete pipe. The neutron measurement points near the outside surface of the high heat input pipe MU4-3 are judged to be of deviant nature and believed to be the effect of an incorrect stress free reference used. In contrast, the agreement between contour method measurements in all three mock-ups is satisfactory and the slight variations likely to be associated with the differences in geometry and the welding heat inputs employed to fabricate the components. In the HAZ location (see Figure 3.73), a high level of consistency was observed with the exception of neutron measurements in the high heat input mock-up MU4-3 inferring the presence of slightly higher tensile stresses. However, the agreement in general is quite good and especially for the contour measurements.

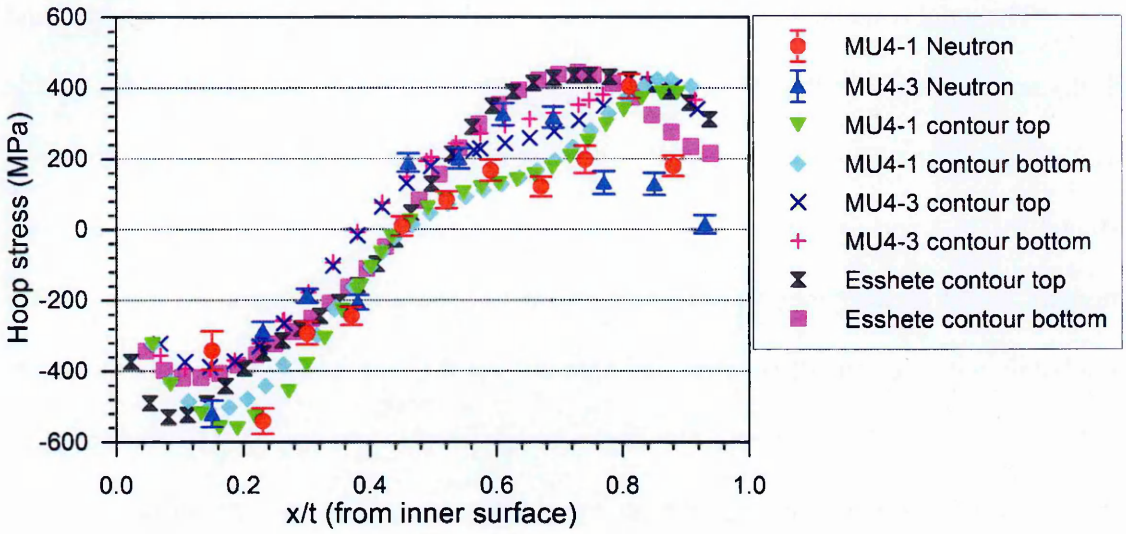

Figure 3.72. Comparison of hoop residual stress distributions at the WCL measured using neutron diffraction and the contour method in the thick pipes (MU4-1, MU4-3 and Esshete).

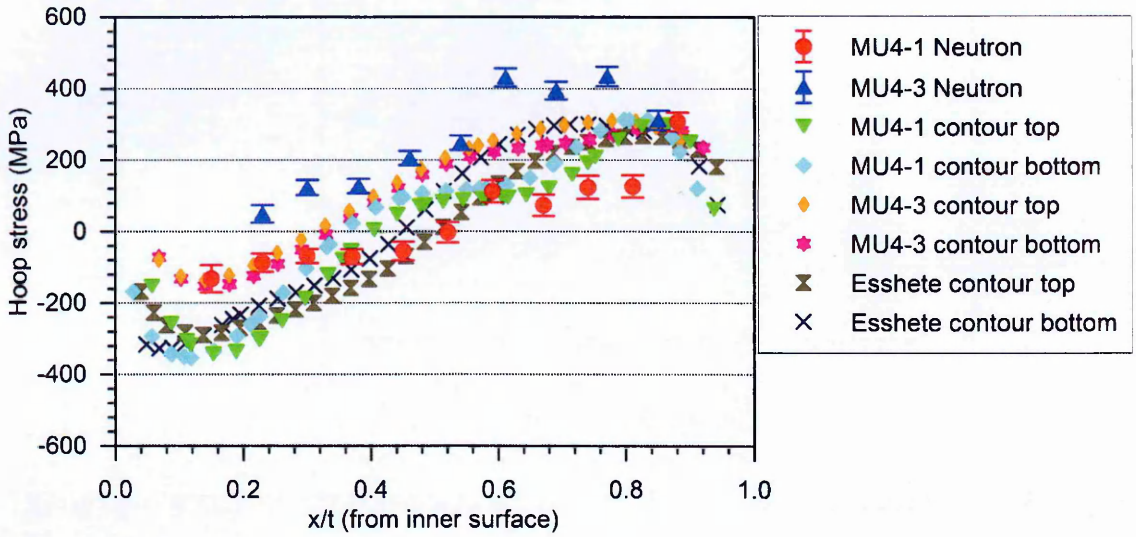

Figure 3.73. Comparison of hoop residual stress distributions at the HAZ measured using neutron diffraction and the contour method in the thick pipes (MU4-1, MU4-3 and Esshete).

The axial residual stresses in the six pipes (MU4-1 MU4-3, Esshete, Low, Med and High) are compared at the WCL and HAZ locations in Figures 3.74 and 3.75. A wide scatter was observed especially at the WCL (see Figure 3.74) although the stress profiles in MU4-1, MU4-3 and Esshete show a similar shape. However the stress profiles in the low, medium and high heat input pipes do not seem to have any correlation with the thicker mock-ups; note the state of compression approaching the outer surface. The measurements at the HAZ location (see Figure 3.75) display comparatively less scatter. Thus the variation of stresses with respect to change in heat input and geometry has a greater influence in the axial direction than the hoop.

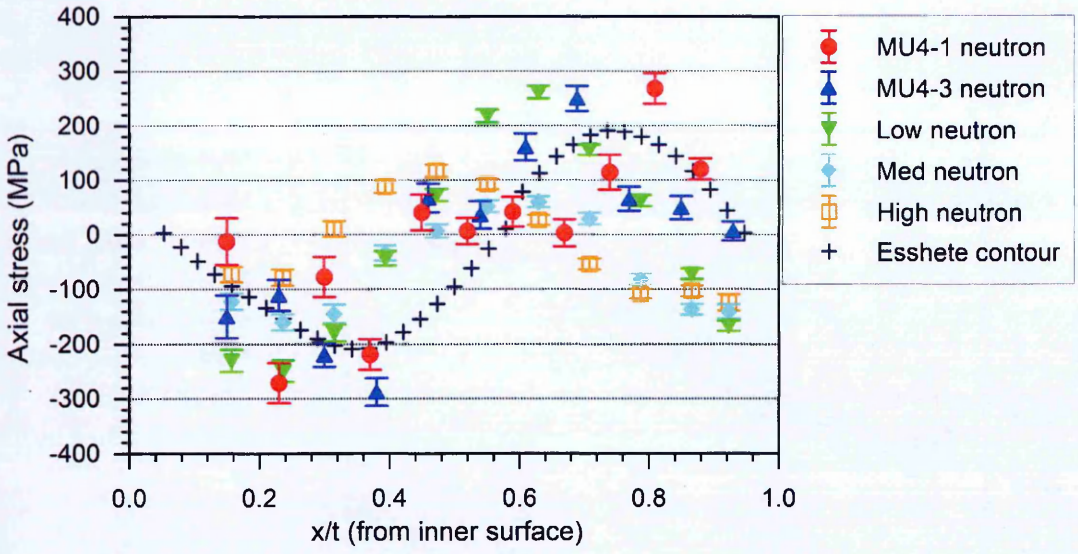

Figure 3.74. Comparison of axial residual stress distributions at the WCL measured using neutron diffraction and the contour method in all mock-ups (MU4-1, MU4-3, Esshete, Low, Med and High).

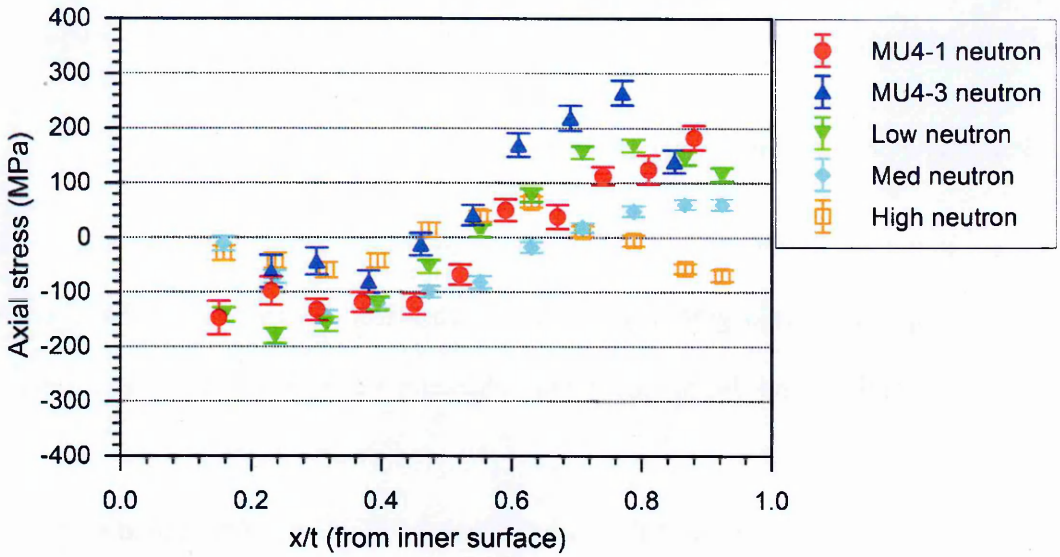

Figure 3.75. Comparison of axial residual stress distributions at the HAZ measured using neutron diffraction and the contour method in all mock-ups (MU4-1, MU4-3,Esshete, Low, Med and High).

3.6 Conclusions

The findings reported in this chapter can be summarised as follows,

- Six new pipe weldments have been fabricated with a range of wall thickness, weld heat input and weld groove geometries. Cross-sections for each weldment have been examined and the microstructure characterised by microscopy and hardness mapping.
- Residual stresses in each of the girth welded mock-ups were measured by neutron diffraction using the SALSA neutron diffractometer at the ILL (France) and the contour method using the in-house facility at the Open University, UK.
- The measured residual stress profiles obtained using different techniques have been compared with each other at WCL and HAZ locations. Significant scatter is observed among the residual stress profiles especially with the neutron diffraction measurements and the spread of measured data from different techniques can be more than 200 MPa in many cases which is associated with the typical nature of residual stresses in multi-pass welds.
- The measurements reported using different techniques showed high level of agreement in the respective pipes with the exception of stress profiles measured using neutron diffraction along the WCL in the half inch thick pipe welds. The discrepancy associated with the neutron measurements is believed to be associated with uncertainties in stress-free lattice parameter measurements for austenitic weld metal owing to compositional variations, texture, large grain sizes or plasticity.
- Measurement of axial stress profiles using the contour method was successfully attempted in the Esshete girth weld by employing multiple cuts. Several through-thickness line profiles were extracted along the circumference and compared. The scatter observed in the measured data at the weld centre line ranged from 100 MPa to more than 200 MPa.

- Overall, contour method measurements were found to provide more consistent results than neutron diffraction especially in the weld metal.

The measurements acquired from the girth welded pipes are of high quality and will be used to support the development and validation of the neural network approach for predicting residual stress profiles for use in integrity assessments of defective structures discussed in the coming chapter.

Chapter 4

Neural network modelling

4.1 Background

The human brain is considered to be very unique as it can perform astonishing tasks on a day to day basis, possesses phenomenal power to learn and understand complex activities. Artificial neural network (ANN) is a field of computation that seeks inspiration from the brain and tries to reproduce some of its amazing characteristics. By adopting a brain style computation, there are many advantages over computers such as parallelism, noise tolerance, ability to learn and generalise patterns as described in [140]. ANNs have the potential to deal with non-linear multi-variable systems with a high level of noise, where developing an analytical model is either not feasible, or too time consuming.

4.1.1 Theory

According to the world of computing, Artificial Neural Networks (ANN) is a class of algorithms that has the ability to learn and generalize non-linear systems thus making it conducive for solving problems in real life scenarios. A neural network can be 'trained' using historical data or a set of example input and output data. The training process can be defined as a search for the optimum non-linear relationship between the input and output data and is computationally intensive. Once the network is trained the estimation of outputs for any unseen set of inputs can be performed rapidly. The training process consists of adapting a set of coefficients (referred to as weights and biases) which in combination with the activation or transfer function relate the input to the output via a suitable algorithm

such as back-propagation [141]. The fitting of a network function to a set of data continues until it reaches a minimal state of the error function, such as the sum of the squares error. For multilayer networks [142] the search for the minimum error generally occurs in an iterative fashion starting with some random values assigned to the weights. The basic procedure to train an ANN structure is to use a database of observations and then evaluate the predictive capacity of the developed model on previously unseen data. The main disadvantages of using neural networks are the reliance on good training data, inability to extrapolate into new regions of input space, susceptibility to overfitting and the need for adequate training data.

Single and multi-layer networks

An ANN comprises processing elements, or building blocks, called neurons arranged in hierarchical groups and operate in a parallel manner to generate outputs for several inputs. A simple model of a neural network with one neuron is shown in Figure 4.1.

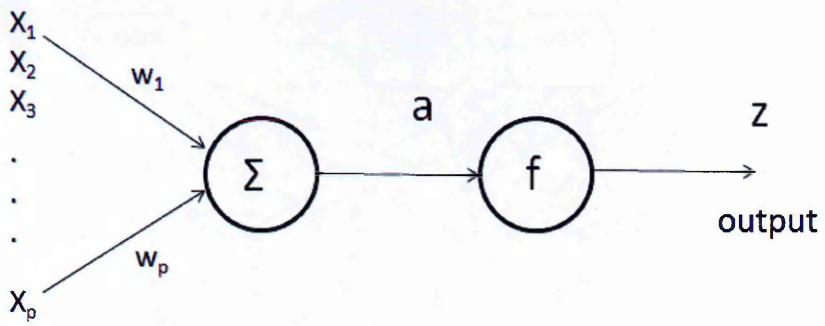

Figure 4.1 Structure of a single layer neural network.

The input signal x_i (x_1, x_2, x_3... x_p) is first multiplied by a parameter w_i known as a weight (parameter which is analogous to the synaptic strength of a biological neuron) and is then summed up with all the weighted input signals to give a total input to the neuron given by equation (1),

$$a = \sum_{i=1}^{p} w x_i \qquad (1)$$

The net output from a neuron is given by $z = f(a)$ where f represents a non-linear function and is known as an activation or transfer function. The weights can be of either sign (excitatory or inhibitory) and are optimised during the training process by minimizing a regularised error function based on the network output.

A feed-forward network is described as a non-linear mathematical function which transforms a group of inputs into outputs to produce a mapping and is governed by the parameters called weights. The feed-forward network used in this study consists of 2 layers of neurons interconnected as shown in Figure 4.2. The first layer is referred to as 'hidden layer' and its neurons as hidden units or processing units. The numbers of hidden units greatly influence the complexity of the network and their activation function which is non-linear, could either be a *tanh* or *logh* function. The hidden layer greatly contribute in helping the model to identify complex interactions between the variables.

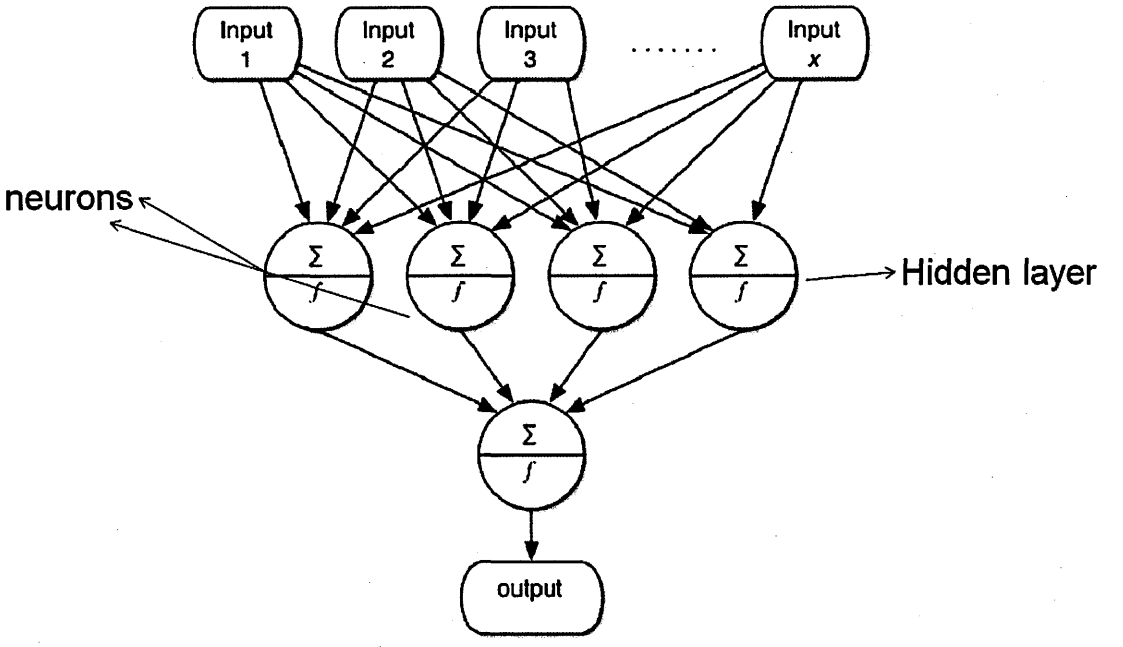

Figure 4.2. A two layer feed-forward network identical to the one used in this study.

In a Multi-Layer Perceptron (see Figure 4.2), a neuron (node) of each layer is connected to a neuron of the next layer through a synaptic weight and bias. The output of the input variables is fed to the hidden layer and the output of the hidden layer is then progressively fed to the output layer. The error function can be regarded geometrically as an error surface resting over a weight space, as schematically indicated in Figure 4.3. The network training is a search process to determine the minimum of the error surface. An absolute minimum of the error function, indicated by the weight vector W^A is called a global minimum and there may also exist other minima's, such as the one corresponding to the weight vector W^B which is referred to as local minima [11]. Many algorithms performing the minimization of the error function make use of the derivatives of the error function with respect to the weights in the network. These derivatives form the components of the gradient vector $VE(w)$ of the error function, which gives the gradient of the error surface at an arbitrary point, as indicated in Figure 4.3. The approach of using direct gradient descent has improved in recent years by the development of more sophisticated search algorithms such as scaled conjugate gradients [143] which provide a significantly faster convergence. It is generally agreed that there is a considerable benefit to use the gradient information during training, for instance calculation of the Hessian matrix or second order derivatives of the error function with respect to the weight matrix play an important role in a number of advanced network algorithms.

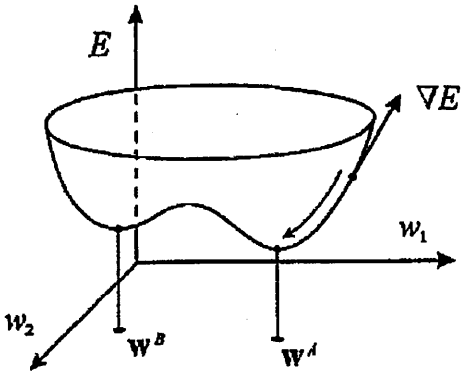

Figure 4.3. Schematic illustration of the error function *E(w)* as a surface resting over the weight space (space spanned by values of the weight and bias W= $\{w_1,w_2,...w_n\}$. The weight vector W^A and W^B corresponds to the global and local minimum of the error function [128].

4.1.2 Practical aspects of neural network training

Overfitting

The phenomenon of overfitting occurs when the network gives a relatively small error with respect to the training data, but is poor in generalising the underlying trend in the data and therefore gives poor predictions for new or unseen set of data. There is a possibility of overfitting the data as the functions used in neural networks are very flexible. Overfitting can be avoided by controlling bias and variance, by adding penalty terms to the error function to promote the network mapping to have appropriate smoothness properties, also known as regularization [10].

Choice of input variables

There is a natural tendency to include a maximum number of variables to train the network in order to make it more robust. However, in pattern recognition problems it was identified that simply discarding some of the input variables could actually lead to improved generalization ability. This is because the size of the training dataset required to specify a

mapping would generally grow exponentially with the dimensionality of the input space. This paradoxical phenomenon is known as the curse of dimensionality [144].

Pre and post processing of data

It is considered to be advantageous to apply pre-processing transformations to the raw data before it is presented to a network as well as post-processing to give the required output values of the network (see Figure 4.4) [145]. The pre-processing and post-processing steps may consist of simple fixed transformations such as normalising the values to a range between -1 to +1. For practical applications, data pre-processing can often have a significant effect on generalization performance as it may involve a reduction in the dimensionality of the input data.

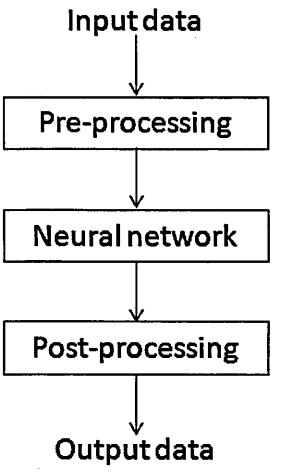

Figure 4.4. Pre-processing and post-processing transformations applied to the data.

Committee model

The models with a different number of hidden units will give different predictions as the complexity largely depends on the number of hidden units. It is a common practice in the training process to have many different networks and then to select the best, on the basis of performance on an independent validation set. The drawback with the above approach being all the effort put in training the remaining networks is of no purpose and the network with the best performance during training may not perform the best with the test data. This

can be overcome by combining the networks together to form a committee This approach can be useful as it can lead to significant improvements in the predictions on new data, with additional computational effort. In fact, the performance of a committee of networks can be better than the performance of the best single network used in isolation [145, 146].

Software implementation and applications

There are various neural network software packages available in the market, ranging from simple demonstration software to large commercial packages supporting a range of network architectures and training algorithms such as in MATLAB and PYTHON. These software programs can be very useful for quick prototyping, possess sophisticated graphical interfaces and provide an easy way to gain hands-on experience with neural networks. Neural networks can also be implemented in high level programming languages such as C, PASCAL and FORTRAN. Neural network algorithms are relatively straightforward to implement, and much of the effort of developer is often devoted to application specific requirements and the user interface.

Neural networks are used to solve problems in a wide range of applications such as optimization, control, signal processing, classification, pattern recognition and stock market prediction. Neural network modelling has been successfully implemented for estimation of retained austenite in austempered ductile irons [147], stock market forecasting [148], prediction of daily global solar irradiation data [149], fatigue life prediction of composite materials [150], austenite formation in steels [151], decoding litho-facies boundaries from well-log data [152], sediment classification of downhole log data [153], forecasting pre-processed daily solar radiation time series [154] and subset simulation for reliability analysis [155].

4.1.3 Artificial neural network modelling of residual stresses

Artificial Neural Network (ANN) and support vector regression models [156, 157] have been applied to predict residual stresses in dissimilar metal welding but have not been validated using experimental measurements. A simple three layer neural network model has been developed by Dimitrui et al. [158] for determining residual stresses in a ball bearing as a function of contact pressure, hoop stress, number of revolutions, inner ring temperature and depth. ANN have been successfully implemented to predict the welding response for wide variety of geometric and process parameter combinations [159] and to determine the residual stress distribution [160, 161] without having to perform the full finite element analysis.

Recently, a hybrid model based on finite element and a neural network have been developed to predict welding induced residual stresses in butt welding [162, 163]. The data sets from the FE model were used to train the neuro-hybrid models using arc efficiency, welding speed, voltage and current as input parameters and the predicted stress values were validated using X-ray diffraction with an rms error of less than 5 %. Na et al. [164] predicted the residual stresses of dissimilar pipe welds at nuclear power plants using R/t, heat input, yield stress of weld metal and constraint of welded pipes as input variables to observe an rms error of less than 5 % when compared with a parametric finite element analysis. Toparli et al. [165] used residual stress data calculated from finite element analysis in cylindrical steel bars to train a neural network and validated it using finite element simulations. Recently Toktas et al. [166] presented an artificial neural network based solution to determine the hoop stress encircling a split-sleeve cold expanded fastener hole by using training data generated from an analytical fourier series method. Toktas et al. [166] reported that the ANN approach was able to provide realistic information about the stress distributions with the analysis carried out at a faster pace.

4.2 Rational for this work

With rapid development in destructive and non-destructive experimental techniques to characterise residual stresses in welded structures, there are now sufficient historical data available for welds. In this work, an abundance of published measurement data for austenitic stainless girth welded pipes were available and thus paved the way for applying artificial neural networks to analyse residual stress data. In the present study, through-thickness residual stress profiles of pipe girth welds are acquired using multiple experimental techniques for comparison and validation of a neural network approach. Owing to the geometry and thickness, neutron diffraction and contour method were chosen to be the most appropriate methods. Despite the evidence found in literature, researchers have not extensively validated the methods developed based on the application of the neural networks related to residual stress prediction. Furthermore, acquiring high quality residual stress data for a specific class of material or geometry could be difficult.

4.2.1 Training and validation

A Multi-layer Perceptron (MLP) [142] network architecture chosen for the regression model was undertaken in the MATLAB neural network toolbox [167]. The multilayer perceptron structure has a particularly simple topology consisting of two layers of weights, with full connectivity between inputs and hidden units and between hidden units and the outputs. In principle, it is not essential to consider other architectures, since the 2 layer network already has universal approximation capabilities [10] and was used in this study.

A feed-forward artificial neural network can be considered as a set of nonlinear mathematical functions which transform a set of input variables into an output. The transformation process is in effect governed by a set of parameters called weights whose values are determined based on a set of examples of input and output data. The process of

determining these parameters is called training, and may be more computationally intensive than simulating the output for a given dataset. 'Weights' control the influence of the inputs on neurons, and are continuously changing during the training, to optimize the relationship between the variables.

Back-propagation algorithm [141] based training of feed-forward networks is a process of minimisation of an error function. In this, the network output performance is quantified in terms of the difference between the predicted values and true target values applied to a set of training data. However, for a given problem, it is difficult to say which training function is most suitable as it depends on many factors such as the complexity of the problem, number of data points, number of weights and biases [168]. Levenberg Marquadt is one of the fastest algorithms used for training the neural networks but perform poorly in pattern recognition problems. Improved gradient descent based search algorithms such as scaled conjugate gradients [143], are capable of providing convergence at a rate comparable to Levenberg-Marquadt. However, both algorithms were attempted in this study and the Scaled conjugate gradient algorithm was able to give consistent solutions than the Levenberg Marquadt.

The use of a nonlinear transfer function makes a network capable of storing non-linear relationships between the input and the output. It is found empirically that using a tanh activation function in the hidden layer could be beneficial as it can result in faster convergence rate than the logsig function [10]. However in this study, it was found that the log-sig activation function could give better solutions when used in tandem with the histogram method (discussed later in section 4.2.2) not accounting for the processing time required. The non-linear capability of the network was implemented by using the logh transfer function between the input and hidden layer and a linear function was used between the hidden layer and the output layer. The net output y from the output layer is represented by equation (2) as,

$$y = \sum_j w_{kj} \log h\left[\sum_i w_{ji} p_i + b_j\right] + b_k \qquad (2)$$

where w_{ji} is the weight matrix of the hidden layer, w_{kj} the weight matrix of the output layer, b_j the bias vector of the hidden layer, b_k the bias vector of the output layer, i the number of input variables and j was the number of hidden nodes. An illustration of the transfer functions used in hidden layer and output is shown in Figure 4.5.

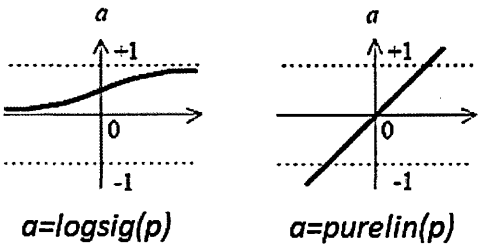

Figure 4.5. Transfer functions used in the first and second layers.

The dataset initially used for training comprises measurements made in eight different mock-ups of nuclear plant welded pipes made from AISI Type 316 austenitic stainless steel having various weld groove geometries and using mainly manual metal arc (MMA) and submerged arc (SAW) welding processes. The welded pipes cover a wide range of electrical heat input (E = 1-2.4 KJ/mm), wall thickness (16-110 mm) and R/t ratio (1.8-25). Historical residual stress measurement data for the weld centre-line and heat affected zone (HAZ), collated in [18], were used to train the ANN taking into account the pipe geometry, welding process, heat input, yield strength and through wall position.

The network parameters used in this study are illustrated in Table 4.1. The input parameters were presented to the network in the most simplified manner in view of the dimensionality phenomenon [144] which states that the size of the training set required to specify a mapping can grow exponentially with the dimensionality of the input space. This suggests that removing some of the input variables can actually improve the generalisation ability of the network. All the input values were scaled between –1 and 1 by using a simple

transformation; normalised input = 2 × (input – minimum input) / (maximum input – minimum input) – 1.

Table 4.1. Details of ANN parameters used in this study

Network type	Feedforward back-propagation
Training function	Scaled conjugate gradient (TRAINSCG)
Input parameters	x/t – through thickness position
	R/t – mean radius over thickness
	T = thickness
	Q – Net heat input (KJ/mm)
Output parameter	Residual stress (axial or hoop) normalised by the yield strength of the material
Number of hidden units	4, 5 and 6
Number of hidden layer	1
Hidden layer function	Log-sig
Output layer function	Purlin
Performance function	MSE (mean squared error)

The number of neurons in the hidden layer and training functions were optimised in the preliminary stages based on the minimum 'sum of the squares' error (i.e. square of the difference of output and target value). The data were configured and presented to a series of MLP networks with optimised set of parameters. For example, in order to optimize the number of neurons in the hidden layer, the ANN was characterized while altering the number of neurons from 4 to 6 where 5 neurons in the hidden layer was found to give consistently low values of 'sum of squares' error as given in Table 4.2.

Table 4.2. Optimisation of the number of neurons in the hidden layer based on the sum of squares error.

Training function	Stress component	Number of neurons in the hidden layer	Sum of squares error
Scaled Conjugate Gradient (SCG)	Axial	4	32.46
		5	28.52
		6	31.34
	Hoop	4	32.71
		5	28.38
		6	27.55

The normalised axial and hoop stresses were post-processed using the histogram method to give the desired output using the respective yield strength (1% PS) of parent and weld material. Hence the yield strength of the material is indirectly accounted by normalising the stress values during training though it is not included as an input parameter.

The measurement density of DHD data points used for training was significantly higher than measurements performed by other techniques. This difference was nullified by reducing the density of DHD measurement points by a factor of 10 using the interpolation tool in MATLAB ensuring any sort of bias is eluded in the data treatment. An illustration of the data reduction in DHD measurements performed in the mock-up S5Old is shown in Figure 4.6. However there wasn't any noticeable difference in the magnitude of predictions using the modified dataset as shown in Figure 4.7 and considerable computational time was saved.

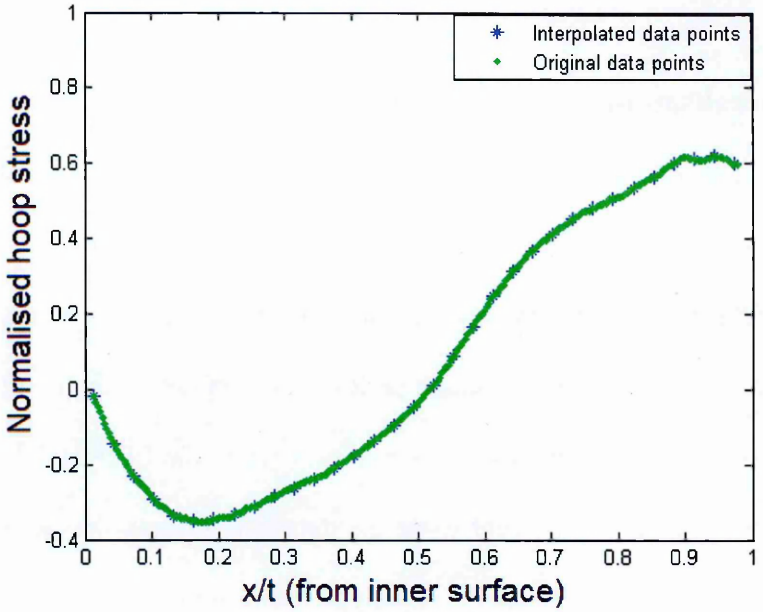

Figure 4.6. An illustration of the data reduction in DHD measurement points performed using the interpolation tool in MATLAB for mock-up S5Old.

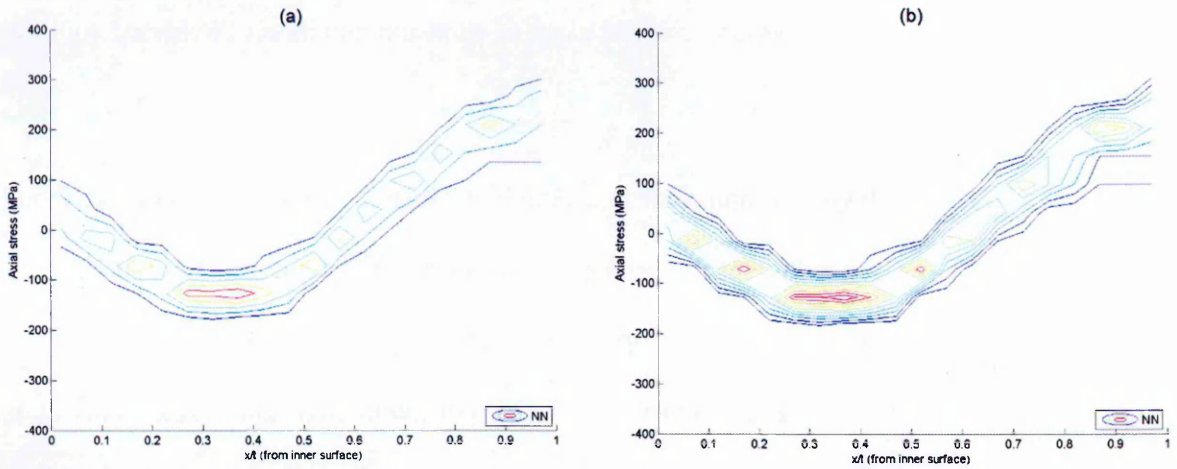

Figure 4.7. A comparison of the ANN predicted stress profiles using (a) raw data and (b) reduced data using interpolation tool for a low heat input pipe girth weld (MU4-1).

4.2.2 Generalisation

The generalisation ability is assessed based on the amount of information stored in the network. Good generalisation ability of the network is characterised by its ability to infer the underlying structure of the data rather than by any noise present. There is evidence to suggest that generalisation performance depends more on the magnitude of the weights [10]. ANNs sometimes perform poorly when the 'weights' are reported to have implausibly large values in order to fit the details in the training data. A simple way to implement regularisation is to use a weight decay term in the error function. A more sophisticated basis for regularisation can be found in the Bayesian evidence approach for training [169]. Instead of finding a unique value of the network weights and biases corresponding to the optimised value, the Bayesian technique marginalises over all possible combinations of the weights, assuming that the resulting weight matrix has a posterior probability distribution centered close to or at the maximum likelihood solution [170].

In fact, the Bayesian approach is a simple extension of the maximum likelihood model selection which embodies the principle of Occam's razor that states the importance of preferring simpler models over complex ones. This approach is particularly useful for network weight regularisation, optimisation of hyper-parameters and additionally it is possible to estimate confidence bounds on the output predictions [171]. Full implementation of the Bayesian technique requires the computation of the Hessian matrix (second order partial derivatives of the weight matrix) and was not included in the present work.

The generalisation ability of the output prediction was assessed by the Bayesian error function $E(w)$, which is defined by the sum of the squares error function and a term

that accounts for the weight matrix. The expression for $E(w)$ is given by the equation (3) as,

$$E(w) = \beta Es + \alpha E_R \qquad (3)$$

where β is the hyper parameter controlling the variance in noise, α is the hyper parameter controlling the weight decay or the regularisation coefficient

$$Es = \frac{1}{2}\sum_{i=1}^{R}\{x - o(p,w)\}^2 \qquad (4)$$

$$E_R = \frac{1}{2}\sum_{i=1}^{R}\left|wi\right|^2 \qquad (5)$$

and p is the input vector, w the weight vector, x the target value and o the output. Estimated values of α and β were used for the studies (More details of the neural network hyper-parameters can be found in appendix 1).

Bayesian methods offer a number of important features to the application of neural networks. They allow different models (e.g. networks with different numbers of hidden units) to be compared using only the training data. A Bayesian approach automatically penalizes highly complex models and helps to select the optimal model without resorting to the use of independent data for validation or 'cross-validation'. The regularisation term favours small values of network weights and biases thereby decreasing the susceptibility of the model to over-fit noise in the training data. The hyper-parameters are usually inferred from the data and largely influence the simplicity of the model. The use of over-complex models compared with simpler models is not justified according to the Bayesian approach [169, 170]. For minimizing the error for a particular weight vector, the effective value of the regularisation parameter depends strongly on the α/β ratio. This is because for a succession of training sets with number of patterns N, the first term E_S becomes more dominant with increasing N whilst the second term E_R is independent of N.

The network was trained using a Scaled Conjugate Gradient (SCG) training regime and a committee of networks was formed by running 250 independent training sessions starting at different randomly chosen points on the error surface. A range of networks was classified conforming to the minimum value of the error function and the histogram of the output distribution is presented as a contour plot. A histogram was mainly developed to manage scatter within the neural network predictions and to provide best estimate of the stresses. The 10% of predictions with lowest Bayesian error were determined from a committee of 250 networks and the histogram of output distribution was divided into 10 segments. Model predictions expressed as a contour plot generated from the histograms of network outputs are compared with other experimental measurements to assess the performance of the ANN. The histogram network was developed to improve the consistency of predictions as the training process starts at random points in the weight matrix and hence gives a different set of adapted weights and bias during convergence each time the model is run.

Residual stresses evidently exhibit a high degree of scatter especially in welds [104]; creating a sufficiently large committee of networks and determining the optimum network output using the error function is arguably an effective way of increasing confidence in model predictions. The histogram network can also provide a reliable prediction interval of the estimated stress distributions. This is considered to be a novel contribution in the field of application of neural networks and can serve the purpose of accounting for uncertainty in the predictions. A rigorous way to estimate uncertainty in the ANN predictions is to examine both the modelling and measurement uncertainty separately. The disadvantages of using such an approach is that as the modelling uncertainty is ideally calculated from the inverse Hessian of the weight matrix, there are computational difficulties due to the complexity involved and it is extremely time consuming. Moreover, the measurement uncertainty of the experimental technique is often

an estimated value and may not be necessarily accurate in most cases. The ANN prediction presented is intended to provide a decisive best estimate of stresses and is validated by comparing predictions with new experimental measurements at the WCL and HAZ locations in a range of welded pipes.

4.3 Validation of the ANN approach

Validation is an integral part of implementing ANN based approaches for any pattern recognition problem i.e. how well it can generalise or predict for a new set of data. The dataset used for validation should be ideally different from the training dataset but within the same process parameter space. ANNs are unable to extrapolate into new regions of the input data space. Their generalisation ability is usually assessed based on the performance in predicting validation data.

4.3.1 Validation using weld centre line measurement data

The WCL experimental data used to train and validate the ANN are summarized in Table 4.3. Residual stresses were performed along both axial and hoop directions. The reason for not including radial stresses is because they are usually of low magnitude in pipe girth welds and are rarely considered in defect tolerance assessments of conventional welds.

Table 4.3. WCL experimental data used for training and validation of the ANN.

	Mock-ups	Net heat input kJ/mm	R/t	t (mm)	Yield stress (p,w) (MPa)	Experimental measurements
Training						
1	Weld C	2.2	25	15.9	338, 476	BRSL
2	SP19	1.12	10.5	19.6	272, 446	Neutron
3	SP37	1.76	5.3	37	328, 446	DHD
4	S5VOR	1.92	2.8	65	328, 446	DHD
5	S5Old	1.12	2.8	65	328, 446	DHD
6	S5New	0.8	2.8	65	328, 446	DHD
7	S5NG	1.32	3.0	62	328, 446	DHD
8	RR	1.8	1.8	110	274, 483	DHD
Validation						
1	MU4-1	0.8	4.5	25	290, 450	Neutron, Contour
2	MU4-3	1.5	4.5	25	290, 450	Neutron, Contour
3	Esshete	1.6	2.1	35	370, 564	Contour

*where p, w are the parent and weld material yield strength at 1% proof stress.

Residual stress measurements made in the validation mock-ups are discussed in Chapter 3 (sections 3.3 and 3.4). The ANN prediction for residual stresses in the axial direction of MU4-1 (low heat input mock up) is compared with neutron measurements and Incremental Deep Hole Drilling (performed at the University of Bristol) in Figure 4.8. The agreement between neutron measurements and the model prediction is promising considering the wide scatter observed in the data. IDHD compressive stresses of about 300 MPa at x/t < 0.3 are outside the ANN predicted region. In general, the ANN best estimate stresses match well with the neutron measurements but not the IDHD measurements.

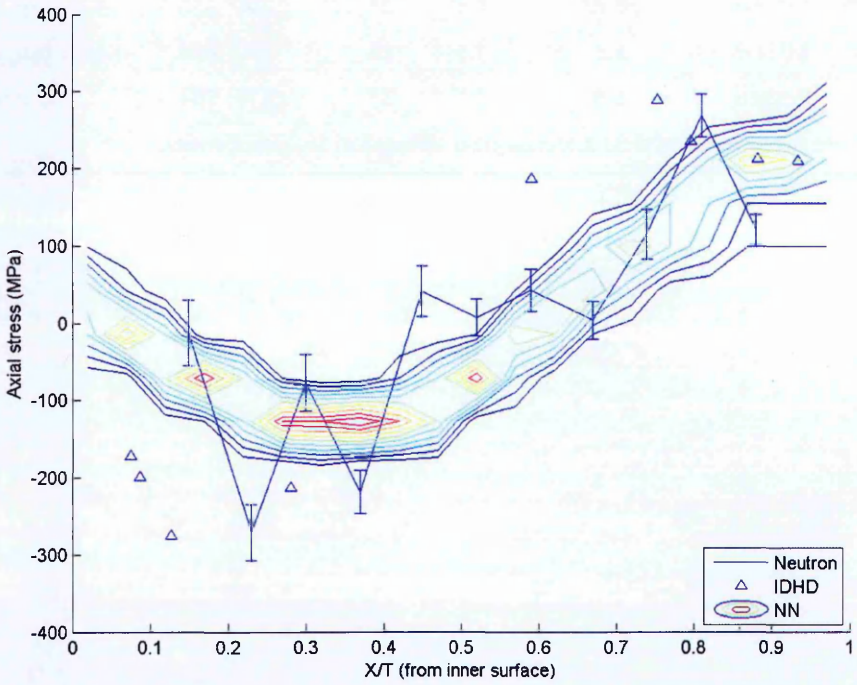

Figure 4.8. ANN model prediction of axial stress distribution of the STYLE pipe butt weld MU4-1 at the WCL (Input parameters: R/t = 4.5, t = 25 mm and Q = 0.8 kJ/mm).

The ANN prediction for hoop stresses at the WCL is compared with validation measurements made by neutron diffraction, IDHD and the contour method, for both the top and bottom of the pipe as shown in Figure 4.9. Agreement between the neutron and contour experimental measurements is excellent but some mismatch is seen with IDHD measurements in the through wall position (x/t) = 0.2 - 0.7. However, the ANN prediction is substantially more tensile towards the inner surface of the pipe and a disagreement of about 400 MPa is observed at x/t = 0.2. This is explained as follows, compressive hoop stresses of the level measured in MU4-1 (more than 500 MPa) are not evident in any of the training data. The presence of high compressive stresses near the inside surface is likely to be the result of the specific weld procedure employed for MU4-1 and MU4-3 (with a wide weld preparation and backing plate). Despite this the ANN is in favourable agreement with the measurements from mid thickness to the outer radius position, and at all positions over-predicts the tensile magnitude of stresses.

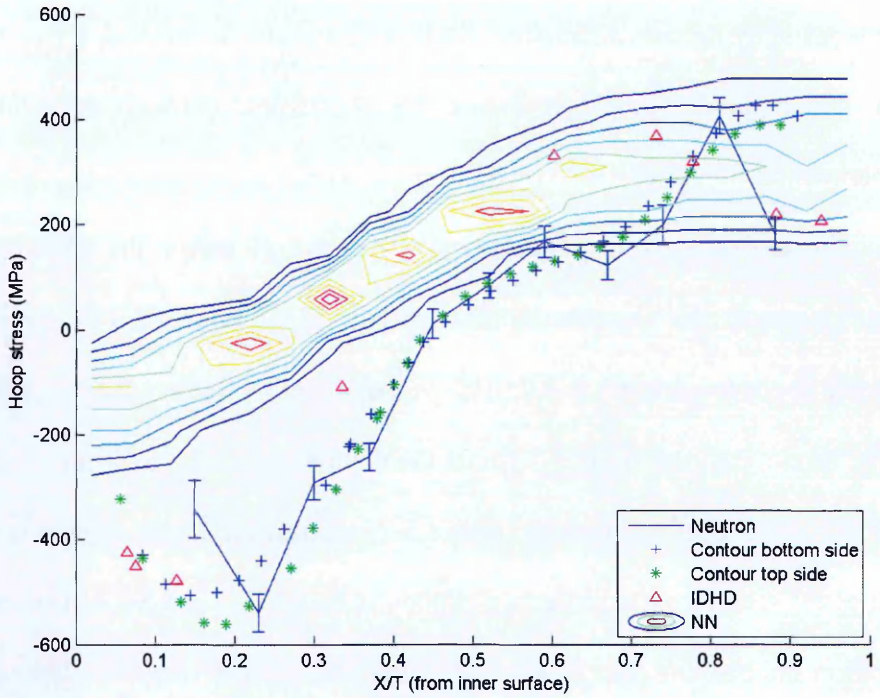

Figure 4.9. ANN model prediction of hoop stress distribution of the STYLE pipe butt weld MU4-1 at the WCL (Input parameters: R/t = 4.5, t = 25 mm and Q = 0.8 kJ/mm).

Predicted and measured axial residual stress profiles for MU4-3 are illustrated in Figure 4.10. The ANN histogram map is compared with the neutron measurements in the axial direction where reasonable agreement is seen up to the through-wall position x/t = 0.7. However the disagreement of more than 200 MPa is observed from x/t > 0.7 approaching the outer surface. The hoop stress measurements (see Figure 4.11) deviate from the ANN map for (x/t) < 0.3 in the same manner as MU4-1; this is to be expected because the pipe was welded in the same way. The hoop stress measurements near the outer surface (x/t) > 0.7 are noticeably lower than the contour measurements which closely follow the ANN predictions. A similar trend is observed in the axial stress measurements approaching the outer radius of the weld. The lower magnitude of axial and hoop stresses measured by neutron diffraction for (x/t) > 0.7 may be associated with uncertainties in the stress-free lattice parameter measurements for austenitic weld metal. But the consistency of

the neural network predictions is verified by the contour method measurements of both top and bottom cut surface carried out in the hoop direction (see Figure 4.11).

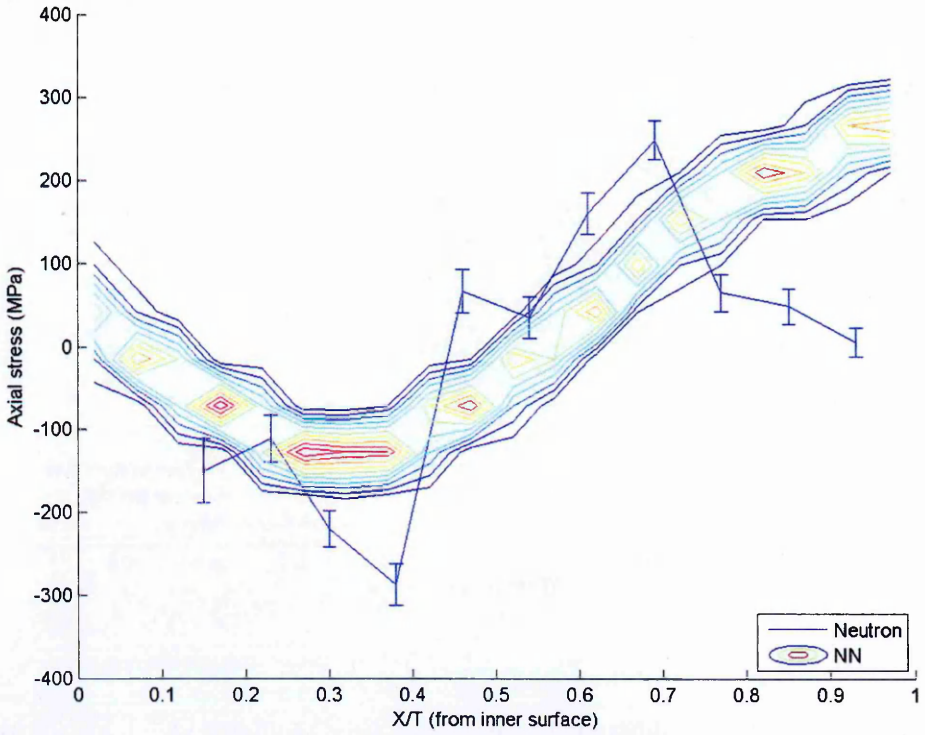

Figure 4.10. ANN model prediction of axial stress distribution of the STYLE pipe butt weld MU4-3 at the WCL (Input parameters R/t = 4.5, t = 25 mm and Q = 1.5 kJ/mm).

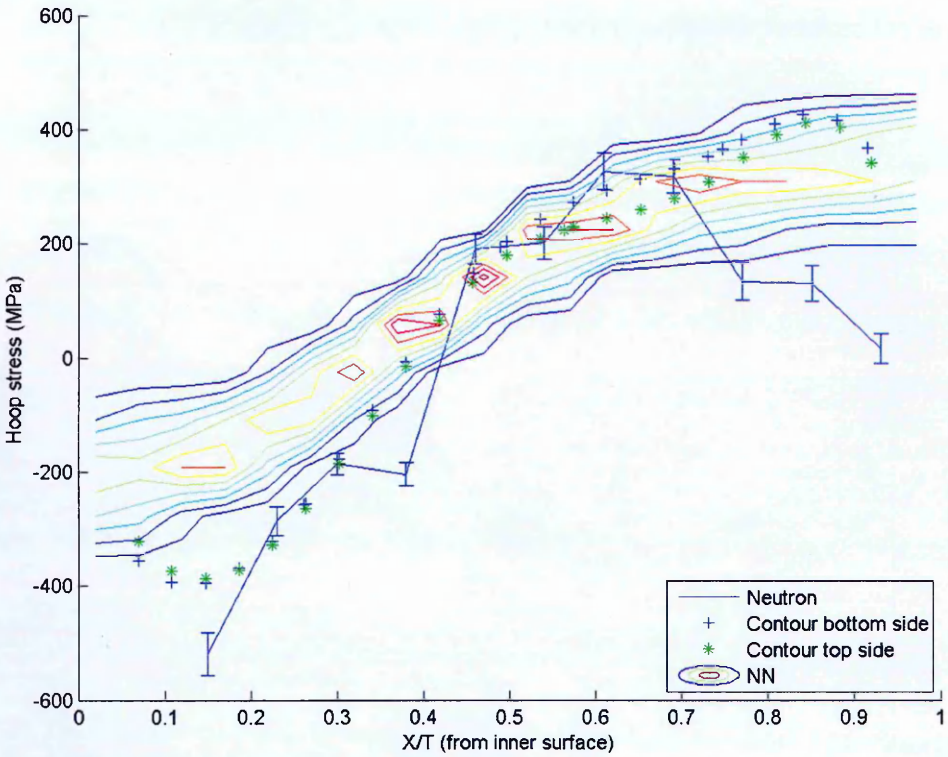

Figure 4.11. ANN model prediction of hoop stress distribution of the STYLE pipe butt weld MU4-3 at the WCL (Input parameters R/t = 4.5, t = 25 mm and Q = 1.5 kJ/mm).

In Figure 4.12, the ANN prediction for the Esshete pipe is compared with the contour method measurements done at the WCL. A map of axial stress distribution at the WCL was obtained and the lines profiles were extracted at 36°, 90°and 144°, and an averaged profile (see section 3.4.2). The predicted stress profile matches well with the contour method measurements up to through wall position (x/t) = 0.8. The measured stress profiles then falls into a state of compression approaching the outside diameter. However, the model prediction was seen to continue with a slightly higher magnitude of tensile stresses and the disparity is clearly seen at the through thickness positions close to the outer surface. This inability to follow the measured stress profile close to the outer surface is considered to be a major limitation of the ANN approach and the mismatch in predicted and measured stress distribution close to the outer surface is likely to be associated with a lower density of surface measurement data used to train the ANN.

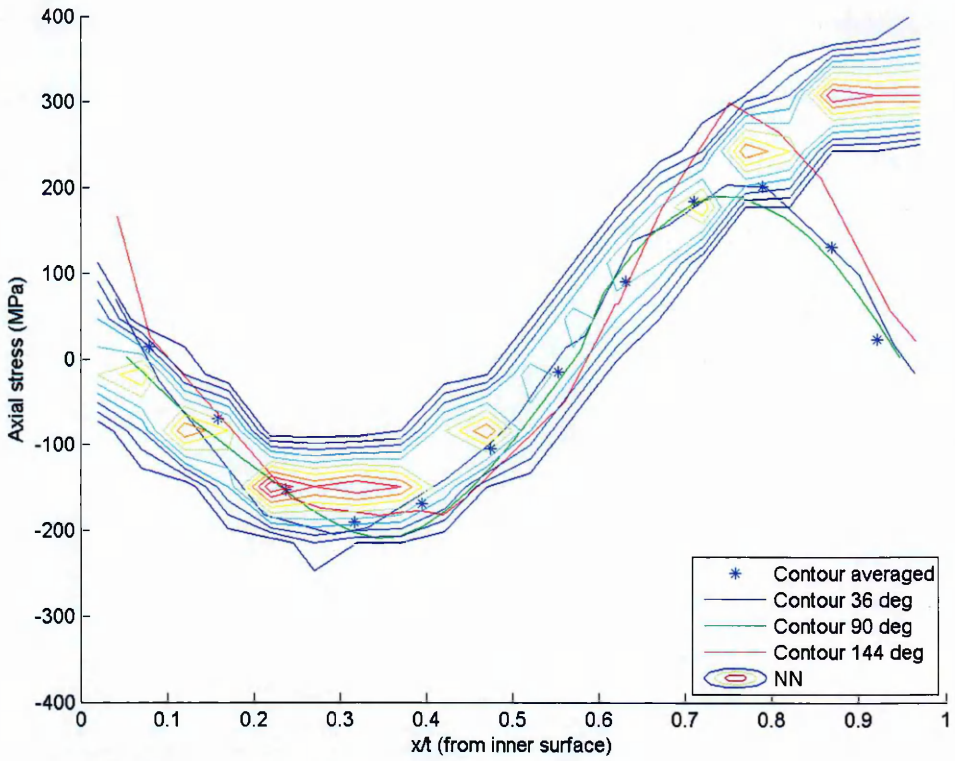

Figure 4.12. ANN model prediction of axial stress distribution of the Esshete pipe butt weld at the weld centre line (Input parameters R/t = 2.1, t = 35 mm and Q = 1.6 kJ/mm).

Additionally the hoop stress profiles predicted by the ANN approach for the Esshete mock-up are in good agreement with the measurements made using the contour method (see Figure 4.13). The ANN model slightly over predicted the stresses close to the inside surface and also the region near the outside surface but the mismatch observed is not more than 200 MPa.

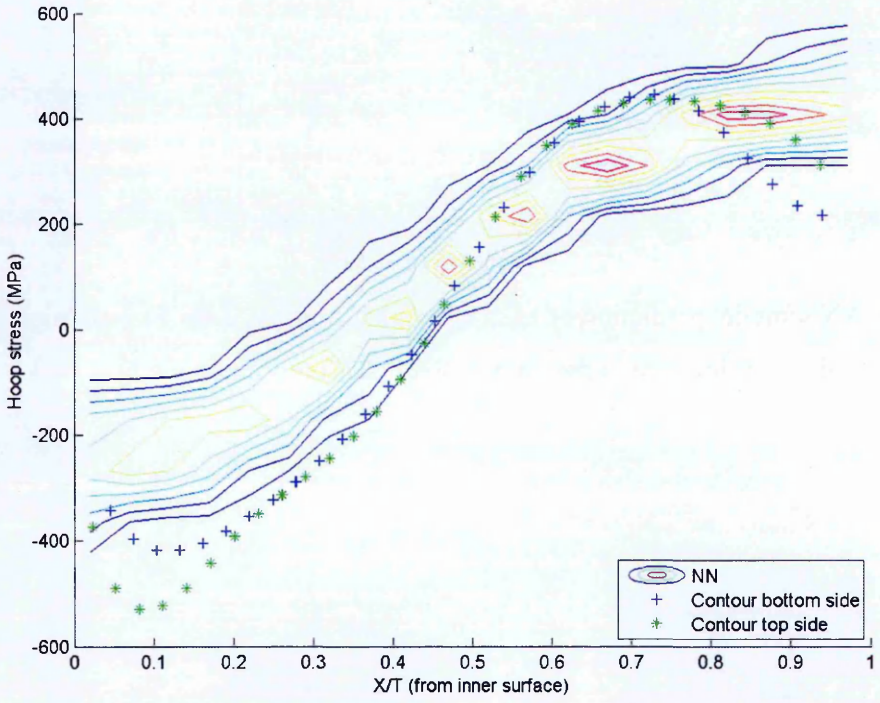

Figure 4.13. ANN model prediction of hoop stress distribution of the Esshete pipe butt weld at the weld centre line (Input parameters R/t = 2.1, t = 35 mm and Q = 1.6 kJ/mm).

4.3.2 Validation using heat affected zone measurement data

The HAZ experimental data used to train and validate the ANN are summarized in Table 4.4. Residual stress measurements were performed along both axial and hoop directions. The details of only six mock-ups were included in the training dataset for HAZ profiles compared to eight for the WCL dataset.

Table 4.4. Process parameter envelope of training data in heat affected zone.

	Mock-ups	Net heat input kJ/mm	R/t	t (mm)	Yield stress (p,w) (MPa)	Experimental measurements
Training						
1	SP19	1.12	10.5	19.6	272, 446	Neutron
2	OU20	1.36	3.8	20	264, 446	Neutron
3	SP37	1.76	5.3	37	328, 446	DHD
4	S5VOR	1.92	2.8	65	328, 446	DHD
5	S5New	0.8	2.8	65	328, 446	DHD
6	S5NG	1.32	3.0	62	328, 446	DHD
Validation						
1	MU4-1	0.8	4.5	25	290, 450	Neutron, Contour
2	MU4-3	1.5	4.5	25	290, 450	Neutron, Contour
3	Esshete	1.6	2.1	35	370, 564	Contour

*where p, w are the parent and weld material yield strength at 1% proof stress.

ANN model prediction of the axial stress distribution in the MU4-1 HAZ (low heat input mock up) is compared with the neutron measurements in Figure 4.14. Very good agreement was seen in the measured and modelled stresses with the exception of the region close to the inside diameter. Only two neutron measurements points were found outside of the ANN prediction band. Note, the WCL profile for the same mock-up was also found to be in good agreement with the ANN prediction (see Figure 4.8). However, the overall pattern of through-thickness stress profiles predicted by the ANN in the HAZ was quite different from the WCL profile. This shows that the ANN predicted region varies depending upon the training data used and is able to capture the underlying pattern.

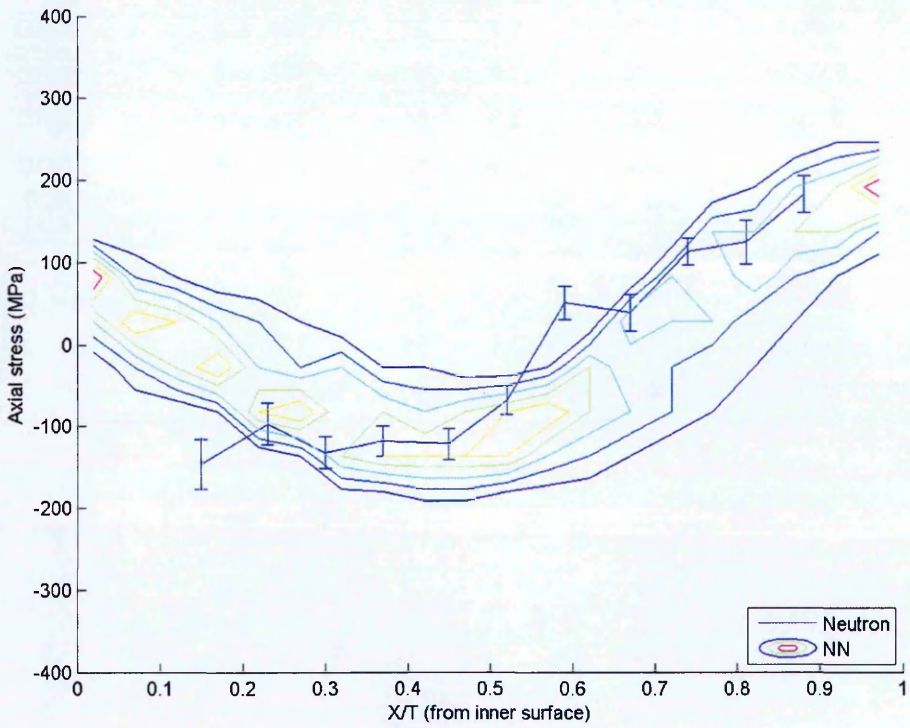

Figure 4.14. ANN model prediction of the axial stress distribution in the STYLE pipe butt weld MU4-1 at the HAZ (Input parameters R/t = 4.5, t = 25 mm and Q = 0.8 kJ/mm).

In the hoop direction (see Figure 4.15), the comparison between the contour method measurements and the ANN prediction for STYLE MU4-1 shows a mismatch of more than 200 MPa. But the neutron measurements agree well with the ANN prediction at

all the through thickness locations. The spread of the ANN prediction was significantly higher than previous results (of the order of 200 MPa or more) and is believed to be the result of insufficient training data in the HAZ location where only the data points from six mock-ups were used compared with eight for the WCL.

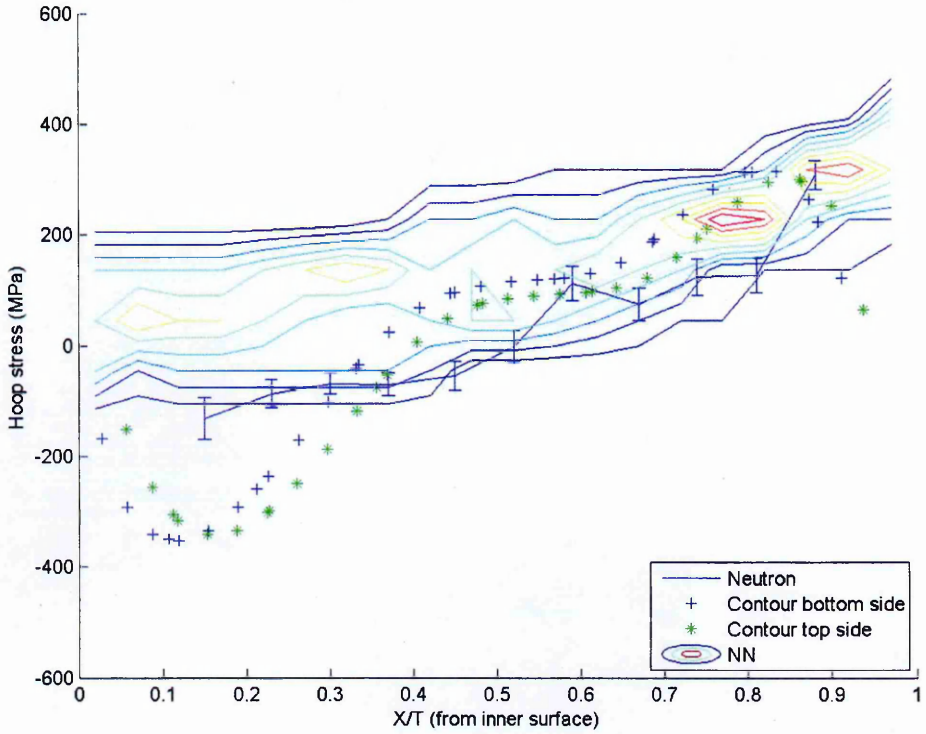

Figure 4.15. ANN model prediction of hoop stress distribution of the STYLE pipe butt weld MU4-1 at the HAZ (Input parameters R/t = 4.5, t = 25 mm and Q = 0.8 kJ/mm).

The model prediction comparison with neutron measurements described in section 3.3.2 for the axial direction of the MU4-3 mock up (see Figure 4.16) shows under-prediction of the stresses at many points in the through thickness range (x/t) = 0.4 - 0.8 by a margin of more than 100 MPa. Despite the difference, the ANN prediction closely follows the pattern observed in the neutron measurements. This is one of the rare cases where the ANN has under-predicted the stresses continuously for three or more points in the through-thickness direction.

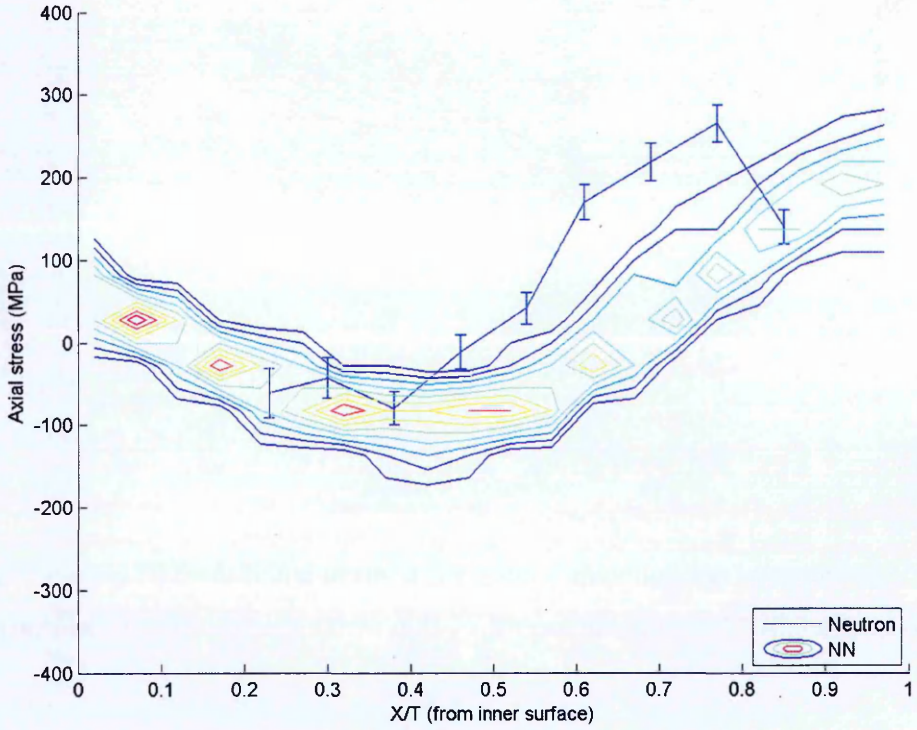

Figure 4.16. ANN model prediction of axial stress distribution of the STYLE pipe butt weld MU4-3 at the HAZ (Input parameters R/t = 4.5, t = 25 mm and Q = 1.5 kJ/mm).

In the case of the hoop stress profile (see Figure 4.17) the ANN prediction was found to be consistent with the measured stresses using the contour method. The neutron measurements infer the presence of higher stresses at through wall position (x/t) = 0.6 - 0.8 what is suspected to be an issue with the stress free reference measurement as this was also observed in the axial stress distribution in Figure 4.16 (see section 3.3.2).

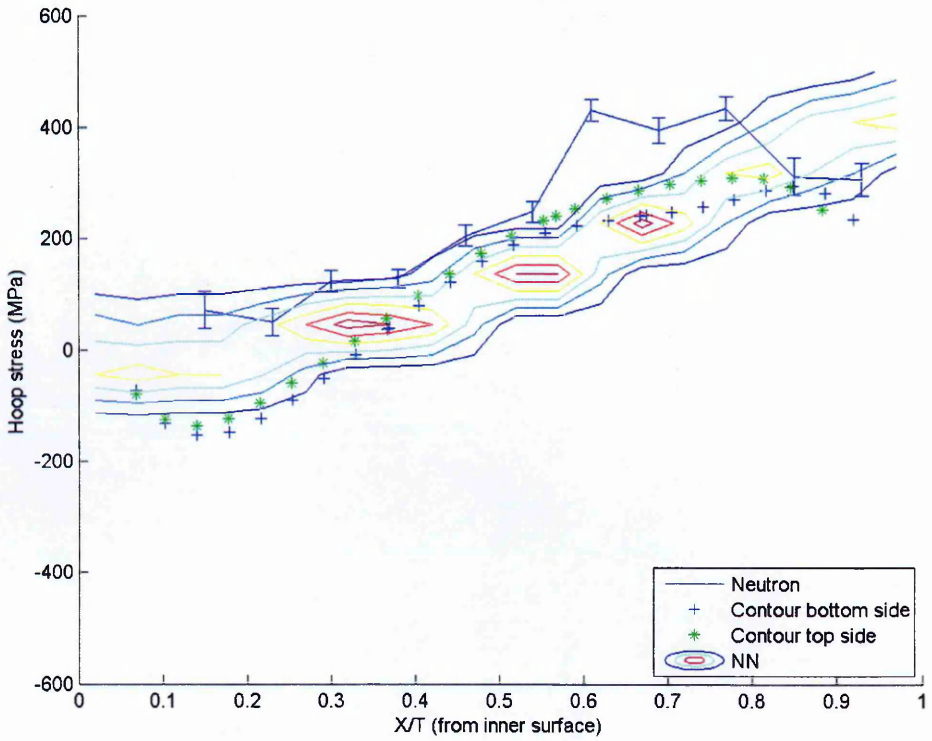

Figure 4.17. ANN model prediction of hoop stress distribution of the STYLE pipe butt weld MU4-3 at the HAZ (Input parameters R/t = 4.5, t = 25 mm and Q = 1.5 kJ/mm).

The ANN model prediction is in favourable agreement with contour measurements performed in the hoop direction for the Esshete pipe weld (see Figure 4.18). The agreement is especially good up to the through thickness range (x/t) < 0.8 and thereafter the stresses characterised using the contour method indicates a decrease approaching the outside diameter in both top and bottom cut faces. However, the ANN prediction fails to capture this decrease where a maximum difference of about 300 MPa was observed at the surface. This could be due to inadequate training data as pointed out earlier for the HAZ profiles.

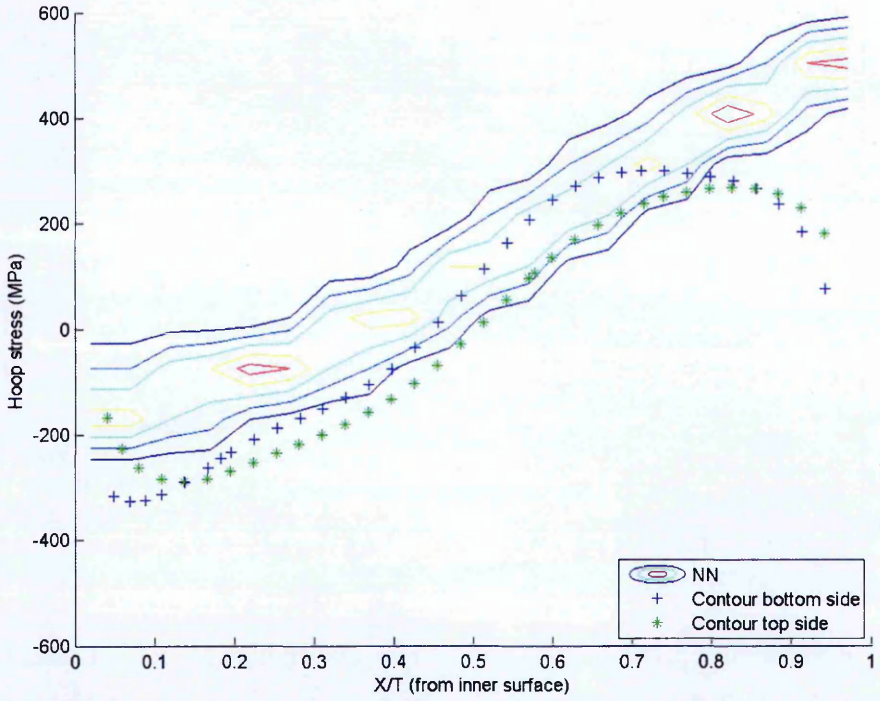

Figure 4.18. ANN model prediction of hoop stress distribution of the Esshete pipe butt weld at the HAZ (Input parameters R/t = 2.1, t = 35 mm and Q = 1.6 kJ/mm).

4.4 Sensitivity studies of input variables used in the model

The sensitivity studies presented here are mainly intended to demonstrate the robustness of the ANN approach by considering input parameters at the boundaries of the training dataset. Since the test data need to be essentially independent of the training data, input parameters resembling three hypothetical pipe welds (H1, H2 and H3) were considered for this study. For the sake of understanding, it is assumed that pipe welds having the same geometry made using the same welding parameters will have same residual stress profiles. However, this may not be the case in actual scenarios and the motivation here to evaluate the predictive capacity of the ANN and to understand how biased the end results can be depending on the chosen points in the process parameter space. Three hypothetical mock-ups and their representation in the existing process parameter space of WCL training data are shown in Figure 4.19.

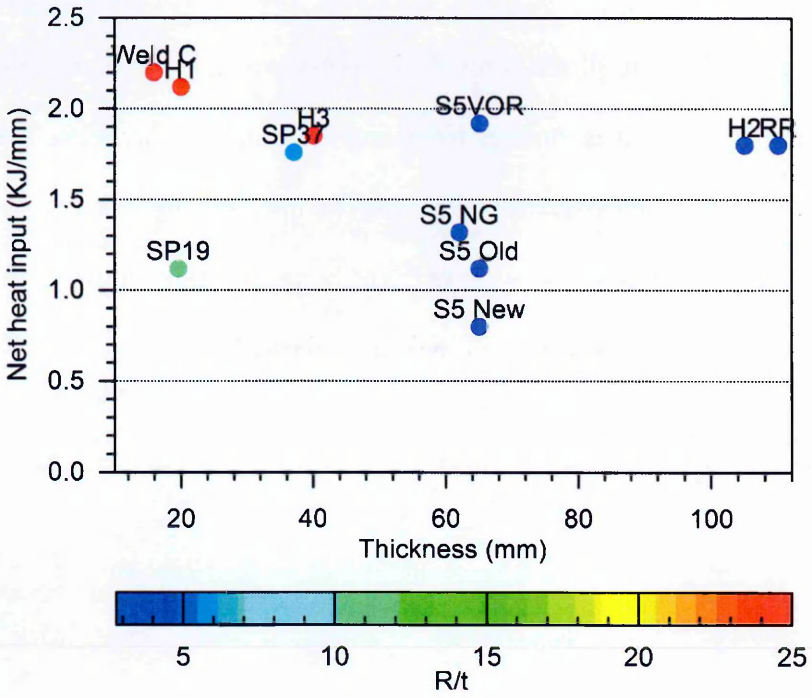

Figure 4.19. Process parameter space of WCL training data used for sensitivity studies. Hypothetical pipe welds denoted as H1 (Input parameters R/t = 24, t = 20 mm and Q = 2.12 kJ/mm), H2 (Input parameters R/t = 3, t = 105 mm and Q = 1.8 kJ/mm) and H3 (Input parameters R/t = 25, t = 40 mm and Q = 1.85 kJ/mm).

4.4.1 Effect of Heat input (Q)

To study the effect of heat input in the ANN prediction, a hypothetical pipe weld (H1) having very similar input parameters of mock up Weld C was considered. The reason for choosing the mock up resembling Weld C is because it had the maximum heat input in the WCL data set used for training. Moreover, the hoop stress distribution determined using the BRSL technique was very different from what was observed in other mock ups. A tensile stress close to the yield strength of the material was reported in Weld C. Presumably, the ANN predictions in the validation dataset didn't have an identical stress distribution as Weld C probably because the heat input used for welding the pipes was not as high. The predicted stresses using ANN for the hypothetical pipe weld (H1) are presented in Figure 4.21. The region of prediction is wide near the inner surface where there are inadequate data reported for training and the input parameters of H1 lie just within the boundaries of the process parameter space. The ANN prediction closely matches the BRSL measurements at all the through thickness positions. It is pleasing to see the predicted band of best estimate stresses following the nature of the BRSL measurements. Even though the BRSL measurements themselves may not be accurate as they were performed several years back and nowadays the technique is rarely in use, there is no better example to demonstrate the robustness of the ANN approach.

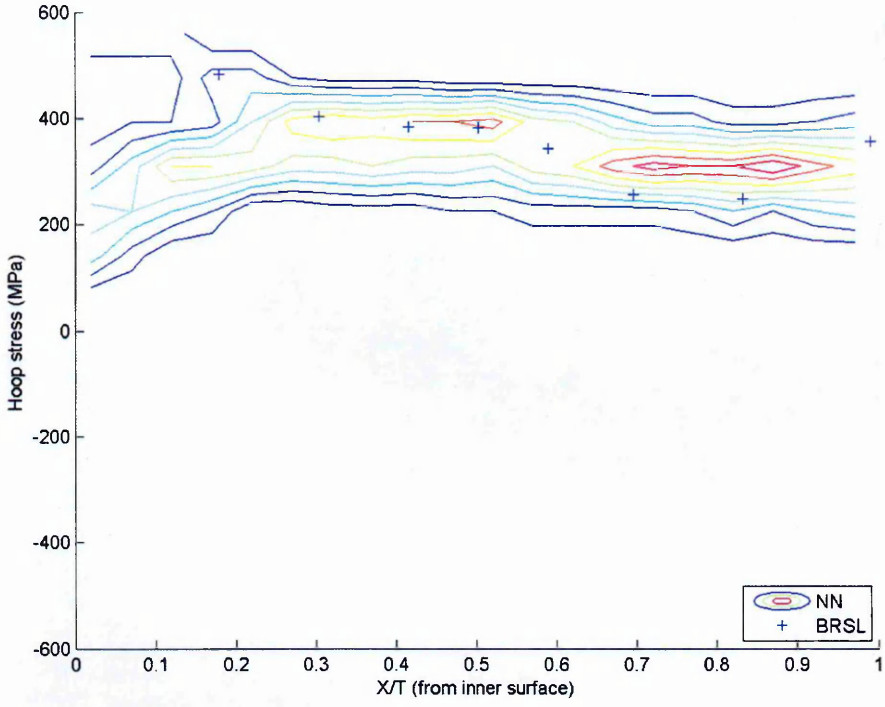

Figure 4.20. Sensitivity studies on the effect of heat input in the model prediction of hoop stress distribution of the Hypothetical pipe weld (H1) at the WCL (Input parameters R/t = 24, t = 20 mm and Q = 2.12 kJ/mm).

4.4.2 Effect of thickness (t)

The effect of thickness on the resulting best estimate stresses predicted by the ANN is demonstrated by considering a hypothetical pipe weld (H2) that has very similar characteristics to mock up RR. This mock-up was chosen as it was 110 mm thick and distant from other mock ups with respect to the thickness parameter in the training dataset. The predicted stress profile is shown in Figure 4.21 where a strong bias was seen to occur to the stress profile of the RR mock up. The flat region of the predicted best estimate stresses in the through wall thickness range (x/t) = 0 - 0.4 is a characteristic feature of the RR mock up and is clearly seen in the predicted data.

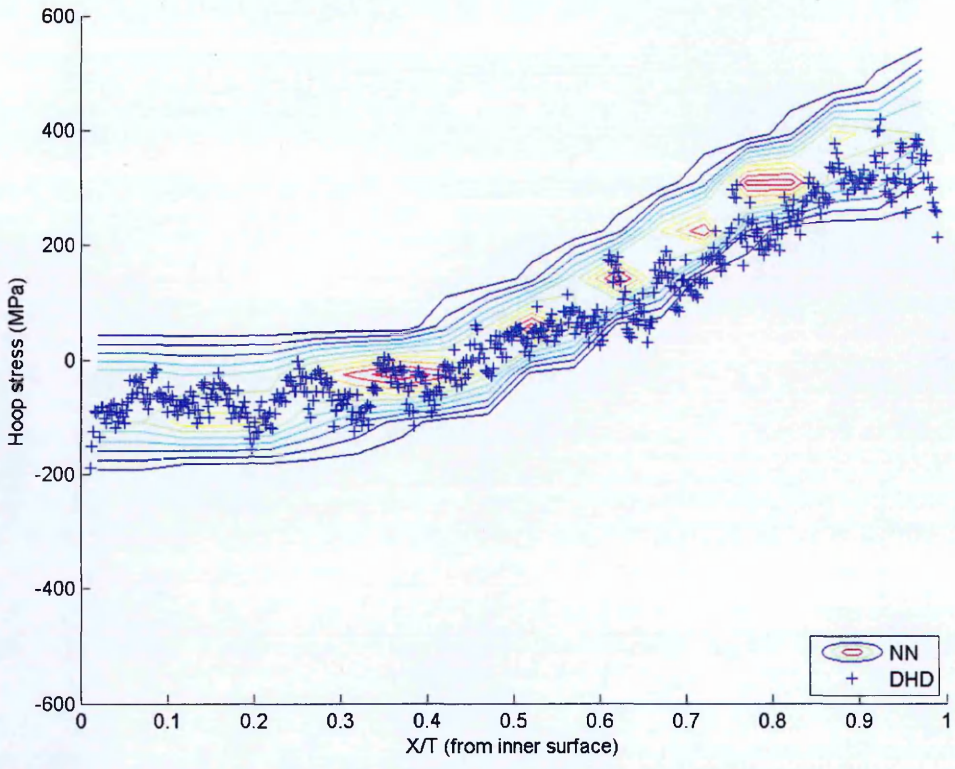

Figure 4.21. Sensitivity studies on the effect of thickness in the model distribution of hoop stress distribution the Hypothetical pipe weld (H2) at the WCL (Input parameters R/t = 3, t = 105 mm and Q = 1.8 kJ/mm).

4.4.3 Effect of R/t ratio

The effect of R/t ratio is illustrated in Figure 4.22. For demonstrating the robustness of the developed approach, a hypothetical pipe weld (H3) resembling Weld C considered as it had the highest value of R/t. The other parameters were however somewhat different. Despite this the predicted output is strongly biased to the stress profile reported in Weld C. However the scatter of the predicted output is much higher compared to Figure 4.15 and is arguably because of the difference in the other input parameters. Therefore it can be seen that the predicted results have a strong bias to the training data particularly with identical input parameters and are highly data dependent. These studies are particularly useful in understanding the efficacy of the developed ANN approach.

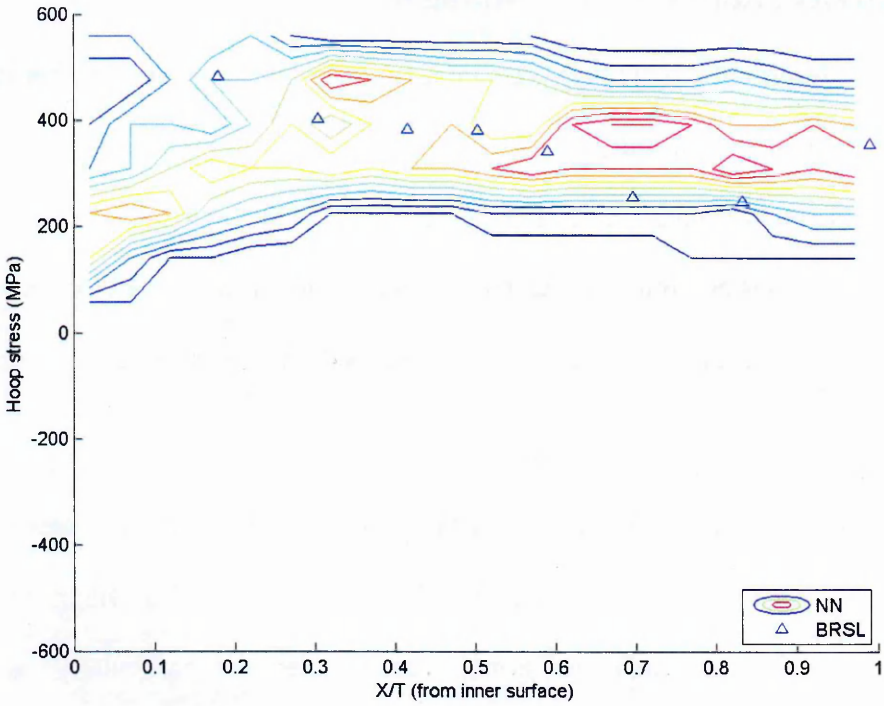

Figure 4.22. Sensitivity studies on the effect of R/t in the model distribution of hoop stress distribution of the Hypothetical pipe weld (H3) at the WCL (Input parameters R/t = 25, t = 40 mm and Q = 1.85 kJ/mm).

4.5 Sensitivity studies in the training data

The sensitivity studies presented here were undertaken mainly to verify whether the ANN prediction can improve with addition of new experimental data in the training dataset. The database of experimental measurements is expected to grow in future and the full potential of the ANN approach can only be realised if studies can show that the predictions can improve with more measurement data included in training. To evaluate this, studies are performed in three levels.

1. The effect of adding new training data within and outside the process parameter space is examined. Although it is well-known that the ANNs cannot extrapolate outside the input parameter space, these studies are particularly useful for understanding their limitations.
2. The stress profiles of all mock-ups in the hoop direction at the WCL and HAZ are re-evaluated with the addition of acquired data from the half inch thick pipes (low and high), and compared with the old predictions discussed in section 4.3.1
3. All the measured data i.e. for training and validation are used extensively for training with the exclusion of the data for which the output is generated. These studies were used to compare stress profiles in MU4-1, MU4-3 and Esshete mock-ups along the hoop direction in the WCL locations. Additionally, the data used for training the ANN initially were swapped with the validation data and the stress profiles in mock-ups SP37, S5Old, S5New and S5VOR are simulated.

4.5.1 Training with additional measurements in half inch thick pipes

The modified WCL experimental data used to train and validate the ANN are summarized in Table 4.5.

Table 4.5. Modified process parameter envelope of training data in weld centre line.

	Mock-ups	Net heat input kJ/mm	R/t	t (mm)	Yield stress (p,w) (MPa)	Experimental measurements
Training						
1	Weld C	2.2	25	15.9	338, 476	BRSL
2	SP19	1.12	10.5	19.6	272, 446	Neutron
3	SP37	1.76	5.3	37	328, 446	DHD
4	S5VOR	1.92	2.8	65	328, 446	DHD
5	S5Old	1.12	2.8	65	328, 446	DHD
6	S5New	0.8	2.8	65	328, 446	DHD
7	S5NG	1.32	3.0	62	328, 446	DHD
8	RR	1.8	1.8	110	274, 483	DHD
9	Low	0.7	10	12.7	320, 450	Contour
10	High	1.2	10	12.7	320, 450	Contour
Validation						
1	MU4-1	0.8	4.5	25	290, 450	Neutron, Contour
2	MU4-3	1.5	4.5	25	290, 450	Neutron, Contour
3	Esshete	1.6	2.1	35	370, 564	Contour
4	Med	1.0	10	12.7	320, 450	Contour

*where p, w are the parent and weld material yield strength at 1% proof stress.

The model prediction of hoop stress for the medium heat input pipe using the initial training dataset, without including the low and high heat input pipes (Table 4.3) is compared with the predictions using the modified training data given in Table 4.5. Figure 4.23 (a) shows the poor performance of ANN in predicting the stress profile without having been trained with the stress profiles in pipes of that geometry. On the other hand, the predicted stresses in the hoop direction of the medium heat input pipe (see Figure 4.23 (b)) are in good agreement with the contour measurements at the top and bottom surfaces. The ANN marginally under-predicts the stresses at some points in the range (x/t) = 0.6 - 0.8.

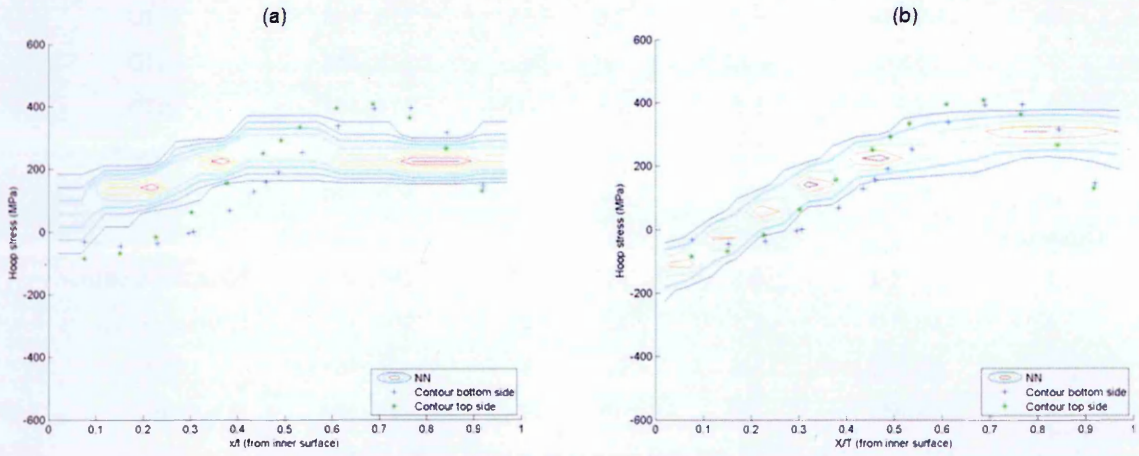

Figure 4.23. ANN model prediction of hoop stress distribution of the medium heat input pipe butt weld at the WCL (Input parameters R/t = 10, t =12.7 mm and Q = 1.0 kJ/mm) using (a) Initial training data given in Table 4.3 and (b) Modified training data given in Table 4.5.

The model prediction of the hoop stress distribution in the HAZ location of the medium heat input girth weld using the different training datasets are compared with the contour measurement at the top and bottom cut surface in Figure 4.24. Both model predictions in (a) and (b) showed good agreement with the measurements for most of the through thickness positions. It is worth noting that the magnitude of stresses were not very high (< 200MPa) and the difference in model predictions illustrating the learning

capabilities of the ANN was not effectively identified. The only drawback of the model prediction is the inability to follow the contour method measurements approaching the outer surface.

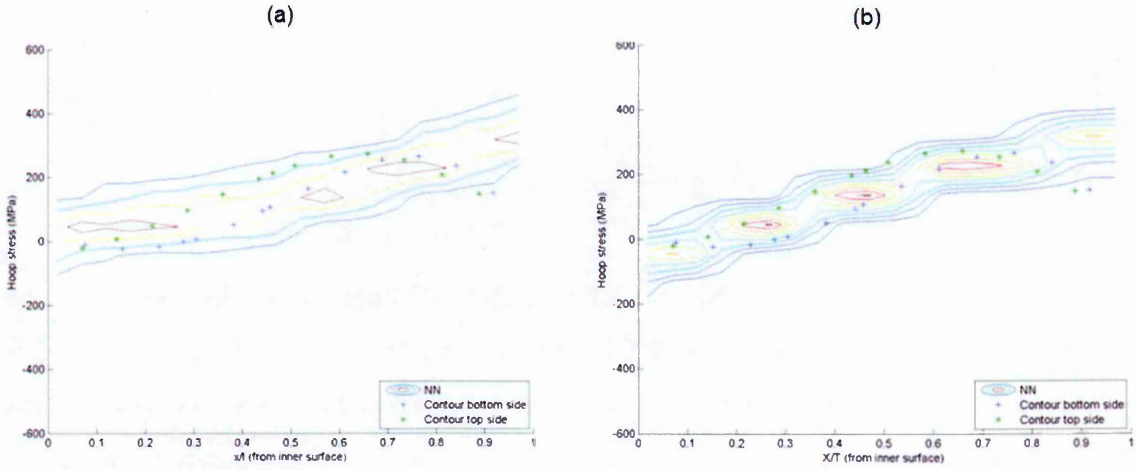

Figure 4.24. ANN model prediction of axial stress distribution of the medium heat input pipe butt weld at the HAZ (Input parameters R/t = 4.5, t = 25 mm and Q = 1.5 kJ/mm) using (a) Initial training data given in Table 4.4 and (b) Modified training data given in Table 4.6.

The comparison of the ANN prediction for the MU4-1 using the initial set of training data (Table 4.3) and the new set with the measurement data of low and high heat input mock-ups (see Table 4.5) is illustrated in Figure 4.25. There was a noticeable difference found in the predicted stresses where the spread of the prediction band was seen to narrow down with the addition of the new set of data. The same phenomenon repeated in the high heat input mock-up MU4-3 (Figure 4.26) with minor differences in the peak tensile and compressive stresses. This was again consistently observed in the predicted stresses of the Esshete mock-up (see Figure 4.27). In general, the ANN predictions were not found to improve with the addition of new WCL data.

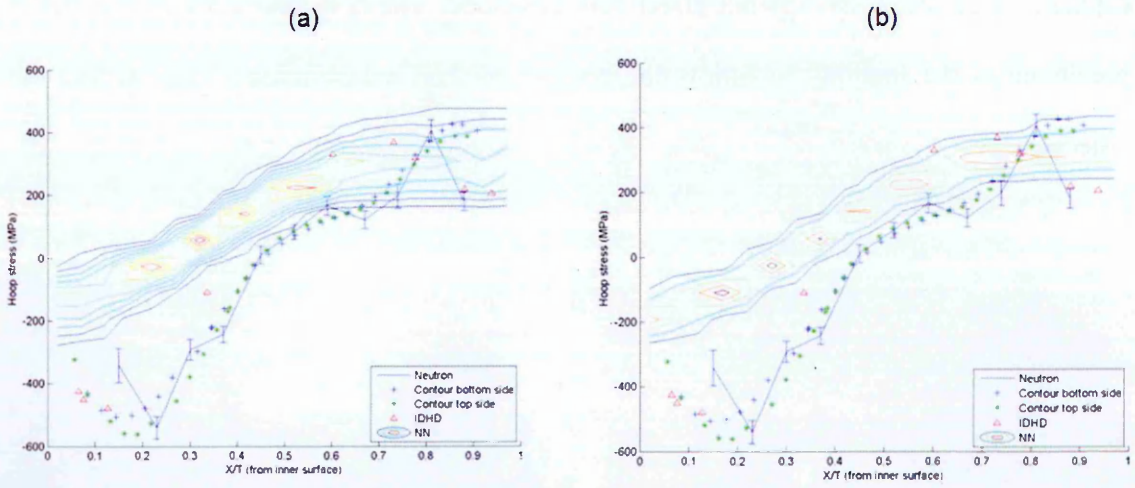

Figure 4.25. Comparison of ANN model prediction of hoop stress distribution in the STYLE pipe butt weld MU4-1 at the WCL (Input parameters R/t = 4.5, t = 25 mm and Q = 0.8 kJ/mm) using (a) Initial training data given in Table 4.3 and (b) Modified training data given in Table 4.5.

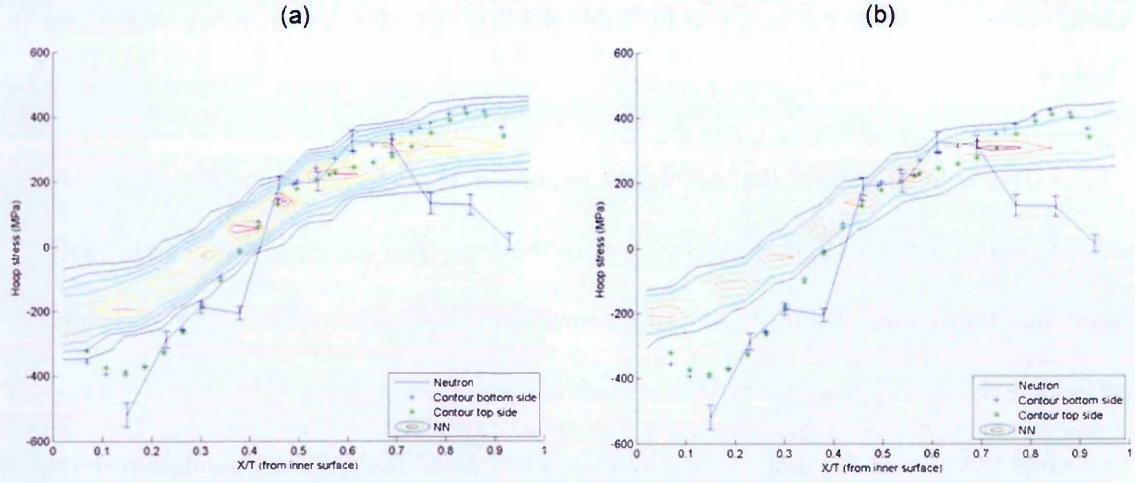

Figure 4.26. Comparison of ANN model prediction of hoop stress distribution in the STYLE pipe butt weld MU4-3 at the WCL (Input parameters R/t = 4.5, t = 25 mm and Q = 1.5 kJ/mm) using (a) Initial training data given in Table 4.3 and (b) Modified training data given in Table 4.5.

capabilities of the ANN was not effectively identified. The only drawback of the model prediction is the inability to follow the contour method measurements approaching the outer surface.

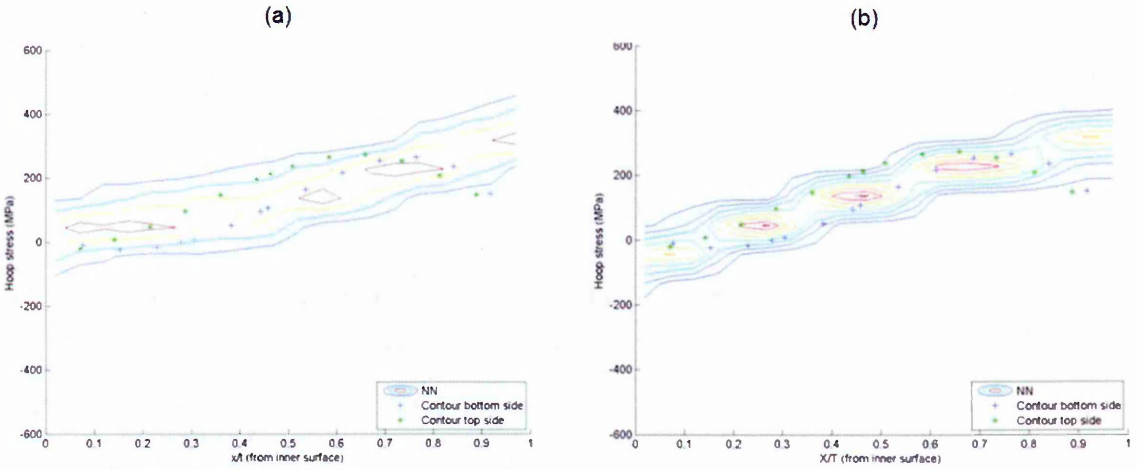

Figure 4.24. ANN model prediction of axial stress distribution of the medium heat input pipe butt weld at the HAZ (Input parameters R/t = 4.5, t = 25 mm and Q = 1.5 kJ/mm) using (a) Initial training data given in Table 4.4 and (b) Modified training data given in Table 4.6.

The comparison of the ANN prediction for the MU4-1 using the initial set of training data (Table 4.3) and the new set with the measurement data of low and high heat input mock-ups (see Table 4.5) is illustrated in Figure 4.25. There was a noticeable difference found in the predicted stresses where the spread of the prediction band was seen to narrow down with the addition of the new set of data. The same phenomenon repeated in the high heat input mock-up MU4-3 (Figure 4.26) with minor differences in the peak tensile and compressive stresses. This was again consistently observed in the predicted stresses of the Esshete mock-up (see Figure 4.27). In general, the ANN predictions were not found to improve with the addition of new WCL data.

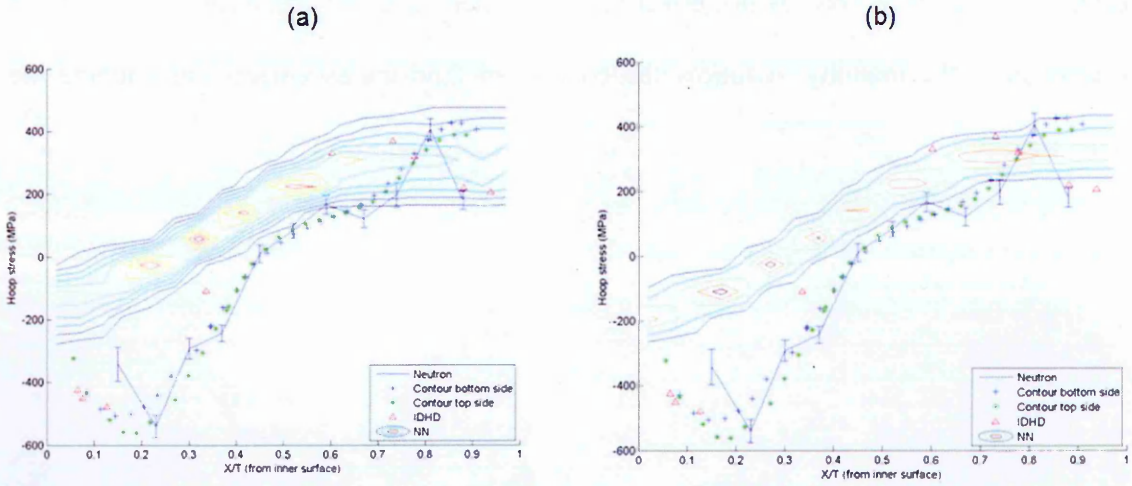

Figure 4.25. Comparison of ANN model prediction of hoop stress distribution in the STYLE pipe butt weld MU4-1 at the WCL (Input parameters R/t = 4.5, t = 25 mm and Q = 0.8 kJ/mm) using (a) Initial training data given in Table 4.3 and (b) Modified training data given in Table 4.5.

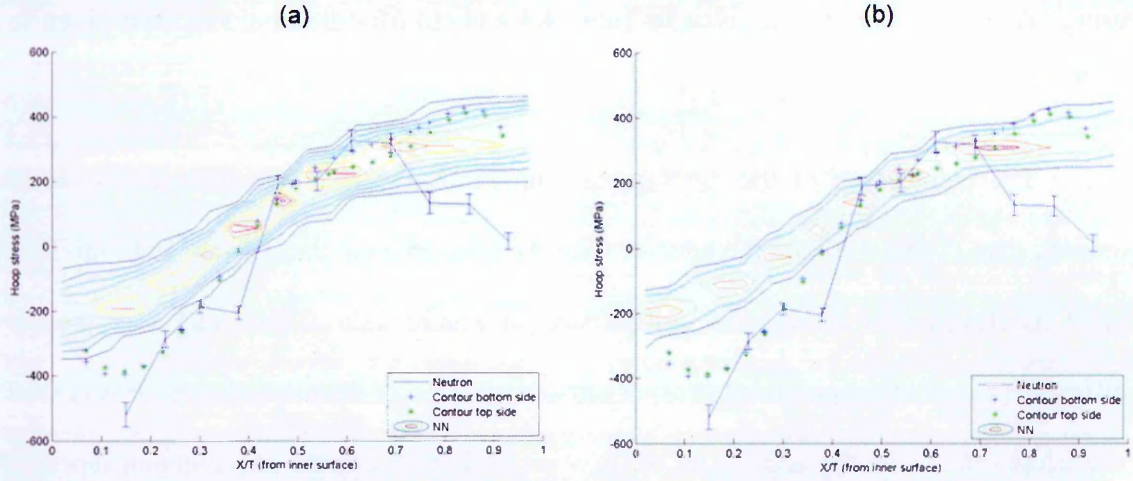

Figure 4.26. Comparison of ANN model prediction of hoop stress distribution in the STYLE pipe butt weld MU4-3 at the WCL (Input parameters R/t = 4.5, t = 25 mm and Q = 1.5 kJ/mm) using (a) Initial training data given in Table 4.3 and (b) Modified training data given in Table 4.5.

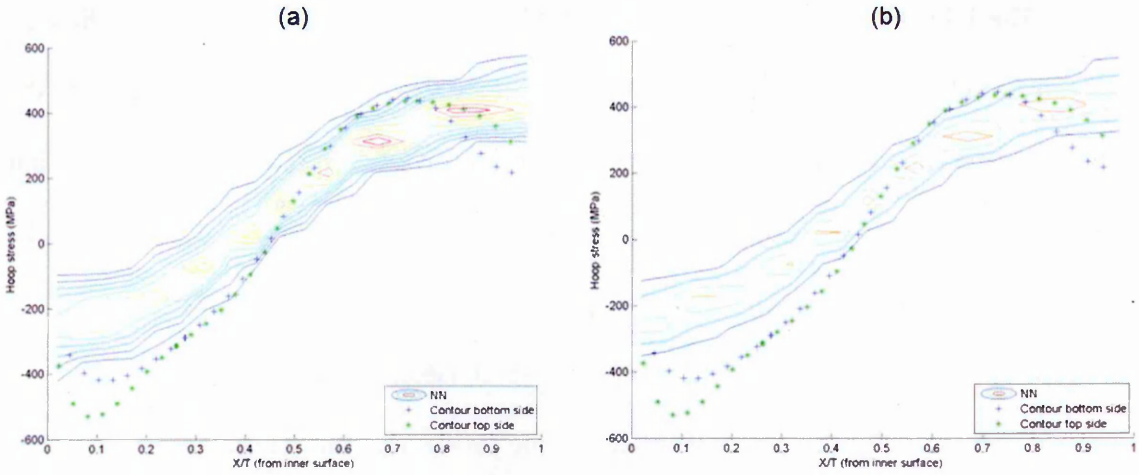

Figure 4.27. Comparison of ANN model prediction of hoop stress distribution in the Esshete pipe butt weld at the WCL (Input parameters R/t = 2.1, t = 35 mm and Q = 1.6 kJ/mm) using (a) Initial training data given in Table 4.2 and (b) Modified training data given in Table 4.4.

The modified HAZ experimental data with additional data of the half inch thick pipes are summarized in Table 4.6.

Table 4.6. Process parameter envelope of training data in heat affected zone.

	Mock-ups	Net heat input kJ/mm	R/t	t (mm)	Yield stress (p,w) (MPa)	Experimental measurements
Training						
1	SP19	1.12	10.5	19.6	272, 446	Neutron
2	OU20	1.36	3.8	20	264, 446	Neutron
3	SP37	1.76	5.3	37	328, 446	DHD
4	S5VOR	1.92	2.8	65	328, 446	DHD
5	S5New	0.8	2.8	65	328, 446	DHD
6	S5NG	1.32	3.0	62	328, 446	DHD
7	Low	0.7	10	12.7	320, 450	Contour
8	High	1.2	10	12.7	320, 450	Contour
Validation						
1	MU4-1	0.8	4.5	25	290, 450	Neutron, Contour
2	MU4-3	1.5	4.5	25	290, 450	Neutron, Contour
3	Esshete	1.6	2.1	35	370, 564	Contour
4	Med	1.0	10	12.7	320, 450	Contour

*where p, w are the parent and weld material yield strength at 1% proof stress.

The initial set of predictions (using Table 4.4) is compared with new predictions using the modified training dataset (Table 4.6) in Figures 4.28 – 4.31. In Figure 4.28, the ANN prediction using the training data was found to give better results as the prediction band seem to match the experimental measurements and the discrepancy at the inside surface was found to diminish. The ANN prediction was in excellent agreement with the neutron measurements and found to be in reasonable agreement with the contour measurements besides the differences seen at the inside and outside diameter. The ANN predictions were found to improve in the high heat input girth weld (see Figure 4.29) as the disparity with the neutron measurements at through wall positions (x/t) = 0.5 – 0.8 was found to decrease. In Figure 4.30, the ANN predictions provided a very similar stress distribution where as in the through-thickness range (x/t) = 0.15 – 0.5, the old prediction seems to be in better agreement.

Overall, there was considerable improvement in prediction of stress profiles in the HAZ location compared to the WCL. However, the improvement is not very obvious in all cases and more evidence need to be presented to justify that adding new experimental measurements in the training dataset can improve the ANN prediction using the discussed approach.

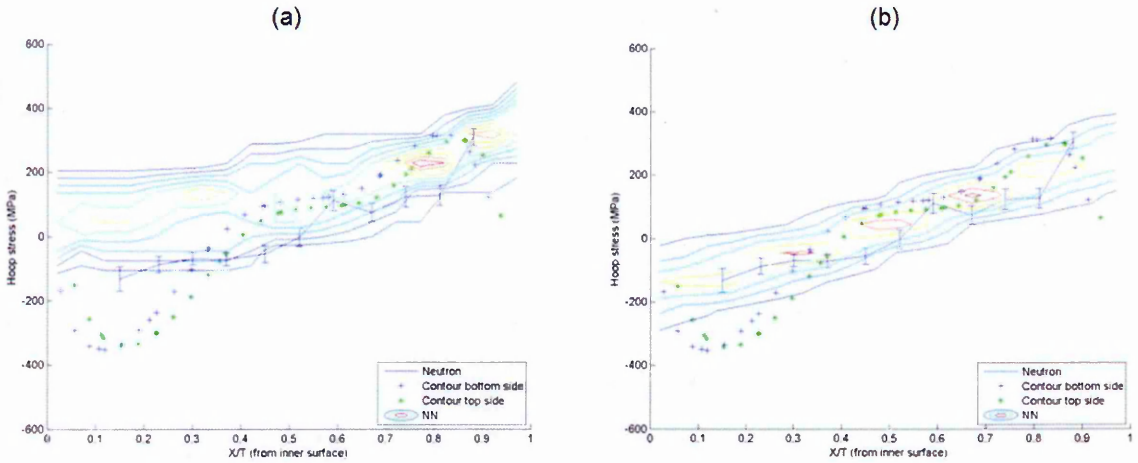

Figure 4.28. Comparison of ANN model prediction of hoop stress distribution in the STYLE pipe butt weld MU4-1 at the HAZ (Input parameters R/t = 4.5, t = 25 mm and Q = 0.8 kJ/mm) using (a) Initial training data given in Table 4.4 and (b) Modified training data given in Table 4.6.

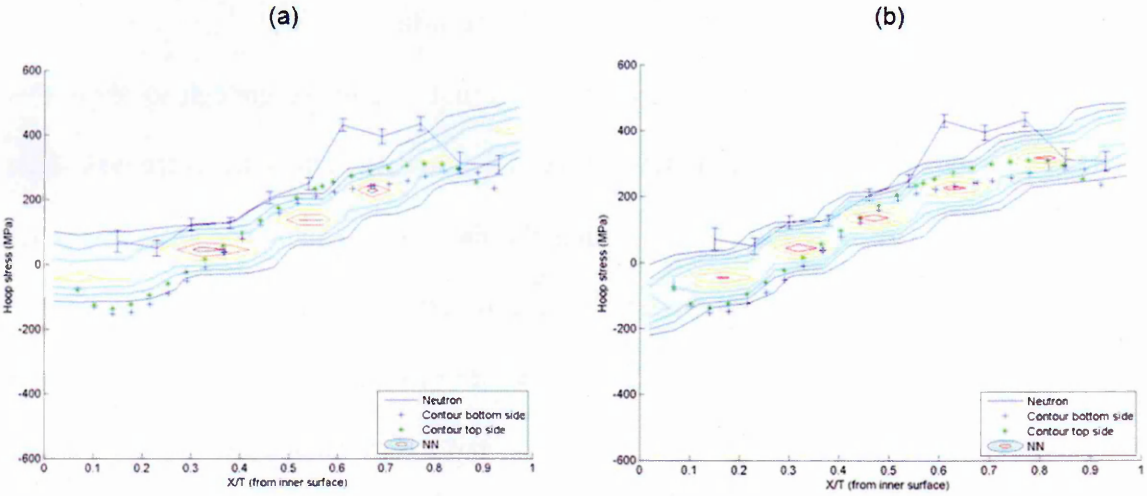

Figure 4.29. Comparison of ANN model prediction of hoop stress distribution in the STYLE pipe butt weld (MU4-3) at the HAZ (Input parameters R/t = 4.5, t = 25 mm and Q = 1.5 kJ/mm) using (a) Initial training data given in Table 4.4 and (b) Modified training data given in Table 4.6.

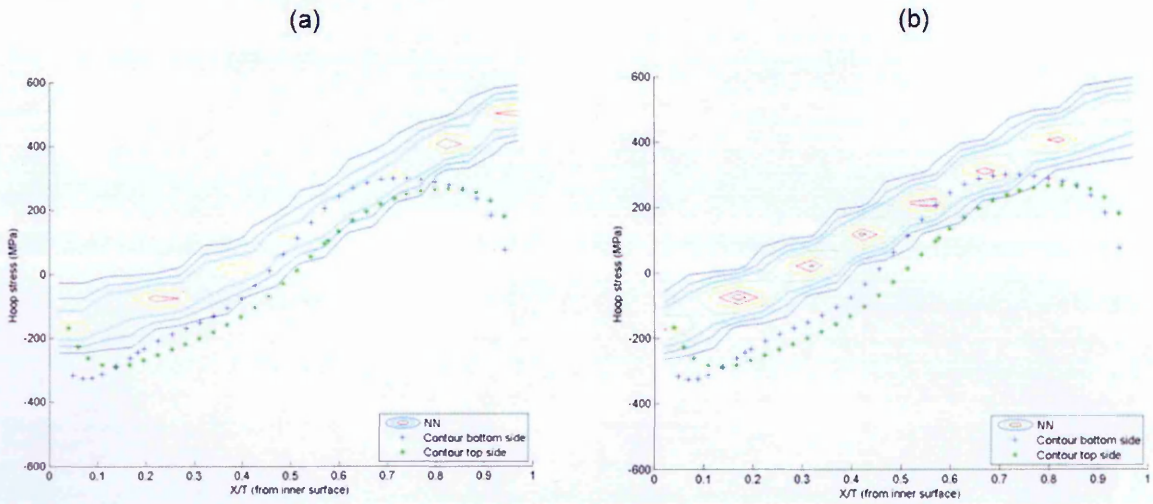

Figure 4.30. Comparison of ANN model prediction of hoop stress distribution in the Esshete pipe butt weld at the HAZ (Input parameters R/t = 2.1, t = 35 mm and Q = 1.6 kJ/mm) using (a) Initial training data given in Table 4.4 and (b) Modified training data given in Table 4.6.

4.5.2 Training using all-inclusive measurement data

The studies reported in section 4.5.1 were not conclusive enough to show that adding new experimental data can improve the ANN model predictions. There was slight improvement in the predictions after adding the data of two half inch thick pipes for training at the HAZ location and this encouraged to perform further investigation. One of the major drawbacks of the model prediction has been its inability to predict the stresses close to the inside surface along the hoop direction in the girth welded pipes MU4-1, MU4-3 and Esshete. It can be argued that the magnitude of compressive stresses observed in most of the validation mock-ups is not evident in the training data and hence it is inappropriate to question the performance of the ANN as extrapolation beyond the process parameter space is outside its scope. However, there is a sufficient amount of new data accumulated in the WCL along the hoop direction in girth welded pipes and by adding all of them in the training dataset, with only the exclusion of data for which the output is simulated, the efficacy of the developed approach can be determined. This is performed in three cases (Girth welded pipes MU4-1, MU4-3 and Esshete) and is compared with the

predictions using the initial training data. The old predictions are compared with the new in Figure 4.31. There is a significant improvement in the model predictions reducing the discrepancy by about 100 MPa at the inside surface mainly due to the inclusion of MU4-3 and Esshete pipe data in the training. This difference in magnitude is remarkable considering the range of residual stress distributions in austenitic stainless steel pipe girth welds.

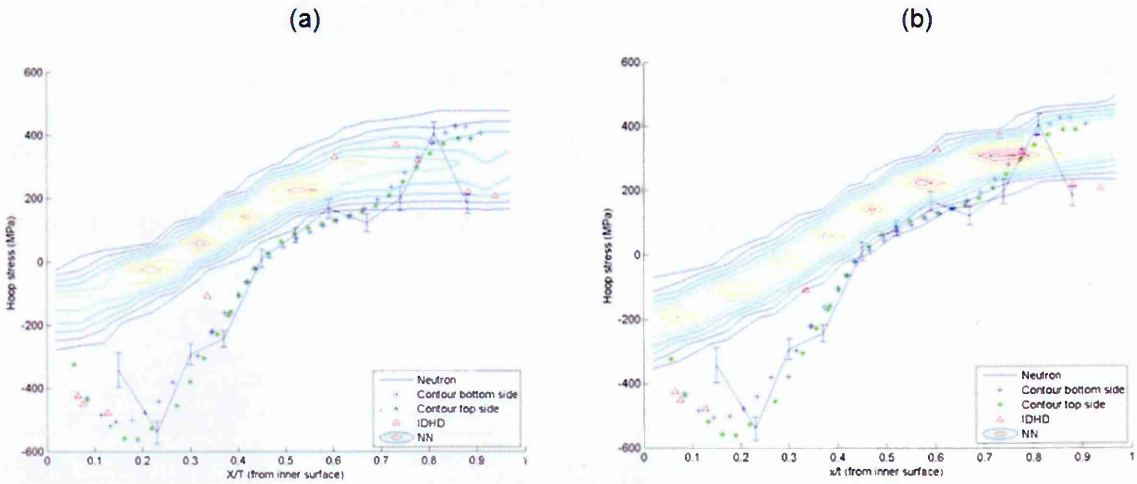

Figure 4.31. Comparison of ANN model prediction of hoop stress distribution in the low heat input pipe butt weld (MU4-1) at the HAZ (Input parameters R/t = 4.5, t = 25 mm and Q = 0.8 kJ/mm) using (a) Initial training data given in Table 4.3 and (b) all-inclusive measurement data at the WCL location.

The next case is illustrated in Figure 4.32 where a similar kind of improvement is evident with the ANN prediction giving better agreement with the contour method measurements close to the inside surface. This is also repeated in the case of Esshete pipe weld (see Figure 4.33) where the ANN model prediction is seen to come closer to the contour method measurements close to the inside diameter. The mean line profile of the best estimate stresses using the ANN predictions are compared with each other in Figure 4.34. The difference in predictions close to the ID is about 100 MPa in MU4-1 weldment and more than that with the case of MU4-3 and Esshete pipes. This is considered to be a significant change considering the magnitude of hoop residual stresses in girth welded pipes. Overall, the improvement is consistent and has demonstrated repeatability in all the three cases.

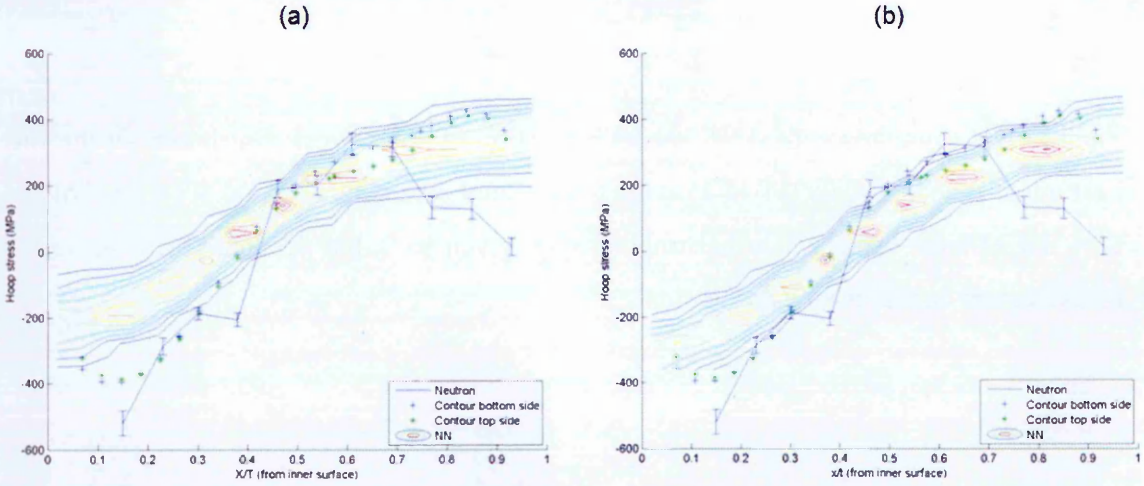

Figure 4.32. Comparison of ANN model prediction of hoop stress distribution in the high heat input pipe butt weld (MU4-3) at the heat affected zone (Input parameters R/t = 4.5, t = 25 mm and Q = 1.5 kJ/mm) using (a) Initial training data given in Table 4.3 and (b) all-inclusive measurement data at the WCL location.

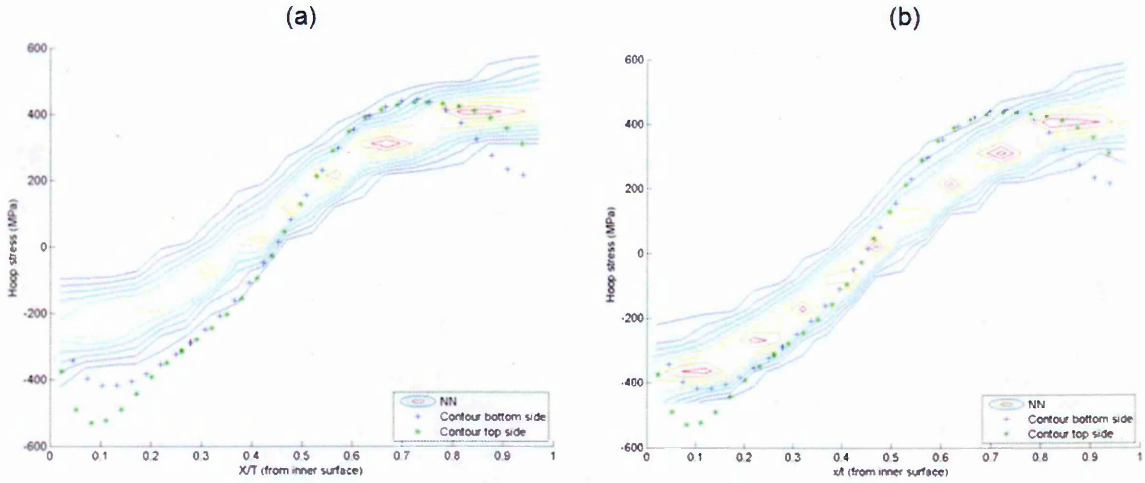

Figure 4.33. Comparison of ANN model prediction of hoop stress distribution in the Esshete pipe butt weld at the HAZ (Input parameters R/t = 2.1, t = 35 mm and Q = 1.6 kJ/mm) using (a) Initial training data given in Table 4.3 and (b) all-inclusive measurement data at the WCL location.

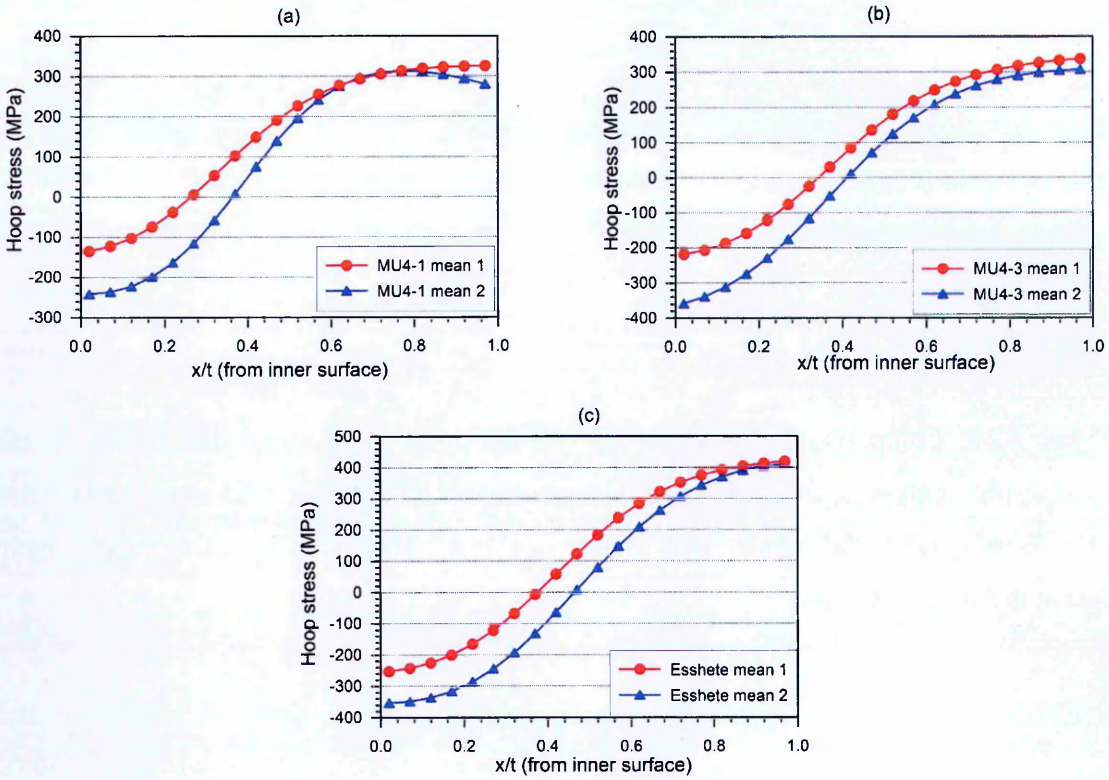

Figure 4.34. Comparison of mean profile from the ANN model prediction of hoop stress distribution in the pipe butt weld (a) MU4-1 (b) MU4-3 and (c) Esshete using initial training data (denoted as 'mean 1') given in Table 4.3 and all-inclusive measurement data (denoted as 'mean 2') at the WCL location.

As a final test criterion, the data initially used for training is swapped with the validation data and the performance of the ANN is evaluated. Note, all the measurements reported were used for training with the exclusion of the dataset for which the stress profile is modelled. A total of four cases were considered and the results are shown in Figure 4.35. Very good agreement was seen between the DHD measurements and the model predictions in all the four cases which increases the confidence in predictions of the ANN approach. The ANN predictions were able to capture the peak stresses and it is interesting to see that the ANN has not under-predicted the stresses close to the inside surface in any of the four cases.

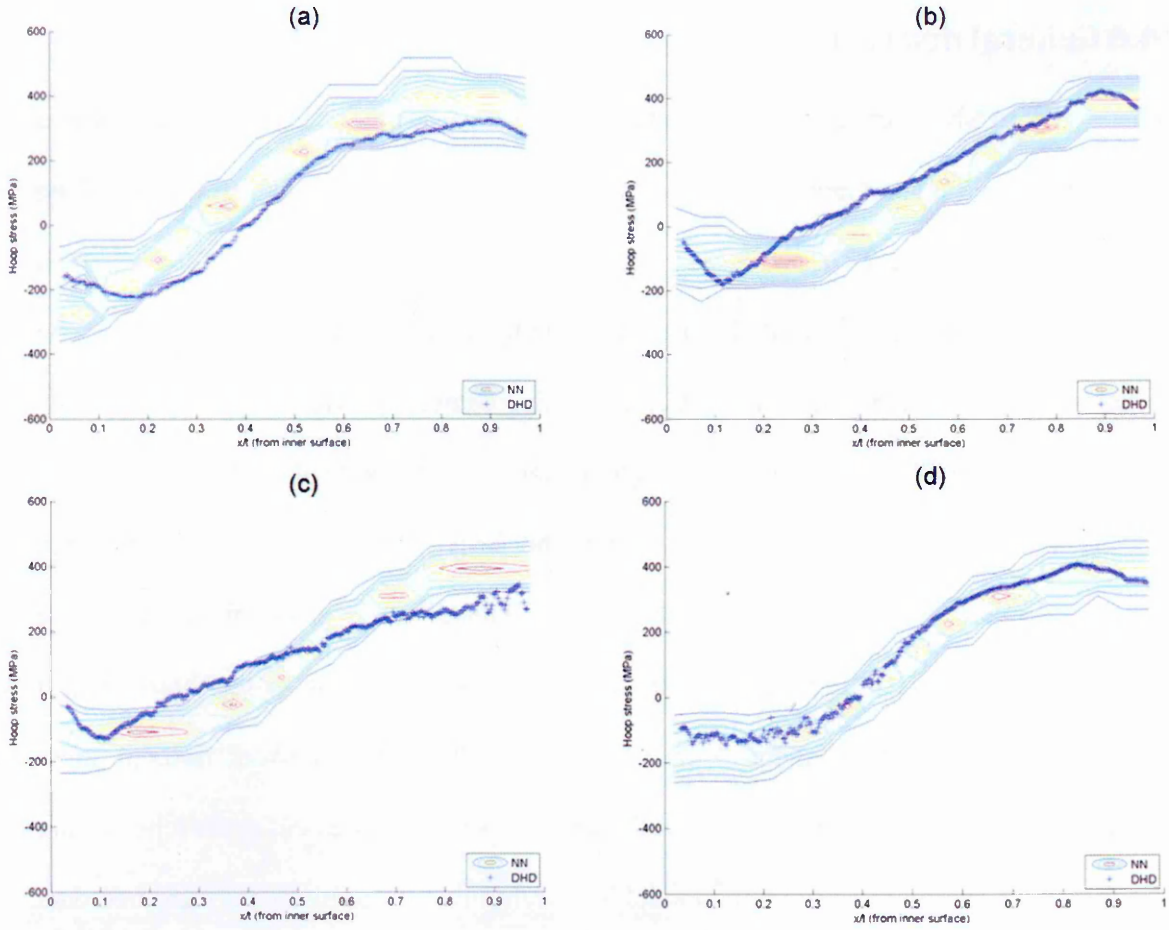

Figure 4.35. Comparison of ANN model prediction of hoop stress distribution at the weld centre line in the four validation mock-ups included for training at the outset, (a) SP37 mock-up (Input parameters R/t = 5.3, t = 37 mm and Q = 1.76 kJ/mm), (b) S5Old mock-up (Input parameters R/t = 2.8, t = 65 mm and Q = 0.8 kJ/mm), (c) S5New mock-up (Input parameters R/t = 2.8, t = 65 mm and Q = 1.12 kJ/mm) and (d) SVOR mock-up (Input parameters R/t = 2.8, t = 65 mm and Q = 1.92 kJ/mm).

4.6 General discussion

The ANN approach has been validated by comparing the predicted profiles with a comprehensive range of new experimental measurements using neutron diffraction and the contour method at the WCL and HAZ locations. The robustness of the developed approach is demonstrated by sensitivity studies performed in hypothetical pipes H1, H2 and H3. The sensitivity studies performed using different training datasets provide additional examples of validation and shows how the predictions can improve with the addition of more experimental data. Interestingly, in most cases the ANN model rarely under-predicts the tensile magnitude of the measured stresses by a large margin. This is a useful characteristic if ANN residual stress profiles are to be used in fracture assessments for safety critical structures. The advantage of the ANN method for defining through-wall residual stress profiles compared with computational weld mechanics or measurement approaches is that the information required to train the model is straightforward and historical measured data can be used. A drawback is that the weldment for which a prediction is to be made must fall within the range of weld types used to train the model. For the application of the ANN approach in structural integrity assessment, it is essential to have a consistent solution for the upper bound profiles and the associated stress intensity factors must be more realistic and less conservative than the profiles currently in use. This is discussed in the next chapter where the development of ANN upper bound profiles determined from the best estimate prediction are presented, following a critical evaluation by comparison with the profiles used in API and R6 fracture assessment codes.

4.7 Conclusions

The findings described in the chapter are summarized as follows,

- A neural network model has been developed that can characterise the through-wall distribution of residual stress of a stainless steel pipe girth weld, providing the weldment type lies within the boundary of the training data envelope used.
- The histogram network developed can provide a reliable prediction interval of the estimated stress distributions and is considered to be a novel contribution in the field of application of neural networks.
- The ANN approach has been validated by comparing predicted profiles with a comprehensive range of new experimental measurements using neutron diffraction and contour method in the weld centre line and heat affected zone locations.
- In most of the cases, ANN over predicted the tensile stresses in the welded pipes and has under-predicted the stresses only on few occasions.
- The robustness of the developed approach is demonstrated by sensitivity studies in input variables by considering few examples of extreme cases in hypothetical pipes.
- The sensitivity of the ANN model to the training data is illustrated by providing a number of case studies that demonstrate that adding more experimental data can improve the predictions significantly.

The next chapter describes how the ANN approach can be applied to define residual stress profiles suitable for use in structural integrity assessments.

Chapter 5

Application to structural integrity

5.1 Introduction

Structural integrity assessment codes have been developed to ensure economic and safe management of operating nuclear power plants, offshore industries and petrochemical industries. Structural integrity assessment codes such as R6 [4], BS7910 [7], and API 579 [8] simplify the three dimensional residual stress field at a welded joint by selecting an idealized one dimensional stress distribution along a line through the wall thickness. Some of the bounding through-thickness profiles used in these procedures are designed based on expert judgment, examination of residual stress measurements that exhibit wide scatter and weld residual stress simulations. As a consequence, structural integrity assessment of defects in welded components can be overly conservative by a large margin, and may lead to unnecessary and costly repair or inspection. Hence development of new profiles that are more realistic is highly desirable. This chapter describes a new approach for developing upper bound profiles using artificial neural networks. The performance and suitability of the ANN upper bound profiles are discussed by comparison with stress profiles recommended in the API and R6 procedures and followed by an assessment of whether the use of neural network bounding profiles can lead to non-conservative estimates of stress intensity factor in fracture assessments.

5.2 Development of upper bound profiles

5.2.1 Background

Defect assessment procedures such as BS7910, R6 and API-579 provide simplified estimates or upper bound profiles that can be used to characterize residual stresses present in a weld. The profiles recommended in API provide an upper bound solution resulting from extensive finite element analysis and study of results available in literature. The residual stress characterisation approaches in R6 are divided into three levels; the simplest being Level 1 where it assumes a uniformly distributed tensile residual stress equal in magnitude to the mean material yield strength. Level 2 is defined to be an upper bound profile of residual stress through the wall-thickness for a class of weld being considered. R6 Level 1 and Level 2 approaches are considered to be very conservative which paved the way for a Level 3. R6 Level 3 represents a more realistic description of the residual stress field developed based upon non-linear analytical modelling of the welding process coupled with experimental measurements.

The purpose of upper bound profiles is to bound experimental measurements thereby exhibiting some level of conservatism to ensure a safe design. R6 level 2 profiles are considered to be overly conservative whereas R6 level 3 (Bouchard's formulation) and API-579 profiles can be non-conservative especially in the axial direction. More realistic formulations for through-thickness residual stress profiles in pipe girth welds have been proposed recently by Bouchard [18], Dong [111] and Teng et al. [121] where the pipe geometry (thickness and radius) and welding heat input are identified as critical governing parameters. Teng et al. [120] has developed a heuristic approach for statistical analysis of residual stress data that is based on the combination of weighted least squares and expert judgment. Nadri et al. [127] used a statistical approach based on Bayes theorem to analyze residual stress data to define parametric formulations that can predict hoop and axial stresses in pipe girth welds. Overall these more realistic methods depend, to some extent,

on expert judgment and may sometimes provide unreliable stress profiles thus emphasizing the need to develop new reliable and pragmatic upper bound profiles.

5.2.2 Upper bound profiles using ANN

In the previous chapter a novel application of artificial neural networks capable of predicting residual stress profiles in austenitic stainless steel pipe girth welds was illustrated where the network is trained using a set of baseline experimental residual stress data and then validated using previously unseen data. An upper bound curve was determined from the histogram network of output distributions that represent the best estimated stresses. Each individual network was trained with 250 independent training sessions using a Scaled Conjugate Gradient (SCG) training regime starting at different randomly chosen points on the error surface and the best 10% of predictions were determined among the committee of networks. A range of networks was classified conforming to the minimum Bayesian error and the histogram of the output was obtained as a distribution plot. The mean of the distribution plot was then calculated and one standard deviation ($+1\sigma$) of the mean profile was obtained as illustrated in Figure 5.1. The artificial neural network upper bound (ANN UB) profile is calculated from the minimum of the $+1\sigma$ of the mean profile and the yield stress of the material. It is important to note the approach used to calculate the ANN upper bound profile is fairly simple and the stress equilibrium condition (zero force over radial-hoop plane) along the axial direction is not fulfilled. This is because the upper bound stress profiles are defined by effectively adding a uniform stress value, based on one standard deviation.

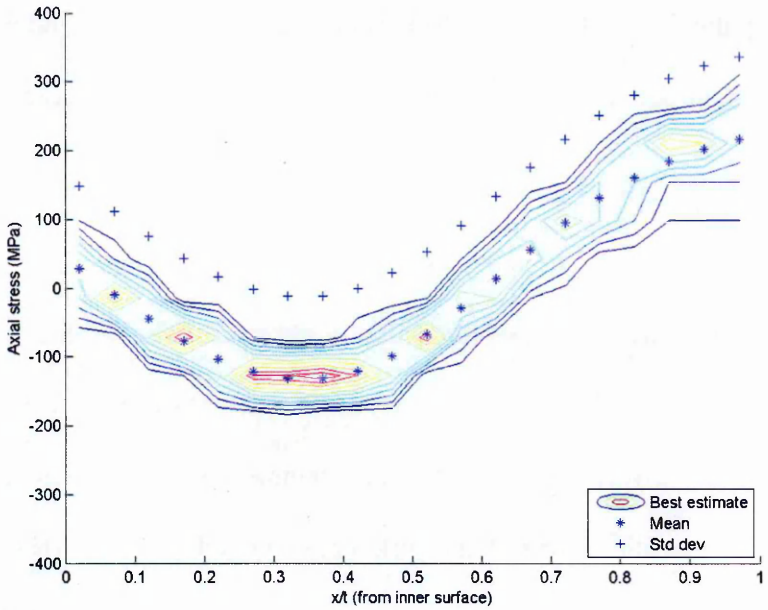

Figure 5.1. Representation of ANN upper bound axial residual stress profiles from the histogram network.

5.2.3 Comparison of different upper bound profiles

The stress profiles used in R6 and API-579 procedures are compared with the ANN upper bound profiles and the experimental measurements acquired in this study. For the sake of understanding ANN mean profiles are also included. In Figure 5.2, the neutron and incremental deep hole drilling (IDHD) measurements at the weld centre line of the low heat input girth weld (MU4-1) are compared with upper bound profiles in the axial direction. R6 level 2 bounds all the measurements of the low heat input girth weld but seems to be highly conservative, whereas R6 level 3 (Bouchard's formulation) underestimates most of the measurements in the range x/t = 0.3 – 0.6 as shown in Figure 5.2. In this particular case API-579 provides a comparatively better upper bound solution with respect to the neutron measurements. However the artificial neural network upper bound (ANN UB) profile bounds all the neutron measurements and is more realistic than the R6 level 2 profile. The IDHD measurements indicate the presence of slightly higher tensile stresses in the region x/t = 0.6 - 0.8 compared with the neutron measurements and is

only bounded by the R6 level 2 profile. Noticeably, the ANN upper bound profile does not cover the high magnitude IDHD measurements mainly at x/t = 0.6 by about 50 MPa.

In the hoop direction (see Figure 5.3) the trend is somewhat different as none of the upper bound profiles could provide a realistic estimate of the stresses near the inside surface, a maximum difference of 400 MPa is observed. The profiles based on API underestimate the stresses slightly approaching the outer surface, R6 level 3 appears to be more realistic and effectively bounds the neutron, contour method and IDHD measurements. The artificial neural network upper bound profile (ANN UB) is more realistic than R6 level 2 but exhibits slight conservatism near the inside surface compared with the R6 level 3 and API-579 profiles.

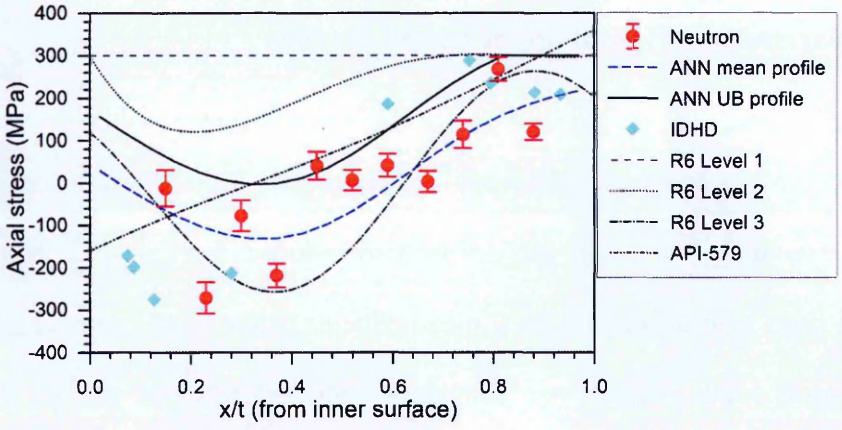

Figure 5.2. Comparison of upper bound profiles in the weld centre line for the low heat input girth weld MU4-1 in the axial direction.

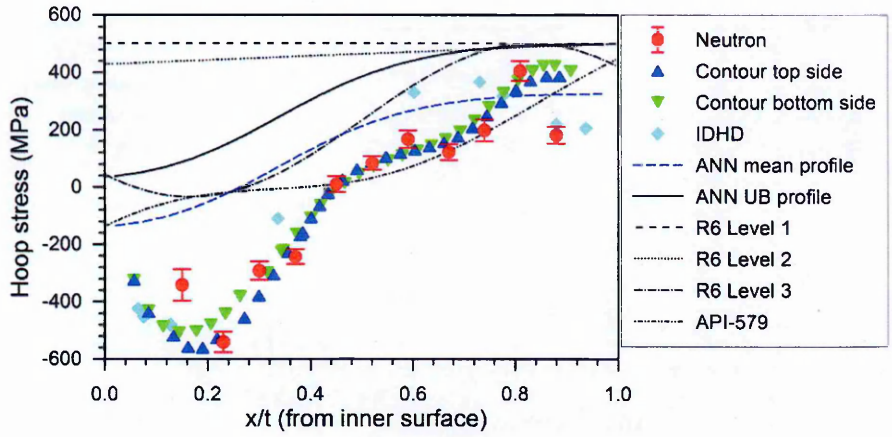

Figure 5.3. Comparison of upper bound profiles in the weld centre line for the low heat input girth weld MU4-1 in the hoop direction.

Neutron stress measurements in the axial direction at the weld centre line for the high heat input welded component (MU4-3) are compared with different upper bound profiles in Figure 5.4. The non-conservative region of the R6 level 3 profile was found to shift to the outer surface (x/t = 0.5 - 0.7) as shown in Figure 5.4. The API profile failed to bound all the measurements but overall was found to be reasonable whereas R6 level 2 was highly conservative for all the through thickness positions. Overall, the ANN upper bound profile was found to be the more consistent among all the upper bound profiles considering the scatter observed in neutron measurements and never underestimated the measurements at any point. For the hoop stress distribution (Figure 5.5) the trend observed is similar with the exception that the API upper bound profile was less conservative and incapable of bounding most of the neutron and contour method measurements approaching the outside surface where the difference was found to be as high as 200 MPa. The ANN profiles were more pragmatic than the R6 level 2 and level 3 profiles but continued to exhibit conservatism near the inside surface and were successful in providing bounding stress profiles.

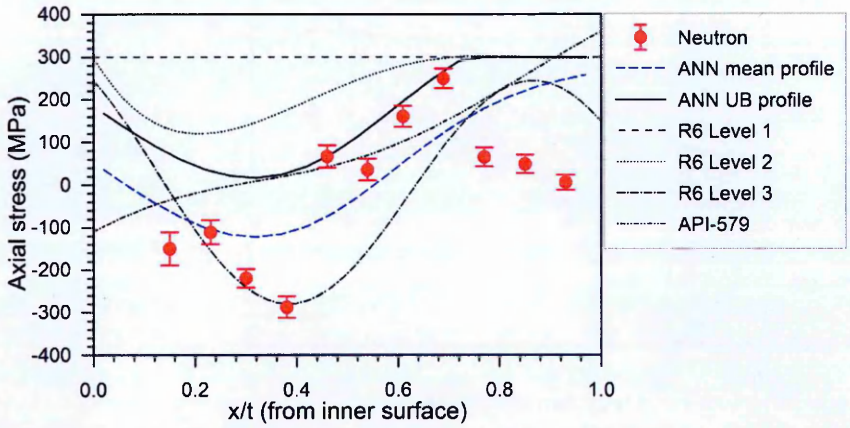

Figure 5.4. Comparison of upper bound profiles in the weld centre line for the high heat input girth weld MU4-3 in the axial direction.

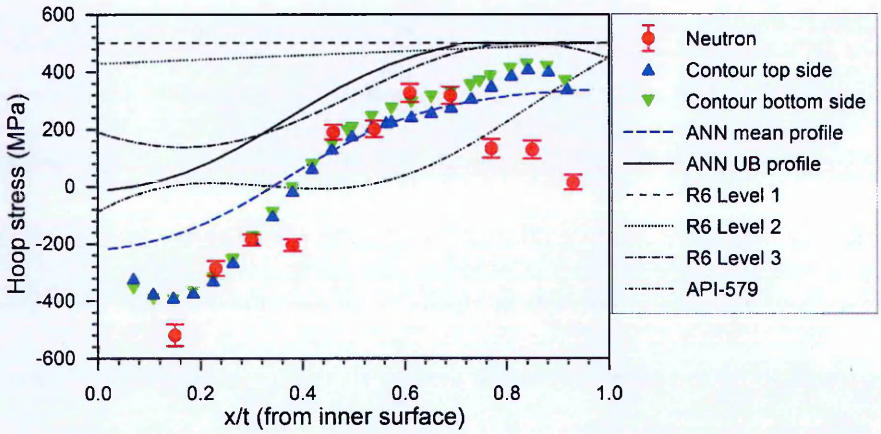

Figure 5.5. Comparison of upper bound profiles in the weld centre line for the high heat input girth weld MU4-3 in the hoop direction.

The stress profiles at the weld centre line measured using the contour method in the axial direction of the Esshete girth weld are compared with different upper bound profiles as shown in Figure 5.6. R6 level 2 appears to be over-conservative where as R6 level 3 is non conservative in the through-thickness range (x/t) = 0.2 – 0.7. API-579 profile under-estimates the stresses close to the inside surface by a large margin of about 300 MPa and tend to over-estimate the stresses close to the outside surface. The ANN upper bound profile seems to be the most realistic out of all the other profiles and effectively bounds all the contour method measurements. However the ANN profile over-estimates the stresses close to the outside surface similar to the upper bound profile recommended in API-579.

However, the pattern observed in the hoop direction (see Figure 5.7) is very different with the exemption of R6 level 1 and level 2 being overly conservative. The API profile slightly under-estimated the stresses in the through wall region (x/t) = 0.5 - 0.8. Interestingly, R6 level 3 and the ANN upper bound profile matched closely at all positions and both were successful in providing bounding profiles that were realistic and less conservative.

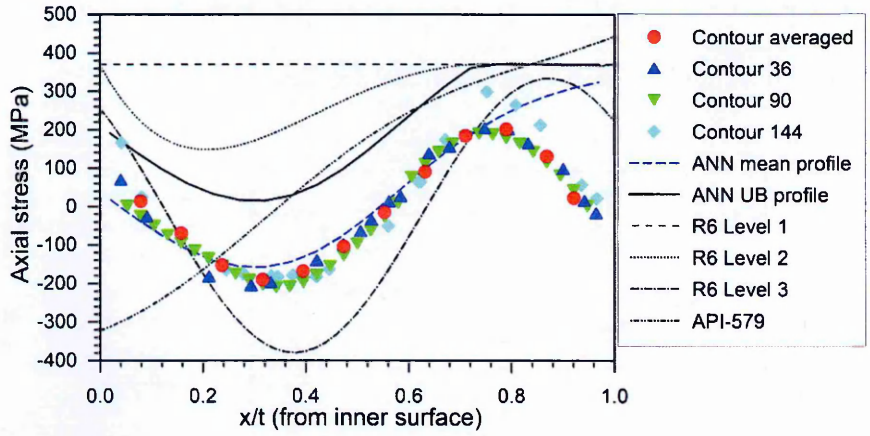

Figure 5.6. Comparison of upper bound profiles in the weld centre line of the Esshete girth weld in the axial direction.

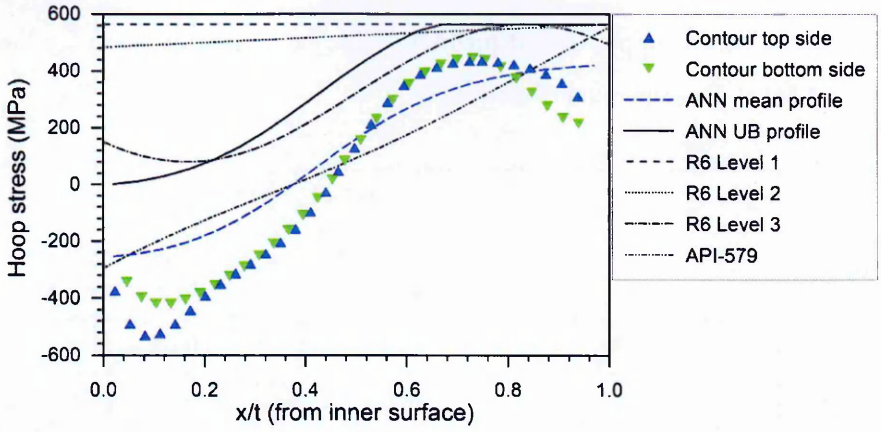

Figure 5.7. Comparison of upper bound profiles in the weld centre line of the Esshete girth weld in the hoop direction.

Figure 5.8 shows a comparison of upper bound stress profiles with the neutron measurements at the heat affected zone in the axial direction of the low energy girth weld (MU4-1). The R6 level 2 profile is highly conservative where as R6 level 3 profile under-estimates the measured stresses in the through-wall position range (x/t) = 0.2 - 0.6. The

API-579 bounds all of the neutron measurements and the ANN upper bound profile gives the most realistic bounding estimate for most of the measured stresses. The same pattern is evident in the hoop stresses reported in the heat affected zone of the same mock-up (refer Figure 5.9). But in this case the R6 level 3 provides a better fit over the inner half of the wall thickness compared to the ANN bounding profile. Interestingly, the ANN UB profile exhibits a linear nature unlike the previous cases but nonetheless provides a more pragmatic bound than the R6 Level 2 and API-579 profiles.

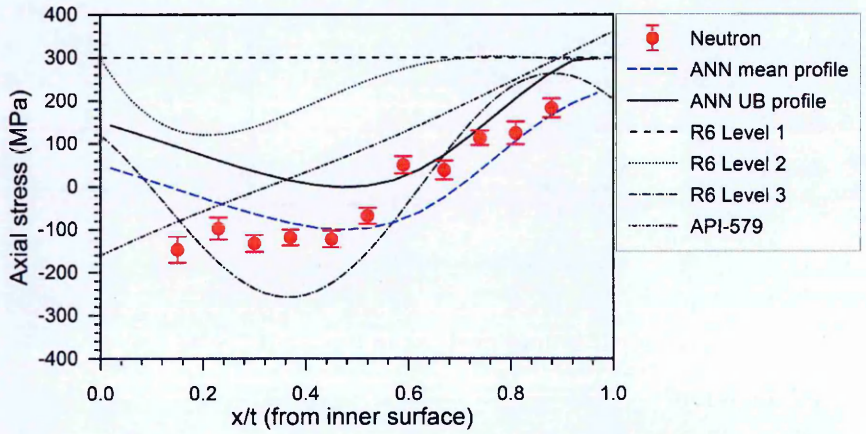

Figure 5.8. Comparison of upper bound profiles in the heat affected zone for the low heat input girth weld MU4-1 in the axial direction.

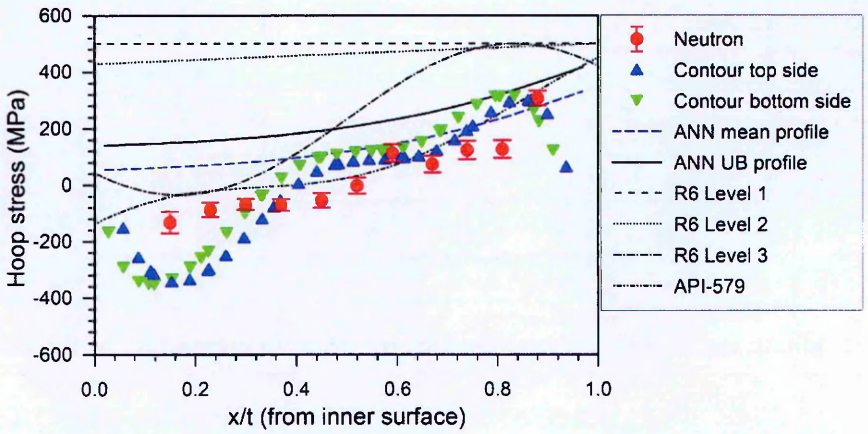

Figure 5.9. Comparison of upper bound profiles in the heat affected zone for the low heat input girth weld MU4-1 in the hoop direction.

The upper bound profiles along the axial and hoop directions at the heat affected zone in the high heat girth weld (MU4-3) are compared in Figures 5.10 and 5.11

respectively. In the axial direction (see Figure 5.10) the ANN upper bound profile fails to bound the neutron measurements in the through-wall thickness position (x/t) = 0.5 - 0.8 with the maximum difference of 200 MPa at x/t = 0.6. The mean ANN like R6 level 3 predominantly under-estimates the stresses at almost all the though thickness positions and API-579 upper bound profile seemed to be more realistic. In the hoop direction, the ANN upper bounds profile bounded most of the neutron and contour method measurements. In contrast, the API-579 profile provides non conservative estimates of stresses and the R6 level 3 profile bounds all the measurements.

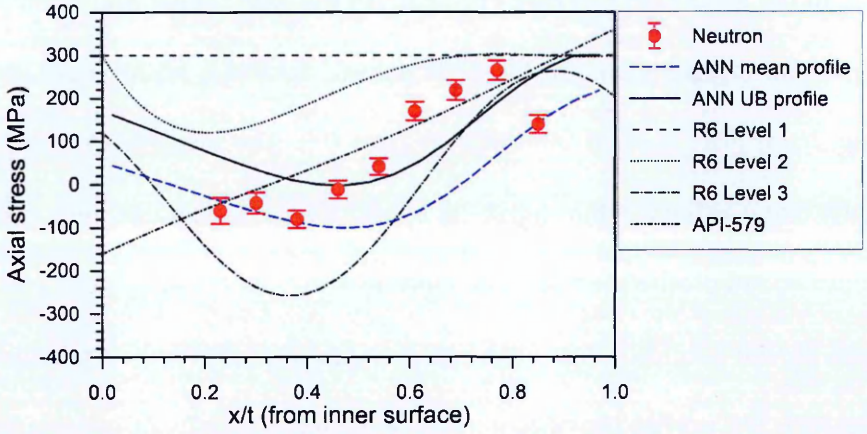

Figure 5.10. Comparison of upper bound profiles in the heat affected zone for the high heat input girth weld MU4-3 in the axial direction.

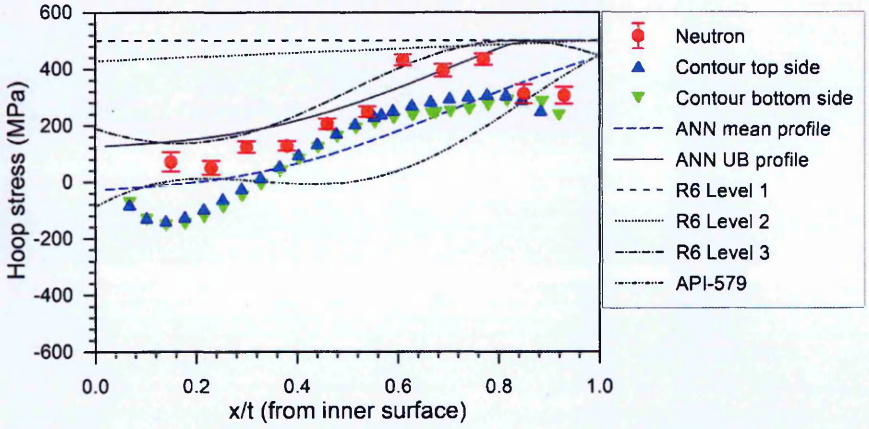

Figure 5.11. Comparison of upper bound profiles in the heat affected zone for the high heat input girth weld MU4-3 in the hoop direction.

The upper bound profiles for hoop stress in the heat affected zone of the Esshete pipe are compared with contour method residual stress measurements in Figure 5.12. In this case, R6 level 2 remains overly conservative where as R6 level 3 closely resembles the ANN upper bound profile. Both the R6 level 3 and the ANN upper bound profiles are conservative by about 200 MPa. The mean ANN profile and API-579 give the most realistic estimate of residual stresses measured using the contour method measurements.

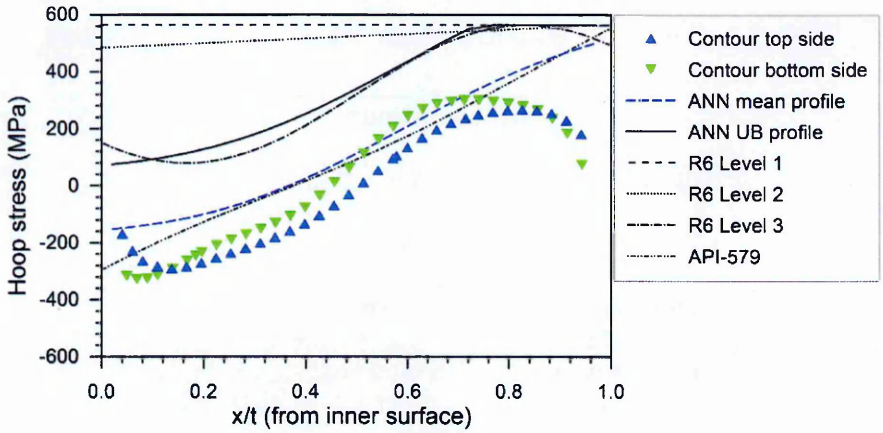

Figure 5.12. Comparison of upper bound profiles in the heat affected zone for the Esshete girth weld in the hoop direction.

5.3 Stress intensity factors for structural integrity assessment

5.3.1 Estimation of stress intensity factors

The stress intensity factor (i.e. elastic crack driving force) gives a true measure of the degree of conservatism in an "upper bound" residual stress profile for fracture mechanics assessment purposes. In fracture mechanics analyses of welded components, the accuracy or degree of conservatism in the calculated stress intensity factor associated with the residual stress field is critical. The ultimate test for an upper bound profile is whether it exceeds the stress intensity factor based on the measured profile. In this study the stress intensity factor (SIF) was calculated using R-Code [172] software assuming a surface breaking extended crack oriented in circumferential and axial directions at the internal location of the pipe. Table 5.1 illustrates the test conditions used to evaluate the stress intensity factors. The linear elastic stress intensity factors for internal surface-breaking fully circumferential and axial cracks (subjected to mode I loading) is examined at the weld centre line and heat affected zone of different welded pipes.

Table 5.1. Conditions used to evaluate the stress intensity factors

SIF conditions	
Structure type	Hollow cylinder
Crack type	Surface
Crack shape	Extended
End constraints	Unrestrained
Number of cracks	Single
Orientation	Circumferential and axial
Position	Internal
Primary load factor	1
Depth of defect	5 mm
Polynomial order	3
Stress	Axial and hoop

5.3.2 Comparison of stress intensity factors

Stress intensity factors based on functions fitted to experimental measurements and ANN upper bound profiles are compared with SIFs based upon upper bound profiles recommended in the R6 and API codes in Figures 5.13 – 5.18. In Figure 5.13, the SIFs based on R6 level 1 and R6 level 2 were found to be overly conservative for all the cases. For the circumferential crack in Figure 5.13 (a), R6 level 3 was found to give non-conservative estimates of SIFs for both internal and external cracks with $a/t > 0.3$. R6 level 3 predicts a large zone of compressive stresses that peaks around $x/t = 0.35$ and hence the magnitude of the SIFs based on R6 level 3 are considerably lower than the SIFs based on neutron and IDHD measurements. SIFs from the API-579 profile were found to under-predict the SIFs based on neutron measurements for shallow cracks (< 0.1t through-wall extent) whereas the SIFs based on the ANN upper bound profile were more realistic and overestimated the SIFs based on measured data for any crack length. In the case of axial crack as illustrated in Figure 5.13 (b), the SIFs representing neutron, contour and IDHD

measurements matched closely with each other. R6 level 1 and level 2 profiles were found to be very conservative followed by the ANN upper bound profile. The conservative nature of the ANN UB profile could be associated with the over-estimation of hoop stresses near the inside surface. The SIFs based on the ANN UB profile were observed to be more conservative than the R6 level 3 and API-579 but the difference was not substantial.

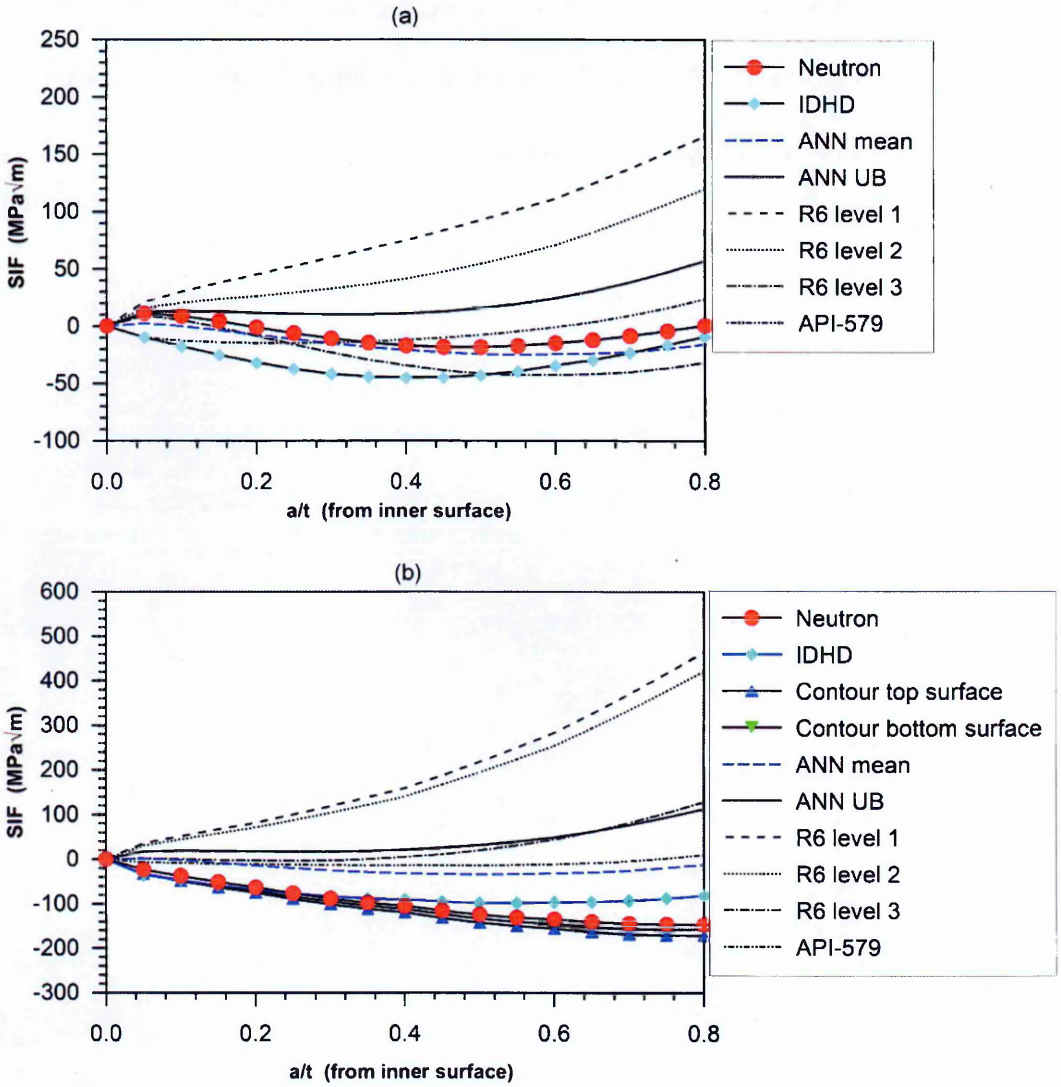

Figure 5.13. Comparison of SIFs at the weld centre line of low heat input weld MU4-1 based on measurements and upper bound profiles for: internal surface breaking (a) circumferential crack (b) axial crack.

The SIFs based on measured data and upper bound profiles in MU4-3 are presented in Figure 5.14. The pattern observed in the SIF solutions in MU4-3 was consistent with the case of circumferential crack assumed at the internal location of MU4-1 (see Figure 5.14 (a)). Both R6 level 3 and API underestimated the SIFs based on measured data whereas the ANN UB profile were able to provide more consistent bounding estimates of SIFs compared to measured data. In the case of axial cracks (see Figure 5.14 (b)), SIFs based on ANN UB profile and R6 level 3 are in close agreement and provided conservative bounding estimates of SIFs compared to measured data.

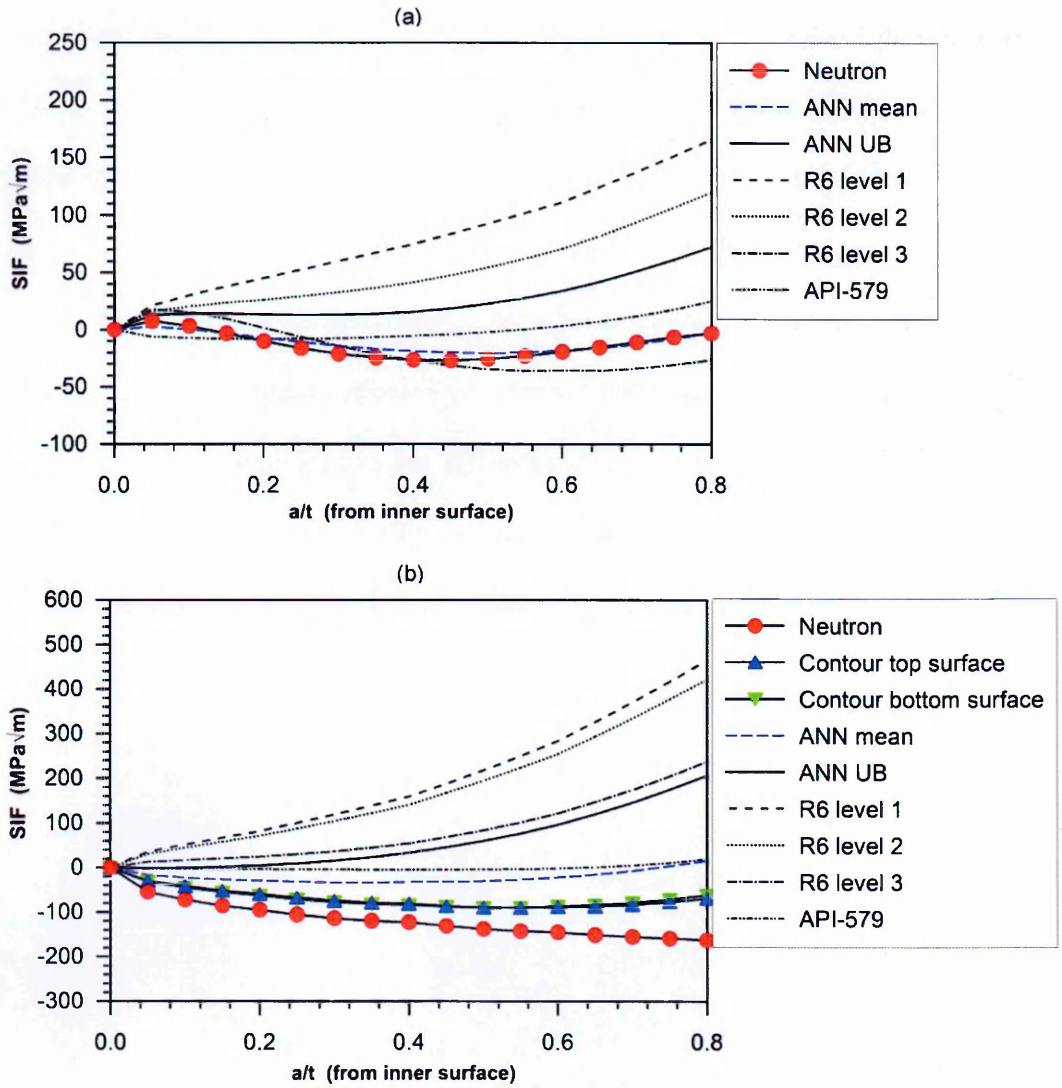

Figure 5.14. Comparison of SIFs at the weld centre line of high heat input weld MU4-3 based on measurements and upper bound profiles for: internal surface breaking (a) circumferential crack (b) axial crack.

The SIF solutions assuming a circumferential crack at the WCL location of the Esshete pipe weld are illustrated in Figure 5.15. The R6 level 1 and level 2 profiles are overly conservative by a large margin compared to SIFs based on the contour measurements at various locations. SIFs based on API underestimate the measured SIFs for shallow crack with a/t < 0.1 where as SIFs based on R6 level 3 underestimate for deep crack with a/t > 0.3 in the circumferential orientation. The SIFs based on ANN UB profile are consistent in providing pragmatic estimates of SIF solutions compared with the SIFs based on contour measured data. For the crack in the axial orientation, the same pattern

was observed with R6 level 1 and level 2 profiles being overly conservative while close agreement seen between R6 level 3 and ANN upper bound profiles. SIFs based on API-579 was found to be least conservative compared to other upper bound profiles for axially oriented crack although the API upper bound profiles in the hoop direction was not able to bound all the experimental measurements reported. Overall, the SIFs based on ANN upper bound profiles in the axial direction were consistently better than the profiles recommended in the R6 and API codes. However for the axially oriented crack, the SIFs calculated from ANN UB profiles matched closely with R6 level 3 profiles but was found to be rather conservative compared to the SIFs based on API upper bound profiles.

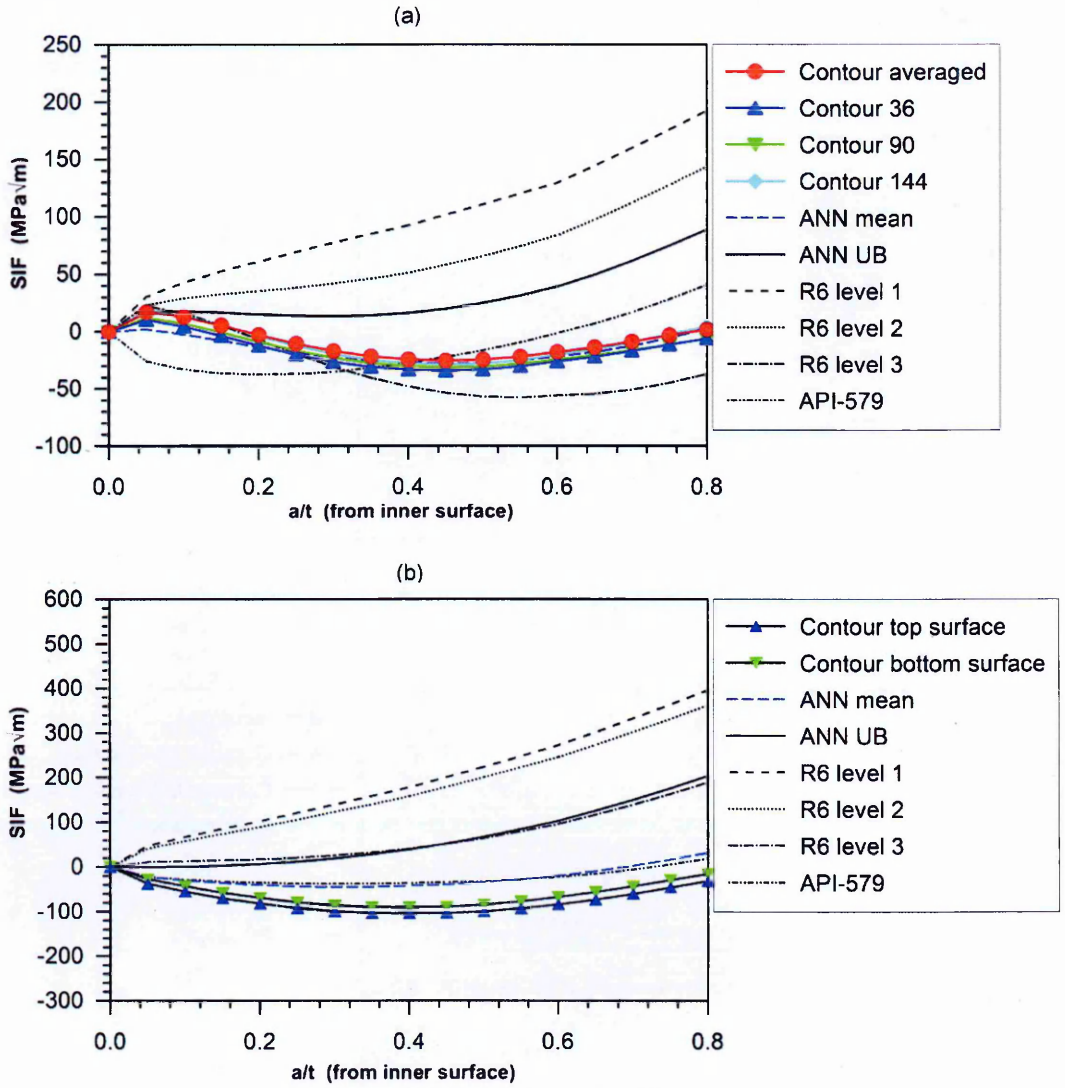

Figure 5.15. Comparison of SIFs at the weld centre line of Esshete butt welded pipe based on measurements and upper bound profiles for: internal surface breaking (a) circumferential crack (b) axial crack.

The SIF solutions at the HAZ location for internal surface breaking cracks in axial and circumferential orientation in different pipes are illustrated in Figures 5.16 – 5.18. In Figure 5.16 (a) and (b) SIFs based on upper bound profiles and experimental measurements are compared assuming a circumferentially oriented crack. The trend observed in the HAZ location is very similar to the WCL with SIFs based on ANN UB profiles overestimating the SIFs calculated from measured data in both cases. Along the hoop direction, the pattern is repeated with SIFs based on ANN UB profiles in good

agreement with the R6 level 3 profiles. However, the ANN based bounding SIFs are more conservative compared to the API profiles.

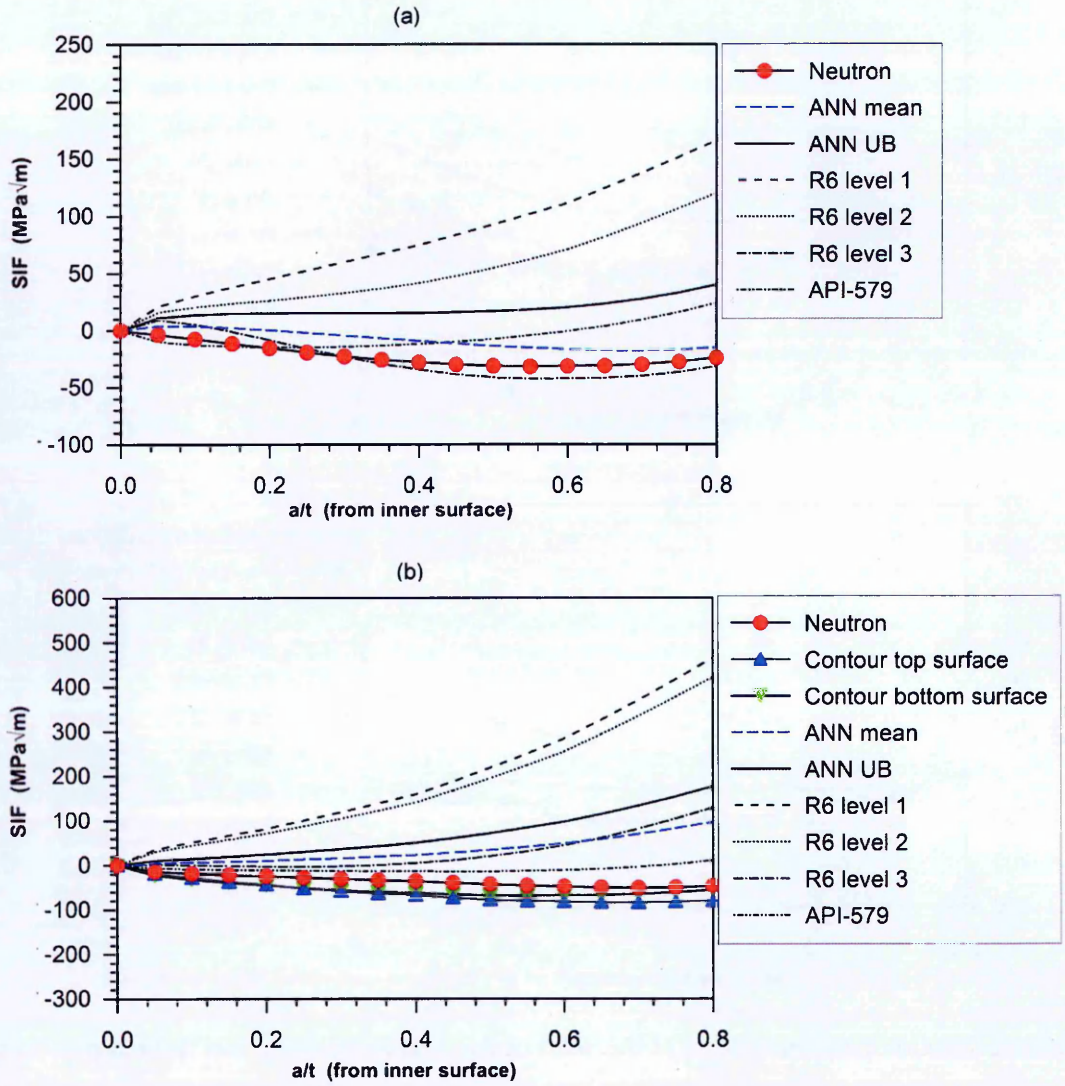

Figure 5.16. Comparison of SIFs at the heat affected zone of low heat input weld MU4-1 based on measurements and upper bound profiles for: internal surface breaking (a) circumferential crack (b) axial crack.

In the case of MU4-3, the observations are very different as the SIFs based on neutron measurements are exceeding the SIFs calculated from R6 level 1 and 2 profiles for $a/t < 0.2$. But this is considered to be very unrealistic and it should be noted that the SIF solutions are heavily dependent on the polynomial fit used for the particular case and require careful extrapolation to the surfaces. The third order polynomial fit for the set of neutron measurement data is illustrated in Figure 5.19 and arguably, the discrepancy is due to the over extrapolation near the inner surface. Moreover, due to the lack of additional measurement data in the axial direction, there was no opportunity to compare with alternate measured SIFs. This is one of the limitations when using R-code software for calculating SIFs based upon neutron measurements where there are relatively few data points.

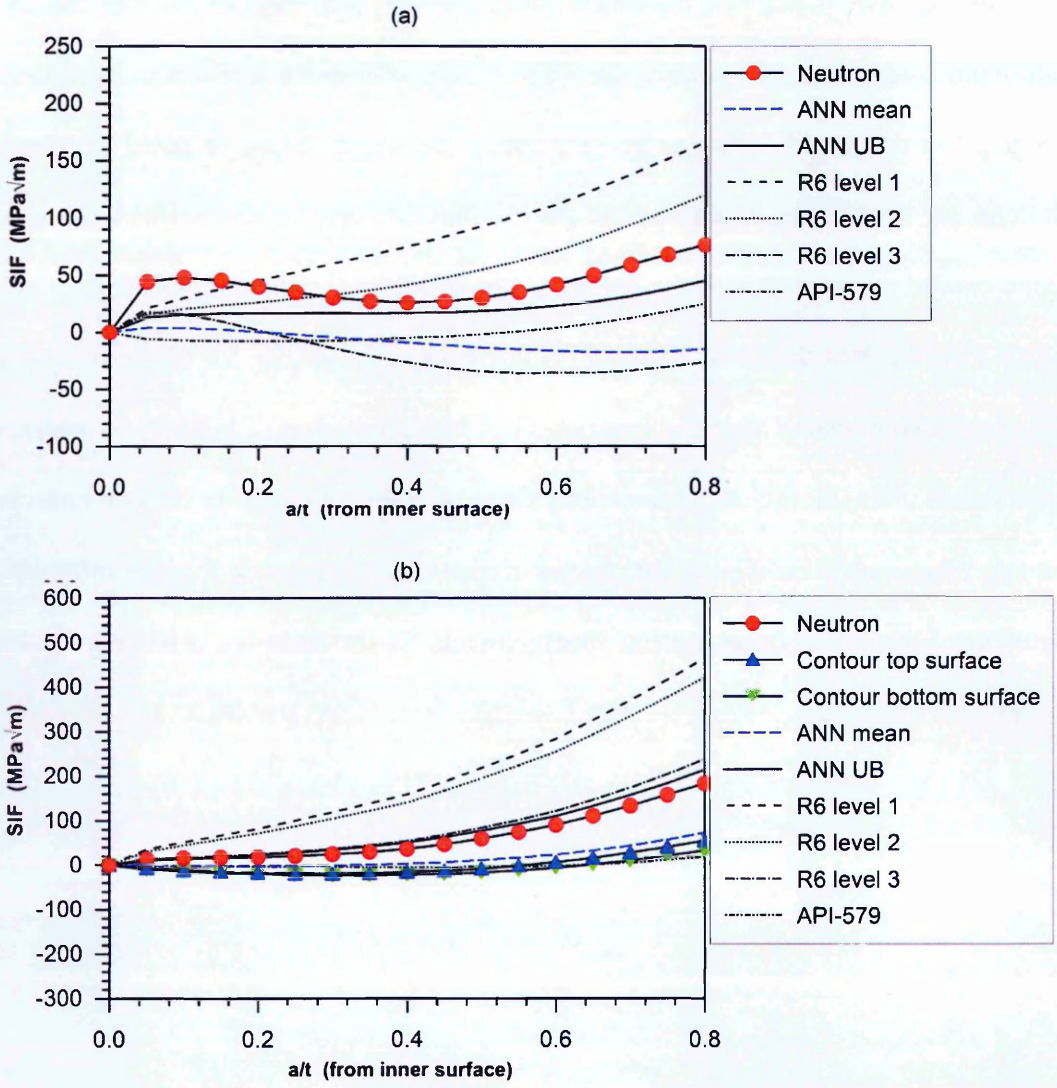

Figure 5.17. Comparison of SIFs at the heat affected zone of high heat input weld MU4-3 based on measurements and upper bound profiles for: internal surface breaking (a) circumferential crack (b) axial crack.

Comparison of SIF solutions in the hoop direction of the high heat input pipe weld (MU4-3) suggest that the SIFs based on API profiles can be non-conservative as shown in Figure 5.17 (b). The SIFs based on neutron measurements are significantly higher and are non-conservative for shallow and deep cracks. However, R6 level 3 and ANN UB profiles successfully demonstrated its consistency by over predicting the SIFs from measured data. The last case of SIFs is presented in Figure 5.18 considering an axial crack in the HAZ location of Esshete pipe. The ANN UB profiles were bounding the measured SIFs

effectively and thus appear to be the most realistic and reliable of all the upper bound profiles.

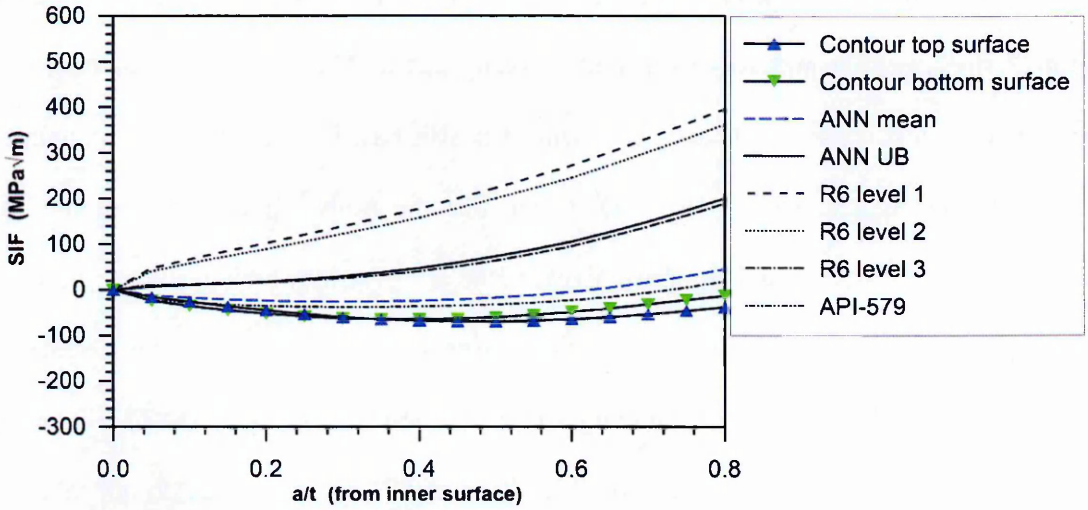

Figure 5.18. Comparison of SIFs at the heat affected zone of Esshete butt welded pipe based on measurements and upper bound profiles for: surface breaking axially oriented internal cracks.

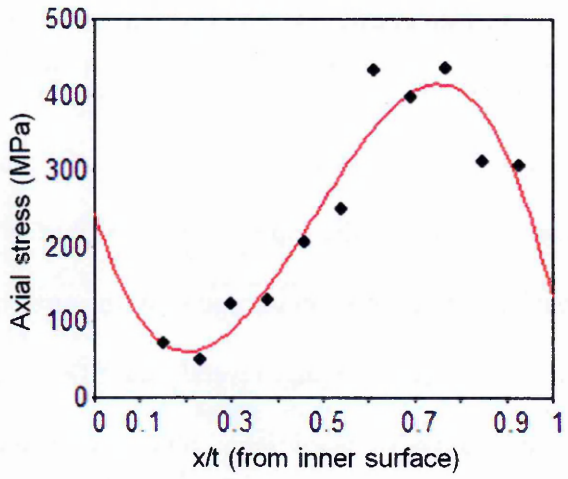

Figure 5.19. Illustration of the third order polynomial fit used to determine the SIF solutions of neutron measurements along axial direction assuming an internal surface breaking extended crack in high heat input mock-up (MU4-3).

5.4 General discussion

The ANN upper bound residual stress profiles were able to consistently bound the measured data consistently in WCL and HAZ locations in both axial and hoop directions. The stress intensity factor gives a true measure of the degree of conservatism in an "upper bound" stress profile and was evaluated in many cases. The SIFs based on ANN UB profiles were less conservative and consistent than SIFs based on any of the recommended profiles in the R6 and API codes. It is evident that the ANN UB profiles presented are suitable for use in structural integrity assessments because they will result in the crack driving force being overestimated for all of the cases presented. Moreover, the ANN based profiles have the advantage of providing location specific (WCL and HAZ) SIF results depending on the training data used where as R6 and API based profiles do not take into account the measurement location. It should be of interest that R6 level 2 profiles consider the key parameters such as welding heat input and pipe geometry only in a certain range. On the other hand, there is a risk that use of the R6 Level 3 profiles for deep cracks in the circumferential orientation or API-579 profiles for shallow cracks in the axial orientation can lead to non-conservative estimates of the SIFs which could cause the cracks to grow and potentially threaten the integrity of the structure. Interestingly, SIFs based on the ANN upper bound profiles are overestimated for any crack length, location and orientation. Furthermore there is scope for refining the approach used to develop the ANN upper bound profiles since the approach at present does not account for the uncertainty in modelling and experimental measurements used for training. Overall, the SIFs calculated from the ANN UB profiles were found to bound SIFs based upon polynomial functions fitted to measured data and hence they seem to be a promising candidate for use in fracture assessments instead of the profiles currently recommended in assessment codes.

5.5 Conclusions

The findings reported in this chapter can be summarized as follows:

- An artificial neural network based method for providing upper bound residual stress profiles has been developed for stainless steel pipe butt welds.
- The artificial neural network upper bound profiles were found to be more realistic and consistent than profiles recommended in API 579 and the R6 Procedure both in axial and hoop directions.
- Stress intensity factor solutions were determined from different upper bound profiles for various cases and compared with the SIFs based on measured data. The ANN upper bound profiles were found to provide more pragmatic estimates of stress intensity factors than profiles recommended in assessment codes assuming a circumferentially and axially oriented surface breaking extended crack in three different mock-ups.

Chapter 6

Conclusions and Future work

Conclusions

The work described in this thesis presents a novel application of an artificial neural network that can predict through-wall residual stresses profiles in girth welded pipes. The ANN approach is validated by a comprehensive range of experimental measurements using neutron diffraction and the contour method acquired as part of this study. Sensitivity studies using the input parameters and training data performed demonstrated the efficacy of the developed ANN approach. The approach can be particularly useful as the information required to train the network is simple and the output is dependent largely on the training data. The ANN approach can be potentially used in fracture assessment of welded components. Upper bound profiles using the ANN model are presented and compared with the upper bound profiles currently recommended in structural integrity assessment codes such as R6 and API. The SIFs based on the upper bound profiles are critically assessed for internal and external surface breaking extended cracks for three different welds. Based on the studies conducted in this dissertation the following conclusions can be drawn:

- Six new pipe welds have been fabricated with a range of wall-thickness, weld heat input and weld groove geometries. Residual stresses in each of the girth welded mock-ups were measured by neutron diffraction using the SALSA neutron diffractometer at the ILL, France and the contour method using the in-house facility at The Open University, UK.

- The measured residual stress profiles have been compared with each other and good agreement was found in most of the cases. However, there was some discrepancy with the neutron measurements at the weld centre line of half inch thick pipes which is believed to be associated with uncertainties in stress-free lattice parameter measurements for austenitic weld metal owing to compositional variations, texture, large grain sizes or plasticity. Overall the contour method measurements provided more consistent results than the neutron measurements especially in the weld metal.
- A novel approach based on the application of artificial neural networks has been developed that can characterise the through-wall distribution of residual stress at the centre-line of a stainless steel pipe girth weld, providing the weldment type lies within the boundary of the training data envelope used.
- The best estimate prediction of stresses using ANN is validated by diverse experimental techniques such as neutron diffraction, incremental deep hole drilling and contour method measurements in four mock ups made of different geometry and welding parameters.
- The ANN approach has been validated by comparing predicted profiles with a comprehensive range of new experimental measurements and the robustness of the developed approach has been demonstrated by performing sensitivity studies with input parameters and training data.
- The training data sensitivity studies demonstrate that adding more experimental data can improve the predictions significantly. Therefore the ANN approach should be essentially linked with a large database of experimental measurements to realise its full potential.
- An ANN based method for providing upper bound profiles has been developed that can consistently provide bounding through-thickness profiles relative to the experimental data.

- The ANN upper bound profiles were found to be more realistic and consistent than profiles recommended in API 579 and the R6 procedure both in axial and hoop directions.
- Stress intensity factors were determined from different upper bound profiles for various cases using R-code software and compared with the SIFs based on measured data. The ANN upper bound profiles were found to provide more pragmatic estimates of stress intensity factors than profiles recommended in assessment codes assuming a circumferentially and axially oriented internal surface breaking extended crack in three different mock-ups.

Future work

The findings in this project are expected to make a significant impact in the area of modelling and measurement of residual stresses as they can provide an alternative approach for prediction of residual stresses in welded components. Future potential research activities are described below,

1. **Application of the neural network based method to a different material and/or weld geometry**
    - Ferritic steels are of special interest as predicting residual stresses has been notoriously difficult because of microstructural changes and phase transformation effects.
    - Application of the method in a different weld geometry such as butt welded plates, T joints or nozzle welds. The governing input parameters needed to train the artificial neural network will have to be identified to determine the efficacy of the developed approach.

2. **Analyse contour method measured data to train the NN to model a stress map**

Experimental measurements using Contour method in six mock ups (STYLE mock-ups MU4-1 and MU4-3, Esshete and three half inch thick pipes) for determining the hoop stresses were performed in the PhD project. All six measurements results obtained are of high quality (for example, refer Figure 3.61) and hence the contour measured data can be used to train the ANN for modelling the 2-D hoop stress map of an arbitrary pipe of given geometry and weld parameters which is within the input parameter space. This is considered to be more challenging with the inclusion of more complex factors with particular attention to the modelling of weld fusion boundary profile. It would also hold the advantage of being the first mathematically modelled stress map of a weldment without use of the finite element approach.

3. Implementation of the Bayesian technique

Future work developing the approach should consider full implementation of the Bayesian technique using an evidence framework [169] as it is desirable for optimising neural network parameters. This includes development of an iterative technique to optimise the network weights and hyper-parameters. Moreover it is possible to quantify modelling uncertainty by evaluating the inverse of the Hessian matrix of the regularised error function. In the Bayesian approach, a suitable prior distribution of weights is considered before observing the data instead of a single set of weights. The Bayesian technique holds several other advantages such as model comparison and automatically embodies Occam razor that penalizes over-complex models. Instead of considering a single solution to the problem, the Bayesian technique takes into account an entire distribution of solutions and does not require a separate cross-validation data set.

4. Software development

A funding of £2000 was secured for software development by winning The Open University enterprise competition held in July, 2013. The objective of the proof-of-principle study was to develop a software prototype capable of reading the input data for the excel spreadsheet, training the network followed by generating output for a given set of data provided by the user without having MATLAB application installed in the target machine. The attempt to create a software prototype was carried out by invoking the .NET assembly (made from MATLAB library) from the user interface through the DLL file. Figure 6.1 shows a screenshot of the developed user interface.

Role of Consultant

The user interface was developed by the consultant using Microsoft .NET technologies targeting Microsoft windows desktop operating system. The user interface takes input from the end user, invoke the MATLAB library to perform the analysis, feedback the user and

store the analysis output. The format of the input and output files and the feedback display requirements was designed to cater the needs of the end user.

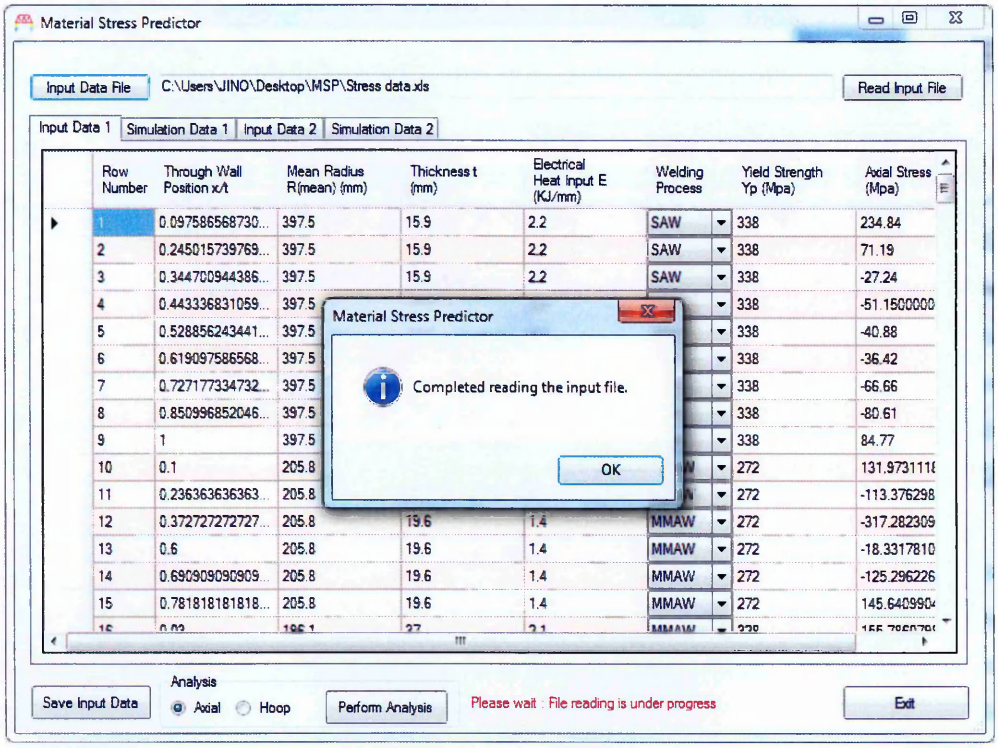

Figure 6.1. Screenshot of the developed user interface.

Miscellaneous problem with integration

MATLAB doesn't allow compiling a program that trains a neural net (Mathworks [173] prohibits for commercial reasons). However, this was identified in the final stages of the proof-of-principle study. Compiled programs can work with pre-trained neural nets, but this may not of much use as it is no longer dynamic. A possible way to get around this problem is to transform the Matlab function to python script and then create a .NET assembly. There are many Python open source alternatives for Matlab Neural Network Toolbox [167] such as Pybrain [174], neurolab [175] and FFnet [176]. It requires re-writing the Matlab code in python scripting language followed by optimisation and integration with the interface.

Forthcoming activities

The neural network approach has the potential to be used in future fracture assessments of welded components and has generated significant interest among external industrial stakeholders. One of the possible routes for industrial application will be to include the prototype in the R-Code software [172], developed and maintained by EDF Energy. The database of residual stress measurements such as the one developed by VEQTER [177] should be essentially linked to the software to exploit its full potential.

Appendix 1

Back-propagation algorithm and network hyper-parameters

Error Back-propagation algorithm

The back-propagation algorithm has been used in the training process of the ANN and is central to the work presented in this dissertation. The mathematical description of working of the algorithm as reproduced from [140].

Consider p as the number of input units and μ the number of input patters $\mu = 1, 2, 3.....p$

For an input pattern μ, the input to node j in the hidden layer is

$$h_j^{\mu} = \sum_k w_{jk} \xi_k^{\mu} \qquad (1)$$

And the activation of the hidden node becomes

$$V_j^{\mu} = g\left(h_j^{\mu}\right) = g\left(\sum_k w_{jk} \xi_k^{\mu}\right), \qquad (2)$$

where g is the sigmoid function. Output unit is

$$h_j^{\mu} = \sum_j W_{ij} V_j^{\mu} = \sum_j W_{ij} g(\sum_k w_{jk} \xi_k^{\mu}) \quad (3)$$

Substituting in the activation function g,

$$O_i^{\mu} = g(h_i^{\mu}) = g\left(\sum_j W_{ij} V_j^{\mu}\right) = g\left(\sum_j W_{ij} g\left(\sum_k w_{jk} \xi_k^{\mu}\right)\right) \qquad (4)$$

Error function is defined as (5),

$$E(w)=\frac{1}{2}\sum_{\mu,i}\left[\varsigma_i^{\mu}-O_i^{\mu}\right]^2=\frac{1}{2}\sum_{\mu,i}\left[\varsigma_i^{\mu}-g\left(\sum_j W_{ij}g\left(\sum_k w_{jk}\xi_k^{\mu}\right)\right)\right]^2=\frac{1}{2}\sum_{\mu,i}\left[\varsigma_i^{\mu}-\left(g\sum_j W_{ij}V_j^{\mu}\right)\right]^2$$

Using a gradient descent algorithm to determine weights (6),

$$\Delta W_{ij}=-\eta\frac{\partial E}{\partial W_{ij}}=\eta\left[\varsigma_i^{\mu}-O_i^{\mu}\right]g'\left(h_i^{\mu}\right)V_j^{\mu}=\eta\sum_n\delta_i^{\mu}V_j^{\mu}$$

For sigmoid functions the derivatives can be expressed as (7) and (8)

$$g'(h_i^{\mu})=O_i^{\mu}\left(1-O_i^{\mu}\right) \qquad (7)$$

$$\delta_i^{\eta}=O_i^{\mu}\left(1-O_i^{\mu}\right)\left(\varsigma_i^{\mu}-O_i^{\mu}\right) \qquad (8)$$

Weight changes from the hidden layer to the output layer giving,

$$\Delta W_{ij}=-\eta\frac{\partial E}{\partial W_{ij}}=\eta\sum_{\mu}\delta_i^{\mu}V_j^{\mu}=\eta\sum_{\mu}O_i^{\mu}\left(1-O_i^{\mu}\right)\left(\varsigma_i^{\mu}-O_i^{\mu}\right)V_j^{\mu} \qquad (9)$$

Applying chain rule we get (10),

$$\Delta W_{ij}=-\eta\frac{\partial E}{\partial W_{ij}}=-\eta\frac{\partial E}{\partial V_j^{\mu}}\frac{\partial V_j^{\mu}}{\partial W_{jk}}$$

Finally change in weights is given by (11),

$$\Delta W_{ij}=\eta\sum_{\mu}\delta_j^{\mu}\xi_k^{\mu}$$

where $\delta_j^{\mu}=g'\left(h_i^{\mu}\right)\sum_i W_{ij}\delta_i^{\mu}=V_j^{\mu}\left(1-V_j^{\mu}\right)\sum_i W_{ij}\delta_i^{\mu}$ (12)

The back-propagation algorithm has the following steps,

(1) Initialise weights to small random numbers

(2) Choose a pattern ξ_k^{μ} from the training set

(3) Propagate the activation through the network: $V_i^m=g\left(h_i^m\right)=g\left(\sum_j w_{ij}V_j^{m-1}\right)$ (13)

(4) Compute the deltas for output layer M: $\delta_j^M=g'\left(h_i^M\right)\left[\varsigma_i^{\mu}-V_i^M\right]$ (14)

(5) Compute the deltas for the preceding layer by successively propagating the error backwards $\delta_j^{m-1} = g'\left(h_i^{m-1}\right)\left(\sum_j w_{ji}{}^m \delta_j^m\right)$ (15)

(6) Use $\Delta w_{ij}{}^m = \eta \delta_i^m V_j^{m-1}$ to update connections given as $\Delta w_{ij}{}^{new} = \Delta w_{ij}{}^{old} + \Delta w_{ij}$ (16)

(7) Return to step 2 and repeat steps for next pattern

Network hyper-parameters

The hyper-parameters α (weight decay coefficient or regulariser) and β (coefficient controlling the variance in noise) greatly influences the complexity of the ANN model. Large value of α will constraint the interpolant to be smooth and too low a value will cause overfitting of the data. Hence it is important to have a balance between the hyper-parameters as the Bayesian error function is a function of both α and β. The values of hyper-parameters were determined using simplistic estimates as given in [169].

The optimum value of α and β implies that the total misfit $M = \alpha E_S + \beta E_D$ (17) satisfies the equation $2M = N$ (18),

In which case α and β should individually satisfy the condition $\alpha = \frac{1}{\sigma_w^2}$ and $\beta = \frac{1}{\sigma_v^2}$ (19)

Where $E_S = \frac{1}{2}\sum_{i=1}^{R}\{x - o(p,w)\}^2$ (20)

$E_R = \frac{1}{2}\sum_{i=1}^{R}|wi|^2$ (21)

and p is the input vector, w the weight vector, x the target value, o the output, σ_w standard deviation of weight vector and σ_v is the standard deviation of the output data.

References

[1] Withers, P.J. (2007) Residual stress and its role in failure. Reports on Progress in Physics.70, p2211-2263.

[2] Withers, P.J., Bhadeshia, H. K. D. H., (2001) residual stress Part 2 – Nature and origins. Mater. Sci. Tech. 17, p366-375.

[3] Leggatt, R.H., (2008) Residual stresses in welded structures. Int. J. Pres. Ves. Pip. 85, p144-151.

[4] Procedure R6 Revision 4, Assessment of the integrity of structures containing defects, Gloucester: British Energy Ltd; 2011.

[5] BBC news, "EDF shuts two nuclear power stations temporarily", 2014.[online]. Available: http://www.bbc.co.uk/news/business-28738074. [Accessed:13-Aug-14].

[6] EDF Energy "Life extension of the EDF Energy nuclear fleet", 2013.

[7] British standards Institution, Guide to methods for assessing the acceptability of flaws in metallic structures, BS 7910:2013.

[8] API 579-1/ASME FFS-1, Fitness-for-Service, Second edition January 2007.

[9] Zhou, J., Tsai, H.L. Feng, Z., (2005) Welding heat transfer, processes and mechanisms of welding residual stress and distortion. Woodhead Publishing in Materials, p32–98.

[10] Bishop, C.M. (1994) Neural networks for Statistical Pattern Recognition. Oxford University Press, Oxford, United Kingdom.

[11] Bishop, C.M. (1994) Neural networks and their applications. *Rev. Sci. Instrum.* 65 (6), p1803-1833.

[12] Hutchings, M.T., Withers, P.J., Holden, T.M., Lorentzen, T. (2005) Introduction to the characterization of residual stress by neutron diffraction: Taylor and Francis, London.

[13] Francis, J.A. Bhadeshia, H.K.D.H. and Withers, P.J. (2007) Welding residual stresses in ferritic power plant steels. *Mater. Sci. Technol.* 23, p1009-1020.

[14] Withers, P.J., Bhadeshia, H.K.D.H. (2001) Residual stress Part 1– Measurement techniques. *Mater. Sci. Technol.* 17, p355-365.

[15] Cordiano, H. V. (1970) Effect of residual stress on the low cycle fatigue life of large scale weldments in high strength steel. *ASME J. Eng. Ind.* 92, p86-92.

[16] Bouchard, P. J. (2001) Residual stresses in lifetime and structural integrity assessment. *Encyclopedia of Materials: Science and Technology*. Oxford, UK: Elsevier, p8134–8142.

[17] Webster, G.A., Ezeilo, A.N. (2001) Residual stress distributions and their influence on fatigue lifetimes. *Third International Conference on Fatigue Damage of Structural Materials*, pS375-S383.

[18] Bouchard, P. J. (2007) Validated residual stress profiles for fracture assessments of stainless steel pipe girth welds. *Int. J. Pressure Vessels Piping*. 84, p195-222.

[19] Cerjak, H. (2008) The role of welding in the power generation industry. Houdremont Lecture, 61st IIW Annual Assembly, Graz.

[20] Bate, S.K., Green, D. (1997) A review of the residual stress distributions in welded joints for the defect assessment of offshore structures. Health and safety executive: Offshore technology report OTH 482.

[21] Materials UK. (2007) "Fossil-fuelled power generation," Materials UK Energy Review, Report 2.

[22] Honeycombe, R.W.K. (1981) Steels: Microstructure and properties. Edward Arnold, London.

[23] Marshall, P. (1984) Austenitic stainless steels: Microstructure and mechanical properties. Elsevier applied science publishers, London.

[24] Paddea, S., Francis, J.A., Paradowska, A.M., Bouchard, P.J. et al. (2012) Residual stress distributions in a P91 steel-pipe girth weld before and after post weld heat treatment. *Materials Science and Engineering A*. 534, p663-672.

[25] Zdhanov, I.M., Gonchar, A.K. (1978) Determining the residual stresses at a depth in metal. *Autom. Weld.* 31 (9), p22–4.

[26] Leggatt, R.H. (1986) Residual stresses and distortion in multi-pass butt welded joints in type 316 stainless steel. *Residual Stresses Sci. Technol.* 2, p997–1004.

[27] Leggatt, R.H. (1984) Residual stresses at girth welds in pipes. Welding in energy related projects. Oxford: Pergamon, p429–40.

[28] Ogawa, K., Chidwick, L.O., Kingston, E.J., Dennis, R.J., et al. (2008) The measurement and modelling of residual stresses in a stainless steel pipe girth weld. *ASME Pressure Vessels & Piping Division Conference*, Chicago, Illinois, USA, July 27-31, PVP2008-61542, p527-534.

[29] Haigh, R.D., Hutchings, M.T., James, J.A., Ganguly. S. et al. (2013) Neutron diffraction residual stress measurements on girth welded 304 stainless steel pipes with weld metal deposited upto half and full pipe wall thickness. *Int. J. Pressure Vessels Piping*. 101. p1-11.

[30] Veqter (2014) Residual stress measurement techniques [Online]. http://www.veqter.co.uk. Accessed 24 December 2014

[31] TWI (2014) Residual stress measurement techniques [Online]. http://www.twi-global.com/ [Accessed 17 March 2015].

[32] Grant, P.V., Lord, J.D., Whitehead, P.S. (2006) Measurement of residual stresses by the incremental hole drilling technique. Measurement good practice guide No. 53-Issue 2.

[33] ASTM (2008) Determining residual stresses by the Hole-drilling Strain-Gage Method.

[34] ASME (2012) Hole drilling [Online]. http://www.asminternational.org/emails/etsspraytips/090809/tssenews090809.html. [Accessed 24 December 2014].

[35] Ueda, Y., Fukuda, K., Endo, S. (1989) New measuring method of three dimensional residual stresses in long welded joints using inherent strains as parameters. *Trans. ASME, J. Engng Mater. Technol.*, 11, p1-8.

[36] Liwu, W., Weijing, H., Smith, S. (2011) The effects of loadings on welding residual stresses and assessment of fracture parameters in a welding residual stress field. *ASME Pressure Vessels & Piping Division Conference*, Baltimore, Maryland, USA, July 17-21, 2011, PVP2011-57518, p1503-1513.

[37] Rybicki, E.F., Shadley, J.R. (1986) A three dimensional finite element evaluation of a destructive experimental method for determining through thickness residual stresses in girth welded pipes. *Journal of Engineering Materials and Technology*, 108, p99-106.

[38] Leggatt, R. H., Smith, D. J., Smith, S. D., Faure, F. (1996) Development and Experimental Validation of the Deep Hole Drilling Method for Residual Stress Measurement. *Journal of Strain Analysis*. 31(3), p177-186.

[39] Kingston, E.J. Advances in the deep hole drilling technique for residual stress measurement. PhD thesis, 2003: University of Bristol

[40] George, D. Kingston, E., Smith, D.J. (2000) Measurement of through thickness stresses using small holes. *Journal of Strain Analysis*. 37 (2), p125-139.

[41] Goudar, D.M., Truman, C.E., Smith, D.J. (2011) Evaluating uncertainty in residual stress measured using the deep hole drilling technique. *Journal of strain*. 47, p62-74

[42] Smith, D.J., Bouchard, P.J., George, D. (2000) Measurement and prediction of residual stresses in thick-section steel welds. *Journal of Strain Analysis*. 35 (4), p287-305.

[43] Hossain, S., Residual Stresses under Conditions of High Triaxiality, PhD. Thesis, Bristol, University of Bristol, 2005.

[44] Mahmoudi, A. H., Hossain, S., Pavier, M. J., Truman, C. E., Smith , D. J. (2009) A New Procedure to Measure near yield residual stresses using the deep hole drilling technique. *Exp. Mech.* 49, p595-604.

[45] Mahmoudi, A. H., Pavier, M. J., Truman, C. E., Smith, D. J. (2007) Accurate Measurement of Highly Triaxial Residual Stresses. The Society of Experimental Mechanics (SEM), USA.

[46] Prime, M.B. and Gonzales, A.R. (2000) The contour method: simple 2-D mapping of residual stresses. Proceedings of the sixth international conference on residual stresses, 10-12 July, Oxford, UK, 1, p617-624.

[47] Prime, M.B. (2001) Cross-sectional mapping of residual stresses by measuring the surface contour after a cut. *Journal of Engineering Materials and Technology*. 123 (2), p162-168

[48] Bueckner, H.F. (1958) The propagation of cracks and the energy of elastic deformation. *Transactions ASME*, 80, p1225-1230.

[49] Zhang, Y., Ganguly, S., Edwards, L., Fitzpatrick, M.E. (2004) Cross-sectional mapping of residual stresses in a VPPA weld using the contour method. *Acta Materialia*. 52, p5225-5232.

[50] Turski, M., Edwards, L. (2009) Residual stress measurement of a 316 L stainless steel bead-on-plate specimen utilising the contour method. *Int. J. Pressure Vessels Piping*. 86, p126-131.

[51] Brown, D.W., Holden, T.M., Clausen, B., Prime, M.B. et al. (2011) Critical Comparison of Two Independent Measurements of Residual Stress in an Electron-Beam Welded Uranium Cylinder: Neutron Diffraction and the Contour Method. *Acta Materialia.* 59 (3), p864-873.

[52] Pagliaro, P., Prime, M.B., Robinson, J.S., Clausen, B. et al. (2010) Measuring inaccessible residual stresses using multiple methods and superposition. *Exp. Mech.* 51 (7), p1123-1134.

[53] Johnson, G. (2008) Residual stress measurements using the contour method. Ph.D. Dissertation, University of Manchester.

[54] Zhang, Y., Ganguly, S., Stelmukh, V., Fitzpatrick, M.E. et al. (2003) Validation of the Contour Method of Residual Stress Measurement in a MIG 2024 Weld by Neutron and Synchrotron X-ray Diffraction. *Journal of Neutron Research.* 11 (4), p181-185.

[55] Hosseinzadeh, F., Toparli, M. B., Bouchard, P. J. (2012) Slitting and Contour Method Residual Stress Measurements in an Edge Welded Beam. *Journal of Pressure Vessel Technology.* 134, p114021-26.

[56] Zhang, Y., Pratihar, S., Fitzpatrick, M.E., Edwards, L. (2005) Residual stress mapping in welds using the contour method, *Materials Science Forum.* 490/491. p294-299.

[57] Traore, Y., Paddea, S., Bouchard P.J., Gharghouri, M. (2013) Measurement of the Residual Stress Tensor in a Compact Tension Weld Specimen, *Exp. Mech.* 53 (4), p605-618.

[58] Prime, M. B., Kastengren, A. L. (2010) The Contour Method Cutting Assumption: Error Minimization and Correction. *Experimental and Applied Mechanics.* 6, p233-250.

[59] Traoré, Y., Hosseinzadeh, F., Bouchard, P. J., (2014) Plasticity in the Contour Method of Residual Stress Measurement. *Advanced Materials Research.* 996, p337-342.

[60] Hosseinzadeh, F., Kowal, J., and Bouchard, P. J. (2014) Towards good practice guidelines for the contour method of residual stress measurement. *The Journal of Engineering.* (Online only).

[61] Pagliaro, P., Prime, M.B., Swenson, H., Zuccarello, B. (2010). Measuring multiple residual-stress components using the contour method and multiple cuts. *Exp. Mech.* (50), p187-194.

[62] Hosseinzadeh, F., Bouchard, P.J. (2012) Mapping Multiple Components of the Residual Stress Tensor in a Large P91 Steel Pipe Girth Weld Using a Single Contour Cut, *Exp. Mech.* 53 (2), p171-181.

[63] Prime M, Sebring R, Edwards J, Hughes D, Webster P (2004) Laser surface-contouring and spline data-smoothing for residual stress measurement. *Exp. Mech.* 44 (2), p176-184

[64] Hosseinzadeh, F., Bouchard, P.J. (2011) Residual stress measurement in a welded P91 pipe using the contour method. *ASME Pressure Vessels & Piping Division Conference*, Baltimore, Maryland, USA, July 17-21, 2011, PVP2011-57526.

[65] Fitzpatrick, M.E. Fry, A.T., Holdway, P., Kandil, F.A., Schackleton, J. et al., (2005) Determination of residual stresses by X-ray diffraction. Measurement good practice guide No. 52- Issue 2.

[66] Ganguly, S., Fitzpatrick, M.E., Edwards, L. (2007) Use of Neutron and Synchrotron X-ray diffraction for evaluation of residual stresses in a 2024-T351 Aluminium alloy variable polarity plasma arc weld. *Metallurgical and Materials transactions A*. 37A, p411-420.

[67] Liljedahl, C.D.M., Zanellato, O., Edwards, L, Fitzpatrick, M.E. (2007) Evolution of residual stresses with fatigue crack in a variable polarity plasma arc-welded aluminium alloy compact tension specimen. *Metallurgical and Materials transactions A*.39A, p2370-2377.

[68] Pratihar, S., Stelmukh, V., Hutching, M.T., Fitzpatrick, M.E. et al. (2006) Measurement of the residual stress field in MIG-welded Al-2024 and Al-7150 aluminium alloy compact tension specimens. *Material Science and Engineering A*. 437, p46-53.

[69] Neeraj, T., Herold, T.G., Prask, H.J., Ayer, R. (2011) Residual stresses in girth welds of carbon steel pipes: neutron diffraction analysis. *Science and Technology of welding and joining*. 16 (3), p249-253.

[70] Webster, G.A., Wimpory, R.C. (2002) Development of procedures for the measurement of residual stress by neutron diffraction. *Appl. Phys. A*. 74, p1227-1229.

[71] Cullity, B.D. (1956) Elements of X-ray diffraction Addison Wesley Publications, Reading, Massachusetts.

[72] Braggs law [Online]. Available: http://ralc.tistory.com/980: Accessed [19-Nov-2014].

[73] Fitzpatrick, M.E., Lodini, A. (2003) Analysis of residual stress by neutron and synchrotron radiation. Taylor and Francis.

[74] Withers, P.J., Preuss, M., Steuwer, A., Pang, J.W.L. (2007) Methods for obtaining the strain-free lattice parameter when using diffraction to determine residual stress. *J. Appl. Cryst.* 40, p. 891-904.

[75] Webster, G. A., Youtsos, A. G., Ohms, C., Wimpory. R. C. (2004) Draft Standard for the Measurement of Residual Stresses by Neutron Diffraction. Recent Advances in Experimental Mechanics SE - 44, E. Gdoutos, Ed. Springer Netherlands, p467–476.

[76] Webster, G. A. (2001) Polycrystalline Materials – Determinations of Residual Stresses by Neutron Diffraction. ISO/TTA3 Technology Trends Assessment.

[77] Kandil, F. A., Lord, J. D., Fry, A. T. and Grant, P. V. (2001) A Review of Residual Stress Measurement Methods – A Guide to Technique Selection. NPL Report MATC (A) 04.

[78] Woo, W., An, G.B., Kingston, E.J., DeWald, A.T. et al. (2013) Through-thickness distributions of residual stresses in two extreme and deep hole drilling study. *Acta Materialia*. 61, p3564–3574.

[79] Asadi, M. and Goldak, J.A. (2011) A framework for designer driven exploration of computational weld mechanics design space. *ASME Pressure Vessels & Piping Division Conference*, Baltimore, Maryland, USA, July 17-21, 2011, PVP2011-57917, p1633-1642.

[80] Lewis, S.J., Alizadeh, H., Gill, C., Vega, A. et al. (2009), Modelling and measurement of residual stresses in autogenously welded stainless steel plates: Part 1 – fabrication and modelling. *Int. J. Pressure Vessels Piping*. 86, p798-806.

[81] Yaghi, A.H., Hyde, T.H., Becker, A.A., Sun, W. et al. (2010) A comparison between measured and modelled residual stresses in a circumferentially butt-welded P91 steel pipe. *Journal of Pressure Vessel Technology*. 132 (1).

[82] Bate, S. and Hurrell, P. (2010) The development of tools and methods to manage residual stresses in the future design of nuclear plant. *Int. J. Pressure Vessels Piping*. 87, p637-642.

[83] ABAQUS (2010) ABAQUS/standard documentation version 6.10.2 ABAQUS, Inc.

[84] Smith, M.C., Bouchard, P. J., Turski, M., Edwards, L., Dennis, R. J. (2012) Accurate prediction of residual stress in stainless steel welds. *Comp. Mater. Sci.* 54, p312-28.

[85] Lemaitre, J., Chaboche, J.L., (1990) Mechanics of Solid Materials, Cambridge University Press.

[86] Bouchard, P.J. (2009) The NeT bead-on-plate benchmark for weld residual stress simulation. *Int. J. Pressure Vessels Piping*. 86, p31-42.

[87] Gilles, P., Ahmar, W.E., Jullien, J.F. (2009) Robustness analyses of numerical simulation of fusion welding NeT-TG1 application: ''Single weld-bead-on-plate''. *Int. J. Pressure Vessels Piping*. 86, p3-12.

[88] Ficquet, X., Smith, D.J., Truman, C.E., Kingston, E.J., Dennis, R.J. (2009) Measurement and prediction of residual stress in a bead-on-plate weld benchmark specimen. *Int. J. Pressure Vessels Piping*. 86, p20-30.

[89] Bate, S.K., Charles, R., Warren, A. (2009) Finite element analysis of a single bead-on-plate specimen using SYSWELD. *Int. J. Pressure Vessels Piping*. 86, p73-78.

[90] Ohms, C., Wimpory, R.C., Katsareas, D.E., Youtsos, A.G. (2009) NET TG1: Residual stress assessment by neutron diffraction and finite element modeling on a single bead weld on a steel plate. *Int. J. Pressure Vessels Piping*. 86, p63-72.

[91] Smith, M.C., Smith, A.C., Wimpory, R., Ohms, C. (2014) A review of the NeT Task Group 1 residual stress measurement and analysis round robin on a single weld bead-on-plate specimen. *Int. J. Pressure Vessels Piping*. 120-121, p93-140.

[92] Smith, M.C., Muransky, O., Smith, D.J., Do., S.C., Bouchard, P.J. et al. (2014) Modelling and measuring residual stresses in pipe girth welds – lessons from the style framework 7 project. *ASME Pressure Vessels & Piping Division Conference*, Anaheim, California, USA, July 20-24, 2014, PVP2014-29005.

[93] Dennis, R.J., Leggatt, N.A., Smith, M.C., Bouchard, P.J. (2010) R6 weld modelling guidelines-application to groove weld worked example. *ASME Pressure Vessels & Piping Division Conference*, Bellevue, Washington, USA, July 18-22, 2010, PVP2014-29005, p1435-1448.

[94] Teng, T.L., Chang, P.H. (1997) A study of residual stresses in multi-pass girth-butt welded pipes. *Int. J. Pressure Vessels Piping*. 74, p59-70.

[95] Katsuyama, J., Onizawa, K. (2011) Analytical study of the relaxation of welding residual stress by excessive loading for austenitic stainless steel piping welds. *Journal of Pressure Vessel Technology*,133 (3).

[96] Ogawa, K., Chidwick, L.O., Kingston, E.J., Dennis, R. et al. (2008) The measurement and modelling of residual stresses in a stainless steel pipe girth weld. *ASME Pressure Vessels & Piping Division Conference*, Chicago, Illinois, USA, July 27-31, 2008, PVP2008-61542, p527-534.

[97] Muranky, O., Smith, M.C., Bendeich, P.J., Hamelin C.J. et al. (2012) Prediction and measurement of weld residual stresses in thermally aged girth-welded austenitic

steel pipes. *ASME Pressure Vessels & Piping Division Conference*, Toronto, Ontario, Canada, July 15-19, 2012, PVP2012-61542, p1147-1156.

[98] Elcoate, C.D., Dennis, R.J. Bouchard, P.J., Smith, M.C. (2005) Three dimensional multi-pass repair weld simulations. *Int. J. Pressure Vessels Piping*. 82: p244-257.

[99] Dong, P., Hong, J.K., Bouchard, P.J. (2005) Analysis of residual stresses at weld repairs. *Int. J. Pressure Vessels Piping*. 82, p258-269.

[100] Dong, P., Brust, F.W. (2000) Welding Residual stresses and effects on fracture in pressure vessel and piping components: A Millennium review and beyond. *ASME J. Press. Vessel Technol.* 122, p329-338.

[101] Budden, P. J., Sharples, J. K., (2003) Treatment of secondary stresses. *Comprehensive structural Integrity*. 7.07, p245-287.

[102] Bouchard, P.J., Withers, P.J. (2006) Identification of residual stress length scales in welds for fracture assessment. Proceedings of the ECF16, Alexandroupolis, July.

[103] Bouchard, P.J., Withers, P.J. (2004) The relevance of residual stress length scale in structural integrity. *J. Neutron Res.* 12 (1-3). p81-91.

[104] Bouchard, P. J. (2008) Code characterisation of weld residual stress levels and the problem of innate scatter. *Int. J. Pressure Vessels Piping*. 85, p152-165.

[105] Hayes, D.J. (1975) Origins of the stress intensity factor approach to fracture. *Journal of Strain analysis*. 10, p198-200.

[106] Hayes, D.J. (2009) Origins of the energy balance approach to fracture. *Journal of Strain analysis*. 1975. 10 (4), p195-197.

[107] Budden, P.J., Sharples, J.K., Dowling, A.R. (2000) The R6 procedure: recent developments and comparison with alternative approaches. *Int. J. Pressure Vessels and Piping*. 77, p895-903.

[108] Lin, Y.C., Xie, Y.J. and Wang, X.H. (2004) Probabilistic fracture failure analysis of nuclear piping containing defects using R6 method. *Nuclear Engineering and Design*. 229, p237-246.

[109] Burdekin, F.M., (1981) Practical aspects of fracture mechanics in engineering design. *Proceedings of the institution of mechanical engineers*. 195, p73-86

[110] Bao, R, Zhang, X. and Yahaya, N.A. (2010) Evaluating stress intensity factors due to weld residual stress by the weight function and finite element methods. *Engineering fracture mechanics*. 77, p2550-2566.

[111] Dong, P., (2011) On the mechanics of residual stresses in girth welds. *Journal of Pressure Vessel Technology*. 129, p345-354.

[112] Dong, P. (2008) Length scale of secondary stresses in fracture and fatigue, *Int. J. Pressure Vessels Piping*. 85, p128–143.

[113] Dong, P. and Hong, J.K., (2006) On the residual stress profiles in new API 579 Appendix E," IIW Doc.X-1612-2006/XI-852.

[114] Dong, P., Zhang, J. (1999) Residual stresses in strength-mismatched welds and implications on fracture behaviour, *Engineering Fracture Mechanics*, 64 (4), p485-505.

[115] Dong, P., Shaopin, S., Jinmiao, Z., Myung, H.K. (2014) on residual stress precriptions for fitness for service assessment of pipe girth welds, *Int. J. Pressure Vessels Piping*. 123-124, p19–29.

[116] Brickstad, B., Josefson, B.L (1998). A parametric study of residual stresses in multi-pass butt-welded stainless steel pipes. *Int. J. Pressure Vessels Piping*. 75, p11-25.

[117] Bradford, R.A.W (2000). Through-thickness distributions of welding residual stresses in austenitic stainless steel cylindrical butt welds. Proceedings of the ICRS-6. IOM Communications Ltd., p1373-81.

[118] Bouchard, P.J., Bradford, R.A.W. (2000) Validated axial residual stress profiles for fracture assessments of austenitic stainless steel pipe girth welds. [online]. http://rickbradford.co.uk/BouchardandBradford.pdf. [Accessed:13-Aug-14]

[119] Daymond, M.R., Johnson, M.W., Sivia, D.S. (2002) Analysis of neutron diffraction strain measurement data from a round robin sample. *Journal of strain analysis*. 37 (1), p73-85.

[120] Teng, H., Bate, S.K., Beardsmore, D.W. (2008) Statistical analysis of residual stress profiles using a heuristic method. *ASME Pressure vessels & Piping division Conference*, Chicago, Illinois, USA, July 27-31, PVP2008-61378, p37-42.

[121] Teng, H., Bate, S.K., Beardsmore, D.W. (2009) Determination of residual stress profiles of pipe girth weld using a unified parametric function form. *ASME Pressure vessels & Piping division Conference*, Prague, Czech Republic, USA, July 26-30, PVP2009-77316, p381-388.

[122]Teng, H., Bate, S.K. (2014) Residual stress profiles of pipe girth weld using a stress decomposition method. *ASME Pressure Vessels & Piping Division Conference*, Anaheim, California, USA, July 20-24, 2014, PVP2014-28247.

[123] Sivia, D.S, Skilling, J. (2006) Data Analysis: A Bayesian tutorial, 2nd edition. Oxford University Press Inc, New York.

[124] Nadri, B., Bouchard, P.J., Truman, C.E., Smith, D.J. (2008) A statistical framework for analysing weld residual stresses for structural integrity assessment. *ASME Pressure vessels & Piping division Conference*, Chicago, Illinois, USA, July 27-31, PVP2008-61339, p369-376.

[125] Nadri, B., Bouchard, P.J., Smith, M.C., Truman, C.E. (2007) Statistical analysis of residual stresses in a stainless steel edge welded beam. *ASME Pressure vessels & Piping division Conference*, San Antonio, Texas, USA, July 22-26, PVP2007-26265, p1013-1020.

[126] Nadri, B., Bouchard, P.J., Truman, C.E., Smith, M., Smith, D.J. (2010) Modelling and statistical treatment of residual stress distributions in an edge welded stainless steel beam. *Journal of strain*. 47(6), p505-517.

[127] Nadri, B., Bouchard, P.J., Truman, C.E., Smith, M.C., Smith, D.J. (2009) Statistical analysis of pipe girth weld experimental residual stress data. *ASME Pressure vessels & Piping division Conference*, Prague, Czech Republic, July 26-30, PVP2009-77571, p491-500.

[128] Bouchard, P.J., Nadri, B., Smith, M.C., Truman, C.E. (2011) Residual stress profiles for structural integrity assessments of pipe girth welds. Draft.

[129] Wimpory, R.C., Ohms, C., Hofmann, M., Schneider, R., Youtsos. (2009) A.G. Statistical analysis of residual stress determinations using neutron diffraction. *Int. J. Pressure Vessels and Piping*. 86, p48-62.

[130] Pirling, T., Bruno, G., Withers, P.J. (2006) SALSA, a new concept for strain mapping at the ILL. *Mater. Sci. Eng. A*, 437, p. 139-44.

[131] Rybicki, E.F. and Shadley, J.R. (1986) A three dimensional finite element evaluation of a destructive experimental method for determining through thickness residual stresses in girth welded pipes, *Journal of Engineering Materials and Technology*. 108, p99-106.

[132] Heussner, S., Nicak, T., Keim, E. STYLE – A European project on structural integrity: Progress of the work after two years. Report: Areva NP Gmbh. Germany

[133] Non-destructive testing (2005) Standard test method for determining residual stresses by neutron diffraction DD CEN ISO/TS21432.

[134] LAMP, the Large Array Manipulation Program. [online] http://www.ill.eu/data_treat/lamp/the-lamp-book/ [Accessed: 23-October-14]

[135] Boor, C. (2000) Spline toolbox user's guide. The Math Works, Inc., Natick, MA, p. MATLAB.

[136] Hosseinzadeh, F., Bouchard, P.J. (2011) Residual stress measurement in a welded P91 pipe using the contour method. *ASME Pressure Vessels & Piping Division Conference*, Baltimore, Maryland, USA, July 17-21, 2011, PVP2011-57526.

[137] Withers, P.J., Preuss, M., Steuwer, A., Pang, J.W.L. (2007) Methods for obtaining the strain-free lattice parameter when using diffraction to determine residual stress. *J. Appl. Cryst.* 40, p. 891-904.

[138] Manufacturing of additional Esshete 1250 specimens for materials testing (2006), Report 16718/1/06 EDF Energy.

[139] Muranky, O., Smith, M.C., Bendeich, P.J., Hamelin C.J. et al. (2012) Prediction and measurement of weld residual stresses in thermally aged girth-welded austenitic steel pipes. *ASME Pressure Vessels & Piping Division Conference*, Toronto, Ontario, Canada, July 15-19, 2012, PVP2012-61542, p1147-1156.

[140] Pfeifer, R., Damian, D., Fuchslin, R. (2010) Neural networks. University of Zurich. Switzerland.

[141] Rumelhart, D.E., Hinton, G.E., Williams, R.J. (1986) Learning representations by back-propagating errors. *Nature*. 323, p533-536.

[142] Rosenblatt, F. (1958) The perceptron: A probabilistic model for information storage and organisation in the brain. *Psychol. Rev.* 65, p386-408.

[143] Moller, M. (1993) A scaled conjugate algorithm for fast supervised learning. *Neural Networks*. 6, p525-533.

[144] Bellman, R.E. (1961) Adaptive Control Processes. Princeton University Press, Princeton, NJ.

[145] Perrone, M. P. (1994) General averaging results for convex optimization. In M. C. Mozer et al. (Eds.), Proceedings 1993 Connectionist Models Summer School, p. 364-371.

[146] Perrone, M. P. and L. N. Cooper (1993) When networks disagree: ensemble methods for hybrid neural networks. In R. J. Mammone (Ed.), *Artificial Neural Networks for Speech and Vision*, p126-142.

[147] Yescas, M.A., Bhadeshia, H.K.D.H. and Mackay, D.J. (2001) Estimation of the amount of retained austenite in austempered ductile irons using neural networks. *Material Science and Engineering.* A311, p162-173.

[148] Ticknor, J.L. (2013) A Bayesian regularised artificial neural network for stock market forecasting. *Expert systems with applications.* 40, p5501-5506.

[149] Yacef, R., Benghanem, M., Mellit, A. (2012) Prediction of daily global solar irradiation data using Bayesian neural network: A comparative study, *Renewable energy* vol 48, p146-154.

[150] Bezazi, A., Pierce, S.G., Worden, K., Harkati, E.H. (2007) Fatigue life prediction of sandwich composite materials under flexural tests using a Bayesian trained artificial neural network. *International journal of fatigue.*29, p738-747.

[151] Gavard, L., Bhadeshia, H.K.D.H., Mackay, D.J.C., Suzuki, S. (1996) Bayesian neural network model for austenite formation in steels. *Material science and technology.* 12, p453-463.

[152] Maiti, S., Tiwari, R.K. (2010) Neural network modelling and an uncertainty analysis in Bayesian framework: A case study from the KTB borehole site, *J. Geophys. Res.* 115, B10208, p1-28.

[153] Ojha, M., Maiti, S. (2013) Sediment classification using neural networks: An example from the site-U1344A of IODP Expedition 323 in the Bering sea. *Deep-sea Res.* II (In press).

[154] Paoli, C., Voyant, C., Muselli, M. and Nivet, M.L. (2010) Forecasting of pre-processed daily solar radiation time series using neural networks. *Solar energy.* 84, p2146-2160.

[155] Papadopoulos, V., Giovanis, D.G., Lagaros, N.D., Papadrakakis, M. (2012) Accelerated subset simulation with neural networks for reliability analysis. *Comput. Methods Appl. Mech. Engrg.* 223-224, p70-80.

[156] Lim, D.H., Bae, L.H, Na, M.G. and Kim, J.W. (2010) Prediction of residual stresses in the welding zone of dissimilar metals using data based models and uncertainty analysis. *Nuclear engineering and technology*. 39 (4), p337-348.

[157] Na, G.M., Kim, J.W., Lim, D.H, Kang, Y.J. (2008) Residual stress prediction of dissimilar metals welding at NPPs using support vector regression. *Nuclear engineering and Design*. 238, p1503-1510.

[158] Dimitriu R.C. and Bhadeshia, H.K.D.H. A neural network model for residual stress. [Online]. http://aiforia.com/documents/radu.pdf/ p43-51. [Accessed:18-September, 14]

[159] Klein, R. Mucino, V.H., Klinckhachorn, P. (2002) Predicting the elasto-response of an arc-weld process using artificial neural networks. *Systems theory - Proceedings of the thirty fourth south eastern symposium*. p440-444.

[160] Mucino, V.H., Avang, M., Klein, R., Klinkhachorn, P. Effects of welding process parameters on residual stresses in curved steel plates: A finite element neural network approach.

[161] Sharma, K., Singh, R.K, Vaze, K.K., Kushwaha, H.S. Residual stress estimation in the inelastic range with non-linear finite element and artificial neural network analysis. BARC newsletter, issue No. 249.

[162] Kumanan, S., Kumar, R.A., Edwin, R.J.D. (2007) Development of a welding residual stress predictor using a function-replacing hybrid system. *Int. J. Manuf. Technol.* 31, p1083-1091.

[163] Edwin, R.J.D., Kumanan, S. (2011) Modelling of residual stress in butt welding. *Materials and manufacturing processes*. 26, p942-947.

[164] Na, G.M., Kim, J.W., Lim, D.H. (2007) Prediction of residual stresses for dissimilar metals welding at nuclear power plants using fuzzy neural network models. *Nuclear engineering and technology*. 39 (4), p337-348.

[165] Toparli, M., Sahin, S., Ozkaya, E., Sasaki, S. (2002) Residual thermal stress analysis in cylindrical bars using finite element method and artificial neural networks. *Computers and structures*. 80, p1763-1770.

[166] Toktas, I., Ozdemir., A.T. (2011) Artificial neural networks solution to display residual hoop stress field encircling a split-sleeve cold expanded aircraft fastener hole. *Expert systems with applications*. 38, p553-563.

[167] MATLAB and Neural Network Toolbox Release 2012a, The MathWorks Inc., Natick, Massachusetts, United States.

[168] Choose a multilayer neural network function (2015). [online] Available: http://uk.mathworks.com/help/nnet/ug/choose-a-multilayer-neural-network-training-function.html Accessed: [04-August-2015]

[169] Mackay, D.J.C. (1991) Bayesian methods for adaptive methods. PhD thesis, California Institute of Technology.

[170] Mackay, D.J.C. (1992) Bayesian interpolation. *Neural Computation*. 4 (3), p415-447.

[171] Mackay, D.J.C. (1992) A practical Bayesian framework for back-propagation networks. *Neural Computation*. 4 (3), p448-472.

[172] R-CODE Software for assessing the integrity of structures containing defects, version 4. Gloucester: British energy generation ltd; 2009.

[173] Mathworks (2014). [online]. Available: http://www.mathworks.com/products/. Accessed: [13-November-14].

[174] Pybrain (2014). [online]. http://pybrain.org/ Accessed: [13-November-14].

[175] Neurolab (2014). [online]. https://pypi.python.org/pypi/neurolab Accessed: [13-November-14].

[176] FFnet (2014). [online]. http://ffnet.sourceforge.net/ Accessed: [13-November-14].

[177] Veqter database (2014).[online]. http://www.veqter.co.uk/residual-stress-database. Accessed: [13-November-14].